Electronic Thesis and Dissertation Repository

3-1-2023 3:00 PM

Use of Electrochemical Techniques and Statistical Analysis to Investigate The Pitting Probability of Copper

Sina Matin, *The University of Western Ontario*

Supervisor: James Jamie Noel, *The University of Western Ontario*
A thesis submitted in partial fulfillment of the requirements for the Doctor of Philosophy degree in Chemistry
© Sina Matin 2023

Follow this and additional works at: https://ir.lib.uwo.ca/etd

Part of the Analytical Chemistry Commons, Materials Chemistry Commons, and the Metallurgy Commons

Recommended Citation

Abstract

The development of a safe permanent disposal plan is essential for the long-term disposal of used fuel bundles. Nuclear Waste Management Organization (NWMO) has been investigating the deep geologic disposal of nuclear waste which offers the optimum passive safety system with a negligible probability of release of radionuclides into the environment.

The proposed used fuel containers (UFC) for the permanent disposal of high-level nuclear waste in Canada is comprised of a carbon steel vessel coated with a 3 mm corrosion-resistant copper layer deposited using a combination of electrodeposition and cold spray deposition. Although copper is often considered to be thermodynamically stable in anoxic conditions, different corrosion processes might occur upon exposure to aggressive anions, such as chloride, sulfate, and sulfide. The presence of oxygen could increase the possibility of passive film formation on Cu which might result in localized corrosion (specifically pitting) and unexpected failure of UFC; so, the pitting corrosion probability of Cu in these conditions should be evaluated carefully.

This research has focused on the development of a new technique to investigate the pitting probability of copper (Cu) in Deep Geological Repository (DGR) conditions using multielectrode arrays and statistical models. Investigation of pitting probability of Cu required the combination of different types of electrochemical experiments including potentiodynamic and potentiostatic polarizations since potentiodynamic polarization test gives us information about the E_b and E_{rp}, however, potentiosatic polarizations simulates the natural condition in which a constant potential is applied to the Cu electrode. As a result, two different applied potentials were chosen based on histograms of E_{corr} and E_b which had been collected using potentiodynamic polarization experiments to simulate the natural conditions. $E_{corr}+ 20$ mV and E_b-20 mV vs SCE were selected as the highest and lowest applied potentials, respectively. Also, the morphology and composition of various types of passive films were investigated using SEM and XPS techniques. These information gave us useful information to evaluate the pitting possibility of Cu in the presence of different types of passive films such as Cu_2O, CuO, and $Cu(OH)_2$ as well as which film was more resistant to pitting corrosion.

Keywords

Summary for Lay Audience

The development of a safe permanent disposal plan is essential for the long-term disposal of used fuel bundles. Nuclear Waste Management Organization (NWMO) has been investigating the deep geologic disposal of nuclear waste which offers the optimum passive safety system with a negligible probability that radionuclides will be released into the environment. In this proposed plan, used fuel bundles will place into used fuel containers (UFC) buried around 500 m underground in suitably dense intact rock or sedimentary deposit, while employing a multi-barrier system. The proposed UFC for the permanent disposal of high-level nuclear waste in Canada is comprised of a carbon steel vessel coated with a 3 mm corrosion-resistant copper layer deposited using a combination of electrodeposition and cold spray deposition. Uniform corrosion of Cu under these conditions has been investigated extensively and the corrosion allowance of Cu in these conditions is determined to be less than 1.5 mm over a million years. However, the presence of oxygen could increase the possibility of passive film formation on Cu which might result in localized corrosion (specifically pitting) and unexpected failure of UFC. This research focused on the pitting probability of Cu in unary and binary solutions containing chloride, sulfate, and carbonate. It is important to note that corrosion parameters are deterministic, however, they are sensitive to different factors such as the composition of the solution, temperature, surface condition, etc. As a result, we are dealing with distributed data either because of the solution to which the surface is exposed or the stochastic nature of passive film rupture. We have developed two different types of methodologies to investigate the breakdown of materials.

I.   Evaluating the susceptibility of Cu to pitting corrosion based on the difference between corrosion potential (E_{corr}) and breakdown potential (E_b).

II. Investigating the pitting probability of Cu based on the difference between E_{corr} and Repassivation potential ($E_{rp)}$ which we named it conservative pitting probability. In this method, pitting initiates when E_{corr} rose above the E_{rp} and repassivation occurs when the E_{corr} drops below the E_{rp}.

A new type of electrochemical experiment has been developed that enables the instrument to perform electrochemical experiments for up to 50 electrodes all in one test. This feature allowed us to have the same conditions for all electrodes as much as possible which

improved the accuracy and reliability of statistical models significantly by decreasing the possibility of errors including human errors. Moreover, Python and R programming languages were used to fit the distribution curves of E_{corr}, E_b, and E_{rp} with possible distribution models. As a result, the probabilities of pitting, conservative pitting, and repassivation of Cu were determined by calculating the overlap between distribution curves of E_{corr} and E_b, E_{corr} and E_{rp} (When the distribution curve of E_{rp} was located on the left side of E_{corr}), and E_{corr} and E_{rp} (When distribution curve of E_{rp} was located on the right side of E_{corr}) respectively. Various electrochemical experiments including potentiodynamic polarization, potentiostatic polarization, and statistical analysis have been conducted to investigate the pitting probability of Cu in different conditions. Furthermore, X-ray photoelectron spectroscopy (XPS) and scanning electron microscopy (SEM) have been used to investigate the composition and morphology of corrosion products formed under these conditions. Moreover, FIB-SEM has been used to evaluate the morphology and thickness of the different types of passive films as well as the distribution of corrosion damage on the Cu/film interface.

Co-Authorship Statement

This thesis includes published and submitted data. I, Sina Matin, was the primary investigator and writer with the following contribution from co-authors.

Chapter 3: Sina Matin performed these experiments. SM and Arezoo Tahmasebi conducted the statistical analysis of the data with the assistance of Dr. James. J. Noël and Dr. Matt Davison. surface analysis was conducted by SM with the assistance of Brad Kobe. Dr. James. J. Noël and Dr. David. W. Shoesmith assisted with editing. All authors assisted in editing the original manuscript. This chapter has been published in the Journal of The Electrochemical Society.
S. Matin, A. Tahmasebi, M. Momeni, M. Behazin, M. Davison, D.W. Shoesmith, J.J. Noël, Use of multielectrode arrays and statistical analysis to investigate the pitting probability of copper. Part I: The Effect of chloride, Journal of The Electrochemical Society, 169 (2022).

Chapter 4: Sina Matin performed these experiments. SM and Arezoo Tahmasebi conducted the statistical analysis of the data with the assistance of Dr. Jamie Noel and Dr. Matt Davison. surface analysis was conducted by SM with the assistance of Brad Kobe. Dr. James. J. Noël assisted with editing. All authors assisted in editing the original manuscript. The final revision of the paper related to this chapter has been submitted to the Journal of The Electrochemical Society for publication.
S. Matin, A. Tahmasebi, A. Morgan, M. Behazin, D. Zagidulin, M. Davison, D.W. Shoesmith, J.J. Noël, Use of multielectrode arrays and statistical analysis to investigate the pitting probability of copper. Part I: The effect of sulfate and bicarbonate.

Chapter 5: Sina Matin performed these experiments. SM and Dr. Jeffery Henderson performed the surface analysis with the assistance of Dr. Mark Biesinger. Dr. James. J. Noël assisted with editing. All authors assisted in editing the original manuscript. The paper is under review in the journal of npj Materials Degradation.
S. Matin, J. D. Henderson, M. Biesinger, B. Kobe, D. W. Shoesmith, J.J. Noël, Susceptibility of copper to pitting corrosion in bicarbonate buffer solutions: Part I. Effect of chloride

Acknowledgments

I would like to express my gratitude to the many people who have supported me throughout my Ph.D. Journey.

First, I would like to thank my supervisor, Dr. Jamie Noël for his unconditional support, encouragement, and guidance to finish my Ph.D. project. I thought that my writing was not really good when I started my Ph.D., but then I realized that no one can pass your writing exam, even Dave, and it was a relief to me. You were the most patient supervisor and friend that I have seen in my Ph.D. journey and always smiled even in hard times. You, as a supervisor and friend, not only shaped my professional career but taught me how to handle tough people and hard situations in the work environment. I could not have asked for a better supervisor.

I would like to extend my deepest thank to Dr. Dave Shoesmith for being an amazing leader and mentor in my Ph.D. journey. I know that sometimes, I drove you crazy with my ideas about the research but you kindly listened to me and helped me to shape those ideas. You and Chris showed me how a couple can change my entire life with your kindness and support. Chris, I promise you that I would never ask Dave to revise my papers on Saturday.

Next thank goes to Noël's research groups. I want to thank a few individuals who helped me to finish this journey: Dr. Dimitrij Zagidulin, thank you for being such a tough person and giving me hard time even when it was not necessary. You were a driving force in my research and pushed me to a level to do something special in my research. After almost 5 years, I truly believe that you are an asset in Jamie's lab and I am so thankful for all you have done during my Ph.D. project. Dr. Roshan Daljeet, I had so many fun times with you in the lab and Nanofab. You were such a great friend and teammate and I enjoyed every second of my time working with you in the lab. Dr. Mojtaba Momeni, your ideas helped me to shape my research and I truly appreciate all your support. Adam Morgan, you showed me how brilliant an undergraduate student can be. Your hard work helped me to finish one of the biggest parts of this research and I really believe that Jamie is so lucky to have you on his team as a Ph.D. Student.

I would also like to thank the people at Surface Science Western (SSW) whom I was lucky to learn from them and spent amazing time with them at SSW. Dr. Mark Bisinger, Mr. Brad Kobe, Dr. Sridhar Ramamurthy, Mr. Ivan Barker, Dr. Vahid Dehnavi, and Dr. Jeffrey Henderson. I truly appreciate all your support and encouragement during my Ph.D. journey.

Finally, I would like to express my deepest appreciation to my family. To my parent, I could not have done this without your unconditional support. Your unwavering belief in me has been the foundation of my success. I am particularly grateful to the best friend of my life and my wife, Leila (Sahar) for her constant love and support, and patience during the long and challenging Ph.D. journey. Your encouragement and patience during the tough times helped me to finish this journey. Your understanding, unwavering support, and encouragement have been an amazing source of strength for me throughout this journey. To my dearest daughter, Nila, your smile when you woke up in the early morning was the best thing in my entire life. You were my biggest cheerleader that helped me to finish the writing. Watching you grow and develop during these past few months proved that I should have done the writing a long time ago and not spent a single second of my time on my Ph.D. thesis since nothing is more enjoyable than watching and playing with you. I am so proud to be your parent.

This thesis is dedicated to my beautiful wife and daughter,

Leila and Nila

Table of Contents

List of Tables

List of Figures

List of Acronyms and Symbols

Acronyms

BE	Binding Energy
BSE	Backscattered Electron
CDF	Cumulative Density Function
CE	Counter Electrode
Cl^-	Chloride Ion
CPT	Critical Pitting Temperature
Cu	Copper
DGR	Deep Geological Repository
EDS	Energy-dispersive X-ray Spectroscopy
F	Farady
FIB	Focused Ion Beam
H_2O	Water
HCO_3^-	Carbonate Ion
HFM	High-Field Model
KE	Kinetic Energy
MCB	Mass and Charge Balance
MMA	Multichannel Microelectrode Analyzer
Na_2SO_4	Sodium Sulfate

NaCl	Sodium Chloride
NaHCO$_3$	Sodium Bicarbonate
NWMO	Nuclear Waste Management Organization
O$_2$	Oxygen
OCP	Open Circuit Potential
PDF	Probability Density Function
PDM	Point Defect Model
PPR	Pitting Propensity Rating
RE	Reference Electrode
SCE	Saturated Calomel Electrode
SE	Secondary Electron
SEM	Scanning Electrode Microscopy
SHE	Standard Hydrogen Electrode
SKB	Swedish Nuclear Fuel and Waste Management Company
SME	Size Matching Effect
SO$_4^{2-}$	Sulfate Ion
UFC	Used Fuel Container
WE	Working Electrode
XPS	X-ray Photoelectron Spectroscopy
ZRA	Zero Resistance Ammeter

Symbols

C_{crit} Critical Concentration

C_{sat} Saturated Concentration

C_{surf} Surface Concentration

e   Electron

$E°$ Standard Potential (V)

E_b Breakdown Potential (V)

E_{cell} Cell Potential (V)

E_{corr} Corrosion Potential (V)

E_{eq} Equilibrium Potential (V)

E_{pass} Passivation Potential (V)

E_{pit} Pitting Corrosion (V)

E_{rp} Repassivation Potential (V)

ε   Kurtosis

$i_{diff, crit}$ Critical Diffusion Current Density (A/cm^2)

$i_{diss, max}$ Maximum Dissolution Current Density (A/cm^2)

i_L Limited Current Density (A/cm^2)

i_{pass} Passivation Current (A/cm^2)

V   Variation

$α_a$ Transfer coefficient of an anodic half-reaction

α_c	Transfer coefficient of a cathodic half-reaction
γ	Gamma
ΔG	Gibbs free-energy Change (KJ mol^{-1})
$\Delta G°$	Standard Gibbs free-energy Change (KJ mol^{-1})
σ	Standard Deviation
α	Skewness
η	Over-potential (E_{app}-E_e) (V)

Chapter 1

1 Introduction and Literature Review

1.1 Project Motivation: Safe Permanent Disposal of Used Nuclear Fuel

Nowadays, producing inexpensive and environmentally friendly electricity is crucial, because electricity plays a significant role in human life, yet some generating methods cause extensive environmental harm. A nuclear power plant is one of the best choices to supply electricity without producing greenhouse gases. For instance, Sweden produces 40% of its electricity from nuclear power plants [1, 2]. In Canada, 16.4% of all electricity is produced by nuclear power plants [3]. Recently, most countries have focused on the research and development of nuclear power plants to obtain a clean source of energy. Today 440 nuclear power plants generate around 10% of electricity in the world [4]. Most nuclear power plants in Canada are located in Ontario followed by New Brunswick; as a result, around 56% of Ontario's electricity and 38% of New Brunswick's electricity are produced by nuclear power [3-5]. Producing electricity from nuclear materials has some advantages, such as no air pollution; however, management and disposal of nuclear materials is a major undertaking. As of June 2019, 2.9 million nuclear fuel bundles were in wet and dry storage in Canada [6]. Spent nuclear fuel bundles have been stored in different facilities across Canada while various permanent disposal scenarios have been investigated since 2002. The Nuclear Fuel Act was enacted to govern the management of nuclear fuel waste in Canada, resulting in the establishment of the Nuclear Waste Management Organization (NWMO). The main goal of NWMO is to design and implement Canada's plan for the long-term management of used nuclear fuel [7]. Finland became the game changer by announcing the start of the construction site in November 2020. The plan is to place the used fuels into copper cylinders followed by the emplacement of cylinders 1300 feet underground which are covered by bentonite clay to prevent water from seeping in and corroding the cylinders [8]. Sweden is also another pioneer country in the management and disposal of spent nuclear fuel. The Kärnbränslesäkerhet (KBS) method introduced by the Swedish Nuclear Fuel and

Management Company (SKB) is an example of a deep geologic repository (DGR) method for the permanent disposal of the spent nuclear fuel [9]. In the proposed Swedish repository (KBS-3 model), the spent fuel container will comprise a cylindrical copper shell and a nodular cast iron insert inside the copper shell. This container will be emplaced 500-1000 m underground in a DGR and then backfilled with bentonite clay. Figure 1.1 shows the schematic of permanent nuclear fuel disposal in a Swedish repository (KBS-3 model).
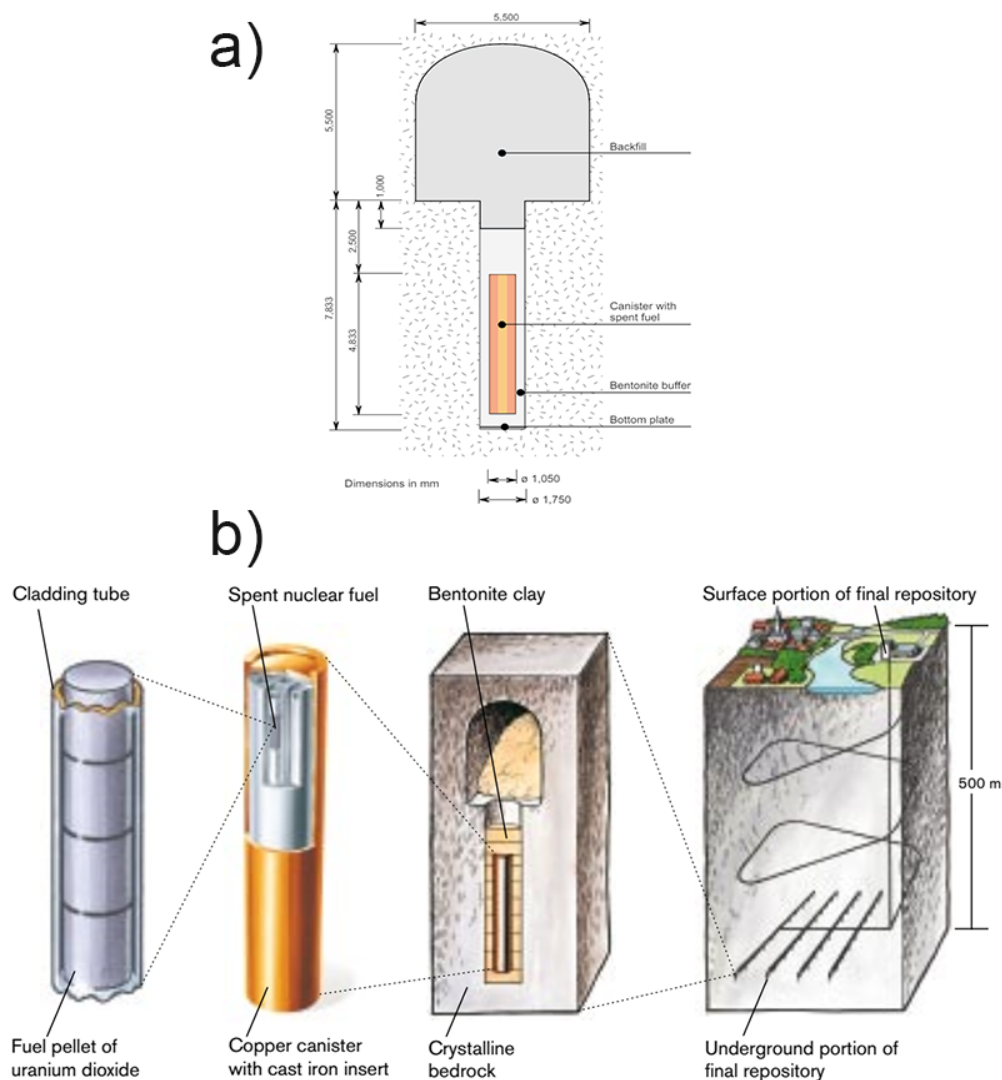
Figure 1.1: a) Schematic design of borehole with bentonite clay that covers the spent nuclear fuel container; b) schematic of proposed KBS-3 deep geological repository (DGR). Images courtesy of SKB [10, 11].

1.1.1   Deep Geological Repository (DGR) Design: Multi-Barrier System

Generally, the disposal of spent nuclear fuel has 3 steps. In the first step, spent fuel from CANDU reactors is placed in a water-filled pool for 7 to 10 years, which allows the temperature and radioactivity of the fuel bundles to decrease. After that, the fuel bundles will be placed in a dry storage container for 50 years, over which time there will be a significant reduction in the radiation level and spent fuel becomes ready for permanent disposal in a DGR [12]. The radiation field of spent fuel (fission products) will still be significant for up to one million years as illustrated in Fig 1.2 and might cause catastrophic damage to the environment in case of the release of radionuclides to the environment [13]. To avoid the nuclear pollution of the environment, a multi-barrier system (natural and engineered barriers) comprises the placement of spent fuel bundles 500-1000 m underground in a DGR followed by the backfill of the used fuel container with bentonite clay.
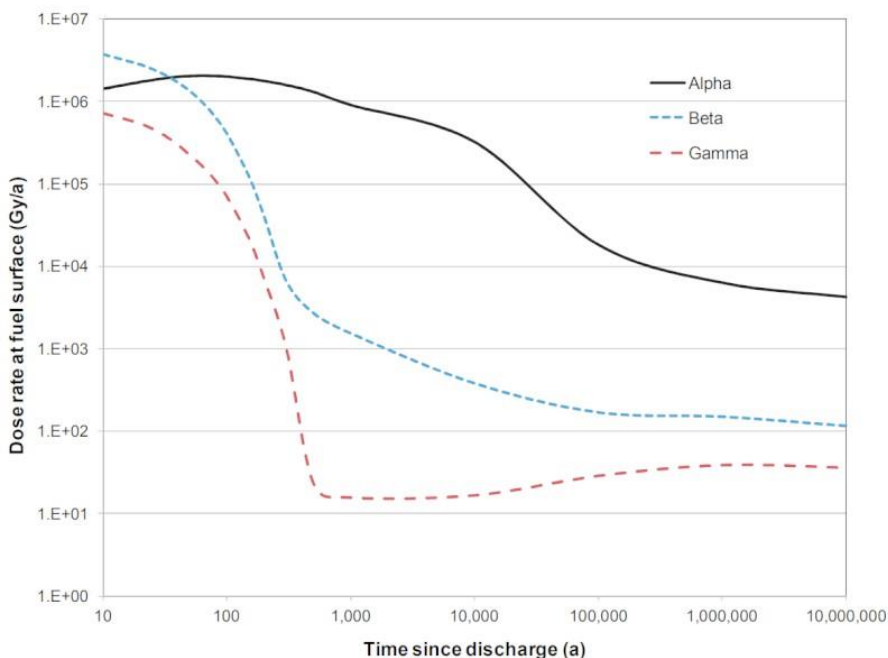
Figure 1.2: Dose rate of radiation over time after discharging from the reactor. CANDU fuel bundles are in contact with water [14].

In Canada, the natural barrier includes a suitable rock structure at a depth ≥ 500 m with specific properties such as low groundwater flow rate and absence of dissolved oxygen (O2) [15], while the engineered barrier consists of nuclear fuel pellet, fuel bundle, robust used fuel container (carbon steel vessel coated with ~3 mm of copper), and bentonite clay as shown in Fig 1.3. The natural barrier in Canada will be either sedimentary or crystalline rock. The used fuel container is emplaced at a depth of approximately 500 m underground. The exact depth of emplacement is dependent on the geology of the selected site (sedimentary or crystalline rock) while it should meet the safety requirements of the project [16]. The movement of groundwater at this depth is really slow (around 1 mm per year) and can take 100,000 years to reach the surface. Therefore, any released radionuclides will have enough time to decay and become harmless before reaching the water table near the surface [17-19].
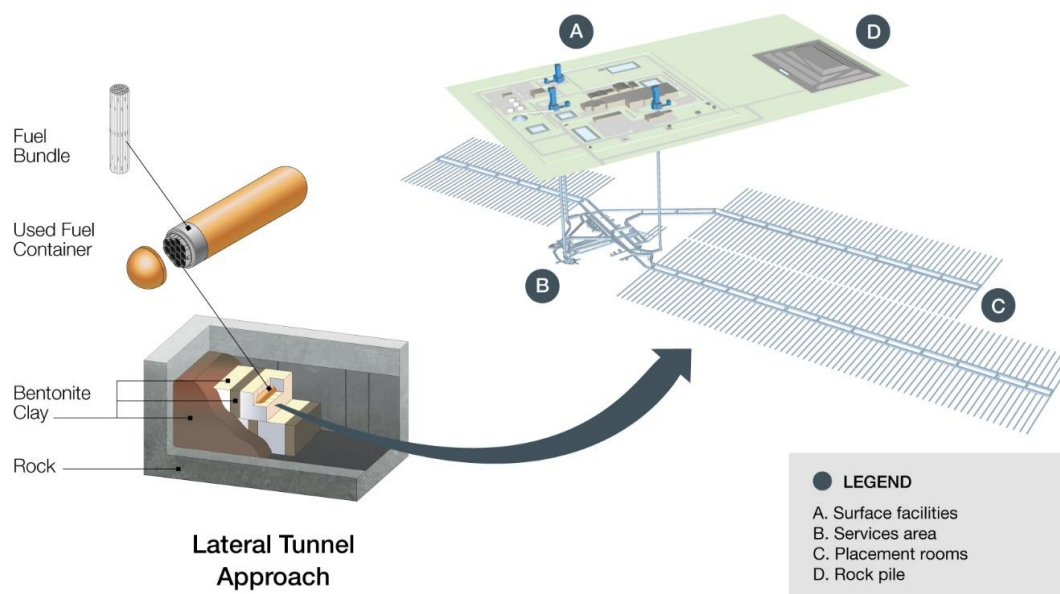
Figure 1.3: Schematic representation of the proposed Canadian Deep Geological Repository (DGR). Image courtesy of NWMO [20].

The engineered used fuel container comprises a carbon steel vessel that provides the mechanical strength to withstand the repository loads (e.g., hydrostatic, lithostatic, and glaciation) and Cu coating which plays a role as a corrosion barrier [16, 21]. The first reference design (Mark I) of the used fuel container consisted of an inner carbon steel

vessel placed inside a 25-50 mm thick outer Cu shell (Fig. 1.4a); however, Kwong [22] and Scully [23] proposed the corrosion allowance of 1.27 mm over 1 million years for Cu under DGR conditions. As a result, the second reference design was introduced (Mark II) as illustrated in Fig. 1.4b. The size of Mark II is much smaller than Mark I which makes the handling and emplacement of used fuel container much easier in the DGR. In addition, a thin layer of Cu (~3mm) is coated directly on top of the carbon steel vessel avoiding any gap between Cu and carbon steel and possible mechanical issues such as creep. It is important to note that the thickness of copper coating still exceeds the conservative corrosion allowance (1.27 mm over 1 million years) [22, 24].
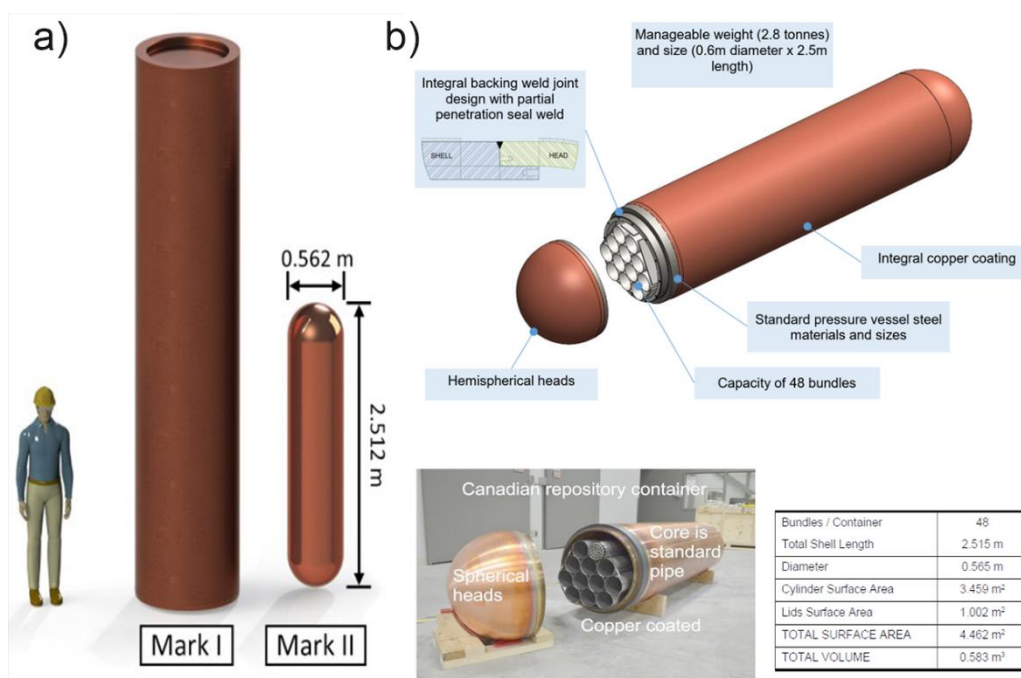
Figure 1.4: a) Comparison between two conceptual designs for the disposal of nuclear waste (Mark I and Mark II); b) schematic of Mark II container proposed by NWMO as current reference design [25].

The proposed coating procedure includes an electrodeposition technique for the main body and head parts and cold spray technique for one of the welded joints between the head and body. The cold spray technique has been chosen since it can be automated and fast after the loading of spent fuel into the used fuel container. The cold spray technique has some drawbacks compared to the electrodeposition technique, such as higher stress,

lower ductility, higher void density, and less uniformity [5, 15, 22]. Finally, the used fuel container will be surrounded with highly compacted bentonite clay to create a second layer of engineered barrier in the DGR environment. The bentonite clay swells upon contact with moisture and seals the whole used fuel container; as a consequence, the used fuel container will be in contact with a local environment in which the rate of water flow and chemical diffuson will be really low. The full saturation of the near field is assumed to take around 50 years for crystalline host rock and 5000 years for sedimentary host rock [26].

1.1.2 Evolution of Repository Conditions

The DGR conditions will evolve with time upon the emplacement of the used fuel container (UFC). The DGR will evolve from a warm, dry, and oxic condition to a cool, wet, and anoxic condition [16, 27, 28]. The oxygen will be present in the first early stage of emplacement due to the excavation process. The corrosion behaviour of UFC should be evaluated carefully in different conditions since environmental factors such as O_2, humidity, concentrations of anions, and saturation will be changed over time as illustrated in Fig. 1.5. The groundwater contains various anions and cations such as Cl^-, SO_4^{2-}, CO_3^{2-}, and Ca^{2+} with a wide range of concentrations. Chloride is the predominant anion in groundwater, with concentrations that vary between 0.1 M and 5 M [24]. The evolution processes at the container surface are related to each other resulting in different corrosion processes over time. At first, the temperature of the used fuel container will increase due to the radioactive decay of radionuclides within the container. As a result, both relative humidity and saturation level decrease in the early stage of emplacement after DGR closure, Fig 1.5. Afterward, bentonite around the used fuel container will be dried with the increase of temperature, and groundwater will flow through the bentonite clay very slowly. The resaturation speed depends on the resaturation properties of bentonite clay, the thermal conductivity of the used fuel container, and the hydraulic conductivity of the host rock. As a result, the used fuel container will cool down and full resaturation of the local environment will occur, followed by consumption of O_2 due to either Cu corrosion processes or reactions with minerals and organic materials in the bentonite [28]. King [29] proposed that oxic conditions would be present for several

decades; however, other researchers suggested a much shorter period from a few weeks to several months [30]. The high temperature and low humidity environment result in a negligible corrosion rate of Cu despite the oxidizing conditions. The concentrations of anions in contact with the container will depend on the initial groundwater composition and rate of reactions. The resaturation time of the repository depends on various parameters and is estimated to be around 50 years in crystalline rock (Fig. 1.5) and much longer in sedimentary clay (i.e., ~5000 years) [28, 30-32].

a) Upon exposure of the container, four different exposure conditions would be expected:

b) Aerated condition with the presence of water vapour on the surface of the container;

c) Aerated water vapour in equilibrium with condensed H_2O on the Cu surface;

d) Anoxic condition with either water vapour in equilibrium with condensed H_2O or fully

e) saturated condition;

f) Fully saturated anoxic condition on Cu surface.
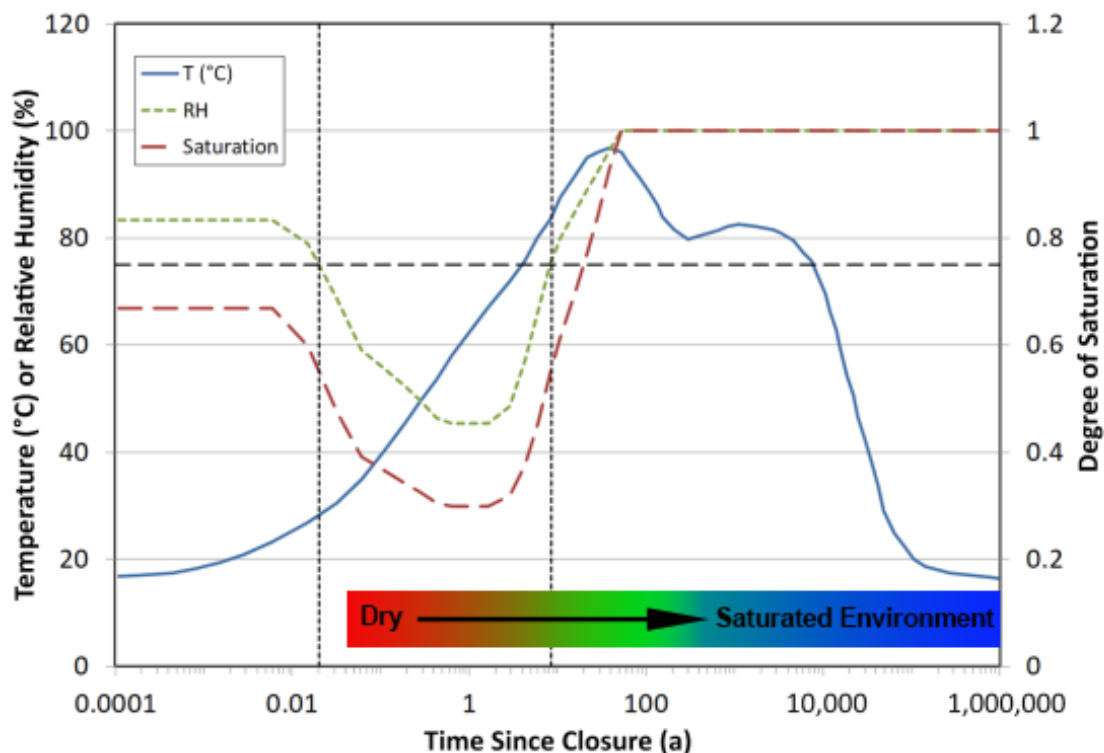
Figure 1.5: Time-dependent evolution of the temperature and saturation profile on the surface of used fuel container in Canadian DGR [28].

The redox condition will be oxidizing in the early stage of emplacement of the used fuel container, due to the presence of O_2. Trapped O_2 will be consumed by the corrosion process and other processes like microbial activities and minerals presented in bentonite clay. redox conditions will also be influenced due to the radiolysis of water resulting from the γ-radiation emitted by the fuel waste form. The γ-dose rate is dominated by the decay of the fission products in the fuel and is calculated to vary at the container surface from ~2 Gy/h after 10 years to ~0.02 Gy/h after 200 years; however, these numbers could be different from container to container depending on what is inside of the container [33]. Therefore, the Cu surface could experience different corrosion processes during this early stage of emplacement via oxidants such as O_2 and radiolysis products (e.g., nitric acid) [34].

Cu is thermodynamically stable under certain anoxic conditions and protects the container from corrosion failure once the initial O_2 has been consumed. However, localized corrosion processes (particularly pitting corrosion) might occur due to the presence of aggressive anions or/and an increase in the pH of the near field solution while the presence of oxygen is the prerequisite for pitting corrosion to occur. So, the susceptibility of Cu to localized corrosion, specifically pitting, must be carefully considered in the early stage of DGR evolution. In general, susceptibility to pitting corrosion is determined by comparing the corrosion potential of the material (E_{corr}) to the breakdown potential (E_b), both of which are distributed parameters. These are distributed parameters due to uncontrollable variations in the structure and local environment at the metal surface and the stochastic nature of passive film rupture. It is important to note that this susceptibility analysis is based on the concept that pitting is only possible if the E_{corr} is equal to, or more positive than the E_b. Since pitting corrosion could result in an unexpected failure of used fuel containers, this thesis has focused on the pitting probability of Cu under different DGR conditions, using electrochemical techniques and statistical models.

1.2   Intorduction to Aquous Corrosion

1.2.1   Thermodynamics of Aqueous Corrosion

Corrosion is the degradation of materials (specifically metals) comprises of chemical and electrochemical reactions. The electrochemical reaction includes two half-reactions, one half-reaction loses electrons (anodic) and another one gains electrons (cathodic), as illustrated in equations 1 through 3 . M is defined as metal, Ox is an oxidant, and Red is a reductant. Cu has three oxidation states, Cu(0), Cu^+ and Cu^{2+}; so the oxidation and reduction processes will involve either one or two-electron transfer (e^-) to produce or reduce Cu(0), Cu^+, or Cu^{2+}.

$M \rightleftarrows M^{n+} + ne^-$ (anodic half-reaction)   1

$Ox + ne^- \rightleftarrows Red$ (cathodic half-reaction)   2

$M + Ox \rightleftarrows M^{n+} + Red$ (overall reaction)   3
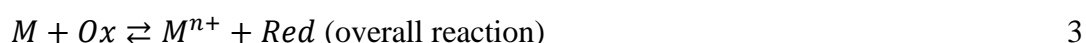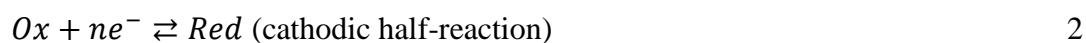
The overall reaction could be a reversible reaction and the direction of reaction depends on the sign of Gibbs free energy (ΔG). A reaction is spontaneous when E is positive resulting in $\Delta G < 0$. Under standard conditions, standard electrochemical potential ($E°$) can be defined for a half-reaction which is equal to E. As a result, $\Delta G°$ can be calculated using standard electrochemical potential ($E°$) of each half-reaction using equation 4. The same equation can be used to calculate the ΔG of non-standard conditions by substituting E^0 with E as shown in equation 5 [35].

$$\Delta G° = -nFE° \hspace{6cm} 4$$

$$\Delta G = -nFE \hspace{6.2cm} 5$$

Where n is the number of electrons transferred in the reaction and F is Faraday's constant (96,485 C/mol). ΔG can be obtained from $\Delta G°$ using equation 6, in which R is the ideal gas constant (8.314 J/mol.K), T is the temperature in Kelvin, and a is the activity, respectively.

$$\Delta G = \Delta G° + RT\ln\left(\frac{a_{red}}{a_{ox}}\right) \hspace{4cm} 6$$

A direct relationship between E and $E°$ can be obtained by substituting equations 4 and 5 into equation 6 which is known as the Nernst equation (equation 8).

$$-nFE = -nFE° + RT \ln \left(\frac{a_{red}}{a_{ox}}\right) \hspace{3.5cm} 7$$

$$E = E° - \frac{RT}{nF} \ln \left(\frac{a_{red}}{a_{ox}}\right) \hspace{4cm} 8$$

Thermodynamics gives information about the spontaneity of reactions. Therefore, the Nernst equation can be used to investigate which reaction is favourable. The cell potential, Ecell, is the potential difference between two half-reactions (cathodic and anodic reactions) and can be calculated by subtracting Eeq of the oxidation half-reaction from Eeq of the reduction half-reaction.

$$E_{cell} = E_{eq}(cathodic\ reaction) - E_{eq}(anodic\ reaction) \hspace{1.5cm} 9$$

Finally, the direction of the overall reaction will be obtained by substituting Ecell into equation 5 [35]. It is important to note that both potentials are written in reduction form in equation 9.

Pourbaix (E-pH) diagram is used to illustrate what phases and species are thermodynamically stable over a range of conditions and corrosion processes [36, 37]. A Pourbaix diagram for Cu is shown in Fig. 1.6, presenting different copper products such as Cu(0), Cu_2O, CuO, CuO_2^{2-}, and $HCuO_2^-$.
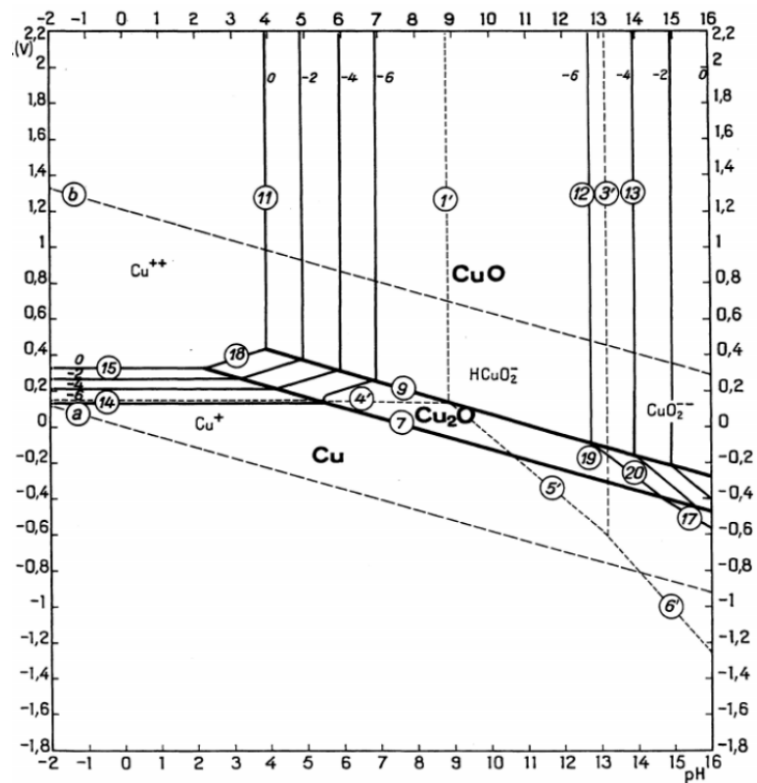
Figure 1.6: Pourbaix (E-pH) diagram of Cu, Cu_2O, and CuO [38].

The lines in the Pourbaix diagram are defined by the Nernst equation and solubility equilibria for specific equilibrium reactions and conditions. The stability regions of different species are defined based on equilibrium potentials, the solubility of solid phases, and complexation constants for metal ions in the aqueous solutions as a function of pH, temperature, and concentration of complex species. The water stability region is indicated with two dashed lines. The upper dashed line indicates the equilibrium potential

for O2/H2O reaction and the lower dashed line defines the equilibrium potential for the H2/H2O reaction [37]. Three different types of lines are defined in the Pourbaix diagram. Vertical lines indicate reactions that are independent of potential. Horizontal lines define the reactions that are only independent of pH, and sloped lines describe the reactions which are dependent on both potential and pH [35, 39]. For instance, both upper and lower dashed lines related to the water stability region are dependent on both pH and potential, like reaction 10, while electrochemical reactions with no pH dependence result in horizontal lines such as reaction 11.

$$2H^+ + 2e^- \rightleftarrows H_2 \qquad\qquad\qquad 10$$
$$Cu^+ + e^- \rightleftarrows Cu \qquad\qquad\qquad 11$$

Chemical dissolution processes have no potential dependence, resulting in vertical lines in the Pourbaix diagram (equation 12).

$$CuO + H_2O \rightleftarrows Cu^{2+} + 2OH^- \qquad\qquad\qquad 12$$

1.2.2   Kinetics of Aqueous Corrosion

Thermodynamics gives information about the possibility of a reaction occurring; however, kinetics indicates the reaction path and rate. Both anodic and cathodic reactions occur at the same rate under equilibrium condition and the rate can be calculated using equation 13 when the reaction is a first-order reaction.

$$R = Kc \qquad\qquad\qquad 13$$

where R is the rate of the reaction, K is the rate constant, and c is the concentration of the reacting species. In electrochemical reactions, the rate is directly proportional to the current density (I) and can be calculated as shown in equation 14:

$$R = \frac{I}{nF} \qquad\qquad\qquad 14$$

where I is the current density, n is the number of electrons transferred in the reaction, and F is Faraday's constant. Since an overall reaction is the combination of two half-

reactions, the rates of anodic and cathodic reactions can be calculated using equations 15 and 16 respectively.

$$I_A = nFk_a c_R \qquad\qquad 15$$

$$I_C = -nFk_c c_O \qquad\qquad 16$$

where Ka and Kc are anodic and cathodic rate constants, and C_R and C_O are the concentrations of the reductant and oxidant, respectively. The overall current is the sum of anodic and cathodic currents and can be written as:

$$I = I_A + I_C = nFk_a c_R - nFk_c c_O \qquad\qquad 17$$

K is an electrochemical rate constant; therefore, it is potential dependent and can be calculated as below for anodic and cathodic reactions:

$$K_a = K_0 \exp\left(\frac{\alpha_a nF\eta}{RT}\right) \qquad\qquad 18$$

$$K_c = K_0 \exp\left(-\frac{\alpha_c nF\eta}{RT}\right) \qquad\qquad 19$$

Where K_0 is the standard rate constant, α is the transfer coefficient, and η is the overpotential (E-E$_{eq}$). The sum of α_a and α_c will be 1 and the terms can be simplified to α and 1- α for the anodic and cathodic reactions, respectively.

$$\alpha_a + \alpha_c = 1 \qquad\qquad 20$$

η indicates how far a reaction is from equilibrium. Substituting equations 18 and 19 into equation 17 yields equation 21.

$$I = nFK^0 \exp\left(\frac{\alpha nF\eta}{RT}\right) c_R - nFK^0 \exp\left(-\frac{(1-\alpha)nF\eta}{RT}\right) c_O \qquad\qquad 21$$

At equilibrium, the current for both anodic and cathodic reactions are the same and equal to exchange current density (I$_0$), the current density that flows equally in equilibrium and both directions; so, equation 21 can be simplified to:

$$I = I_0 \left[\exp\left[\frac{\alpha nF\eta}{RT}\right] - \exp\left[-\frac{(1-\alpha)nF\eta}{RT}\right] \right] \qquad\qquad 22$$

Equation 22 is defined as the Butler-Volmer equation in which I$_0$ is related to the standard rate constant as below:

$$I_0 = nFK^0 c_O^{(1-a)} C_R^a \qquad\qquad 23$$

The butler-Volmer equation is illustrated graphically in Fig. 1.7, where the dashed lines define the cathodic and anodic currents and the solid line denotes the overall current. For instance, when a large anodic overpotential (η_a) is applied, the reaction becomes irreversible and the cathodic current contribution approaches zero; as a result, only an anodic current can be observed (equation 24). The same process would be observed for a large cathodic overpotential (η_c) and the anodic current approaches zero.

$$I = I_A = I_0 \left[exp \left[\frac{\alpha nF\eta}{RT} \right] \right] \qquad 24$$

Equation 24 can be expressed logarithmically resulting in a linear relationship between log(IA) and η with the y-intercept of log(I_0) and the slope of αnF/RT. Therefore, the anodic Tafel slope coefficient is defined as β_A (equation 26). The same procedure can be used to identify the cathodic Tafel slope coefficient (β_C) [35].

$$log(I_A) = log(I_0) + \left(\frac{\alpha nF}{RT} \right) \eta \qquad 25$$

$$\beta_A = \frac{2.303RT}{\alpha nF} \qquad 26$$
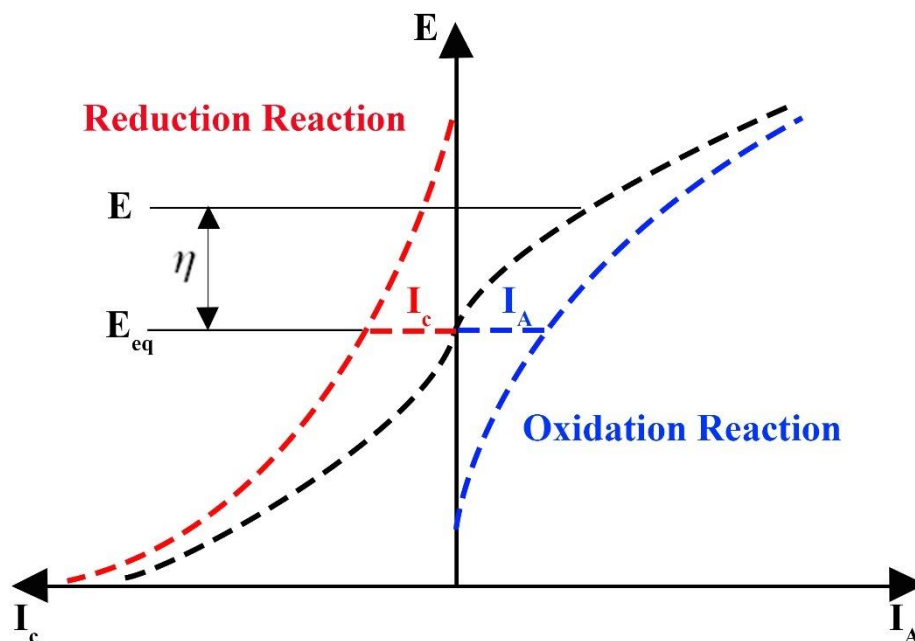
Figure 1.7: The potential-current diagram for an electrochemical reaction based on the Butler-Volmer equation. The blue line represents the anodic current and the red line defines the cathodic current. The overall reaction is shown with a black line. Overpotential as η. At $\eta = 0$, I0=IA=|IC|.

In a corrosion process, the anodic part of one reaction is coupled with the cathodic part of another and both reactions will occur simultaneously dictating the overall process. As a result, both reactions are polarized away from their E_{eq} when coupled and corrosion potential (E_{corr}) lies between Eeq of cathodic and anodic half-reactions. Under corrosion conditions, the electrons produced by oxidation of the metal will be consumed by the coupled cathodic reaction; so, both anodic current (I_a) and cathodic current (I_c) are equal but opposite in sign. This current is defined as corrosion current (I_{corr}).

$$I_a = |I_c| = I_{corr} \qquad\qquad 27$$

The current-potential relationship between the anodic half of one reaction and the cathodic half of another one is determined by Wagner-Traud as illustrated in equation

$$28. I = I_{corr}\left[exp\left[\frac{\alpha_a nF(E-E_{corr})}{RT}\right] - exp\left[-\frac{\alpha_c nF(E-E_{corr})}{RT}\right]\right] \qquad\qquad 28$$

where I_{corr} is the corrosion current at E_{corr} when no external potential is applied, α_a and α_c are the transfer coefficients for anodic and cathodic reactions, respectively, and ($E-E_{corr}$) is the applied potential. It is important to mention that α_a and α_c do not follow the equation 21 since both anodic and cathodic half-reactions are from two different electrochemical reactions.

The Wagner-Traud and Butler-Volmer equations are similar in form; so, the Wagner-Traud equation can be simplified to yield Tafel plots for sufficiently high overpotential. The equation is valid as long as the overall reaction would be under charge transfer control. Various factors would affect the electrochemical reaction rate. For example, when the rate of charge transfer at the electrode/electrolyte interface is high, then the rate of reactant transfer to the electrode surface could become the rate-limiting step. Another factor that might affect the reaction rate is the formation of oxide films on the surface. An oxide film can decrease or even hinder ionic transport contributing to a low corrosion rate. There is a possibility of the formation of corrosion products by the dissolved cations on the electrode surface which might result in limited transport of oxidant to the surface or the metal cation away from the surface. In some situations, the cathodic reaction will occur on the oxide. As a result, the quality and uniformity of the oxide film will control the corrosion rate due to the difference in electrical resistivity of the oxide film compared

to the base metal. Uniform and dense oxide film or corrosion products lead to a lower corrosion rate; however, an imperfect oxide film may result in a higher corrosion rate at the defect. A passive film is a uniform and coherent oxide film that protects the base metal from further dissolution and decreases the rate of corrosion significantly. However, a local breakdown of the passive film results in formation of a large cathode (passive film) and small anode (local breakdown site); so, the film will act as a large cathode and support a small anode at the breakdown site, leading to localized corrosion.

1.2.3   Basics of Cu Corrosion

Based on the Pourbaix diagram (Fig 1.8), Cu is stable over a wide range of pH due to the relatively high E° associated with the conversion of Cu^+ and Cu^{2+} to Cu(0), equations 29 to 31 [38-40]. Cu can be converted to Cu^+ and Cu^{2+} in the presence of oxidants, resulting in the formation of Cu(I) and Cu(II) compounds and soluble species. The compositions of products depend on the type and concentration of anions in the system [41, 42]. It is important to note that Cu^{2+} is dominant in aerated solutions due to the fast conversion of Cu^+ to Cu^{2+}, equation 32; however, Cu^+ never reaches zero due to the potential disproportionation-comproportionation equilibrium, as illustrated in equation 33. Some anions such as Cl^- can make a complex with Cu and form various dissolved species such as $CuCl_2^-$ contributing to a change in the Cu^+/Cu^{2+} ratio [43-47].

$$Cu^{2+} + e^- \rightleftarrows Cu^+ \quad E^0_{eq} = 0.153 \text{ V} \tag{29}$$

$$Cu^{2+} + 2e^- \rightleftarrows Cu \quad E^0_{eq} = 0.342 \text{ V} \tag{30}$$

$$Cu^+ + e^- \rightleftarrows Cu \quad E^0_{eq} = 0.521 \text{ V} \tag{31}$$

$$4Cu^+ + O_2 + 4H^+ \rightleftarrows 4Cu^{2+} + 2H_2O \tag{32}$$

$$2Cu^+ \rightleftarrows Cu^{2+} + Cu \tag{33}$$
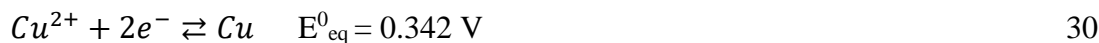
DGR condition will evolve from a warm and oxic condition to a cool and anoxic condition; therefore, different corrosion processes might occur over time. Different anions can affect the stability of Cu under DGR conditions with dissolved O_2, chloride (Cl^-), and sulphide (SH^-) having the most significant effect [48]. The amount of O_2 trapped in the DGR upon closure is determined to be around 13 mol/container based on the current design [49]. Moreover, the groundwater composition in the DGR will be

different depending on the selected location. It is important to note that the bentonite clay will change the groundwater composition and pH leading to the formation of a buffer solution with pH in the range of 7-9 [24]. It also affects the concentrations of other anions while chloride will remain the dominant anion in the DGR [24, 50].

1.2.3.1   Effect of Chloride and Oxygen

Although Cu is thermodynamically stable under an anoxic condition, some corrosion processes might occur under DGR conditions, specifically in the early stages of emplacement and the presence of O_2. As a result, investigation of corrosion processes is crucial for the design and safety of the used fuel container under Canadian DGR conditions. Many researchers have extensively investigated the corrosion behaviour of Cu under DGR conditions and found that dissolved O_2 and Cl^- negatively affect Cu corrosion, while carbonate has a positive effect on the corrosion behaviour of Cu by improving the oxide formation [48, 51-53]. Cu is thermodynamically stable in various $[Cl^-]$ over a large range of pH. Corrosion might occur with increasing $[Cl^-]$ to 1 M and pH < 1, even in the absence of O_2, since the horizontal line between Cu and $CuCl_2^-$ falls below the water stability. The types of corrosion products are varied depending on the pH of solutions. Based on the Pourbaix diagram, the presence of O_2 might oxidize the Cu (Fig 1.8). As a result, the effect of O_2 on the corrosion behaviour of Cu has been investigated by many researchers [24, 51, 54-57]. Cu_2O is thermodynamically stable in aerated solutions with pH within the range of near-neutral to basic. In aerated solutions with pH in the range of neutral to alkaline, Cu_2O can be formed via the following reaction [51-53]:

$$2CuCl_2^- + 2OH^- \rightleftarrows Cu_2O + H_2O + 4Cl^- \hspace{4cm} 34$$
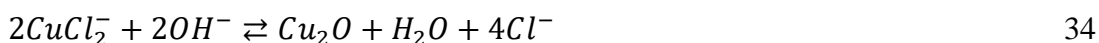
The cathodic reaction will be the oxygen reduction reaction (ORR); therefore, increasing $[O_2]$ will increase the corrosion rate [51].

$$O_2 + 2H_2O + 4e^- \rightleftarrows 4OH^- \hspace{5cm} 35$$

Since the container surface will be surrounded by bentonite clay, the O_2 reduction will be limited by the rate of diffusion through the clay which in turn leads to a lower corrosion rate [51]. Some researchers proposed that there is a possibility that the corrosion rate

might be affected by the diffusion rate of Cu species from the surface, not O_2 through the bentonite clay [51, 52].
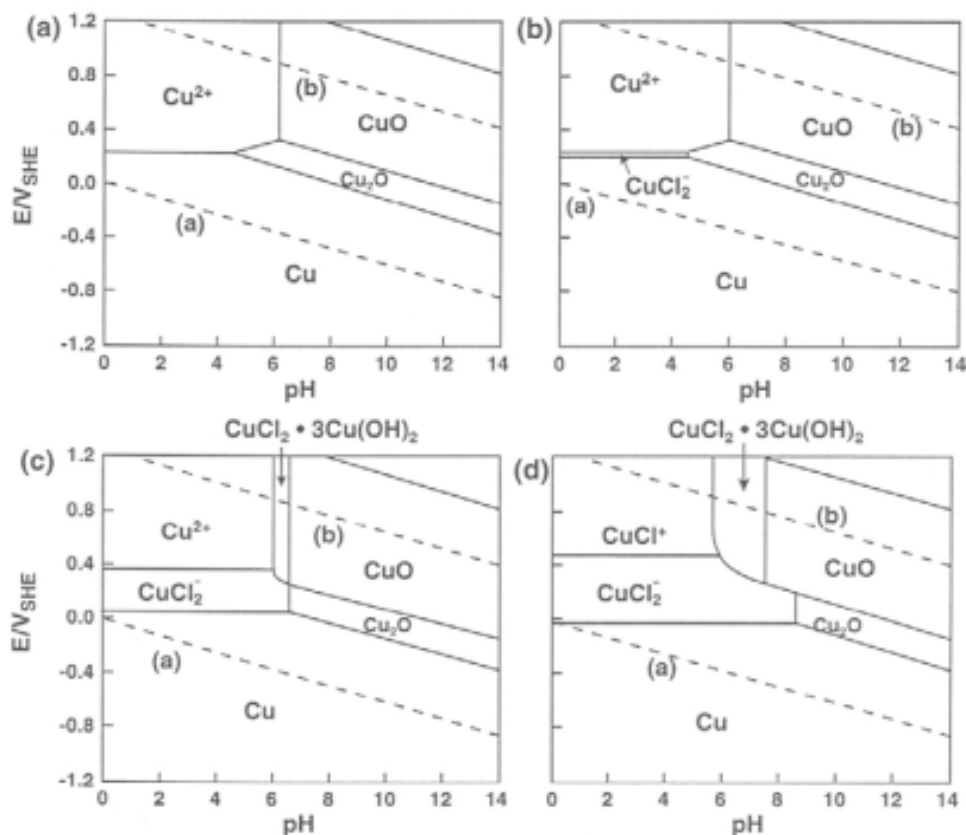
Figure 1.8: Porbaix diagram of Cu/Cl-/H₂O system at room temperature and different chloride concentrations a) 10-3 M, b) 10-2 M, c) 0.1 M, and d) 1 M [51].

Based on equation 35, the pH of the solution increases with increasing of O_2 which might result in the formation of Cu_2O on the surface of Cu, leading to a lower corrosion rate as Cu_2O is stable in slightly alkaline solutions. On the other hand, increasing $[Cl^-]$ increases the solubility of Cu_2O within the range of pH ~9-12, leading to a higher rate of Cu corrosion [51, 53]. Cu^{2+} is the most abundant form of Cu species in aqueous solutions; however, Cl^- can stabilize Cu^+ species. Therefore, Cu^+ is the most dominant species at low $[Cl^-]$, while $CuCl_2^-$ and $CuCl_3^{2-}$ become the prevalent species at higher $[Cl^-]$ [58-60]. King and coworkers [51] reviewed Cu corrosion under both deaerated and aerated conditions in the presence of different anions, such as Cl^-. Fig 1.8 illustrates the effect of

[Cl−] on the stability region of Cu and its products. Cu is stable under anoxic conditions over the full range of pHs with the stability regions of Cu_2O and CuO for pH~5-14 (Fig 1.8a). Cu-Cl complexes become present with increasing Cl^- to 0.01 M. Also, increasing Cl^- to 0.1 M results in the creation of a stability zone of paratacamite ($CuCl_2.3Cu(OH)_2$) in the neutral pH range and the range will become distinctive with increasing [Cl⁻] [61]. The corrosion of Cu by the reduction of water at pH ~1 is possible when [Cl⁻] increases to 1 M, leading to the formation of $CuCl_2$ (Fig 1.8 d). However, different Cu compounds and species such as Cu_2O, CuO, and $CuCl^+$ are thermodynamically possible under aerated conditions. King [61] proposed that corrosion of Cu under aerated conditions is influenced by the presence of Cl^-. Under neutral to acidic conditions, chloride ions stabilize Cu(I) in the dissolved state as complex anions, $CuCl_x^{(x-1)-}$, with the value of x dependent on [Cl⁻] [62]. Under these conditions, active corrosion would be expected to be the anodic dissolution process proceeding via the reaction sequence.

$$Cu + Cl^- \rightarrow CuCl_{ads} + e^- \qquad 36$$

$$CuCl_{ads} + Cl^- \rightarrow CuCl_{2\ (surface)}^- + e^- \qquad 37$$

$$CuCl_{2\ (surface)}^- \rightarrow CuCl_{2\ (bulk)}^- \qquad 38$$

in which the (aq) means the species is aqueous and dissolved in solution; ads means adsorption on the Cu surface, so CuClads on the surface reacts with Cl⁻(aq) from the solution phase to form $CuCl_2^-$ (aq) which will be dissolved in the solution. It is important to note that the mass transport of $CuCl_x^{(x-1)-}$ from the Cu surface has been claimed as the rate-determining step [61]. This mechanism is valid over a wide range of [Cl⁻] from 0.01 M to 5 M [51]. Hydrolysis of CuClads or $CuCl_2^-$ (aq) can also result in the formation of Cu_2O during the active dissolution of Cu in chloride-containing solutions [61].

$$2CuCl_2^- + H_2O \rightarrow Cu_2O + 2H^+ + 4Cl^- \qquad 39$$

$$2CuCl + H_2O \rightarrow Cu_2O + 2H^+ + 2Cl^- \qquad 40$$

As the pH increases from neutral to more alkaline values, the probability of oxide formation increases with the initial formation of oxide involving a competition for surface sites between Cl^- and OH^-,

$$CuCl_{ads} + OH^- \rightarrow Cu(OH)_{ads} + Cl^- \qquad 41$$

$$2Cu(OH)_{ads} \rightarrow Cu_2O + H_2O \qquad 42$$

As a result, the extent of oxide formation will be dependent on the relative $[Cl^-]$ and $[OH^-]$ (i.e., pH) [52, 60-63]. Hydrolysis of dissolved $CuCl_x^{(x-1)\,-}$ can also result in Cu_2O growth.
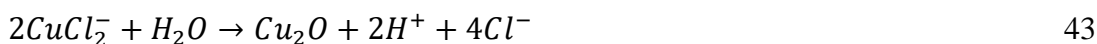
$$2CuCl_2^- + H_2O \rightarrow Cu_2O + 2H^+ + 4Cl^- \hspace{3cm} 43$$

In the presence of a sufficient dissolved $[O_2]$, the homogeneous oxidation of $CuCl_x^{(x-1)\,-}$ can lead to the formation of Cu^{2+} and the deposition of Cu(II) solids, with atacamite being most likely in solutions containing a sufficiently high $[Cl_-]$.

$$2CuCl_2^- + O_2 + H_2O \rightarrow Cu_2(OH)_3Cl + OH^- \hspace{2.5cm} 44$$

This leads to a duplex film comprised of an inner layer of Cu_2O and an outer layer of deposited Cu(II) solids [53, 64-68]. For low $[Cl^-]$ and a sufficiently high pH, the deposited outer Cu(II) film becomes a not well-characterized mixture of CuO and $Cu(OH)_2$ [66] with the thickness increasing with pH. For a sufficiently high pH (≥ 12) the outer layer is dominantly $Cu(OH)_2$ [69].

The role of these films in establishing passivity is partially resolved; although, it is clear that Cl^- exerts a significant effect on the properties and stability of the films. The substitution of monovalent Cl^- ions for divalent O_2^- ions in a Cu_2O lattice results in the formation of less protective films compared to the more passivating film formed in the absence of Cl^- [51, 61, 67, 70]. It has been claimed that islands of CuCl within an otherwise protective (passive) Cu_2O film can act as initiation sites for pitting corrosion [71] that will then be supported by O_2 reduction on the surrounding defective semiconducting Cu_2O. This suggests depending on the $[Cl^-]$, Cu_2O films formed in Cl-containing solutions may be more susceptible to breakdown and pitting [51, 53].

1.3   Passivity and Pitting Corrosion Mechanisms

Some metals and alloys form a compact and cohesive film on the surface upon exposure to an environment that protects the base metal from further dissolution. This film is referred to as a passive film and plays a significant role in maintaining a low corrosion rate for metals and alloys [72, 73]. However, in some situations, the passive film is not stable in a harsh environment or metals cannot form a uniform film, which might result in an unpredictable failure of materials [74-83]. The protectiveness of a passive film

depends on both the nature of an oxide film and the concentration of aggressive anions [84]. For example, both CuO and $Cu(OH)_2$ were more unstable in the presence of chloride compared to sulfate. A protective passive film has specific features such as uniformity, high stability, and continuity. Polarization techniques (e.g potentiodynamic polarization) have been widely used to investigate the active-passive behaviour of materials. For passive materials, the current increases with increasing anodic overpotential up to a certain amount based on the Wagner-Traud equation. However, the current will decrease with a further increase of applied potential and becomes independent of applied potential due to the formation of a protective passive film on the surface of the metallic substrate. The current in this region is known as the passive current (i_{pass}) and either has a small or no change despite a further increase in potential. The potential at which such a transition (active to passive) occurs is defined as the passivation potential (E_{pass}). The range of potential in which the current has a small change and the passive film is stable is referred to as the passive region. At some point, the current increases abruptly within a small range of applied potential due to the local breakdown of the passive film. This potential is defined as the breakdown potential (E_b) (Fig 1.9) [36, 72, 85].
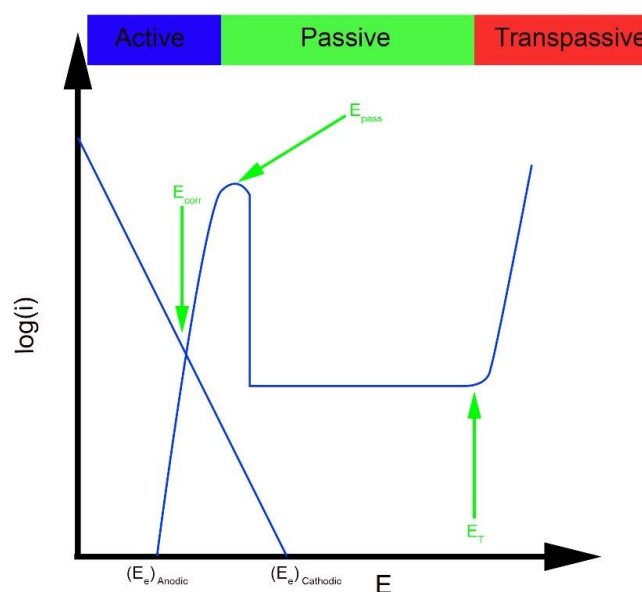
Figure 1.9: A schematic polarization curve for a metal undergoing active-passive behaviour.

Fig 1.9 includes three distinct regions: active, passive, and transpassive regions. The active region is observed when the material is exposed to an aggressive environment in the early stage of immersion. In some cases like the exposure of corrosion-resistant alloys to a non-aggressive environment or the formation of an oxide film before the polarization measurement, the active region may not be observed or be very small. The passive region can be observed when the current approaches the plateau due to the formation of passive film on the surface. Increasing the applied potential to a value equal to or greater than E_b results in a transition from the plateau to an abrupt increase in current leading to the creation of a transpassive region.

Pitting corrosion of metals has been researched for decades. In pitting corrosion, we are dealing with five potentials: (I) corrosion potential (E_{corr}), (II) passivation potential (III) pitting/breakdown potential (E_b), (IV) repassivation potential (E_{rp}), and (V) applied potential.

The corrosion potential (E_{corr}) is the natural potential of a material in which the rate of anodic and cathodic reactions are the same and no net current flows in or out of the material. breakdown potential (E_b) is the potential at which the current increases abruptly in a small range of potential change. Repassivation potential (E_{rp}) is the potential at which the pit current density in the negative-going scan decreases to a value lower than passive current density in the positive-going scan. The Eb depends on the concentration of anions unlike E_{rp}; so, increases in aggressive anion concentration decrease the E_b but has not changed the E_{rp} [86-89].

1.3.1   Passive Film Growth Models and Theories

The mechanism of passive film growth has been a subject of debate for decades and several different models have been proposed to describe the passive film growth mechanism [90-95]. Passive film growth is the combination of interfacial reactions and transport processes within the oxide film. Miller [96] suggested that metal dissolved as metal cations and then precipitated on the surface as metal oxide or hydroxide, depending on the chemistry of the solution. On the other hand, Ambrose [97] claimed passive film formation as a solid-state mechanism (nucleation and growth). In 1976, Shoesmith

rejected Miller's model, observing the nucleation and growth of Cu(OH)$_2$ via a solid-state reaction and the diffusion control process was identified as the rate-determining step [69]. Generally speaking, a potential drop occurs at the metal/electrolyte interface; however, the formation of a passive film on the metal surface leads to the distribution of a portion of the potential across the film. The potential drop at the metal/solution interface and metal/oxide/solution interface is illustrated in Fig. 1.10A and 1.10B, respectively.
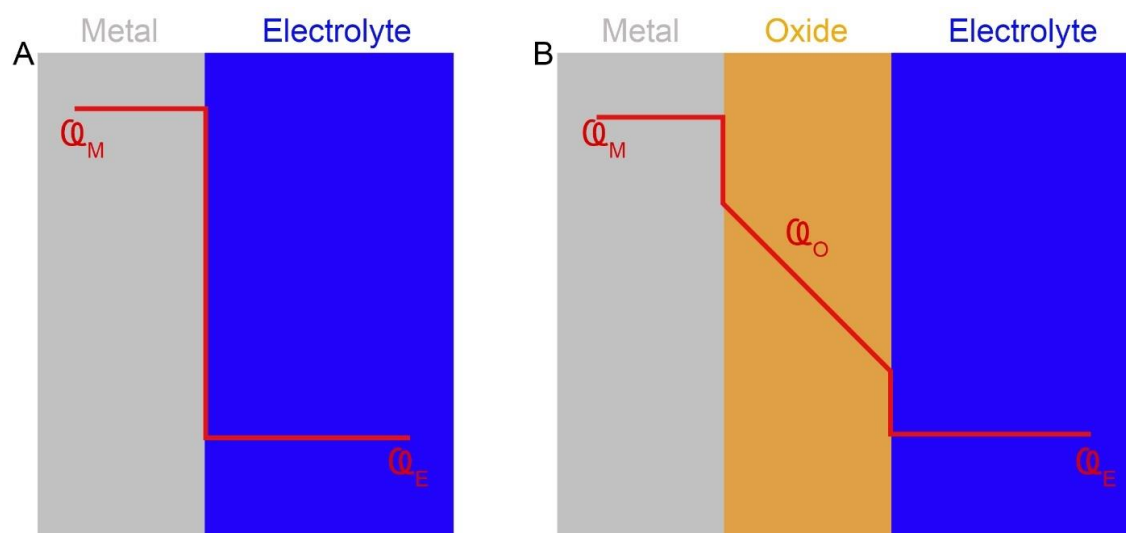
Figure 1.10: Potential map for a) bare metal and b) passive metal immersed in an electrolyte. The potential drop at the metal/electrolyte, metal/oxide, and oxide/electrolyte are shown.

Cabera and Mott [92, 93] introduced a model known as the High-Field Model (HFM) for passive film formation at a low gas temperature. The HFM model is based on the migration of ions in the electric field across the oxide film; so, the small work function allows the thermionic emission of electrons from the metal into the conduction levels of the oxide, resulting in the adsorbtion of oxygen atoms on to the surface of the oxide. The electric field across the oxide film decreases with increasing the thickness until reaching the steady-state thickness. In 1981, MacDonald [98, 99] invented the Point Defect Model (PDM) proposed that film thickness is linearly dependent on the applied potential. The model includes various assumptions as follow:

I.Oxide has both different types of point defect, cation and anion vacancies

II.The point defect generation/annihilation process is a continuous process

III.The electric field is uniform across the oxide film, independent of applied potential

IV.The potential drops at the metal/film interface, across the film, and at the
film/electrolyte interface

V.The potential drop across the film/electrolyte interface is linearly dependent on applied
potential and pH

This model takes into account the transport of vacancies as well as the oxide film dissolution reactions. The first step is the ejection of cation vacancies, at the metal/oxide interface, into the oxide film either by the formation of an anion vacancy or annihilation of a cation vacancy. Then, the metal cations are ejected into the oxide/electrolyte interface either by the chemical or electrochemical dissolution or by the creation of a cation vacancy. Moreover, adsorbed H_2O or O_2 will react with anion vacancies, resulting in the incorporation of oxygen atoms into the film. It is important to mention that the creation and annihilation of vacancies occur at the two different sites. For instance, cation vacancies are created at the oxide/electrolyte interface and annihilated at the metal/oxide interface. On the other hand, anion vacancies are formed at the metal/oxide interface and annihilated at the oxide/electrolyte interface.

Momeni and Wren [100] proposed a model based on the mass and charge balance (MCB) which prognosticates the charge balance of metal-oxide growth and dissolution rates. MCB model takes into account the reactions at the metal/oxide and oxide/electrolyte interfaces and indicates that the metal dissolution rate should be equal to the sum of oxide growth and dissolution rates at all times. The model assumed that the oxide growth and dissolution fluxes have a first-order dependence on the metal oxidation flux. This model can be used to predict the rate of oxidation and dissolution as a function of various parameters such as applied potential, temperature, and pH.

1.3.1.1   Types and morphology of passive film in Cu

Cu can form a passive film in alkaline solutions. The suggested passive film on Cu in moderated alkaline solutions is a double layer oxide film, comprises of an inner Cu_2O

and outer CuO or/and Cu(OH)2 [65, 101-103]. The same results were observed by Holliday [93] in alkaline solutions; however, Ambrose and coworkers [97] reported that the Cu surface was mostly covered with $Cu(OH)_2$. Cu_2O is a porous oxide film and Cu^{2+} can diffuse out to the solution, resulting in a formation of CuO or/and $Cu(OH)_2$ on top of the Cu_2O oxide film [68, 69, 104, 105]. Hurlen [106] suggested that the transition of Cu to Cu (II) was under two consecutive charge transfer processes with an intermediate step of Cu to Cu(I) transition. The rate-determining step was the conversion of Cu(I) to Cu (II) since the conversion rate of Cu to Cu(I) was high. A salt film can also be formed on top of the oxide film depending on the type of anions in the solution [107]. Perez [108] showed that the salt film could play an inhibitive role and prevent pit growth at potentials higher than the pitting potential. Kong [109] proposed the dependence of oxide film composition and morphology on aggressive anions concentrations (with the same applied potential) and corrosion reactions. The role of passive film properties such as structure, composition, and thickness on the pitting corrosion processes have been investigated by many researchers [76, 110-125].

1.3.2   Passive Film Breakdown and Repassivation

While passive films protect the base metals from dissolution and decrease the corrosion rate significantly, their susceptibility to breakdown may result in localized corrosion. The base metal will experience a high corrosion rate in local areas where the passive film was detached from the surface. Since the prediction of localized corrosion rate is difficult, the lifetime assessment will be a challenge and the system may fail within a few months or even a shorter period. In some cases, the passive film is fully removed from the surface, resulting in a high rate of uniform corrosion across the surface. The breakdown of a passive film can occur either due to the depletion of an oxidizing agent (e.g. O_2) which maintains the passivity or the presence of aggressive anions at high potentials [126]. Halide ions (e.g. Cl . I^-, Br^-, F^-) are among the most aggressive anions that damage the passive films, with Cl^- being the most aggressive anion [127, 128]. Kong [127] believed that halide ions did not play a role in passive film properties such as type, uniformity, density, and thickness. However, other researchers supposed that the inner point defects enhanced the adsorption of chloride ions on the passive film, and the introduction of

chloride ions, in turn, increased the transport of point defects, resulting in thinning of passive film at high potentials [119, 129]. Wei [129] confirmed the thinning of the passive film using the impedance technique. The impedance value decreased after immersion of Cu in chloride-containing solution, which showed the thinning process of the passive film. Also, Warburg behaviour was observed, probably due to the adsorption of chloride and reduction of passive thickness. Based on XPS data, chloride was not present after etching the samples for 1800 s, which implied that Cl^- was not incorporated into the film. Halide ions damage the oxide film either by adsorption or penetration mechanism. In the adsorption mechanism, anions are adsorbed on the oxide film resulting in complexation reactions which in turn lead to the breakdown of the passive film [130]. The process is known as thinning mechanism and the resistance of a passive film decreases with decreasing the thickness of the oxide film, resulting in an increase of interfacial potential drop. The resistance of a passive film at grain boundaries is less than that of the homogenous passive film at other locations; so, the grain boundaries become the preferred sites of thinning process [118]. In penetration mechanism, transport of anions from the oxide/solution interface to the metal/oxide interface occurs through the defect structure and high electric field within the oxide. Based on the PDM, cation vacancies increase at the metal/oxide interface due to the incorporation of singly-charged halide ions into doubly charged oxygen vacancies, which disrupts the structure, leading to the formation of voids and mechanical breakdown of the passive film [99]. Sato [131] revealed that the transport of chloride ions from the solution into the oxide film produced large stress which caused the mechanical breakdown of the passive film.

E_{rp} depends on different factors such as pit depth, maximum dissolution current density ($i_{diss, max}$), scan rate, and pit initiation rate [132].

(I) Pit depth:
Multiple stable pits can be formed during the positive-going scan in a potentiodynamic experiment but, the repassivation potential is only dependent on the largest stable pit since any smaller stable pits will repassivate before the measured E_{rp}. E_{rp} decreases with increasing pit depth since a larger pit increases the pit stability which results in lower E_{rp}. This behaviour was observed on SS316L when two sharp current drops were observed in

the negative-going scan due to the repassivation of stable pits and the second current drop at E_{rp} was attributed to the repassivation of the largest stable pit [132].

(II) Maximum dissolution current density ($i_{diss, max}$):

Larger $i_{diss, max}$ generates a deeper pit which results in smaller $i_{diff, crit}$. As a result, repassivation potential decreases with increasing of $i_{diss, max}$.

(III) scan rate:

The scan rate is inversely proportional to the repassivation potential. A slower scan rate provides more time for a pit to grow deeper, resulting in a lower repassivation potential.

(IV) Pit initiation rate:

When the rate of initiation is low, the measured E_b could be postponed to a value well above the normal E_b which can provide extended time for a pit to grow deeper during the negative-going scan, leading to a lower E_{rp}.

1.3.2.1   Measurement of Breakdown and Repassivation Potentials

The breakdown (E_b) and repassivation (E_{rp}) potentials are mostly used to determine the susceptibility of materials to pitting corrosion. Provided that passive conditions can be achieved, the susceptibility to pitting is commonly evaluated by a comparison of the corrosion potential (E_{corr}), measured under open circuit conditions, to the passive film breakdown potential (E_b) measured in a potentiodynamic scan of the applied potential (E) from low to high values. Pitting is taken to be possible if $E_{corr} \geq E_b$; while the pitting propagation will continue when $E_{corr} \geq E_{rp}$ [65, 102, 128]. Both E_{corr} and E_b are distributed parameters due to the surface conditions of the samples or the stochastic nature of passive film breakdown which makes the boundary between non-susceptibility and susceptibility uncertain. A more conservative evaluation of susceptibility involves the evaluation of the difference between E_{corr} and E_{rp}, with the latter recorded by scanning E from above E_b to a value below E_b at which the measured current achieves the low value measured in the passive region. E_{rp} is commonly referred to as the critical pitting potential [133, 134]. Figure 1.11 illustrates the E_b and E_{rp} in a potentiodynamic experiment. As the applied potential is scanned linearly with a constant scan rate in the positive direction, the current increases abruptly within a small range of changes in potential. So, the potential at which the current increases abruptly is known as E_b. in the

backward scan of potential, the current decreases independent of applied potential and creates a hysteresis. The current decreases in the negative-going scan until reaching the passive current density in the positive-going scan. The potential at which the current of the negative-going scan intersects the passive current density on the positive-going scan is defined as E_{rp}.
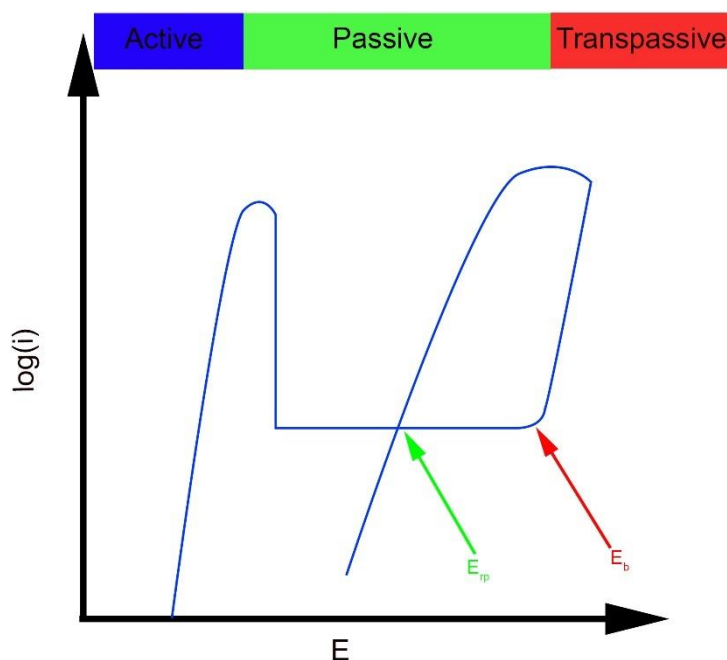
Figure 1.11: Schematic illustration of active-passive behaviour of metals in a solution. Eb and Erp represent the breakdown and repassivation potentials, respectively.

1.3.2.2   Effect of pH, Anions, and Temperature on Corrosion Parameters

Several studies have been conducted to determine the influence of various parameters including the concentration of anions, pH, and temperature on E_{corr}, E_b and E_{rp} [64-66, 107, 127, 135-140]. In general, the dependency of E_b on pH has been debated for decades. Some studies [83, 141] reported that E_b is directly proportional to pH; however, Alvarez [142] proposed two different conditions: (I) E_b is independent of pH for pH < 10 (II) E_b is dependent on pH when pH > 10. Leckie [140] reported a critical pH (pH = 7) above which OH$^-$ played a role as an inhibitor. The same behaviour was observed by

Venu [143]. Based on these studies, three different regions of behaviour have been claimed, based on pH [65]: uniform corrosion for pH < 7; a pitting susceptibility region between pH 7 and 10; and limited susceptibility for pH > 10. However, these boundaries were found to be dependent on the type of anions and concentration, temperature, and $[O_2]$ (when experiments were conducted under open circuit conditions).

Aggressive anions could show different behaviours depending on the solution composition. The concentration of aggressive anions such as chloride and sulfate can affect the pitting parameters like critical pitting temperature (CPT) in stainless steel. Decreasing $[Cl^-]$ will increase the ohmic potential drop of the bulk solution in the pit mouth. As a result, max pitting dissolution current density ($i_{diss, max}$) decreases with the decays of the maximum potential (E_{max}) at the pit surface, contributing to an increase of CPT in stainless steel. Frankel proposed two different transients, depending on CPT [112].

Type I: A fast rise in current followed by a slow decay for higher CPT events. This transient has been observed by other researchers [81, 144-147].

Type II: A slow rise in current followed by an immediate drop (for low CPT events). In type II transients, the final breakdown occurred with an abrupt increase in current -by 4 orders of magnitude in 5 seconds- which indicated a large driving force for pit growth. Higher CPT was observed for a smaller metastable pit compared to a deeper metastable pit. Values of Erp were found to be very dependent on the relative concentrations of various anions (Cl^-, SO_4^{2-}, HCO_3^-/CO_3^{2-}, OH^-), with Cl^- and SO_4^{2-} generally destabilizing passive oxide films, eventually leading to active behaviour, while HCO_3^-/CO_3^{2-} enhanced passivity, with the influence of SO_4^{2-} being ambiguous but with a tendency to promote pitting [111, 127, 135, 137-140, 148]. As a result, an understanding of the corrosion process in solutions containing aggressive anions and the impact of anions on the properties of the oxide film is essential.

Kong [127] proposed that E_b decreased with increasing the concentration of halide ions. Also, the dissolution rate increased at potentials higher than E_{rp}. Souto [107] proposed a critical ratio of OH^-/SO_4^{2-} above which the pit is not able to initiate. The critical value of OH^-/SO_4^{2-} was determined to be 102 times below the sulfate ions that initiated the pitting and above that, a stable film was formed on the surface and protected the base metal from sulfate attack. The sulfate adsorption enhanced the diffusion of vacancies from the metal/oxide interface to the oxide/solution interface, resulting in the breakdown of passive film.

Aerated solutions shift the corrosion potential to more noble values compared to deaerated solutions [109, 137, 138] since oxygen promotes the cathodic reaction on the unbroken area of the oxide surface, leading to the formation of an electrochemical cell with a small anodic site and large cathodic site, which in turn leads to a higher pit initiation and growth rate [148]. The oxygen reduction reaction (ORR) accelerates cathodic reactions, contributing to a more noble E_{corr}, which might increase the probability of pitting when $E_{corr} > E_b$ [138]. King [137] reported that oxygen reduction was inhibited on the copper surface exposed to seawater. He informed that Cu_2O was a good catalyst for O_2 reduction to HO_2^-, but not good for HO_2^- reduction to OH^-. Another parameter that affects the E_{corr} is the concentration of aggressive anions. For instance, the E_{corr} of copper decreased with increasing Cl^- (chloride acts as a cathodic inhibitor). Mayanna [139] reported that chloride accelerated the corrosion rate at low concentrations; however, it played a role as an inhibitor at higher concentrations. Increasing chloride concentration resulted in a higher rate of CuCl formation (solubility of CuCl is reached) which dropped the corrosion potential due to the coverage of the surface. Also, the water activity decreased significantly at high concentrated solutions resulted in a lower corrosion rate [149]. Leckie [140] showed that sulfate had an inhibiting effect in chloride-containing solutions (increasing the $[SO_4^{2-}]$ / $[Cl^-]$ promoted the repassivation process). Mankowski [67] observed a dual behaviour for chloride in sulfate-containing solutions. He observed that chloride presented an inhibitive effect up to 5×10^{-4} M; however, it became the main factor in pit initiation when $[Cl^-]/[SO_4^{2-}] > 5$.

Many researchers have discussed the mechanism of pitting prevention in the presence of carbonate (based on thermodynamic) and believed that the formation of $CuCO_3.Cu(OH)_2$ is the main factor that will prevent copper from pitting corrosion [148, 150]; however, Adeloju [148] proposed that $CuCO_3.Cu(OH)_2$ is a porous, non-protective film resulting from pit initiation and local deterioration of copper oxide films. Nishikata [151] reported a higher rate of copper dissolution with increasing carbonate concentration since $CuCO_3$ became more stable than $Cu(OH)_2$; however, many researchers believe that carbonate plays a role as an inhibitor.

$$Cu(OH)_2 + CO_3^{2-} = CuCO_3 + 2OH^- \qquad\qquad 45$$

Or

$$Cu + H_2O = Cu(OH)_{ads} + H^+ + e^- \qquad\qquad 46$$

$$Cu(OH)_{ads} + CO_3^{2-} + H^+ = CuCO_3 + H_2O + e^- \qquad\qquad 47$$

Carbonate increased passivation time and formed an outer layer of $Cu(OH)_2$ on top of an inner layer of Cu_2O. Milosev proposed a critical concentration of HCO_3^- (0.05 M) above which passive film breakdown will not occur [87]. Carbonate increased the buffer capacity (prevention of local acidification) of the solution; so, a greater amount of carbonate adsorbed on the oxide film and stabilized the oxide film (prevention of chloride from adsorption on the oxide). Also, it changed the oxygen reduction rate by changing the interface properties [148].

A higher dissolution rate of copper oxide films (greater amount of dissolved copper ions) was observed in solutions with a lower concentration of carbonate and higher concentration of chloride [148]. He suggested that carbonate stabilized the passive film that formed before the formation of carbonate salt, resulting in lower pitting probability [148, 152]. So $CuCO_3.Cu(OH)_2$ was not observed when carbonate concentration was higher than the 0.005 M-minimum carbonate concentration required to stabilize the copper oxides.

The effect of temperature on localized corrosion of materials has been studied by several researchers. Carranza [153] proposed a critical temperature (200 ^{o}C) for pitting corrosion of Alloy 800 below which an isolated and deep pit was observed; however, at temperatures higher than 200 ^{o}C, a broad, shallow and more generalized attack was detected. Blasco-Tamarit and coworkers [154] reported that an increase in temperature decreased the quality of the passive film and efficiency of the inhibitor on high-alloyed austenitic stainless steel (UNS N08031), resulting in higher pitting susceptibility of Alloy 31. Mahdi [155] proposed that Eb decreased and the pitting current density increased in X100 steel material with increasing electrolyte temperature. Pitting corrosion was observed at 35 ^{o}C but not at 22 ^{o}C on X100 steel at the open circuit potential. Dong [156] investigated the effect of temperature and chloride concentration on the shape of pits in 2205 duplex stainless steel. He indicated very small and scattered pits at temperatures with hemispherical shape below the CPT, while large and deep pits were observed at higher temperatures and chloride concentrations. Warraky [62] reported that an increase in temperature promoted the active behaviour of copper; although, it had been claimed that passivity was enhanced by an increase in temperature (E_b increased) possibly due to an improvement in film properties.

1.3.3   Pitting corrosion frameworks

Several studies have been performed to introduce a framework for pitting corrosion of materials such as the Point Defect Model (PDM), Membrane Cell Theory (MCT), Salinas-Bravo and Newman (SBN), and Lee-Scully-Frankel (LSF) frameworks [77, 98, 110-113, 132]. Moreover, different factors have been proposed to explain the stable pit growth such as ix, ir, $\sqrt{t}$, and i$_{diss, max}$ where i is the pit current density, x is the pit depth in 1D pit, r is the depth of a hemispherical pit, t is the time, and idiss,max is the maximum dissolution current density [74-76, 118, 120]. Galvele introduced a new definition for pitting potential as the minimum potential at which the pH of the local environment inside the pit becomes acidic [83]. The model was based on the hydrolysis of metal ions inside the pit and the diffusion of ions out of the pit. The hydrolysis process created a local acidification environment resulting in the breakdown of the passive film. He suggested that pit growth was a diffusion-controlled process. Galvele [83] determined

that stable pit growth was only dependent on the pH of the local solution inside of the pit and pH was a current density or/and pit depth-dependent (it decreases with increasing current and pit depth) [83]. He suggested that stable pit growth can be reached at a critical value of ix. Pit initiation and propagation required a critical value of ix for maintaining an aggressive environment inside the pit. ix increased with increasing pH, resulting in a lower probability of pitting. The pit could grow at potentials lower than the pitting potential since the pit depth increased with time. As a result, ix would be greater than the critical value required to keep the pit under active dissolution. The pit will be repassivated either because the ix value decreases to a value lower than the critical value or the potential drops below the corrosion potential inside the pit-acidification cannot be maintained inside the pit.

$$E_p = A + b.logC_{OH^-} \qquad\qquad 48$$

Pistorius and Burstein believed that the local aggressive solution inside the pit can only be maintained if the pit growth was under diffusion control [79]. However, Souto [107] indicated that the instantaneous nucleation and growth of a pit were under a charge transfer controlled process. Lucey [157] proposed that the pitting mechanism depends on the formation of a membrane-shaped film on the surface. The inner layer comprises cuprous chloride and supports the anodic reaction, while the outer layer is a conducting porous cuprous oxide that supports the cathodic reactions. In 2017, Frankel observed an increase in current with an increase of the potential (charge transfer controlled) for metastable pits on SS320 followed by a transition from charge transfer to diffusion control with increasing of maximum dissolution current density (idiss, max) [158]. Burstein [79] modified his model and suggested that salt film can be formed underneath a passive film when the formation rate of cuprous ions (equation 49) is higher than the rate of cuprous oxide or/and cupric ions formations (equations 50 and 51); so, it plays a role either in pit nucleation or propagation [159].

$$Cu + Cu^{2+} \rightleftarrows 2Cu^+ \qquad\qquad 49$$
$$2Cu^+ + H_2O \rightleftarrows Cu_2O + 2H^+ \qquad\qquad 50$$
$$2Cu^+ + O + H_2O \rightleftarrows 2Cu^{2+} + 2(OH)^- \qquad\qquad 51$$

Some researchers [160, 161] indicated that the presence of salt film prevented the transition from metastable to stable pit growth; however, other literature claimed that the metastable to stable pit growth could occur even in the presence of salt film [110-114, 132] and the salt film may facilitate the transition from metastable to stable pit growth [76]. The presence of salt film can decrease the E_b through the enhancement of Cu dissolution [107, 159]. It is generally accepted that the basic mechanism of pitting corrosion is the formation of local acidic solution inside the pit due to the hydrolysis of metal cations. Also, aggressive anions such as Cl⁻ are diffused into the pit to balance the charge of dissolved metal cations; so, accumulation of metal cations inside the pit will maintain the aggressive local environment for a stable pit growth. Shalaby [162] proposed that copper reacted with water and formed Cu_2O (reaction 52). The cuprous oxide film was porous; so, the copper could be oxidized to Cu^+ and reacted with Cl⁻ to form a CuCl compound (reaction 53). CuCl is an unstable compound and would be hydrolyzed rapidly, resulting in the formation of Cu_2O crystals and local acidic solution (reaction 54). This acidification process leads to the local attack of the passive film.

$$2Cu^+ + H_2O \rightarrow Cu_2O + 2H^+ + 2e \qquad\qquad 52$$

$$Cu^+ + Cl^- \rightarrow CuCl \qquad\qquad 53$$

$$2CuCl + H_2O \rightarrow Cu_2O + 2HCl \qquad\qquad 54$$

In the following sections, the most three important frameworks in the field of pitting corrosion of materials will be discussed.

1.3.3.1   Point Defect Model (PDM)

The PDM has been used in many studies to explain the passive film breakdown. The PDM proposed that the breakdown of passive film resulted from the accumulation of cation vacancies at the metal/oxide interface through the oxide/solution interface [87, 107, 129, 163-165]. Kong [127] proposed that the passive film thickness increases with increasing applied potential. The diffusion coefficient of cation vacancies and density of point defects are inversely proportional to the corrosion resistance of the passive film and increase with the adsorption of aggressive anions (e.g. Cl⁻) [128, 129, 166-171]. Adsorption of anions on the oxide surface enhances the diffusion of vacancies, resulting in rapid breakdown of the passive film and a higher pitting probability. Kong and

coworkers [135] confirmed that an increase in chloride concentration contributed to a higher rate of metal vacancies formation and a greater probability of pitting. He modified the PDM model and introduced the size matching effect (SME) theory [127]. Based on SME theory, the pitting potential depends on both size of anion and anion vacancy. If the size of anion vacancy is smaller than halide ions, then anion vacancy should expand to a size greater than halide ion to provide the adsorption condition for halide ion; so, the pitting potential increases due to the energy required to expand the anion vacancy. On the other hand, when the size of anion vacancy is greater than halide ion, then no expansion will be required and halide ion can adsorb easily, resulting in lower pitting potential.

1.3.3.2   Salinas-Bravo and Newman (SBN)

Salinas-Bravo and Newman [77] proposed a pitting framework (SBN) based on the presence of a salt film at the pit surface. A salt film can be formed at the pit surface if the current density increases to a value equal to or greater than the limiting current density (i_L)- current density above which the current density becomes independent of applied potential- and the pit will grow under the diffusion control process. The pit will be repassivated if the current density drops to a value lower than the minimum current density required for stable pit growth which is defined as critical current density (i_{crit}). Although this framework was able to support the stable pit growth at high critical pitting temperature (CPT), it was not able to support the condition when the current density was lower than iL while metastable to stable pit growth was observed.. Some researchers rejected the validity of the SBN framework by observing crystallographic pit morphology at current densities lower than iL, resulting from the absence of salt film at the pit surface [172, 173]. Ruijini [138] reported a crystallographic pit as a repassivated pit; however, this hypothesis could be wrong based on both SBN and LSF frameworks.

1.3.3.3   Lee-Scully-Frankel (LSF)

Both SBN and PDM had some limitations to support different pitting mechanisms; as a result, Frankel and coworkers [110-114, 132] introduced a new framework known as LSF. LSF drives the ix, ir and $i\sqrt{t}$ to the lower and upper limit regions [110-114]. ix, ir and $i\sqrt{t}$ are the result of achieving the critical values (e.g., potential, temperature, and pit

depth); however, upper limits of i_x, i_r and $i\sqrt{t}$ are related to the condition when T, E, and r reach the saturation condition [110]. Frankel and coworkers indicated that the large frequency of passive film breakdown and metastable pitting might not contribute to a stable pit growth if the repair process would be rapid since stable pitting potential are hundreds of mV greater than metastable pitting potential [111, 114]. As a result, the LSF framework has been introduced to cover the gaps and issues of previous frameworks and make a clear horizon in the field of corrosion science, specifically the stable pit growth of metals in aggressive environments. Based on this framework, passive film breakdown is the critical factor when metal is exposed to a less aggressive environment and/or to less susceptible materials and microstructure. In this case, the rate of passive film breakdown is low and once it happens the pit will grow fast. On the other hand, when a material is exposed to an aggressive solution, the pit growth becomes the critical factor due to the large frequency of passive film breakdown and metastable pits. The concentration of a solution or/and intrinsic properties of materials can determine whether the breakdown of passive film or pit growth would be the rate-controlling step in pitting corrosion. Laycock claimed that the role of passive film breakdown on Eb was negligible; however, Frankel suggested that breakdown of the passive film could affect the Eb specifically in the case that the frequency of breakdown was low [114, 174]. Frankel and coworkers[113] proposed that three parameters control the active dissolution inside the pit: surface concentration (C_{surf}), surface potential (E_{surf}), and temperature. If any two of these parameters are fixed, then the third parameter will be the critical factor; therefore, the system will be under active dissolution if the critical parameter is above the critical value for maintaining a local environment inside the pit. For instance, at temperatures below the critical temperature (T_{cirt}), the open pit will be repassivated since maximum dissolution current density ($i_{diss,\ max}$) is smaller than critical diffusion current density ($i_{diff,\ crit}$) and critical concentration (C_{crit}) required for active dissolution cannot be maintained. On the other hand, at a temperature above saturation temperature (T_{sat}), the accumulation of metal cation inside the pit will occur and $i_{diss,\ max} > i_L$. As a result, a salt film will be formed at the pit surface and pit growth will transition to diffusion control. LSF framework indicated that both potential and temperature were inversely proportional to

the pit depth (r). Increasing the pit depth decreases the E_{sat} to a value lower than E_{max}. So, the pit growth transitions from charge transfer to diffusion control.

$$E_{sat}(x) = k - \beta_a log(x) \hspace{4cm} 55$$

Based on the LSF, a sufficiently aggressive local environment inside the pit is required to sustain an active dissolution at the pit surface. So, the concentration of metal cation at the pit surface (C_{surf}) should be equal to or greater than the minimum critical concentration of metal cation (C_{crit}) required for a pit to be under active dissolution. The current associated with the diffusion of metal cations out of the pit can be calculated using equation 56.

$$i_{diff} = 3nFDC_{surf}/2\pi r \hspace{4cm} 56$$

where i_{diff} is the diffusion current density, n is the average oxidation state, F is the Faraday constant, D is diffusion coefficient, C is metal cation concentration, r is pit depth or radius, and $2\pi r/3$ is effective diffusion length.

Based on equation 56, when pit depth is small, then $i_{diff,crit}$ is large and the condition where $i_{diss,max} < i_{diff,crit}$ can be reached easily; so, the pit will be repassivated. As a result, another diffusion barrier such as pit cover is required to maintain the required local environment for active dissolution of pit and prevention of pit repassivation [81, 175-177]. Meanwhile, when the surface concentration (C_{surf}) reaches the saturation concentration (C_{sat}), the current density will reach iL, resulting in increasing of $i_{diss,max}$ to a value greater than $i_{diff,crit}$ ($i_{diss,max} > i_{diff,crit}$); so, the pit will grow without any extra diffusion barrier to support the pit growth [112, 113].

Based on the LSF, an open pit can be stabilized if $i_{diss,max} \geq i_{diff,crit}$ and the concentration of metal cation at the pit surface (C_{surf}) will be equal to or greater than the diffusion rate of metal cation, out of the pit (C_{crit}). It is also important to mention that pit growth can be either under charge transfer control or diffusion control [112, 113].

If $i_{diff,crit} \leq i_{diss,max} < i_L$, then the metal dissolution is the rate-determining step and pit growth is under charge transfer control -with a crystallographic pit surface-. As a result, the actual current density is idiss,max.

If $i_{diss,max} \geq i_L$, then the diffusion of metal cation out of the pit is the rate-determining step and pit growth will transit to diffusion control; So, the actual current density will be i_L. In this situation, a salt film will be formed at the pit surface resulting in an electropolished pit surface.

The above conditions are valid for most of the cases; however, in some specific cases, the applied potential is too low -potentials close to the open circuit potential (OCP)-; So, it will take a long time for a pit to transit from charge transfer to diffusion control. As a result, the pit will grow under charge transfer control for a long time and pit morphology is a crystallographic pit, not an electropolished pit [113]. When the system is under OCP condition, E_{max} will be influenced by a galvanic effect of a cathode that covers the surface outside of a pit, leading to theincreasing ofthe Esurf to a potential greater than E_{corr}. As a result, Emax can obtain a value much higher than Esat and a salt film will be formed at the pit surface [110]. It is noteworthy that salt film is not required for stable pit growth and is just a consequence of metal cation concentration at the pit surface achieving saturation concentration (C_{sat}) [82, 83, 110]. the pit cannot be stabilized as an open pit when $i_{diss,max} < i_{diff,crit}$, but might grow as a metastable pit with the support of diffusion barrier such as pit cover. The role of pit cover is to maintain a local aggressive environment inside the pit and prevent the diffusion out of metal cations from the inside of the pit to the bulk solution. Both metastable pit to stable pit transition and rate-controlling process depend on the perforation size of pit cover (a) and the rupture rate of pit cover [112, 176]. In a covered pit, two perforation sizes are important: critical perforation radius (a_{crit}) and saturation perforation radius (a_{sat}). The pit will be repassivated if a pit cover opening is larger than acrit (e.g. large and abrupt rupture of pit cover opening during metastable pit growth to a size greater than acrit) since the concentration of local environment inside the pit (C_{surf}) will become lower than C_{crit}; however, the system can maintain active dissolution inside the pit when $a_{sat} < a < a_{crit}$ [81, 178]. The salt film is formed at the pit surface when $a < a_{sat}$; so, the pit growth will be under diffusion control [113]. It is important to note that the E_{rp} in this situation differs from the general type of E_{rp}. In general concept, E_{rp} is the potential when the pit is completely repassivated but in this concept where $C_{surf} < C_{crit}$, the E_{rp} is the potential in which pit just starts to repassivate and the final value will depend on the dilution rate of

solutions inside the pit and pit depth. Increasing the pit depth decreases the E_{rp} because the system will experience a slow rate of dilution process inside the pit [111]. Abrupt and large rupture of pit cover results in sudden dilution of solution inside the pit- diffusion out of the metal cation to the bulk solution, contributing to the repassivation of the pit. the pit might still be able to grow under this condition if a salt film is formed at the pit surface. In this condition, the salt film will dissolve into the pit solution and increase the concentration of metal cations to a value above the critical concentration (C_{crit}) required to sustain the pit growth [76, 110]. The competition between the dissolution rate of salt film and diffusion rate of metal cations out to the bulk solution plays the main role in the stability of pit growth or repassivation process [76, 81]. The thickness of a salt film is a crucial factor in maintaining the concentration of metal cation inside of a pit to a value above the C_{crit} for an active dissolution of a pit and is directly proportional to the applied potential (E_{app}) and pit depth (r) but inversely proportional to the opening of pit cover (a) [110].

1.3.4   Types of Pitting Corrosion in Cu

Many industries have used Cu and its alloys as the the primary materials in the products and equipment (e.g. water pipe, heat exchanger, etc) due to their mechanical and physical properties. Although Cu is thermodynamically stable in deaerated conditions, the susceptibility of Cu to localized corrosion (e.g. pitting) in aerated conditions should be considered carefully since the passive film might form on the surface of Cu in oxic conditions. Cu oxides play a significant role in the functionality of Cu depending on the application. For instance, the formation of scales and Cu oxides in heat exchangers results in decreasing of the efficiency of the system; however, oxide films protect Cu from further dissolution in corrosive environments. A requirement for pitting to occur is that the Cu surface must be generally passive in order to support the separation of anodes and cathodes, a prerequisite for this form of corrosion. Passive films can be formed on the surface of Cu by either the dissolution-precipitation mechanism or a solid-state reaction- nucleation and growth of the passive film [69, 87, 96, 179]. The morphology, quality and protectiveness of passive film depend on both material properties and environmental conditions such as the grain size and orientation, concentration of

aggressive anions, exposure time, etc [69, 84, 102, 150, 179-187]. The structure and morphology of passive film have been investigated by many researchers for a decade [69, 107, 162, 181, 187-190]. The structure and morphology of oxide film depend on applied potential, solution composition, and exposure time [181]. Also, some researchers have been investigated the relation between oxide film morphology, local surface activity, and localized corrosion with grain orientation [182, 191-194]. Martinez and coworkers [180] claimed that the corrosion properties of copper not only depend on the grain orientation of individual grains but the orientation of adjacent grains. Three different types of pitting have been introduced for Cu and its alloys based on environmental conditions.

1.3.4.1 Type I pitting

Type I pitting occurs in cold, hard waters and failure occurs in a short time even within 3 months. This type of pitting does not occur in surface-redrived water since organic compounds can play a role as inhibitors [195]. The composition of hard water plays a significant role in the possibility of Cu to type I pitting. The most important factors that trigger this type of corrosion are calcium carbonate saturation index, pH, and organic content. Increasing saturation index and pH increases the pitting probability of Cu; however, organic compounds protect Cu from pitting due to their inhibiting effect. Cornwell and coworkers proposed that the cleaning process of Cu tube affected the pitting susceptibility of Cu since the pitting occurred rapidly in bright annealed tubes with no postanneal internal cleaning; however, no pits were observed for tubes that had been internally cleaned [196]. Moreover, type I pitting was observed in Cu tanks and low-pressure hot water cylinders due to the temperature difference between the top and bottom regions of tanks and cylinders. The corrosion products, mainly cuprous chloride, were formed in the early stage of exposure on the vessel sides and then precipitated on the bottom of the tank resulting in pit initiation and propagation on the lower regions as shown in Fig. 1.12 [157]. Edwards [197] proposed that type I pitting could occur in any environment where the rate of cuprous chloride formation was higher than the rate of its oxidation or hydrolysis to Cu oxide. Type I pitting of Cu in water containing phosphate was reported by Lyte [198]. Phosphate copper is a porous structure film that shields the Cu surface and increases the concentration of cuprous chloride underneath which

contributes to the increase of likelihood of type I pitting. Lucey [157, 159] proposed a pitting propensity rating (PPR) model based on different parameters. He reported that increasing sulfate, sodium and dissolved oxygen increased the pitting propensity; however, increasing chloride, nitrate, and pH decreased it. Edwards [197] developed Lucey's model by evaluating the effect of bicarbonate and revealed that bicarbonate improved the pitting corrosion of Cu; however, he showed that nitrate decreased the pitting propensity which is not in good agreement with Lucey's result. Nomogram proposed by Lucey has some limitations such as it does not support the chloride contents greater than 50 mg/L. Also, while pitting would not occur in waters with no chloride, the nomogram suggests that this type of water is very aggressive [199]. Lucey proposed a theory for type I pitting mechanism which postulated the presence of cuprous chloride as the initiation site for pitting. He found that carbonate scale was not formed in areas close to the pit; however, a large amount of calcium carbonate was observed in the mound above the pit; suggesting the occurrence of the cathodic reaction above the pit [157].
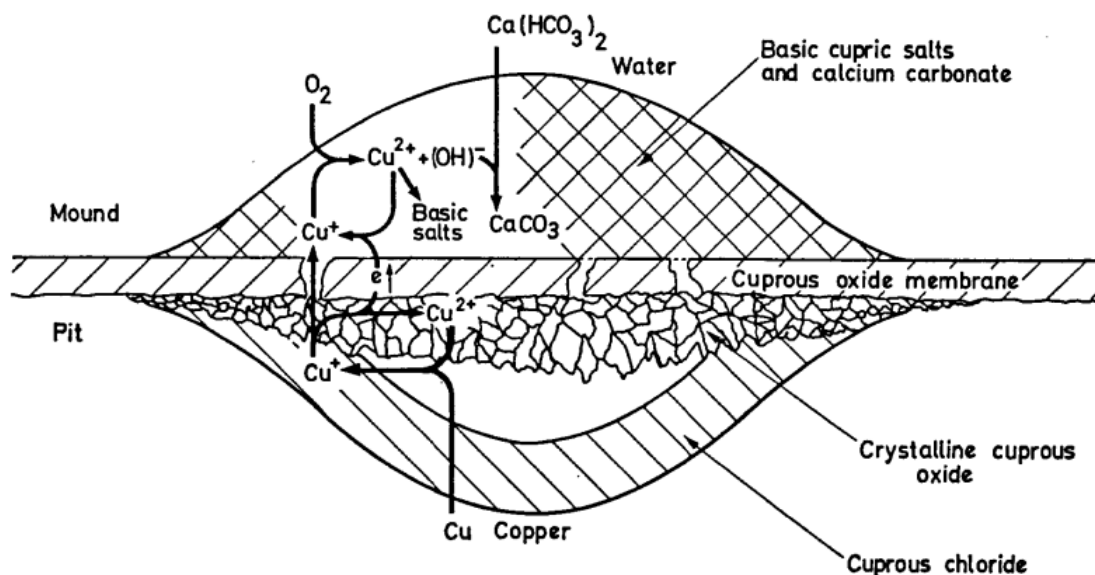
Figure 1.12: Schematic representation of corrosion products and reactions in type I pitting [157].

He introduced the cell membrane theory in which cuprous oxide covers the mouth of the pit and acts as a bipolar membrane; So, the lower surface plays a role as the anode and the upper surface supports the cathodic reaction [157]. The cathodic reaction (reduction

of dissolved oxygen) occurs on the outer surface and the anodic reaction happens on the inner surface of the oxide. So; Cu^+ diffused out from inside to the outside of the film and reacts with oxygen to form Cu^{2+}. This type of corrosion was described as a direct chemical attack of copper [157]. Lucey proposed that the presence of a film on the copper surface enhanced the formation of membrane cells and prevented the diffusion of copper ions away from the surface. He also claimed that increasing chloride concentration reduced the probability of pitting.

1.3.4.2   Type II pitting

Type II pitting corrosion of Cu and its alloys has been observed in high-temperature soft waters of low pH. The type II pitting process is slower than type I and usually occurs within 8 to 12 years of operation. Type II pitting leads to the formation of deep pits with crystalline cuprous oxide and basic copper sulfate at the pit surface and cuprous chloride at the bottom of the pit as illustrated in Fig. 1.13 [199]. Mattson proposed that type II pitting occurred when the pH $<$ 7.4, the bicarbonate/sulfate ratio was less than 1, and the temperature was above 60 °C [200]. Baba and coworkers reported the effect of chlorine on pitting corrosion of Cu pipes and confirmed that residual chlorine in hot water resulted in increasing Cu tube potential (150 mV vs SCE) to values above the pitting potential at 60 °C [201]. Suzuki [202] proposed that rise in potential occurred in 2 steps: In the first stage, the formation of cuprous chloride occurred at potentials above 60 mV vs SCE, while the second stage occurred at potentials between 60 to 150 mV vs SCE due to the absorption reaction of hypochlorous acid (HOCl) and hypochlorite ions. Sato [203] reported that chlorine affected the lifetime of Cu by increasing the dissolution rate of Cu with failures in less than 3 years compared to the failure of Cu within 8 to 12 years in the absence of chlorine.

Brown deposit
Amorphous

Yellowish green deposit
Amorphous

Black film
Cu_2O
CuO

Greenish blue mound
$Cu_4SO_4(OH)_6$

Reddish brown corrosion product Cu_2O

Reddish brown corrosion product Cu_2O

Wall thickness

CuCl
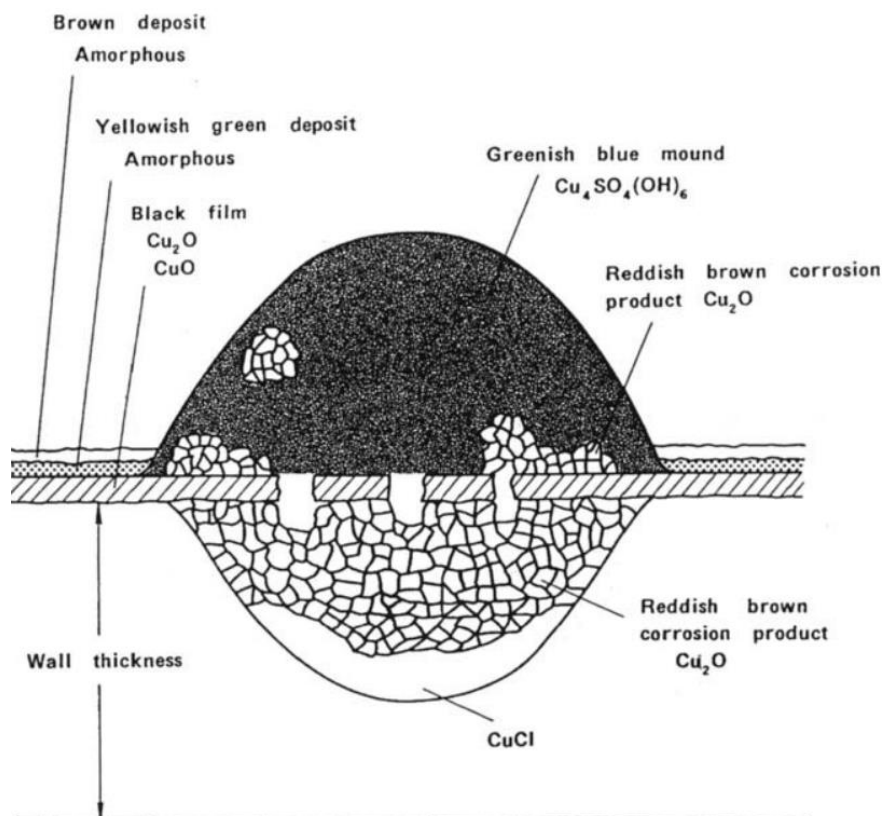
Figure 1.13: Schematic representation of corrosion products and reactions in type II pitting [199].

1.3.4.3   Type III pitting

This type of pitting has been observed in cold or warm soft water of low pH. Campbell reviewed this type of pitting and revealed that type III pitting could occur in both cold water pipes that were located in a warm environment and hot water pipes but in locations far from the heater where the temperature was around 50 °C [195, 199]. Type III pitting mechanism is based on the formation of a biofilm between the metal and the oxide-hydroxide layer. The rupture of biofilm results in a copper ion concentration due to the presence of high copper ion concentration in the exopolymeric layer. The presence of peroxide and hydroperoxide in the biofilm accelerates the cathodic reaction than the reduction of dissolved oxygen resulting in a higher rate of corrosion. Researchers [204] have evaluated the effect of film properties on pitting corrosion of Cu and reported that the type of oxides influenced the type and propensity for pitting. They observed a higher

pitting susceptibility of Cu in stagnant waters containing a large amount of sulfate compared to the flowing water, which revealed that water flow conditions significantly affected the morphology of oxide film.

1.4 Statistics and Stochastic Processes in Corrosion Science

1.4.1 Introduction to Probability and Statistics

The occurrence of random events is defined as probability. Probability is used to evaluate the occurrence of an event. For instance, an event A consists of m out of n where m is equally like events and n is the complete system of a mutually exclusive event; so, the probability of event A can be calculated using equation 57 which is defined as the classic probability [a].

$$P(A) = m/n \qquad \qquad 57$$

In this case, the probability will be between 0 and 1.

Geometrical definition of probability has solved the limitation of the finite number of elementary events in the classical model by using the surface areas of event A and the surface area of the certain event U. The model has some limitations since all points on the board (event U) do not have the same possibility of occurrence; therefore, the surface area is not an appropriate parameter to calculate the probability of occurrence of events [205, 206].

$$P(A) = A/U \qquad \qquad 58$$

Statistical definition of probability supports the infinite repeats of an experiment; So, for a certain event A, that occurs m times out of the n experiments, the relative frequency of the occurrence of the event A can be defined as m(A)/n. So, the probability can be calculated using equation 59 [205, 206].

$$P(A) = \lim_{n \to \infty} \frac{m(A)}{n} \qquad \qquad 59$$

Statistics is a field of science in which a series of processes including collecting, analyzing, and drawing conclusions have been performed on experimental and/or survey data. Statistical procedures have been mainly used in a wide range of scientific fields; however, some specific procedures are used in one or few related fields than in another [207-209]. Scientists need to clarify whether the body of data includes all possible data or a part of a larger body. As a result, a definition has been established which is known as population. The population is the entire set of similar values which are characteristic of a given experiment. Another definition is known as the sample which is a part of a population and might include the entire population values. Since the population can be huge, analyzing the whole population values could be impossible; therefore, we use sample information to make an inference about the population. The sample values should be collected from the population using the principle of randomness; as a result, a statement about the population from which a sample is taken can be made. Sample space (S) is the set of all possible outcomes of a random experiment. E is defined as the subset of S which is known as events. So, P(E) is the probability that the outcome of the random experiment is an element of E. The relative frequency of S will be 1 when S is the entire sample space; so, P(S)=1. If E_1, E_2, … are mutually exclusive subsets of S, no two of these subsets have a common point; therefore, the relative frequency of the union of these sets will be the sum of the relative frequencies of the sets [210].

$$P(E_1 \cup E_2 \cup E_3 \cup \dots) = P(E_1) + P(E_2) + P(E_3) + \cdots \qquad\qquad 60$$

1.4.1.1 Sample Space and Events

Sample space has a certain number of outcomes (elementary events) and all of them are equally likely. Event is a set consisting of possible outcomes of the experiment. For a given event E, the probability of outcomes, n_E, favourable to the event E will be P(E) = n_E/n [205, 210]. However, sample space can be infinite like the corrosion potential of metals in a solution or testing of a concrete cube in a testing machine [205]. A principle is used to determine the number of ways in which events can occur. The counting rule indicates: if an event E includes the occurrence of an event C, followed by the occurrence of an event D, the number of ways that E can occur can be calculated by taking the product of the number of ways that C can occur times the number of ways that C can

occur. Based on this definition, permutations and combinations can be used to determine the number of ways that certain events can occur.

1.4.1.2   Permutations

Permutation is the arrangement of a set of data into a sequence or linear order. The collection of x objects from the n distinguishable objects in any manner is called a permutation of the n objects taken x at a time (equation 61)

$$P(n, x) = \frac{n!}{(n-x)!} \qquad\qquad 61$$

where n! is the total number of possible ways that we can rearrange n objects. So, we can choose the first object in n ways, the second object in n-1 ways,…, and rth object in n-(r-1) ways which are following the counting rule. When x groups of objects are involved and the objects whiting each group are the same but different from the objects of other groups, then, there is a total of N objects of which n_1 are alike, n_2 are alike,…, n_x are alike. As a result, the permutation of N objects taken N at a time is calculated using equation 62

$$P(N; n_1, n_2, …, n_x) = \frac{N!}{n_1! n_2! … n_x!} \qquad\qquad 62$$

1.4.1.3   Combinations

Combination is the collection of x objects from among n objects, regardless of the order of arrangement of the objects among themselves. This process is called a combination of n objects of order *x*. The number of combinations is calculated as illustrated in equation 63

$$\binom{n}{x} = \frac{n!}{(n-x)! \, x!} \qquad\qquad 63$$

It is noteworthy to mention that the order of selection is important in permutations but not in combinations. As a result, the number of permutations is equal to the number of combinations multiplies by the number of permutations of the x objects taken *x* at a time.

$$P(n, x) = \binom{n}{x}x! \qquad\qquad 64$$

1.4.2   Distributions

Researchers have used statistical models to collect, organize, analyze, and present the data. Choosing the best statistical model requires an understanding of data and its properties. As a result, the distribution of data affects the type of model that has been chosen. Theoretical distribution is the most common type of distribution that can be used to determine the actual distribution. So, scientists should have a good understating of the theoretical distributions and their characteristics. Different terms have been used to clarify the characteristics and parameters such as population, sample, sample space, random (stochastic) variable, discrete variable, continuous variable, and cumulative frequency.

A population is the collection of objects with at least one common characteristic. A Sample is the subset of the population. Sample space is all possible outcomes of an experiment. Random variable is a variable from a sample space that is dependent on the outcome of a random phenomenon. A discrete variable is a countable parameter and can be measured in a finite amount of time while continuous variable is a measurable parameter that can take on an uncountable set of values. The difference between the discrete distribution and continuous distribution is that data can only take on certain values in a discrete distribution but can take on any values within a range (two distinct values) in continuous distribution. Cumulative frequency is the sum of all observations that lie below or above a particular value in a data set. It can be calculated by adding each frequency from a frequency table to the sum of its predecessor.

1.4.2.1   Distributions of Random Variables

Random variables include two different categories in statistics and probability, discrete and continuous. Various functions and parameters are used to describe the random variables such as distribution function, probability density function (PDF), and cumulative distribution function (CDF). A wide range of phenomena and experiments in engineering lead to the generation of random variables (e.g. fracture strength of materials) that can be described by real numbers with certain distribution parameters.

Random variable is a variable that might take any of the values in a specified set of values. As explained before, a discrete random variable might only take the isolated values; however, a continuous random variable may take all the possible values of a dataset [205, 210].

$$\Phi(x_j) = P(X \leq x_j) = \sum_{x_i \leq x_j} P(x_i) = \sum_{x_i \leq x_j} P(X = x_i)$$ 65

where X is the random variable, x_i is the number of values in the dataset and $\Phi(x_i)$ is the distribution function.

The probability is calculated as described in equation 66.

$$P_i = P(x_i) = P(X = x_i)$$ 66
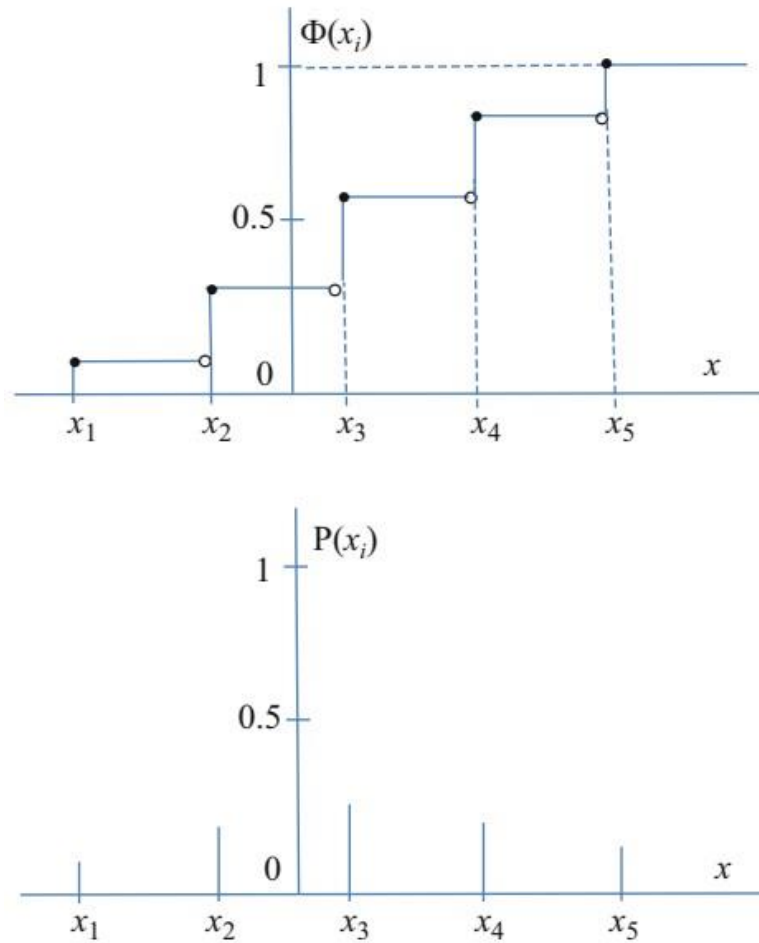
Figure 1.14: Schematic illustration of the distribution function and probabilities of a discrete random variable [205].

For a continuous random variable (X), the distribution function and probability density function are shown by Φ X(x) and φ X(x) respectively. The distribution function can be calculated by integrating the probability density function; as a result, the distribution function is a non-negative and real function. Also, the distribution function can be derived to obtain the PDF (equation 67) [205].

$$\Phi(x) = \int_{-\infty}^{x} \varphi(x)dx \qquad\qquad 67$$

$$\varphi(x) = \frac{d\Phi(x)}{dx} \qquad\qquad 68$$
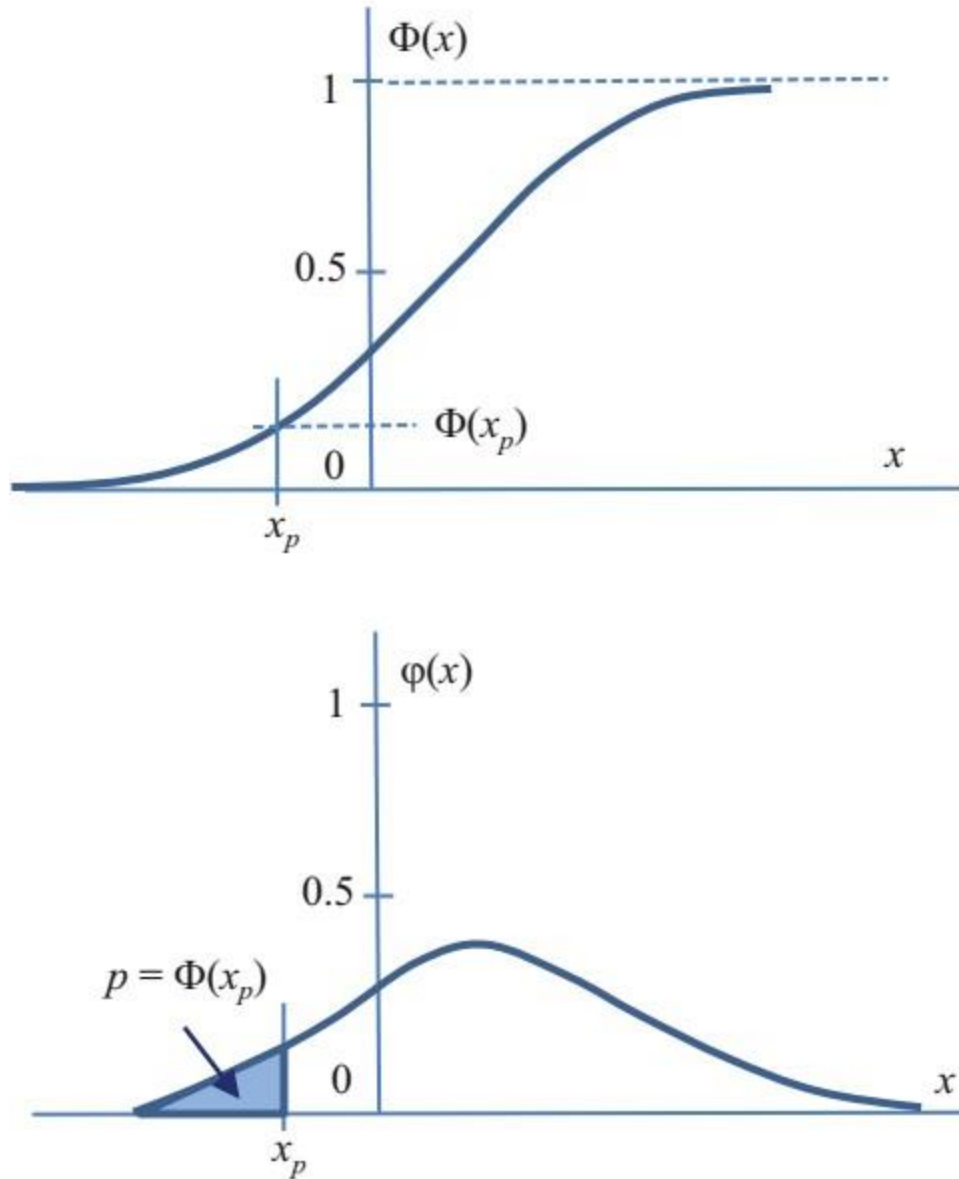
Figure 1.15: Schematic illustration of cumulative and probability density function of a continuous random variable [205].

Distribution parameters are used to define the distribution function and PDF. The most often parameter that has been used to define them is known as general moment and is defined as below.

$$\mu'_1 = \sum_i x_i^l P(x_i) \qquad\qquad 69$$

$$\mu'_1 = \int_x^\infty x^1 \varphi(x) dx \qquad\qquad 70$$

The mean (μ) of the random variable is defined as the general moment of the first order μ_1'.

$$\mu = \mu_1' \tag{71}$$

Central moments of discrete and continuous variables are used to define important parameters such as variance (σ^2) and standard deviation (σ). Standard deviation is used to describe the dispersion of data and the relative measure of dispersion can be defined using the coefficient of variation (V) [205].

$$V = \frac{\sigma}{\mu} \tag{72}$$

Coefficien of Variation is mostly used to describe the relative dispersion of data; however, the standard deviation can be used alternatively if the mean is close to zero.

Skewness defines asymmetry and kurtosis denotes the measure of peakedness in distribution. Skewness (α) and kurtosis (ε) of distribution function can be obtained as shown in equations 73 and 74 respectively [205].

$$\alpha = \frac{\mu_3}{\sigma^3} \tag{73}$$

$$\varepsilon = \frac{\mu_4}{\sigma^4} - 3 \tag{74}$$

Skewness defines how the tail of a distribution lies to the right or left which might affect the probability of overlapping between two distinct distributions. If $\alpha > 0$, then the distribution is skewed to the right and if $\alpha < 0$, then the distribution is skewed to the left. This type of distribution is defined as a heavy tail distribution since a large number of frequencies are located in one tail. Skewness may affect the result of statistical analysis significantly; therefore, data assessment is really important to evaluate the effect of skewness on different parameters such as overlap percentage between two distributions. Kurtosis is the degree of peakedness compared to normal distribution; so, the ε will be positive if the distribution has a relatively high peak and ε will be negative if the distribution is flat-topped [205].

1.4.2.2   Theoretical Distributions

Various types of theoretical distribution are used to describe the properties of statistical data. Among all models, the normal distribution is the most simple and useful model that can be used to explain the frequency distribution of most engineering data; however, some frequency distributions are strongly skewed requiring other models to fit the data. The first step of analyzing data is to plot the experimental data which gives useful information about the shape and type of distribution. Two characteristics (parameters), mean and variance, are considered to give some useful information about the distribution model; however, the type of probability distribution can not be identified with only these two parameters. For instance, two different distributions can have the same mean and variance values. Mean defines the center or middle of the probability distribution and variance gives information about the variation and dispersion of data [210, 211].

1.4.2.3   Discrete Distributions

Various engineering systems can be defined using the same random experiments and variables. The distribution of random variables can be analyzed using statistical models and the results can be used in different applications [211]. Discrete distributions are used to define the elements of a dataset. The data are finite and can be counted such as the number of people in a city. Since the number of data in each case is finite and the step changes between the values of random variables are measurable, a fixed probability known as a probability function can be assigned to each value of the random variable. In this case, the probability function f(xi) can be calculated using equation 75 [210].

$$p(X = x_i) = f(x_i) = \frac{f_i}{N} = \frac{f_i}{\sum_{j=1}^{n} f_j} \qquad\qquad 75$$

where fi is the frequency of occurrence and N is the sum of fi.

The discrete random variable is a random variable corresponding to a point probability function. For instance, the probability of getting any values of a die is 1/6. Another definition is the cumulative distribution function (CDF) which is a nondecreasing function and can be obtained from the probability function as follow [210]:

For $x_1 < x_2 < x_3 < \ldots < x_n$

$$F(x) = p(X \le x) = \begin{cases} 0 & for\ x < x_1 \\ \sum_{i=1}^{r} f(x_i) & where\ x_r < x < x_{r+1} \\ 1 & for\ x > x_n \end{cases} \qquad 76$$

It is noteworthy to mention that cumulative probability can be used to determine the probability mass function of random variables.

1.4.2.4   Continuous Distributions

For a probability density function like f(*t*), the continuous distribution function, F(*x*), can be calculated using equation 77.

$$F(x) = p(X \le x) = \int_{-\infty}^{x} f(t)dt \qquad 77$$

where *X* is the continuous random variable [210, 211].

Density function is usually used to explain the physical properties of system. For instance, the load on a bar would be different depending on the location and thickness of the bar. So, the density function can be used to illustrate the density of loading on the bar at any point. The total load between two certain points can be calculated as the integral of the density function from point a to point b. The probability density function would be the integral of the density function between points a and b as described in equation 78

$$p(a \le X \le b) = \int_{a}^{b} f(x)dx \qquad 78$$

Histogram can be used to give an estimation of the probability density function since the area of each bar in the histogram would be equal to the relative frequency in the interval. So, the probability of a measurement that might fall in the interval can be estimated [211]. The distribution function of continuous random variables does not show any step change with changing the x values since each value would be within an interval due to the measurement of random variables; however, this feature is not allowed in the distribution function of discrete random variables. The common property of continuous random variables is that they are time-dependent parameters and will be changed

continuously with time (e.g. pressure or temperature changes in a system) [210, 211]. The mean and variance of continuous random variables are calculated using equations 79 and 80 respectively.

$$\mu = E(X) = \int_{-\infty}^{+\infty} x f(x) dx \qquad\qquad 79$$

$$\sigma^2 = V(X) = \int_{-\infty}^{+\infty} (x - \mu)^2 f(x) dx = \int_{-\infty}^{+\infty} x^2 f(x) dx - \mu^2 \qquad\qquad 80$$

1.4.3   Selected Models of Discrete and Continuous Distributions

1.4.3.1   Binomial Distribution

The binomial distribution is the most common type of discrete distribution that is used to describe the probability of observations in one or other of two mutually exclusive categories. The binomial distribution would be made quantitively by assigning 0 and 1 to the failure and success, respectively. If n considers as the independent random trials under the same (invariant) conditions, then certain event A will occur with the same probability P(A) = p (probability of success). The probability of failure would be P(A-) = 1-p = q (probability of failure). If x denotes the number of successful trials (event A), then a number of different combinations of x trials can occur that can be calculated using equation 81 [205, 206, 210].

$$k = \binom{n}{x} = \frac{n!}{x!(n-x)!} \qquad\qquad 81$$

where k is the binomial coefficient of the xth term. The probability function is expressed as:

$$p(x, n, p) = \binom{n}{x} p^x q^{n-x} = \binom{n}{x} p^x (1-p)^{n-x} \qquad\qquad 82$$

The mean, variance, standard deviation, skewness, kurtosis, and coefficient of variation of binomial distribution can be calculated using equations 83 through 88, respectively [205, 206, 210].

$$\mu = np \qquad\qquad 83$$

$$\sigma^2 = npq = np(1-p) \qquad\qquad 84$$

$$\sigma = \sqrt{npq} \hspace{6cm} 85$$

$$\alpha = \frac{q-p}{\sqrt{npq}} \hspace{6cm} 86$$

$$\varepsilon = \frac{1-6pq}{npq} \hspace{6cm} 87$$

$$V = \sqrt{\frac{q}{np}} \hspace{6cm} 88$$

1.4.3.2 Normal Distribution

Normal distribution is the most widely used model for the distribution of continuous random variables with a bell-shaped curve which is only dependent on two parameters, σ and μ, described as $N(\mu,\sigma)$. Based on the central limit theorem, the normal distribution can be used for descriptive analysis. In this situation, the distribution of the sample mean, denoted by $\bar{x}$, approaches the normal distribution with a variance of σ_2/n and mean of μ, where n is the sample size. It is important to note that the population variance should be finite for the sample mean to behave normally. The probability density function of the normal distribution can be calculated as illustrated in equation 89 [205, 206, 210].

$$f(x) = \frac{1}{\sigma\sqrt{2\pi}}e^{-(x-\mu)^2/2\sigma^2} \hspace{4cm} 89$$

Increasing standard deviation (σ) results in greater dispersion of the distribution. Meanwhile, for a constant σ, increasing the μ changes the location on the x-axis. In general, small σ indicates that the data is tightly clustered around the mean and the distribution will be high and narrow; however, larger σ corresponds to a low, wide distribution since the data is spread out around the μ [205, 206, 210].
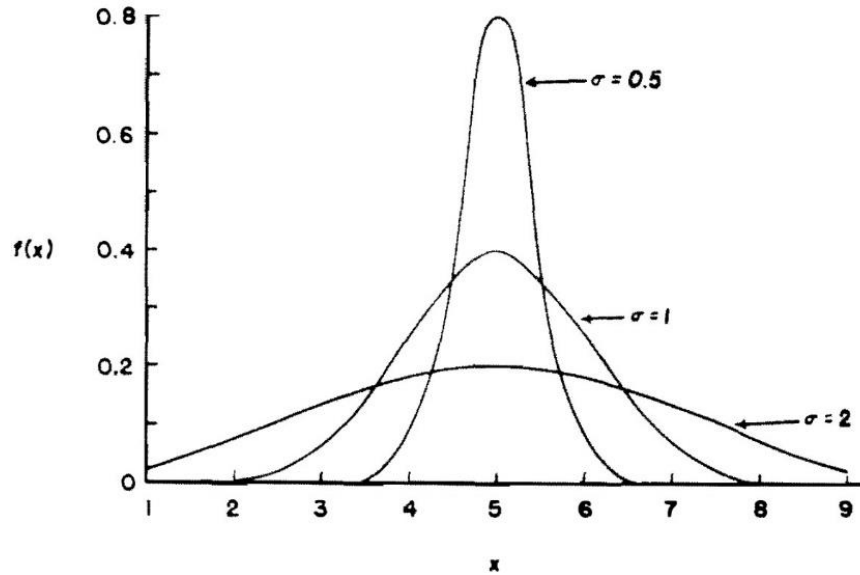
Figure 1.16: Schematic representation of normal distribution curves with the same mean value [210].

The cumulative distribution function (CDF) of a normal distribution is described in equation 90.

$$F(x) = p(X \le x) = \frac{1}{\sigma\sqrt{2\pi}} \int_{-x}^{x} e^{-(x-\mu)^2/2\sigma^2} \, dx \qquad\qquad 90$$

The standard normal distribution (z-distribution) is a normal distribution with μ =0 and σ =1. The standard normal distribution is used to standardize any normal distributions, converting its values into z-score. z-score gives information about how many σ values lie from the μ. By converting a normal distribution to z-distribution, we would be able to calculate the probability and compare different data sets with different means and standard deviations. Equation 91 is used to calculate the z-score.

$$z = \frac{x - \mu}{\sigma} \qquad\qquad 91$$

where x is the individual value, μ is the mean, and σ is the standard deviation.

The total area under a standard normal distribution is 1 or 100%; So, the probability between two points would be the area under the curve with two values as the limits. Each

z-score has its specific p-value giving you the probability of all values occurring below or above the z-score, depending on the convention and z-table (z-table is used to find the probability of each value and corresponding z-score) [205, 206, 210].

1.4.3.3   Log-Normal Distribution

Many processes or phenomena show extreme distribution behaviour instead of normal distribution, such as crystal growth due to the annealing of materials or grinding process. In those examples, either left-skewed or right-skewed distributions have been observed. The log-normal distribution is dependent on three parameters including mean, standard deviation, and skewness. Statistical analysis has revealed that the distribution of log x has the same shape as a normal distribution (bell shape), where x is a random variable. In other words, when y vs x is a log-normal distribution, then y vs log(x) can be a normal distribution as shown in figure 1.17 [205, 210].
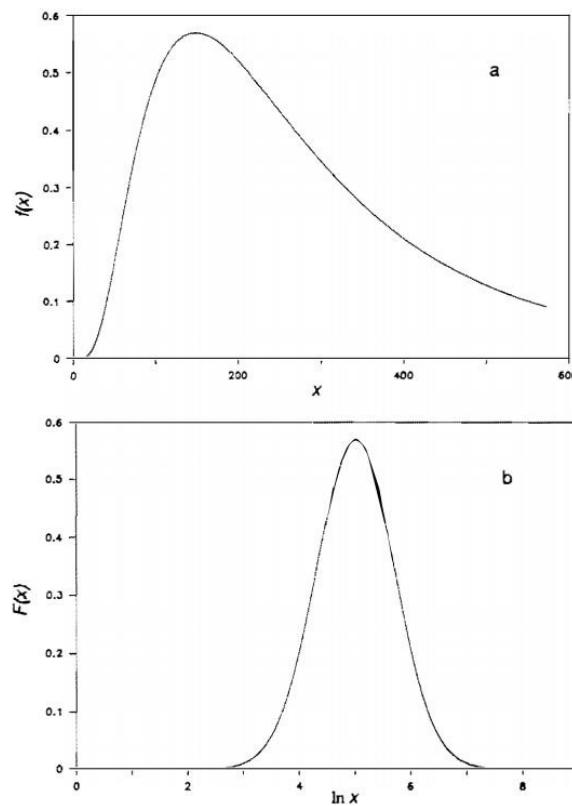
Figure 1.17: Log-normal distribution a) distribution curve of original data b) distribution curve of transformed data to normal distribution [210].

Skewness is unknown or uncertain in some situations; so, lower or upper bounds (x_0) may be used to calculate the normal distribution parameters.

$$Y = \ln|X - x_0| \qquad\qquad 92$$

where X is a random variable and x_0 denotes the lower or upper bound of the variable X. The lower or upper bound can be calculated using equation 93.

$$x_0 = \mu_x - \frac{\sigma_x}{c} \qquad\qquad 93$$

where c is the coefficient and can be expressed as

$$\alpha_x = c^3 + 3c \qquad\qquad 94$$

Since we have a log transformation process in this type of distribution, negative values are not acceptable. The density function of log-normal distribution is defined as illustrated in equation 95 [205, 210].

$$f(x) = \begin{cases} \frac{1}{\sigma x \sqrt{2\pi}} exp(-\frac{(lnx-\mu)^2}{2\sigma^2} & 0 < x < \infty \\ 0 & otherwise \end{cases} \qquad\qquad 95$$

where μ is the mean and σ^2 is the variance of $y = \ln(x)$.

$$\mu = \frac{1}{n}\sum_{i=1}^{n} \ln x_i \qquad\qquad 96$$

$$\sigma^2 = \frac{1}{n-1}\sum_{i=1}^{n}(\ln x_i - \ln x)^2 \qquad\qquad 97$$

1.4.3.4   Exponential Distribution

The exponential distribution is widely used to model the time to failure of processes or determine the reliability of systems. An exponential distribution can be derived from the Poisson point process. Assume that counts occur randomly throughout the interval of real numbers. If interval can be divided into small subintervals with enough length such that:

I.   The probability of more than one count is zero in a subinterval

II.   The probability of one count is the same for all subintervals and proportional to the length of the subinterval

III.   The count in each sub-interval is independent of other subintervals.

then, the random experiment is called a Poisson process and the random variable (X) in the interval is a Poisson random variable. The probability mass function is expressed as:

$$f(x) = \frac{e^{-\lambda}\lambda^x}{x!} \qquad x = 0,1,2,\dots \qquad\qquad 98$$

If we assume that the number of flaws along a certain length of Cu wire is defined as the Poisson distribution, then the distance between flaws is another random variable. So, X is the length from any starting point on the Cu wire until a flaw is found. N is the random variable that defines the number of flaws in x cm of wire and the wire is assumed to be longer than the value of x [205, 210].

$$P(X > x) = P(N = 0) = \frac{e^{-\lambda x}(\lambda x)^0}{0!} = e^{-\lambda x} \qquad\qquad 99$$

The cumulative distribution function can be expressed as:

$$F(x) = P(X \le x) = 1 - e^{-\lambda x} \qquad x \ge 0 \qquad\qquad 100$$

and probability density function of an exponential random variable can be derived from differentiating F(x):

$$f(x) = \lambda e^{-\lambda x} \qquad x \ge 0 \qquad\qquad 101$$

The mean and standard deviation can be calculated using equations 102 and 103, respectively [205, 210].

$$\mu = \frac{1}{\lambda} \qquad\qquad 102$$

$$\sigma^2 = \frac{1}{\lambda^2} \qquad\qquad 103$$

1.4.3.5   Gamma Distribution

Gamma distribution is also known as Pearson's distribution type III. The gamm distribution is a one-sided limited distribution and its probability density function is only dependent on the mean and standard deviation [205, 206].

$$\varphi(x) = \frac{\lambda^k x^k exp(-\lambda x)}{\Gamma(k)} \qquad\qquad 104$$

$$\lambda = \frac{\mu}{\sigma^2} \qquad\qquad 105$$

$$k = \left(\frac{\mu}{\sigma}\right)^2 \qquad\qquad 106$$

where $\Gamma(k)$ is the gamma function of the parameter k. The gamma distribution approaches the normal distribution when k moves toward infinite. Both Gamma and Log-Normal distributions can be used in the same way; however, there is a difference in their skewness parameters since Gamma has a smaller skewness than the Log-Normal distribution [205, 206].

1.4.3.6   Weibull Distribution

The Weibull distribution has been mostly used to model the physical failure of systems over time; so, it can model the time-dependent failure of systems due to its flexibility. The density function probability is expressed in equation 107 [205, 206].

$$f(x) = \frac{\beta}{\delta}\left(\frac{x}{\delta}\right)^\beta exp\left[-\left(\frac{x}{\delta}\right)^\beta\right] \qquad\qquad \text{for x>0} \qquad\qquad 107$$

where δ and β are the scale parameter and shape parameter, respectively. The Weibull distribution approaches the exponential distribution when $\beta=1$. The mean and variance of Weibull distribution can be calculated using equations 108 and 109 respectively.

$$\mu = E(x) = \Gamma\left(1 + \frac{1}{\beta}\right) \qquad\qquad 108$$

$$\sigma^2 = V(x) = \delta^2\Gamma\left(1 + \frac{2}{\beta}\right) - \delta^2\left[\Gamma\left(1 + \frac{1}{\beta}\right)\right]^2 \qquad\qquad 109$$

where $\Gamma(n) = (n-1)!$. Also, The cumulative distribution function can be defined as:

$$F(x) = 1 - e^{-\left(\frac{x}{\delta}\right)^{\beta}}$$
<div align="right">110</div>

1.4.4   Statistics in Corrosion Science

Most researchers have focused on the deterministic behaviour of corrosion parameters; however, localized corrosion changes the deterministic approaches resulting in the generation of scattered data. As a result, the statistical approach and stochastic nature of localized corrosion become important. Statistics is one of the most important topics in materials science and engineering since all analyses are based on extreme values. For instance, extreme-value statistic was used to investigate the failure life of materials and evaluate the max pit depth [212-214]. In terms of the stochastic nature of pitting corrosion, Shibata [215] proposed that the scattering of data was not because of uncontrolled parameters but because of the intrinsic nature of the pitting process. This analysis might be invalid since few parameters such as solution conditions are controlled, not the surface condition of each electrode; so, the surface condition could be another uncontrolled parameter that might result in the dispersion of data. A hypothesis was proposed that pitting corrosion is a deterministic value and not a distributed data, indicating that pitting occurred only when the overall electrode (Cu) potential raised above 375 mV vs SHE in Brussels water [157]. However, this hypothesis was rejected by other researchers [147, 162, 212, 213, 215-219]. Shalaby [162] claimed that pitting potential is not a deterministic value but a distributed value depending on different factors such as scan rate, solution composition, pH, and chemical composition of Cu. Also, critical pitting temperature (CPT) was assumed to be a singular deterministic value [77, 175, 220]; although, Frankel and coworkers determined that CPT is a distributed value and not a deterministic value. His research clarified that CPT distribution range increased with decreasing aggressive anions concentration and was dependent on many factors such as passive film quality, applied potential, surface area, anions concentrations in a solution, and dispersion of metastable pits [112, 116, 147, 216, 221]. For many years, researchers believed that metastable to stable pit growth occurred at temperatures above the CPT; however, Frankel and coworkers observed many metastable pitting events at temperatures above the CPT. As a result, he determined that CPT is neither a deterministic nor an intrinsic material property [112]. While their research gave useful

information about the stochastic nature of CPT, talking about the outliers based on only 5 replicated data is not accurate. In fact, increasing the number of experiments could remove the outliers by changing the range and shape of a distribution. Moreover, the presence and number of outliers depend on the type of test being used. Williams et al. proposed a stochastic pitting model to evaluate the effect of passive film breakdown on pitting probability [222, 223]. This model proposed that improvement of passive film quality increased the pitting potential, specifically when the concentrations of aggressive anions were low. As a result, the frequency of pit initiations decreased leading to a greater driving force required to breakdown the passive film. Also, it might increase the distribution size of corrosion parameters. Pistorius et al. reported that the frequency of metastable pitting events increased with increasing potential and then decreased after reaching a maximum rate [176]. Frankel observed the same behaviour on SS316L and proposed that stable pitting was initiated hundreds of mV higher than the maximum rate of passive film breakdown when the frequency of breakdown decreased significantly. So, passive film breakdown is not the only critical factor in pitting corrosion and stable pit growth can only occur when $i_{diss, max} > i_{diff, crit}$, independent of passive film breakdown [132].

1.5 References

[1] PRIS - Country details. Https://pris.iaea.org/PRIS/countrystatistics/countrydetails.Aspx?Current=SE, IAEA, 2021.

[2] Nuclear energy in sweden. https://www.world-nuclear.org/information-library/country-profiles/countries-o-s/sweden.aspx, world nuclear sssociation, 2021.

[3] M. Davis, M. Ahiduzzaman, A. Kumar, Mapping Canadian energy flow from primary fuel to end use, Energy Conversion and Management, 156 (2018) 178-191.

[4] Nuclear power in Canada. Https://www.world-nuclear.org/Information-Library/Country-Profiles/countries-A-F/Canada-Nuclear-Power.aspx, World Nuclear Association, 2021.

[5] Electric power, annual generation by class of producer, Statistics Canada, 2020.

[6] M. Gobien, M. Ion, Nuclear fuel waste projections in Canada–2019 Update, 2019.

[7] Nuclear Fuel Waste Act, (2002), 2002.

[8] Finland is on the brink of a nuclear power game changer, (2022).

[9] T. Hedman, A. Nyström, C. Thegerström, Swedish containers for disposal of spent nuclear fuel and radioactive waste, Comptes Rendus Physique, 3 (2002) 903-913.

[10] Long-term safety for KBS-3 repositories at Forsmark and Laxemar – A first evaluation, 2006.

[11] Long-term safety for the final repository for spent nuclear fuel at Forsmark, 2011.

[12] Learning more together triennial report 2011 to 2013, Nuclear Waste Management Organization, 2014.

[13] F. King, M. Kolář, Lifetime Predictions for nuclear waste disposal containers, Corrosion, 75 (2018) 309-323.

[14] D. W. Shoesmith, The chemistry-electrochemistry of spent nuclear fuel as a wasteform, Mineralogical Association of Canada, 2013.

[15] J. McMurry, B.M. Ikeda, S. Stroes-Gascoyne, D.A. Dixon, Evolution of a Canadian deep geologic repository: Defective container scenario, Atomic Eenergy of Canada Limited, Atomic Eenergy of Canada Limited, 2004.

[16] D.S. Hall, P.G. Keech, An overview of the Canadian corrosion program for the long-term management of nuclear waste, Corrosion Engineering, Science and Technology, 52 (2017) 2-5.

[17] Multiple-Barrier system, Nuclear Waste Management Organization, 2021.

[18] J. Noronha, Deep geological repository conceptual designs report: crystalline/sedimentary rock environment, Nuclear Waste Mangement Organization (NWMO), 2016.

[19] D.W. Shoesmith, The chemistry/electrochemistry of spent nuclear fuel as a wasteform, Uranium: Cradle to grave, Mineralogical Society of Canada, Short Course Series, 43 (2013) 337-368.

[20] NWMO's program for research and development for long term management of used nuclear fuel, NWMO, 2019.

[21] M. Wu, M. Behazin, J. Nam, P. Keech, Internal corrosion of used fuel container, Nuclear Waste Management Organization, 2019.

[22] G.M. Kwong, Status of corrosion studies for copper used fuel containers under low salinity conditions, 2011.

[23] J.R. Scully, M. Edwards, Review of the NWMO copper corrosion allowance, Nuclear Waste Management Organization, 2013.

[24] J.R. Scully, M. Edwards, Review of the NWMO copper corrosion allowance, Nuclear Waste Management Organization, 2013.

[25] K.B. R. Crowe, J. Freire-Canosa, J. Chen, D. Doyle, F. Garisto, P. Gierszewski, M. Gobien, C. Boyle, N. Hunt, S. Hirschorn, M. Jensen, P. Keech, L. Kennell-Morrison, E. Kremer, C. Medri, M. Mielcarek, A. Murchison, A. Parmenter, E. Sykes, T. Yang, Technical program for long-term management of Canada's used nuclear fuel – Annual report 2016, 2017.

[26] T. Standish, J. Chen, R. Jacklin, P. Jakupi, S. Ramamurthy, D. Zagidulin, P. Keech, D. Shoesmith, Corrosion of copper-coated steel high level nuclear waste containers under permanent disposal conditions, Electrochimica Acta, 211 (2016) 331-342.

[27] T.E. Standish, D. Zagidulin, S. Ramamurthy, P.G. Keech, J.J. Noël, D.W. Shoesmith, Galvanic corrosion of copper-coated carbon steel for used nuclear fuel containers, Corrosion Engineering, Science and Technology, 52 (2017) 65-69.

[28] F. King, D.S. Hall, P.G. Keech, Nature of the near-field environment in a deep geological repository and the implications for the corrosion behaviour of the container, Corrosion Engineering, Science and Technology, 52 (2017) 25-30.

[29] F. King, M. Kolář, A numerical model for the Corrosion of copper nuclear fuel waste containers, MRS Proceedings, 412 (2011).

[30] H.R. Müller, B. Garitte, T. Vogt, S. Köhler, T. Sakaki, H. Weber, T. Spillmann, M. Hertrich, J.K. Becker, N. Giroud, V. Cloet, N. Diomidis, T. Vietor, Implementation of the

full-scale emplacement (FE) experiment at the Mont Terri rock laboratory, Swiss Journal of Geosciences, 110 (2017) 287-306.

[31] Y. Tomonaga, N. Giroud, M.S. Brennwald, E. Horstmann, N. Diomidis, R. Kipfer, P. Wersin, On-line monitoring of the gas composition in the full-scale emplacement experiment at Mont Terri (Switzerland), Applied Geochemistry, 100 (2019) 234-243.

[32] N. Giroud, Y. Tomonaga, P. Wersin, S. Briggs, F. King, T. Vogt, N. Diomidis, On the fate of oxygen in a spent fuel emplacement drift in Opalinus Clay, Applied Geochemistry, 97 (2018) 270-278.

[33] R.P. Morco, J.M. Joseph, D.S. Hall, C. Medri, D.W. Shoesmith, J.C. Wren, Modelling of radiolytic production of HNO_3 relevant to corrosion of a used fuel container in deep geologic repository environments, Corrosion Engineering, Science and Technology, 52 (2017) 141-147.

[34] P.A. Yakabuskie, J.M. Joseph, C.R. Stuart, J.C. Wren, Long-term gamma radiolysis kinetics of NO^{3-} and NO^{2-} solutions, J Phys Chem A, 115 (2011) 4270-4278.

[35] A.J. Bard, L.R. Faulkner, Electrochemical methods: Fundamentals and applications, John Wiley and Sons2001.

[36] E. McCafferty, Introduction to corrosion science, Springer Science & Business Media2010.

[37] P. Roberge, Corrosion engineering: Principles and practice, McGraw-Hill2008.

[38] M. Pourbaix, Atlas of electrochemical equilibria in aqueous solutions, NACE International1974.

[39] W.M. Haynes, D.R. Lide, T.J. Bruno, CRC handbook of chemistry and physics 95th Edition, Taylor and Francis2014.

[40] R. Francis, The corrosion of copper and its alloys: A practical guide for engineers, NACE International2010.

[41] D.A. Palmer, Solubility measurements of crystalline Cu_2O in aqueous solution as a function of temperature and pH, Journal of Solution Chemistry, 40 (2011) 1067-1093.

[42] D.A. Palmer, P. Bénézeth, J. Simonson, Solubility of copper oxides in water and steam, 14th International Conference on the Properties of Water and Steam in Kyoto, 2004, pp. 491-496.

[43] M. Zhong, Y. Wang, P. Krys, D. Konkolewicz, K. Matyjaszewski, Reversible-deactivation radical polymerization in the presence of metallic copper. Kinetic simulation, Macromolecules, 46 (2013) 3816-3827.

[44] Y. Mei, D.M. Sherman, W. Liu, J. Brugger, Ab initio molecular dynamics simulation and free energy exploration of copper(I) complexation by chloride and bisulfide in hydrothermal fluids, Geochimica et Cosmochimica Acta, 102 (2013) 45-64.

[45] E.V. Filimonov, A.I. Shcherbakov, Catalytic effect of copper ions on nitrate reduction, Protection of Metals, 40 (2004) 280-285.

[46] S.A. Awad, K.M. Kamel, Z. Abd El-Hadi, H.A. Bayumi, Mechanism of anodic dissolution of copper in aqueous acidified solutions of different anions, Journal of Electroanalytical Chemistry and Interfacial Electrochemistry, 199 (1986) 341-350.

[47] J.A. Altermatt, S.E. Manaban, Electrochemical behavior of cuprous ion in a noncomplexing aqueous medium, Analytical Chemistry, 40 (1968).

[48] I. Puigdomenech, C. Taxen, Thermodynamic data for copper. Implications for the corrosion of copper under repository conditions, Swedish Nuclear Fuel and Waste Management Co, 2000.

[49] D.S. Hall, T.E. Standish, M. Behazin, P.G. Keech, Corrosion of copper-coated used nuclear fuel containers due to oxygen trapped in a Canadian deep geological repository, Corrosion Engineering, Science and Technology, 53 (2018) 309-315.

[50] F. Garisto, M. Gobien, E. Kremer, C. Medri, Fourth case study: Reference data and codes, Nuclear Waste Management Organization, 2012.

[51] F. King, C. Lilja, K. Pedersen, P. Pitkänen, M. Vähänen, An update of the state-of-the-art report on the corrosion of copper under expected conditions in a deep geologic repository, SKB, 2010.

[52] G. Kear, B.D. Barker, F.C. Walsh, Electrochemical corrosion of unalloyed copper in chloride media—a critical review, Corrosion Science, 46 (2004) 109-135.

[53] F. King, Corrosion of copper in alkaline chloride environment, 2002.

[54] J.R. Scully, D. Feron, H. Hanninen, Review of the NWMO copper corrosion program, NWMO-TR-2015-06, 2016.

[55] E. Huttunen-Saarivirta, P. Rajala, L. Carpén, Corrosion behaviour of copper under biotic and abiotic conditions in anoxic ground water: electrochemical study, Electrochimica Acta, 203 (2016) 350-365.

[56] M. Bojinov, I. Betova, C. Lilja, A mechanism of interaction of copper with a deoxygenated neutral aqueous solution, Corrosion Science, 52 (2010) 2917-2927.

[57] F. King, C.D. Litke, M.J. Quinn, D.M. Leneveu, The measurement and prediction of the corrosion potential of copper in chloride solutions as a function of oxygen concentration and mass-transfer coefficient, Corrosion Science, 37 (1995) 833-851.

[58] F. Arjmand, A. Adriaens, Influence of pH and chloride concentration on the corrosion behavior of unalloyed copper in NaCl solution: A comparative study between the micro and macro scales, Materials, 5 (2012) 2439-2464.

[59] Z. Xiao, C.H. Gammons, A.E. Williams-Jones, Experimental study of copper(I) chloride complexing in hydrothermal solutions at 40 to 300°C and saturated water vapor pressure, Geochimica et Cosmochimica Acta, 62 (1998) 2949-2964.

[60] G. Mengoli, M.M. Musiani, Electrochemical behaviour of copper in neutral aerated chloride solution. I. Steady state investigation, Journal of Apllied Electrochemistry, 18 (1988).

[61] F. King, L. Ahonen, C. Taxen, U. Vuorinen, L. Werme, Copper corrosion under expected conditions in a deep geologic repository, SKB, 2002.

[62] A.E. Warraky, H.A.E. Shayeb, E.M. Sherif, Pitting corrosion of copper in chloride solutions, Anti-Corrosion Methods and Materials, 51 (2004) 25-61.

[63] H.P. Lee, K. Nobe, Kinetics and mechanisms of Cu electrodissolution in chloride media, Journal of Electrochemical Society, 133 (1986) 2035-2043.

[64] H. Cong, J.R. Scully, Effect of chlorine concentration on natural pitting of copper as a function of water chemistry, Journal of The Electrochemical Society, 157 (2010) 200-211.

[65] H. Cong, J.R. Scully, Use of coupled multielectrode arrays to elucidate the pH dependence of copper pitting in potable water, Journal of The Electrochemical Society, 157 (2010) 36 - 46.

[66] H. Cong, H.T. Michels, J.R. Scully, Passivity and pit stability behavior of copper as a function of selected water chemistry variables, Journal of Electrochemical Society, 156 (2009) 16-27.

[67] G. Mankowski, J.P. Duthil, A. Giusti, The pit morphology on copper in chloride- and sulphate-containing solutions, Corrosion Science, 39 (1997) 27-42.

[68] H.H. Strehblow, B. Titze, The investigation of the passive behaviour of copper in weakly acid and alkaline solutions and the examination of the passive film by ESCA and ISS, Electrochimica Acta, 25 (1980) 839-850.

[69] D.W. Shoesmith, T.E. Rummery, D. Owen, W. Lee, Anodic oxidation of copper in alkaline solutions- nucleation and growth of cupric hydroxide films, Journal of Electrochemical Society, 123 (1976) 790-799.

[70] H. Ha, C. Taxen, K. Williams, J. Scully, Effects of selected water chemistry variables on copper pitting propagation in potable water, Electrochimica Acta, 56 (2011) 6165-6183.

[71] E. Mattsson, Corrosion of Copper and Brass: Practical Experience in relation to basic data, British Corrosion Journal, 15 (1980) 6-13.

[72] S.B. Covino, D.S. Cramer, Corrosion: fundamentals, testing, and protection, ASTM, 2003.

[73] H.H. Uhlig, Passivity in metals and alloys, Corrosion Science, 19 (1979) 777-791.

[74] G.S. Frankel, N. Sridhar, Understanding localized corrosion, Materials Today, 11 (2008) 38-44.

[75] R.C. Newman, 2001 W.R. Whitney award lecture- understanding the corrosion of stainless steel, Corrosion, 57 (2001) 1030-1041.

[76] G.S. Frankel, Pitting corrosion of metals: A review of the critical factors, Journal of Electrochemical Society, 145 (1998) 2186-2198.

[77] V.M. Salinas-Bravo, R.C. Newman, An alternative method to determine critical pitting temperature of stainless steels in ferric chloride solution, Corrosion Science, 36 (1994) 66-77.

[78] S.T. Pride, J.R. Scully, J.L. Hudson, Metastable pitting of aluminum and criteria for the transition to stable pit growth, Journal of Electrochemical Society, 141 (1994) 3028-3040.

[79] P.C. Pistorius, G.T. Burstein, Metastable pitting corrosion of stainless steel and the transition to stability, Philosophical Transactions of the Royal Society of London. Series A: Physical and Engineering Sciences, 341 (1992) 531-559.

[80] G.T. Burstein, Revealing corrosion pits, Nature, 350 (1991).

[81] G.S. Frankel, L. Stockert, F. Hunkeler, H. Boehni, Metastable pitting of stainless steel, Corrosion, 43 (1987) 429-436.

[82] G.T. Gaudet, W.T. Mo, T.A. Hatton, J.W. Tester, J. Tilly, H.S. Isaacs, R.C. Newman, Mass transfer and electrochemical kinetic interactions in localized pitting corrosion, AlChE Journal, 32 (1986) 949-958.

[83] J.R. Galvele, Transport processes and the mechanism of pitting of metals, Journal of Electrochemical Society, 123 (1976) 464-474.

[84] F.M. Al-Kharafi, Y.A. El-Tantawy, Passivation of copper: Role of some anions in the mechanism of film formation and breakdown, Corrosion Science, 22 (1982) 1-12.

[85] P. Marcus, Corrosion mechanisms in theory and practice, Marcel Dekker2002.

[86] R.M. Souto, S. González, R.C. Salvarezza, A.J. Arvia, Kinetics of copper passivation and pitting corrosion in Na_2SO_4 containing dilute NaOH aqueous solution, Electrochimica Acta, 39 (1994) 2619-2628.

[87] I. Milosev, M. Metikos-Hukovic, M. Drogowska, H. Menard, Breakdown of passive film on copper in bicarbonate solutions containing sulfate ions, Journal of Electrochemical Society, 139 (1992) 2409-2418.

[88] G. Ruijin, H. Shizhong, An investigation of pitting initiation process, Journal of Chinese Society for Corrosion and protection, 6 (1986) 113-122.

[89] W. Schwenk, Theory of Stainless Steel pitting, Second International Congress on Metallic CorrosionNew York, 1963.

[90] A. Seyeux, V. Maurice, P. Marcus, Oxide film growth kinetics on metals and alloys, Journal of The Electrochemical Society, 160 (2013) C189-C196.

[91] D.D. Macdonald, The history of the point defect model for the passive state: a brief review of film growth aspects, Electrochimica Acta, 56 (2011) 1761-1772.

[92] F.P. Fehlner, N.F. Mott, Low-temperature oxidation, Oxidation of Metals, 2 (1970) 59-99.

[93] N. Cabrera, N.F. Mott, Theory of the oxidation of metals, IOP Science1949.

[94] N. Mott, The theory of the formation of protective oxide films on metals.—III, Transactions of the Faraday Society, 43 (1947) 429-434.

[95] N. Mott, A theory of the formation of protective oxide films on metals, Transactions of the faraday Society, 35 (1939) 1175-1177.

[96] B. Miller, Split-ring disk study of the anodic processes at a copper electrode in alkaline solution, Journal of The Electrochemical Society, 116 (1969).

[97] J. Ambrose, R.G. Barradas, D.W. Shoesmith, Rotating copper disk electrode studies of the mechanism of the dissolution-passivation step on copper in alkaline solutions, Electrochemical Chemistry and Interfacial Electrochemistry, 47 (1973) 65-80.

[98] D. Macdonald, The point defect model for the passive state, Journal of Electrochemical Society, 139 (1992) 3434-3449.

[99] C.Y. Chao, L.F. Lin, D.D. Macdonald, A point defect model for anodic passive films: I . Film growth kinetics, Journal of The Electrochemical Society, 128 (1981) 1187-1194.

[100] M. Momeni, J.C. Wren, A mechanistic model for oxide growth and dissolution during corrosion of Cr-containing alloys, Faraday Discuss, 180 (2015) 113-135.

[101] H.D. Speckmann, M.M. Lohrengel, J.W. Schultze, H.H. Strehblow, The growth and reduction of duplex oxide-films on copper, Ber Bunsen Phys Chem, 89 (1985) 392-402.

[102] M.R.G.D. Chialvo, R.C. Salvarezza, D.V. Moll, A.J. Arvia, Kinetics of passivation and pitting corrosion of polycrystalline copper in borate buffer solutions containing sodium chloride., Electrochimica Acta, 30 (1985) 1501–1511.

[103] J.S. Halliday, The anodic behaviour of copper in caustic soda solutions, Transactions of the Faraday Society, 50 (1954) 171-178.

[104] M.R. Gennero De Chialvo, J.O. Zerbino, S.L. Marchiano, A.J. Arvia, Correlation of electrochemical and ellipsometric data in relation to the kinetics and mechanism of Cu2O electroformation in alkaline solutions, Journal of Applied Electrochemistry, 16 (1986) 517-526.

[105] N.S. McIntyre, S. Sunder, D.W. Shoesmith, F.W. Stanchell, Chemical information from XPS—applications to the analysis of electrode surfaces, Journal of Vacuum Science and Technology, 18 (1981) 714-721.

[106] T. Hurlen, G. Oven, A. Staurset, Kinetics of copper dissolution and deposition in aqueous sulphate solution, Electrochimica Acta, 23 (1978) 39-44.

[107] R.M. Souto, S. Gonzalez, R.C. Salvarezza, A.J. Arvia, Kinetics of copper passivation and pitting corrosion in Na_2SO_4 containing dilute NaOH aqueous solution, Electrochimica Acta, 39 (1994) 2619-2628.

[108] M. Pérez Sánchez, M. Barrera, S. González, R.M. Souto, R.C. Salvarezza, A.J. Arvia, Electrochemical behaviour of copper in aqueous moderate alkaline media, containing sodium carbonate and bicarbonate, and sodium perchlorate, Electrochimica Acta, 35 (1990) 1337-1343.

[109] D.C. Kong, C.F. Dong, X.Q. Ni, A.N. Xu, C. He, K. Xiao, X.G. Li, Long-term polarisation and immersion for copper corrosion in high-level nuclear waste environment, Materials and Corrosion, 68 (2017) 1070-1079.

[110] T. Li, J.R. Scully, G.S. Frankel, Localized corrosion: passive film breakdown vs. pit growth stability: part IV. The role of salt film in pit growth: A mathematical framework, Journal of The Electrochemical Society, 166 (2019) C115-C124.

[111] T. Li, J.R. Scully, G.S. Frankel, Localized corrosion: passive film breakdown vs pit growth stability: part V. Validation of a new framework for pit growth stability using one-dimensional artificial pit electrodes, Journal of The Electrochemical Society, 166 (2019) C3341-C3354.

[112] T. Li, J.R. Scully, G.S. Frankel, Localized corrosion: passive film breakdown vs pit growth stability: part II. A model for critical pitting temperature, Journal of The Electrochemical Society, 165 (2018) C484-C491.

[113] T. Li, J.R. Scully, G.S. Frankel, Localized corrosion: passive film breakdown vs. pit growth stability: part iii. A unifying set of principal parameters and criteria for pit stabilization and salt film formation, Journal of The Electrochemical Society, 165 (2018) C762-C770.

[114] G.S. Frankel, T. Li, J.R. Scully, Localized corrosion: Passive film breakdown vs pit growth stability, Journal of The Electrochemical Society, 164 (2017) C180-C181.

[115] J. Srinivasan, R.G. Kelly, One-dimensional pit experiments and modeling to determine critical factors for pit stability and repassivation, Journal of The Electrochemical Society, 163 (2016) C759-C767.

[116] T. Li, L. Liu, B. Zhang, Y. Li, F. Wang, An investigation on the continuous and uniform thin membrane passive film formed on sputtered nanocrystalline stainless steel, Corrosion Science, 104 (2016) 71-83.

[117] P.M. Natishan, W.E. O'Grady, Chloride ion interactions with oxide-covered aluminum leading to pitting corrosion: a review, Journal of The Electrochemical Society, 161 (2014) C421-C432.

[118] P. Marcus, V. Maurice, H.H. Strehblow, Localized corrosion (pitting): A model of passivity breakdown including the role of the oxide layer nanostructure, Corrosion Science, 50 (2008) 2698-2704.

[119] S.Y. Yu, W.E. O'Grady, D.E. Ramaker, P.M. Natishan, Chloride ingress into aluminum prior to pitting corrosion an investigation by XANES and XPS, Journal of The Electrochemical Society, 147 (2000).

[120] V. Maurice, W.P. Yang, P. Marcus, X-ray photoelectron spectroscopy and scanning tunneling microscopy study of passive films formed on (100) Fe-18Cr-13Ni single-crystal surfaces, Journal of Electrochemical Society, 145 (1998) 909-920.

[121] P. Marcus, Surface science approach of corrosion phenomena, Electrochimica Acta, 43 (1998) 109-118.

[122] N.J. Laycock, M.H. Moayed, R.C. Newman, Metastable pitting and the critical pitting temperature, Journal of The Electrochemical Society, 145 (1998) 2622-2628.

[123] A. Kolics, J.C. Polkinghorne, A. Wieckowski, Adsorption of sulfate and chloride ions on aluminum, Electrochimica Acta, 43 (1998) 2605-2618.

[124] G.P. Halada, D. Kim, C.R. Clayton, Influence of nitrogen on electrochemical passivation of high-nickel stainless steels and thin molybdenum-nickel films, Corrosion, 52 (1996) 36-46.

[125] V. Maurice, W.P. Yang, P. Marcus, XPS and STM investigation of the passive film formed on Cr(110) single-crystal surfaces, journal of Electrochemical Society, 141 (1994) 3016-3027.

[126] G.T. Burstein, Passivity and localized corrosion, Shreir's Corrosion, 2 (2010) 731-752.

[127] D. Kong, C. Dong, X. Wei, C. Man, X. Lei, F. Mao, X. Li, Size matching effect between anion vacancies and halide ions in passive film breakdown on copper, Electrochimica Acta, 292 (2018) 817-827.

[128] J. Soltis, Passivity breakdown, pit initiation and propagation of pits in metallic materials – Review, Corrosion Science, 90 (2015) 5-22.

[129] X. Wei, C. Dong, P. Yi, A. Xu, Z. Chen, X. Li, Electrochemical measurements and atomistic simulations of Cl−-induced passivity breakdown on a Cu2O film, Corrosion Science, 136 (2018) 119-128.

[130] T.P. Hoar, W.R. Jacob, Breakdown of Passivity of Stainless Steel by Halide Ions, Nature, 216 (1967) 1299-1301.

[131] N. Sato, A theory for breakdown of anodic oxide films on metals, Electrochimica Acta, 16 (1971) 1683-1692.

[132] T. Li, J. Wu, G.S. Frankel, Localized corrosion: Passive film breakdown vs. Pit growth stability, Part VI: Pit dissolution kinetics of different alloys and a model for pitting and repassivation potentials, Corrosion Science, 182 (2021).

[133] B.A. Kehler, G.O. Ilevbare, J.R. Scully, Crevice corrosion stabilization and repassivation behavior of alloy 625 and alloy 22, Corrosion, 57 (2001) 1042-1065.

[134] D.S. Dunn, G.A. Cragnolino, N. Sridhar, An electrochemical approach to predicting long- term localized corrosion of corrosion-resistant high-level waste container materials, Corrosion, 56 (2000) 90-104.

[135] D. Kong, C. Dong, M. Zhao, X. Ni, C. Man, X. Li, Effect of chloride concentration on passive film properties on copper, Corrosion Engineering, Science and Technology, 53 (2017) 122-130.

[136] H. Ha, C. Taxén, H. Cong, J.R. Scully, Effect of applied potential on pit propagation in copper as function of water chemistry, Journal of The Electrochemical Society, 159 (2011) C59-C73.

[137] F. King, M.J. Quinn, C.D. Litke, Oxygen reduction on copper in neutral NaCl solution, Journal of Electrochemical Society, 385 (1995) 45-55.

[138] G. Ruijini, S.C. Srivastava, M.B. Ives, Pitting corrosion behavior of UNS N08904 stainless steel in a chloride-sulfate solution, Corrosion, 45 (1989).

[139] S.M. Mayanna, T.H.V. Setty, Role of chloride ions in relation to copper corrosion and inhibition, Proceeding of Indian Academy of Science - Section A, 80 (1974) 184-193.

[140] H.P. Leckie, H.H. Uhlig, Environmental factors affecting the critical potential for pitting in 18–8 stainless steel, Journal of Electrochemical Society, 113 (1966) 1262-1267.

[141] K. Vetter, H.H. Strehblow, Lochfraßpotentiale und Lochfraßinhibitionspotentiale an reinem Eisen, Berichte der Bunsengesellschaft für physikalische Chemie, 74 (1970) 449-455.

[142] M.G. Alvarez, J.R. Galvele, mechanism of passivity breakdown of high purity cadmium, Journal of The Electrochemical Society, 127 (2019) 1235-1241.

[143] K. Venu, K. Balakrishnan, K.S. Rajagopalan, A potentiokinetic polarization study of the behaviour of steel in NaOH-NaCl system, Corrosion Science, 5 (1965) 59-69.

[144] R.S. Lillard, Factors influencing the transition from metastable to stable pitting in single-crystal beryllium, Journal of The Electrochemical Society, 148 (2001).

[145] G.T. Burstein, S.P. Mattin, Nucleation of corrosion pits on stainless steel, Philosophical Magazine Letters, 66 (1992) 127-131.

[146] A.M. Riley, D.B. Wells, D.E. Williams, Initiation events for pitting corrosion of stainless steel?, Corrosion Science, 32 (1991) 1307-1313.

[147] U. Bertocci, M. Koike, S. Leigh, F. Qiu, G. Yang, A statistical analysis of the fluctuations of the passive current, Journal of The Electrochemical Society, 133 (1986) 1782-1786.

[148] S.B. Adeloju, Y.Y. Duan, Influence of bicarbonate ions on stability of copper oxides and copper pitting corrosion, British Corrosion Journal, 29 (1994) 315-320.

[149] N.G. Smart, J.O.M. Bockris, Effect of water activity on corrosion, Corrosion, 48 (1992) 277-280.

[150] S.B. Adeloju, H.C. Hughes, The corrosion of copper pipes in high chloride-low carbonate mains water, Corrosion Science, 26 (1986) 851-870.

[151] A. Nishikata, M. Itagaki, T. Tsuru, S. Haruyama, Passivation and its stability on copper in alkaline solutions containing carbonate and chloride ions, Corrosion Science, 31 (1990) 287-292.

[152] s.B. Adeloju, Y.Y. Duan, Corrosion resistance of Cu_2O and CuO on copper surfaces in aqueous media, British Corrosion Journal, 29 (2013) 309-314.

[153] R.M. Carranza, M.G. Alvarez, The effect of temperature on the passive film properties and pitting behaviour of a Fe-Cr-Ni alloy, Corrosion Science, 38 (1996) 909-925.

[154] E. Blasco-Tamarit, A. Igual-Muñoz, J.G. Antón, D. García-García, Effect of temperature on the corrosion resistance and pitting behaviour of alloy 31 in LiBr solutions, Corrosion Science, 50 (2008) 1848-1857.

[155] E. Mahdi, A. Rauf, E.O. Eltai, Effect of temperature and erosion on pitting corrosion of X100 steel in aqueous silica slurries containing bicarbonate and chloride content, Corrosion Science, 83 (2014) 48-58.

[156] C. Dong, H. Luo, K. Xiao, T. Sun, Q. Liu, X. Li, Effect of temperature and Cl^- concentration on pitting of 2205 duplex stainless steel, Journal of Wuhan University of Technology-Mater. Sci. Ed., 26 (2011) 641-647.

[157] V.F. Lucey, Mechanism of pitting corrosion of copper in supply waters, British Corrosion Journal, 2 (1967) 175-185.

[158] S.T. Pride, J.R. Scully, J.L. Hudson, Metastable pitting of aluminum and criteria for the transition to stable pit growth, Journal of The Electrochemical Society, 141 (2019) 3028-3040.

[159] V.F. Lucey, Developments leading to the present understanding of the mechanism of pitting corrosion of copper, British Corrosion Journal, 7 (1972) 36-41.

[160] D.C. Silverman, Practical corrosion prediction using electrochemical techniques, John Wiley & Sons, Inc.2011.

[161] R.G. Kelly, J.R. Scully, D. Shoesmith, R.G. Buchheit, Electrochemical techniques in corrosion science and engineering, 2002.

[162] H.M. Shalaby, F.M. Al-Kharafi, V.K. Gouda, A morphological study of pitting corrosion of copper in soft tap water, Corrosion Journal, 45 (1989) 536-547.

[163] M.M. Laz, R.M. Souto, S. González, R.C. Salvarezza, A.J. Arvia, The formation of anodic layers on annealed copper surfaces in phosphate-containing solutions at different pH, Electrochimica Acta, 37 (1992) 655-663.

[164] M.R.G.d. Chialvo, M.F.L. De Mele, R.C. Salvarezza, A.J. Arvia, The influence of sodium bromide in the corrosion and passivity of copper in borate buffer, Corrosion Science, 28 (1988) 121-134.

[165] M. Pérez Sánchez, R.M. Souto, M. Barrera, S. González, R.C. Salvarezza, A.J. Arvia, A mechanistic approach to the electroformation of anodic layers on copper and their electroreduction in aqueous solutions containing $NaHCO_3$ and Na_2CO_3, Electrochimica Acta, 38 (1993) 703-715.

[166] X. Lei, H. Wang, F. Mao, J. Zhang, M. Zhao, A. Fu, Y. Feng, D.D. Macdonald, Electrochemical behaviour of martensitic stainless steel after immersion in a H_2S-saturated solution, Corrosion Science, 131 (2018) 164-173.

[167] H. Luo, H. Su, C. Dong, X. Li, Passivation and electrochemical behavior of 316L stainless steel in chlorinated simulated concrete pore solution, Applied Surface Science, 400 (2017) 38-48.

[168] F. Mao, C. Dong, D.D. Macdonald, Effect of octadecylamine on the corrosion behavior of Type 316SS in acetate buffer, Corrosion Science, 98 (2015) 192-200.

[169] R.K. Gupta, N. Birbilis, The influence of nanocrystalline structure and processing route on corrosion of stainless steel: A review, Corrosion Science, 92 (2015) 1-15.

[170] P. Van der Weeën, A.M. Zimer, E.C. Pereira, L.H. Mascaro, O.M. Bruno, B. De Baets, Modeling pitting corrosion by means of a 3D discrete stochastic model, Corrosion Science, 82 (2014) 133-144.

[171] H. Luo, S. Gao, C. Dong, X. Li, Characterization of electrochemical and passive behaviour of Alloy 59 in acid solution, Electrochimica Acta, 135 (2014) 412-419.

[172] R.P. Frankenthal, H.W. Pickering, On the mechanism of localized corrosion of iron and stainless steel, Journal of The Electrochemical Society, 119 (1972).

[173] J.W. Oldfield, W.H. Sutton, Crevice corrosion of stainless steels: II. Experimental studies, British Corrosion Journal, 13 (2013) 104-111.

[174] N.J. Laycock, J.S. Noh, S.P. White, D.P. Krouse, Computer simulation of pitting potential measurements, Corrosion Science, 47 (2005) 3140-3177.

[175] N.J. Laycock, M.H. Moayed, R.C. Newman, Metastable pitting and the critical pitting temperature, Journal of Electrochemical Society, 145 (1998) 2622-2628.

[176] P.C. Pistorius, G.T. Burstein, Metastable pitting corrosion of stainless steel and the transition to stability, Royal Society London, 341 (1992) 531-559.

[177] T. Li, L. Liu, B. Zhang, Y. Li, F. Wang, Growth kinetics of metastable pits on sputtered nanocrystalline stainless steel, Corrosion Science, 124 (2017) 46-55.

[178] H.S. Isaacs, the behavior of resistive layers in the localized corrosion of stainless steel, Journal of The Electrochemical Society, 120 (1973).

[179] J. Ambrose, R.G. Barradas, D.W. Shoesmith, Investigation of copper in aqueous alkaline solutions by cycling voltammetry, Elctrochemical Chemistry and Interfacial Electrochemistry, 47 (1973) 47-64.

[180] E. Martinez-Lombardia, Y. Gonzalez-Garcia, L. Lapeire, I. De Graeve, K. Verbeken, L. Kestens, J.M.C. Mol, H. Terryn, Scanning electrochemical microscopy to study the effect of crystallographic orientation on the electrochemical activity of pure copper, Electrochimica Acta, 116 (2014) 89-96.

[181] A. Naseer, A.Y. Khan, A study of growth and breakdown of passive film on copper surface by electrochemical impedance spectroscopy, Turk J. Chem., 33 (2009) 739 - 750.

[182] K.A. Lill, A.W. Hassel, G. Frommeyer, M. Stratmann, Scanning droplet cell investigations on single grains of a FeAlCr light weight ferritic steel, Electrochimica Acta, 51 (2005) 978-983.

[183] C.J. Park, M.M. Lohrengel, T. Hamelmann, M. Pilaski, H.S. Kwon, Grain-dependent passivation of surfaces of polycrystalline zinc, Electrochimica Acta, 47 (2002) 3395-3399.

[184] M. Drogowska, L. Brossard, H. Menard, Comparative study of copper behaviour in bicarbonate and phosphate aqueous solutions and effect of chloride ions, Journal of Apllied Electrochemistry, 24 (1994).

[185] M.R.G.d. Chialvo, J.O. Zerbino, S.L. Marchiano, Correlation of electrochemical and ellipsometric data in relation to the kinetics and mechanism of Cu_2O electroformation in alkaline solutions, Journal of Apllied Electrochemistry, 16 (1986) 517-526.

[186] M.R.G.d. Chialvo, A.J. Arvia, The electrochemical behaviour of copper in alkaline solutions containing sodium sulphide, Journal of Apllied Electrochemistry, 15 (1985) 685-696.

[187] V. Ashworth, D. Fairhurst, The anodic formation of Cu_2O in alkaline solutions, Journal of Electrochemical Society, 124 (1977) 506-517.

[188] M.R.G. De Chialvo, S.L. Marchiano, A.J. Arvía, The mechanism of oxidation of copper in alkaline solutions, Journal of Applied Electrochemistry, 14 (1984) 165-175.

[189] H.D. Speckmann, M.M. Lohrengel, J.W. Schultze, H.H. Strehblow, The growth and reduction of duplex oxide films on copper, Ber. Bunsenges. Phys. Chem, 89 (1985) 392-402.

[190] M. Weidenauer, K.G. Weil, Studies of the differential double layer capacitance of the copper (111) face in aqueous solutions, Berichte der Bunsengesellschaft für physikalische Chemie, 92 (1988) 1368-1372.

[191] C.J. Park, M.M. Lohrengel, T. Hamelmann, M. Pilaski, H.S. Kwon, Grain-dependent passivation of surfaces of polycrystalline zinc, Electrochimica Acta, 47 (2002) 3395-3399.

[192] M.M. Lohrengel, A. Moehring, M. Pilaski, Electrochemical surface analysis with the scanning droplet cell, Fresenius J Anal Chem, 367 (2000) 334-339.

[193] A. Schreiber, J.W. Schultze, M.M. Lohrengel, F. Kármán, E. Kálmán, Grain dependent electrochemical investigations on pure iron in acetate buffer pH 6.0, Electrochimica Acta, 51 (2006) 2625-2630.

[194] B. Davepon, J.W. Schultze, U. König, C. Rosenkranz, Crystallographic orientation of single grains of polycrystalline titanium and their influence on electrochemical processes, Surface and Coatings Technology, 169-170 (2003) 85-90.

[195] H.S. Campbell, Pitting corrosion in copper water pipes caused by films of carbonaceous material produced during manufacture, J. Inst. Metals, 77 (1950) 345.

[196] F.J. Cornwell, G. Wildsmith, P.T. Gilbert, Pitting corrosion in copper tubes in cold water service, British Corrosion Journal, 8 (1973) 202-209.

[197] M. Edwards, J.F. Ferguson, S.H. Reiber, The pitting corrosion of copper, Journal-American Water Works Association, 86 (1994) 74-90.

[198] D.A. Lytle, C.P. White, The effect of phosphate on the properties of copper drinking water pipes experiencing localized corrosion, Journal of Failure Analysis and Prevention, 14 (2014) 203-219.

[199] H.S. Campbell, A review: pitting corrosion of copper and its alloys, Localized Corrosion, 3 (1974) 625-638.

[200] E. Mattsson, A.M. Fredriksson, Pitting corrosion in copper tubes–cause of corrosion and counter-measures, British Corrosion Journal, 3 (1968) 246-257.

[201] H. Baba, T. Kodama, T. Fujii, Y. Hisamatsu, Effect of oxidizing agents in water on the pitting corrosion of copper tubes in hot water, Corrosion Engineering, 30 (1981) 161-165.

[202] I. Suzuki, Y. Ishikawa, Y. Hisamatsu, The pitting corrosion of copper tubes in hot water, Corrosion Science, 23 (1983) 1095-1106.

[203] S. Sato, T. Minamoto, K. Seki, H. Yamamoto, Y. Takizawa, S. Okada, S. Yamauchi, Y. Hisamatsu, I. Suzuki, T. Fujii, Case studies on pitting corrosion failures of copper tubes in hot water, Corrosion Engineering, 31 (1982) 3-11.

[204] E.P. McIntyre, A.D. Mercer, Corrosion and related aspects of materials for potable water supplies, CRC Press1993.

[205] M. Holický, Introduction to probability and statistics for engineers, Springer Heidelberg New York Dordrecht London2013.

[206] D.C. Montgomery, G.C. Runger, Applied statistics and probability for engineers, John Wiley & Sons, Inc.2003.

[207] M. Holicky, Reliability analysis for structural design, SUN MeDIA Stellenbosch2009.

[208] A.H.-S. Ang, W.H. Tang, Probability concepts in engineering: Emphasis on applications to civil and environmental engineering, John Wiley and Sons, Inc.2007.

[209] J. Devore, N. Farnum, J. Doi, Applied statistics for engineers and scientists, Richard Stratton, Cengage Learning, 2014.

[210] R.M. Bethea, B.S. Duran, T.L. Boullion, Statistical methods for engineers and scientists, Marcel Dekker Inc.1995.

[211] S.M. Ross, Introduction to probability and statistics for engineers and scientists, Elsevier Inc.2021.

[212] P.M. Aziz, Application of the statistical theory of extreme values to the analysis of maximum pit depth data for aluminum, Corrosion, 12 (1956) 35-46.

[213] G.G. Eldredge, Analysis of corrosion pitting by extreme-value statistics and its application to oil well tubing caliper surveys, Corrosion, 13 (1957) 67-76.

[214] G.N. Scott, Adjustment of soil corrosion pit depth measurements for size of sample, Proc. An. Petroleum Inst, 14 (1934) 204.

[215] T. Shibata, 1996 W.R. Whitney award lecture: Statistical and stochastic approaches to localized corrosion, Corrosion, 52 (1996) 813-830.

[216] L. Peguet, A. Gaugain, C. Dussart, B. Malki, B. Baroux, Statistical study of the critical pitting temperature of 22-05 duplex stainless steel, Corrosion Science, 60 (2012) 280-283.

[217] A. Valor, F. Caleyo, L. Alfonso, J. Vidal, J.M. Hallen, Statistical analysis of pitting corrosion field data and their use for realistic reliability estimations in non-piggable pipeline systems, Corrosion, 70 (2014) 1090-1100.

[218] M. Gholami, M. Hoseinpoor, M.H. Moayed, A statistical study on the effect of annealing temperature on pitting corrosion resistance of 2205 duplex stainless steel, Corrosion Science, 94 (2015) 156-164.

[219] Z.S. Asadi, R.E. Melchers, Extreme value statistics for pitting corrosion of old underground cast iron pipes, Reliability Engineering & System Safety, 162 (2017) 64-71.

[220] R. Qvarfort, Critical pitting temperature measurements of stainless steels with an improved electrochemical method, Corrosion Science, 29 (1989) 987-993.

[221] Y.T. Sun, J.M. Wang, Y.M. Jiang, J. Li, A comparative study on potentiodynamic and potentiostatic critical pitting temperature of austenitic stainless steels, Materials and Corrosion, 69 (2018) 44-52.

[222] D.E. Williams, C. Westcott, M. Fleischmann, Stochastic models of pitting corrosion of stainless steels: I. modeling of the initiation and growth of pits at constant potential, Electrochemical Society, 132 (1985) 1796-1804.

[223] D.E. Williams, J. Stewart, P. Balkwill, The nucleation, growth and stability of micropits in stainless steel, Corrosion Science, 36 (1994) 1213-1235.

Chapter 2

2 Materials and Methods

2.1 Introduction

Principles and procedures of sample preparation, solution preparation, electrochemical techniques, and surface analytical techniques with their usage in this research project are briefly discussed in this chapter. The specific details of each technique will be explained in the subsequent data chapters.

2.2 Materials Selection and Preparation

2.2.1 Wrought Copper

All electrochemical experiments and surface analyses were performed on oxygen-free (<5 ppm) and phosphorus-doped (30-100 wt.ppm) Cu samples (> 99.99 %) supplied by the Swedish Nuclear Fuel and Waste Management Company (SKB, Solna, Sweden). The addition of phosphorus (P) improves the mechanical properties of Cu such as creep behaviour as well as reduces the effect of impurities including S, Bi, Pb, etc. on the physical and mechanical properties of Cu [1, 2].

2.2.2 Sample Preparation

2.2.2.1 Multielectrode Arrays

Cu electrodes were machined in the form of bullet specimens (with one rounded end) (Fig. 2.1) to avoid edge effects during electrochemical experiments, with a threaded connection to a stainless steel rod to enable connection to external electrochemical equipment. The stainless steel rods were covered with polytetrafluoroethylene (PTFE) heat-shrink tubing to isolate them from the solution. Cu specimens used in corrosion experiments were rotated at 2700 RPM and ground with a sequence of SiC papers with grit sizes of 600, 800, 1200, 2500, and 4000. The grinding was followed by rinsing in Type I water with a resistivity of 18.2 MΩ.cm (produced by a Thermo Scientific

Barnstead Nanopure 7143 ultra-water system), sonicating in ethanol for 5 min to remove any grinding residues and organic contaminants, and finally drying in a stream of Ar gas.

Figure 2.1: O-free and P-doped copper electrodes.

2.2.2.2   Single Electrode

Cylindrical Cu samples (1cm diameter $\times$ 4 mm thickness) were machined from a wrought Cu block provided by Svensk Kärnbränslehantering AB (SKB), Solna, Sweden as shown in Fig. 2.2. A threaded hole was drilled in the back of each sample to provide the connection to the stainless rods. The stainless steel rods were coated with polytetrafluoroethylene (PTFE) heat-shrink tubing to prevent the possible exposure of dissimilar materials to the environment. Cu samples were mounted in epoxy and subjected to a vacuum for 5 minutes to remove bubbles from the epoxy and to avoid the formation of crevices between the sample and epoxy. Cu specimens were ground with a sequence of SiC papers (P600, P800, P1200, P2500, and P4000), followed by a final polish using a 1 µm diamond suspension to achieve a mirror surface finish. Then, the

samples were rinsed in type I water (18.2 MΩ.cm), sonicated in ethanol and dried in a stream of Ar gas prior to each experiment. Following each electrochemical experiment, Cu specimens were rinsed with Type I water, dried in an Ar stream, and placed in a glovebox with O_2 levels in the range of 1 ppm for surface analyses.

Prior to each electrochemical experiment, either multielectrode arrays or single electrodes were cathodically cleaned at -0.85 V vs a saturated calomel electrode (SCE) for 3 minutes to reduce any air-formed oxides.

Figure 2.2: O-free and P-doped single copper electrode mounted in epoxy

2.3 Solution Preparation

All solutions were prepared using reagent-grade sodium chloride (NaCl, 99.0%), sodium sulfate (Na_2SO_4, 99.0%), sodium carbonate (Na_2CO_3, 99.5%), and sodium bicarbonate ($NaHCO_3$, 99.7%) provided by Fisher Scientific, and type I water (18.2 MΩ.cm) obtained from a Thermo Scientific Barnstead Nanopure water purification system. The multielectrode array was exposed to unary and binary solutions containing various

concentrations of chloride in the range from 0.01 M to 1 M, sulfate-containing solutions with various [SO_4^{2-}] in the range from 0.001 M to 0.1 M, and binary solutions containing 0.01 M SO_4^{2-} and various [HCO_3^-]. The pH of the solutions was adjusted by adding small volumes of NaOH. Single electrodes were exposed to solutions composed of a 0.005 M Na_2CO_3 / 0.005 M $NaHCO_3$ buffer solution with various concentrations of NaCl or Na2SO4 within the range from 0.01 M to 0.1 M. The pH of the solutions was adjusted to 9 using the 0.005 M Na_2CO_3 / 0.005 M $NaHCO_3$ buffer solution. Solution pH was measured using an OrionTM Star pH meter provided by Thermo Scientific.

2.4 Instrumentation and Electrochemical cell

2.4.1   Multichannel Multielectrode Analyzer (MMA)

The MMA is a specific type of potentiostat/galvanostat that can perform experiments on up to either 50 or 100 electrodes at the same time depending on the configuration of the instrument. The instrument is equipped with 10 zero resistance ammeter (ZRA) and 10 electrometers to measure the current and potential of 50 electrodes individually. The MMA is populated with 5 current measurement group modules and 5 potential measurement group modules for a total of 100 channels. The MMA is able to polarize each group of electrodes to a separate potential if current measurement group modules are used. As a result, an additional potential can be applied to an electrode group and that specific group of electrodes will be away from the base potential. The system defines the anodic and cathodic current with red and blue colours, respectively. Each segment is coloured white, red, or blue depending on the sign and magnitude of the current. White represents zero current, red represents positive current, and blue corresponds to the negative current. The intensity of colours has been changed with current value as shown in Fig. 2.3. The MMA has been used in various applications, such as corrosion science, biosensors, chemical sensors, simulated and real crevice monitoring, and batteries and fuel cells.
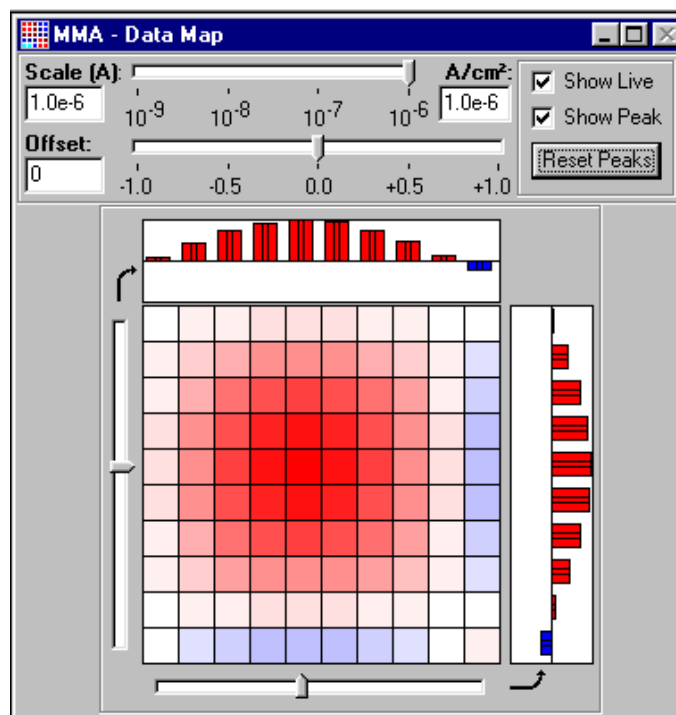
Figure 2.3: Data map of electrodes. White represents the neutral condition, red indicates the anodes, and blue defines the cathodes.

In this research, 5 groups of MMA were equipped with 100 μA ZRA and 5 groups were equipped with electrometers to measure the current and potential of 50 electrodes respectively.

2.4.2   Electrochemical Cell

Electrochemical experiments were performed using either a one-compartment cell or a three-compartment cell depending on the intended test condition.

2.4.2.1   One-compartment Cell

All electrochemical experiments related to multielectrode arrays were performed in a one-compartment electrochemical cell using 30 Cu specimens as working electrodes, a Ti plate as the counter electrode, and a saturated calomel reference electrode (SCE, 0.242 V vs. SHE). The counter electrode had a large surface area (200 cm^2) and was not a limiting factor in the current measurements. Electrochemical experiments were conducted using a Multichannel Microelectrode Analyzer 910 (MMA, Scribner Associates) connected to a

computer equipped with MMAlive software. The instrument was equipped with 100 μA zero resistance ammeters (ZRA). The electrochemical cell was placed inside a Faraday cage to reduce electrical noise from external sources. Fig. 2.4 shows a schematic illustration of the experimental arrangement.
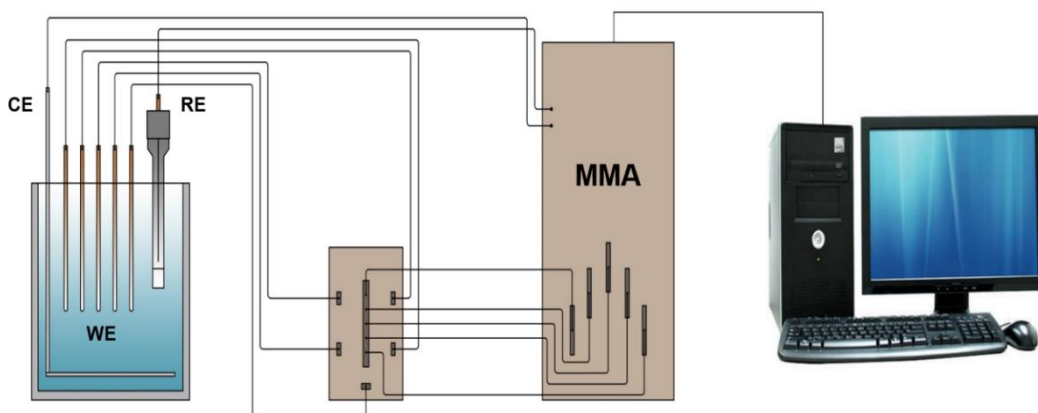
Figure 2.4: Schematic of multichannel microelectrode analyzer (MMA) connected to a multielectrode array.

2.4.2.2　Three-compartment Cell

A three-compartment cell was used to conduct the electrochemical experiments on single electrodes. The working electrode (WE) was placed in the central part of the cell while the reference electrode (RE) and counter electrode (CE) were placed in separate compartments. A dense glass frit was used to separate the solution in the central compartment where the WE was located from that in the RE and CE compartments. Also, a Luggin capillary was used to connect the RE compartment to the central compartment in order to minimize the potential drop (IR) between WE and RE compartments. All data measurements related to single electrodes were performed using a three-compartment cell, with a Pt plate as CE, SCE, and Cu with the exposed surface area of 0.785 cm^2 as WE. The electrochemical cell was placed inside a Faraday cage to reduce electrical noise from external sources. Electrochemical experiments were conducted using a ModuLab XM ECS Solartron potentiostat connected to a computer equipped with XM-studio software. A schematic illustration of the experimental arrangement is shown in Fig. 2.5.
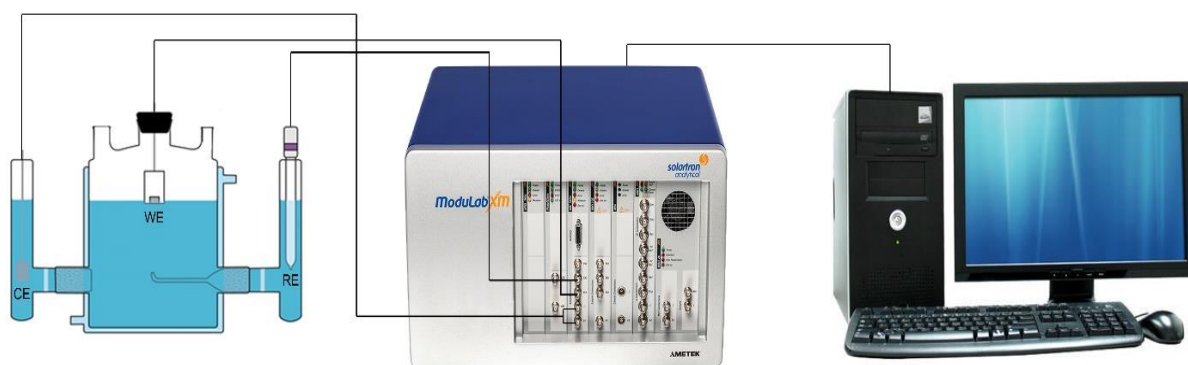
Figure 2.5: Schematic of single electrode cell setup.

2.5 Electrochemical Techniques

2.5.1 Corrosion Potential (E_{corr}) Measurements

The corrosion potential (E_{corr}), also known as the open circuit potential (OCP), is the potential of a freely corroding specimen with respect to the RE when no current flows through an external system [3, 4]. In this condition, the electron count for both anodic and cathodic reaction rates are equal and the Ecorr is controlled by the kinetics of both anodic and cathodic half-reactions [5]. As a result, the absolute current density values for both anodic and cathodic half-reactions are equal. It is important to mention that Ecorr is not able to provide quantitative rate information but it is able to provide qualitative kinetics information about the corrosion reaction. For instance, the increase or decrease of E_{corr} over time provides qualitative information about the change in the kinetics of anodic and cathodic reactions. For instance, E_{corr} of Cu decreases with time in chloride-containing solutions due to the dissolution of Cu in aggressive environments and will become stable once a protective film is formed on the surface, hindering further dissolution of Cu.

2.5.2 Potentiodynamic Polarization Measurements

In the potentiodynamic polarization (PDP) experiment, a potential (E) is scanned linearly and the current (I) response is recorded as a function of potential. PDP is a destructive test since a wide range of potentials, around 1 V, is scanned. The curve is known as the polarization curve and can provide information about the behaviour of a given system as

a function of scanned potential. A wide range of information including the regions of active, passive, and transpassive behaviour can be identified using a polarization curve. Moreover, breakdown (E_b) and repassivation (E_{rp}) potentials can be obtained from the cyclic voltammetry technique. In this research, positive-going and negative-going scans were conducted separately to measure the E_b and E_{rp} respectively since the surface condition of all electrodes should be the same in each measurement.

2.5.2.1   Breakdown Potential (E_b) Measurements

The breakdown potential (E_b) or pitting potential (E_{pit}) is the potential at which the current increases abruptly over a small range of potential change. The E_b is determined from the intersection of the tangent to the current in the passive range and that of the rising current in the potential range after breakdown [6, 7]. Pitting is taken to be possible if $E_{corr} \geq E_b$ [8-10]. However, both E_{corr} and E_b are distributed parameters, due to the stochastic nature of passive film breakdown, making the boundary between non-susceptibility and susceptibility uncertain. In this research, values of E_b were measured using potentiodynamic scans in unary and binary solutions containing different concentrations of Cl^-, SO_4^{2-}, and HCO_3^-. A schematic of E_b measurement is shown in Fig. 2.6.

Positive-going Scan
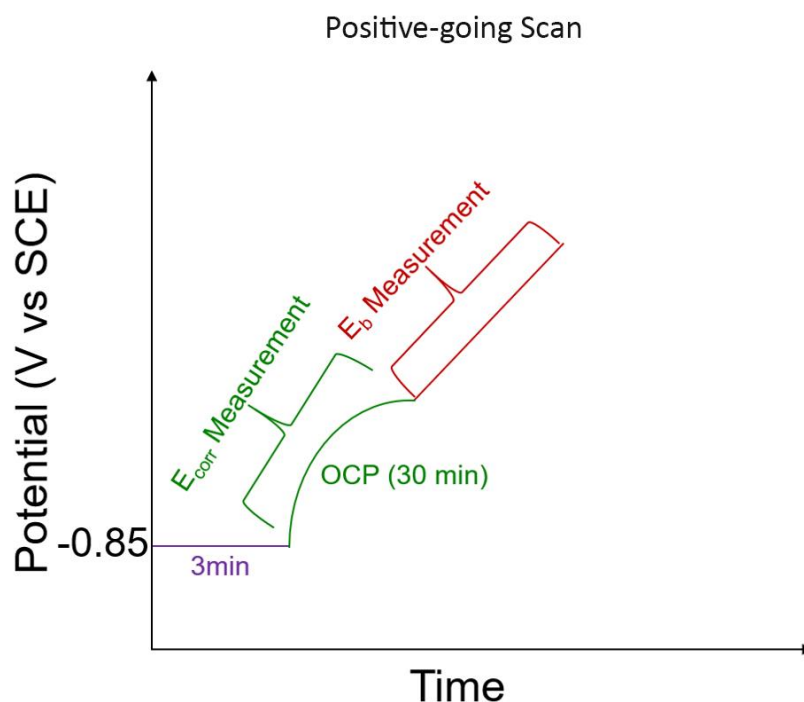
Figure 2.6: Schematic of potentiodynamic experiment for the measurement of E_{corr} and E_b.

2.5.2.2   Repassivation Potential (E_{rp}) Measurements

The repassivation potential (E_{rp}) is the potential at which the current on the negative-going scan achieves the value of the original passive current observed on the positive-going scan. A more conservative evaluation of susceptibility of materials to pitting involves the evaluation of the difference between E_{corr} and E_{rp} recorded by scanning E from above E_b, on an electrode undergoing pitting corrosion, to a value below Eb at which the measured current achieves the low value in the passive region. E_{rp} is commonly referred to as the critical pitting potential [8, 9].

In this research, we measured the E_{rp} of specimens under the same conditions; however, to ensure that any observed variation in E_{rp} values was not a result of differences introduced during E_b measurement, we attempted to prepare all specimens identically, in terms of both the surface preparation and the state of pit development before the repassivation scan. To do this, Cu samples were ground based on the sample preparation

section to ensure that the surface condition of all electrodes was the same before the pitting process. After cathodic cleaning and a 30-minute period of oxide growth at E_{corr}, all electrodes were simultaneously polarized in one step to a potential equivalent to the highest E_b value measured previously, such that pitting should initiate on all electrodes simultaneously. A potentiodynamic scan in the negative direction was then conducted at a scan rate of 10 mV/min until the current of all electrodes reached the passive current density to determine the E_{rp} of each Cu electrode (Fig. 7).
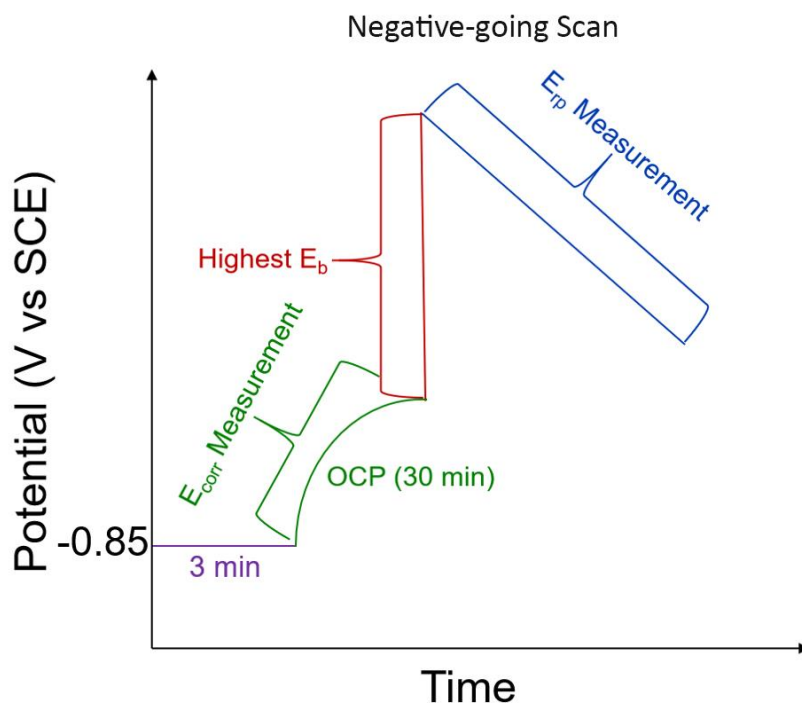
Figure 2.7: Schematic of potentiodynamic experiment for the measurement of E_{rp}.

The mean value of the passive currents (mean current in Fig. 2.8) recorded on all the Cu electrodes on the positive-going scan was calculated and used to determine the E_{rp} of electrodes in the negative-going scan. The intersection of the negative-going scan of each electrode and mean current is considered to be the E_{rp}, as shown in Fig. 2.8.
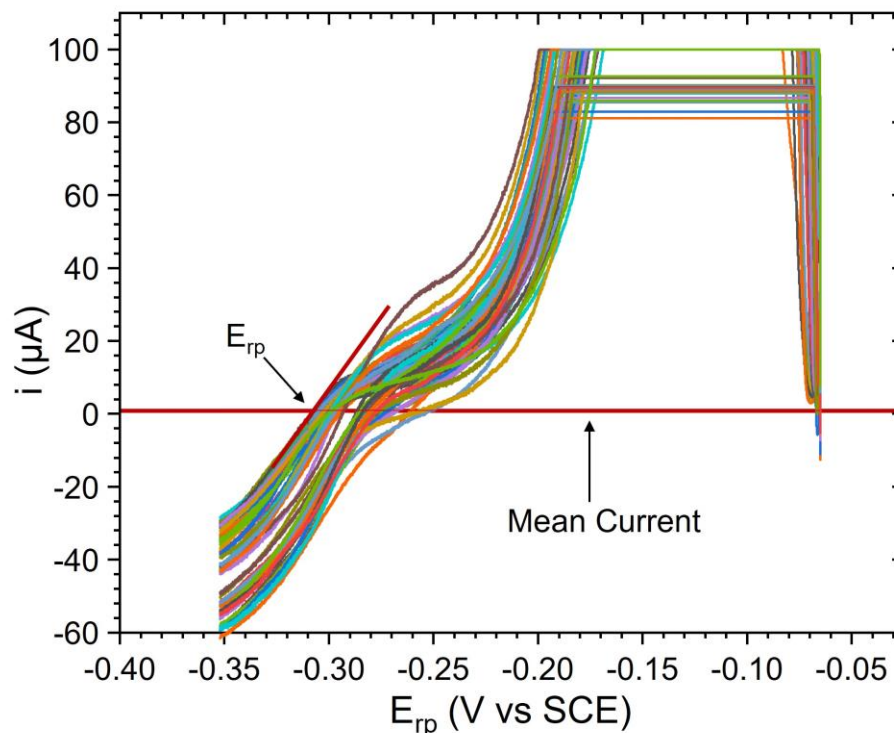
Figure 2.8: Determination of repassivation potential regarding the mean current of the positive-going scan experiment.

2.5.3 Potentiostatic Polarization (PSP) Measurements

In potentiostatic polarization (PSP) experiments, a constant potential is applied to the WE and the current response is recorded as a function of time. This technique can be used to investigate the anodic and cathodic reactions of materials over a certain period of time, depending on the value of selected applied potential. Anodic or cathodic behaviour can be investigated when the applied potential is higher or lower than Ecorr, respectively. Moreover, the passive film formation and breakdown of active/passive materials can be investigated using the PSP technique. Commonly, a WE is held at a potential within the passive region and the current density decreases with time, resulting from the nucleation and growth of a passive film while an abrupt increase in current followed by a gradual decrease shows the occurrence of a localized breakdown on the passive film.
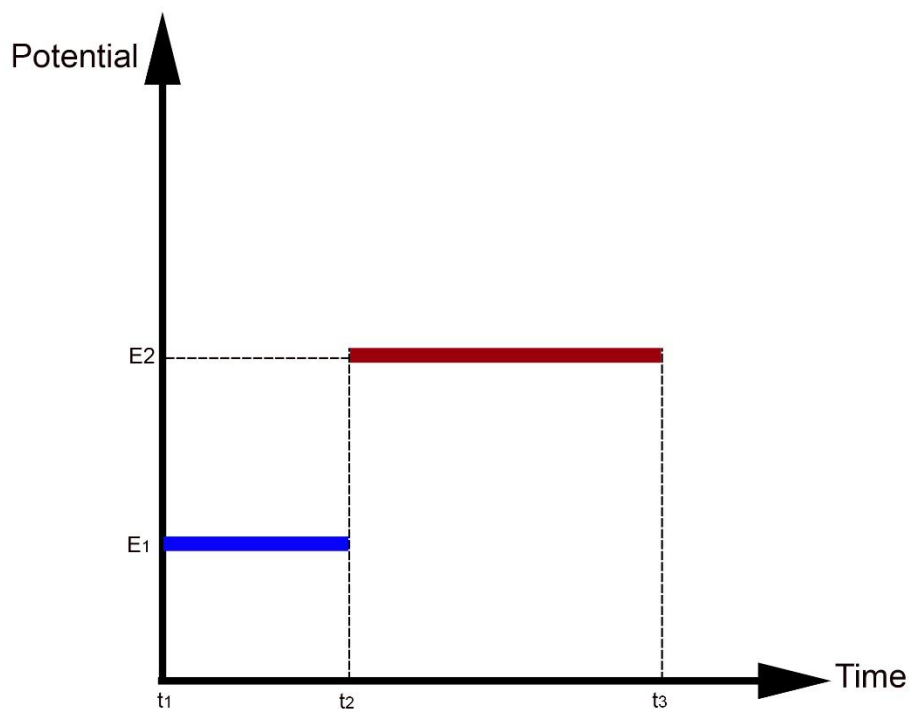
Figure 2.9: The schematic of the potential-time profile used in Potentiaststic experiment. The sample was cathodically cleaned at E_1 for a period of t_2-t_1 and then potential of E_2 was applied to the electrode for a period of t_3-t_2.

In this study, potentiostatic experiments were conducted using a ModuLab XM ECS Solartron potentiostat and XM-studio software. Applied potentials ranging from E_{corr} + 20 mV to E_{corr} + 105 mV or E_b^{min} - 20 mV and E_{corr}^{max} + 20 mV were selected based on plotted histograms from potentiodynamic experiments using multielectrode arrays and the MMA. Also, another set of potentials was selected to investigate the dependence of passive film morphology and composition on potential and charge density using the potentiostatic technique. It is important to note that all samples were immersed in the solution immediately after the surface preparation process, followed by a potentiostatic experiment for 6 hours, and the current was monitored as a function of time.

2.6   Surface Analytical Techniques

2.6.1   Scanning Electron Microscopy and Energy-dispersive X-ray Spectroscopy

Scanning electron microscopy (SEM) has become one of the most available techniques in research labs and industries due to its relatively low cost of maintenance and wide range of features. In this method, a high-energy electron beam is used to probe the surface of a material and produces a high-resolution image with a magnification range from 10 to 1,000,000 [11, 12]. A metal filament like tungsten generates a primary electron beam and then accelerates it toward the sample surface with an applied voltage of 0.1 to 50 keV. A series of electromagnetic condenser lenses and an objective lens are used to converge and position the electron beam. First, the electron beam is passed through a series of condenser lenses to optimize the initial spot size of the electron beam (around 10-3 times its original size). Then an objective lens is used to determine the spatial resolution. The fine electron beam rasters across a certain area of the specimen surface in X and Y directions [12, 13].
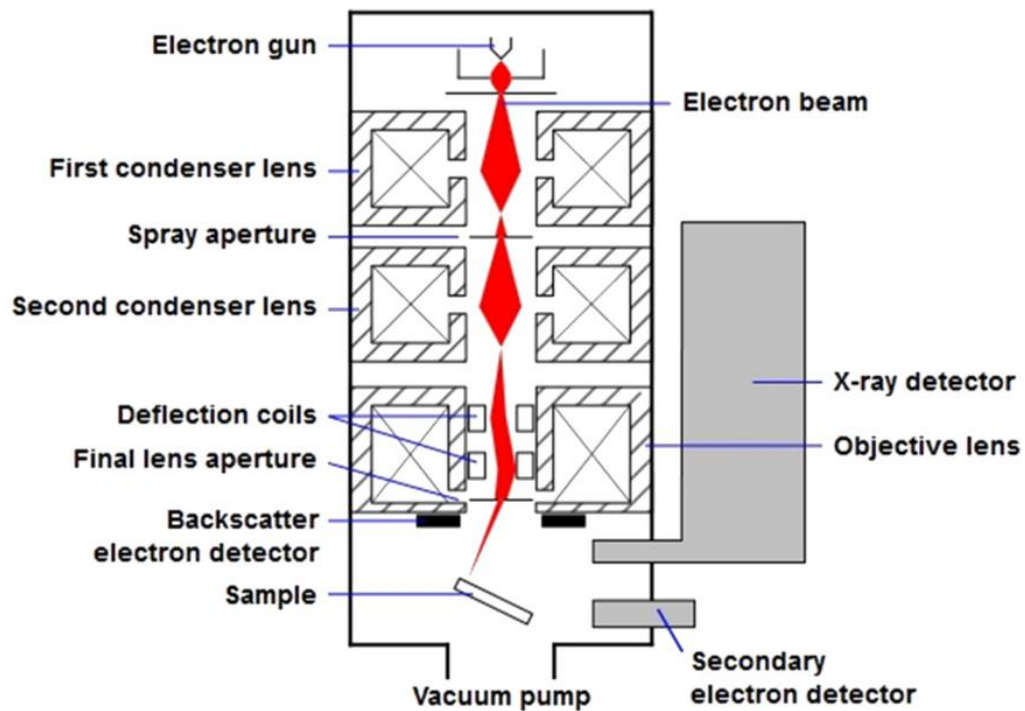
Figure 2.10: Schematics of a secondary electron microscope [14].

Different emission signals, such as secondary electrons (SE), backscattered electrons (BSE), and characteristic X-rays can be generated due to the interaction of the primary electron beam and specimen [11, 13]. As a result, multiple detectors are used to collect these signals since each signal provides useful information like topography, composition, etc.
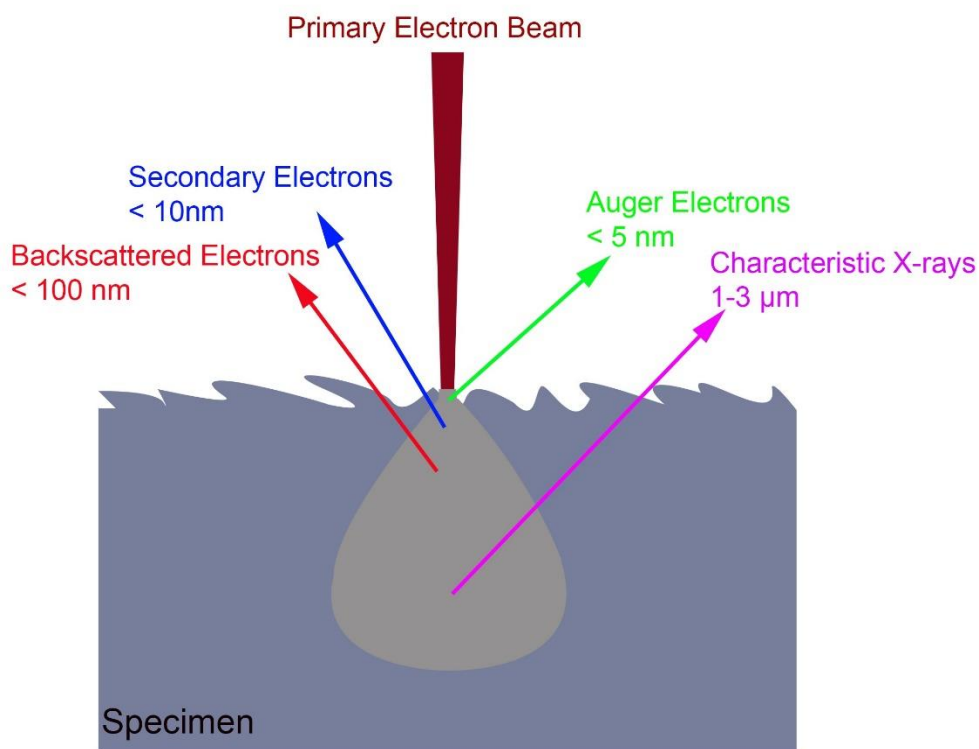
Figure 2.11: Schematics of different emission products resulting from the interaction of primary electrons and specimen.

2.6.1.1   Secondary Electron (SE)

Inelastic collisions of primary electrons with the specimen generate secondary electrons (SE),

which carry information that can be used to produce an image. Secondary electrons can escape from the first outer part of the interaction between primary electrons and material due to their low energy (less than 50 eV). During this interaction, a part of the energy of the primary electrons is transferred to electrons in the specimen atoms. These electrons

can exit the specimen as secondary electrons if their transferred energy is greater than the work function of the material. Secondary electron images can be used to create high spatial resolution images and analyze the surface topography. Secondary electrons give us this opportunity to have a brighter image as they are emitted from a shallow level within the specimen. The brightness of the image depends on the emission depth of the electron. It is important to note that darker areas in the image result from reaching the deeper areas of the specimen [15].

2.6.1.2   Backscattered Electron (BSE)

Elastic collisions of primary electrons with specimen atoms result in backscattered electrons with kinetic energy close to the primary electrons since the exchange energy during this interaction is low. so BSEs escape from the deeper portion of the interaction volume [13]. The probability of producing an elastic collision is higher for larger atoms (higher atomic number) due to their greater cross-sectional area; so, the number of BSE reaching a BSE detector is proportional to the mean atomic number (Z) of the sample. As a consequence, greater mean Z and lower mean Z in the sample result in bright and dark areas in SEM images, respectively. This feature can be used to create an image including composition and crystallographic information of the specimen surface [13, 15].

2.6.1.3   Energy-dispersive X-ray spectroscopy (EDS)

The interaction of primary electron and specimen may result in the ejection of a SE. As a result, an outer-shell electron falls into the core vacancy to fill the vacancy and minimize energy, resulting in the emission of an X-ray [12]. Useful information about the elemental composition of specimens can be obtained from the measurement of X-rays using an energy-dispersive X-ray spectrometer [12, 15]. It is important to mention that X-rays are generated at a depth of around 1-3 μm, since the penetration depth of X-rays is greater than that of electrons, as shown in Fig. 2.11.

In this project, SEM and EDS techniques were used to investigate the surface morphology and composition of the film using a Hitachi SU8230 (Regulus Ultra High-Resolution Field Emission SEM) equipped with a FlatQuad EDS (Bruker X-Flash FQ5060 Annular Quad) at Surface Science Western (SSW). A LEO 1540XB SEM

equipped with a focused ion beam (FIB) (Zeiss Nano Technology System Division, Germany) at Western Nanofabrication Facility was used to examine the cross-sectional morphology and thickness of oxide films.

2.6.2   X-Ray Photoelectron Spectroscopy

X-ray photoelectron spectroscopy (XPS) is a unique technique that can be used to investigate the elemental composition and oxidation state of the top few layers (5-30 Å) of materials [16, 17]. The technique is based on the measurement of kinetic energies of photoelectrons ejected from the specimen when a soft X-ray within the range of 1-2 keV irradiated the surface as shown in Fig. 2.12.
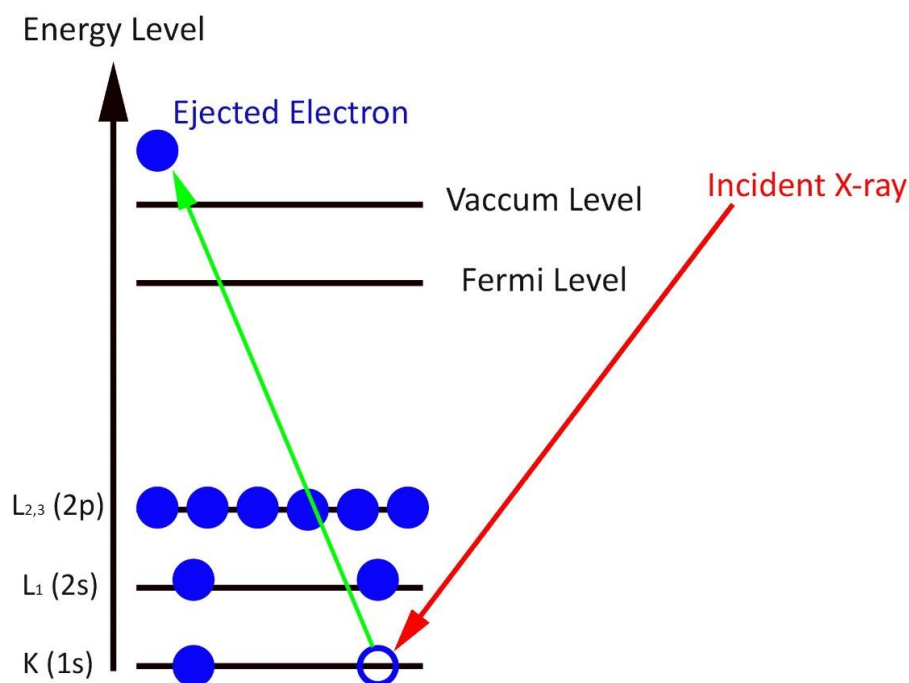
Figure 2.12: A schematic of interaction between the incident X-ray and core level (1s) electron. The KE of the ejected photoelectron is measured by a spectrometer.

XPS is a surface-sensitive technique since the ejected photoelectrons have relatively low kinetic energy (KE) and can only escape from shallow depths, 5-10 nm [18]. An xX-ray photoelectron with the energy of hν hits the specimen surface. If the photon energy (hν) is greater than the binding energy (BE), then ionization will occur. The ejected electron

has a specific KE that can be measured using a spectrometer. As a result, the binding energy can be calculated using equation 1.

$$BE = h\nu - KE - \varphi \tag{1}$$

Where φ is the work function of the spectrometer [16, 19, 20]. Usually, the XPS spectrum is presented as a graph of photoelectron intensity (counts per second) versus BE. Since each peak of a spectrum corresponds to a specific element, the intensity of signals depends on the atomic concentrations of elements.

A Kratos AXIS Supra equipped with a monochromatic Al-Kα X-ray source (1486.6 eV) was used for X-ray photoelectron spectroscopic analyses. The instrument work function was calibrated to give BE of 83.96 eV for the Au 4f7/2 line for metallic Au and the spectrometer dispersion was adjusted to give a BE of 932.62 eV for the Cu 2p3/2 line of metallic Cu. Survey spectra were recorded over a BE range of 0 to 1200 eV using a pass energy of 160 eV at a step size of 1 eV. High-resolution spectra were collected for the Cu 2p3/2, O 1s, and C 1s lines and the Auger CuL3M4,5M4.5 peak using a pass energy of 20 eV and a step size of 0.1 eV. In all cases, the Cu 2p3/2 and Auger LMM lines were collected first to mitigate the effects of X-ray degradation of the Cu(II) state. All spectra were corrected for charging using the adventitious carbon peak (C 1s, 284.8 eV). Data processing was carried out using CasaXPS (v. 2.3.14) with a Shirley background subtraction. The deconvolution procedures were taken from previously determined fitting parameters [21].

2.7 References

[1] Design, production and initial state of the canister, Swedish Nuclear Fuel and Waste Management Co, Svensk Kärnbränslehantering AB, (2010).

[2] H.W. Bowyer, The effects of impurities on the properties of OFP copper specified for the copper iron canister, 1999.

[3] E. McCafferty, Introduction to corrosion science, Springer Science & Business Media, (2010).

[4] R.G. Kelly, J.R. Scully, D. Shoesmith, R.G. Buchheit, Electrochemical techniques in corrosion science and engineering, (2002).

[5] Z. Ahmad, Principles of corrosion engineering and corrosion control, Elsevier Science & Technology Books, (2006).

[6] F. Mao, C. Dong, S. Sharifi-Asl, P. Lu, D.D. Macdonald, Passivity breakdown on copper: Influence of chloride ion, Electrochimica Acta, 144 (2014) 391-399.

[7] G. Mankowski, J.P. Duthil, A. Giusti, The pit morphology on copper in chloride- and sulphate-containing solutions, Corrosion Science, 39 (1997) 27-42.

[8] H. Cong, J.R. Scully, Effect of chlorine concentration on natural pitting of copper as a function of water chemistry, Journal of The Electrochemical Society, 157 (2010) 200-211.

[9] H. Cong, J.R. Scully, Use of coupled multielectrode arrays to elucidate the pH dependence of copper pitting in potable water, Journal of The Electrochemical Society, 157 (2010) 36 - 46.

[10] M.R.G.D. Chialvo, R.C. Salvarezza, D.V. Moll, A.J. Arvia, Kinetics of passivation and pitting corrosion of polycrystalline copper in borate buffer solutions containing sodium chloride., Electrochimica Acta, 30 (1985) 1501–1511.

[11] W. Zhou, Z.L. Wang, Scanning microscopy for nanotechnology, Springer Science+Business Media, LLC, (2006).

[12] K.D. Vernon-Parry, Scanning electron microscopy: An introduction, III-Vs Review, 13 (2000) 40-44.

[13] R.F. Egerton, physical principles of electron microscopy, Springer Science+Business Media Inc., (2005).

[14] L.V. Goncharova, Basic surfaces and their analysis, Morgan & Claypool Publishers, (2018).

[15] L. Reimer, Scanning electron microscopy: Physics of image formation and microanalysis, Springer-Verlag Berlin Heidelberg, (1998).

[16] P.V.d. Heide, X-ray photoelectron spectroscopy: An introduction to principles and practices, John Wiley & Sons, Inc., (2012).

[17] J.F. Moulder, W.F. Stickle, P.E. Sobol, K.D. Bomben, Handbook of X-ray photoelectron spectroscopy, Perkin-Elmer Corporation, (1992).

[18] J.F. Watts, J. Wolstenholme, An introduction to surface analysis by XPS and AES, John Wiley & Sons Ltd, (2003).

[19] D. Briggs, J.T. Grant, Surface analysis by auger and x-ray photoelectron spectroscopy, Surface and Interface Analysis, 36 (2004) 1647-1647.

[20] N.H. Turner, J.A. Schreifels, Surface analysis: X-ray photoelectron spectroscopy and auger electron spectroscopy, Analytical Chemistry, 72 (2000).

[21] M.C. Biesinger, Advanced analysis of copper X-ray photoelectron spectra, Surface and Interface Analysis, 49 (2017) 1325-1334.

Chapter 3

3 Use of multielectrode arrays and statistical analysis to investigate the pitting probability of copper. Part I: The effect of chloride

Abstract

Under some conditions, copper and copper alloys are either immune from corrosion or undergo slow uniform corrosion, generally considered a favourable situation, since predicting the damage incurred by the metal during a period of uniform corrosion is relatively straightforward. However, under conditions leading to surface passivation of Cu, localized corrosion might occur in the presence of aggressive oxidants. Therefore, the susceptibility of Cu to localized corrosion must be considered carefully to avoid unpredictable failures in Cu-based structures. Understanding the pitting probability of Cu is important for various applications, including the use of Cu-coated containers for the permanent disposal of used nuclear fuel. In this study, the pitting probability of Cu in chloride-containing solutions crudely representing the groundwater that might be found in a deep geologic repository (DGR) was investigated using electrochemical techniques and statistical analysis. The probabilities of both pitting and repassivation of Cu were found to increase with increasing [Cl$^-$]. The surface morphologies of copper electrodes in the same solution were also evaluated using scanning electron microscopy (SEM). The passive film on the surface of the copper electrode with the highest breakdown potential (E_b) was found to be more protective than that on the electrode with the lowest E_b.

3.1 Introduction

Corrosion scientists have primarily focused on the deterministic behaviour of corrosion parameters. Macdonald and coworkers investigated the deterministic behaviour of corrosion processes on a wide variety of materials, including copper, nickel, aluminum, carbon steel, manganese steel, and Fe-17Cr [1-5]. They modified damage function analysis (DFA) by making a connection between DFA and statistical methods such as extreme value statistics, unifying the deterministic and statistical approaches for

predicting localized corrosion [5]. Although the detailed corrosion mechanisms surely differ between the various materials and classes of materials, yet the concepts of determinism and statistical distributions of parameters can be considered universally.

MacDonald and coworkers proposed that the pitting potential is distributed normally when the diffusivity of the cation vacancy in the oxide follows a log-normal distribution [3, 4]. Moreover, a Monte-Carlo model was used to develop a deterministic model for evaluating the delayed repassivation rate constant of stable pits, with a focus on carbon steel [1]. However, due to the stochastic nature of localized corrosion, a statistical approach can be extremely powerful in providing additional insight into the possibility of localized corrosion processes occurring, and their distribution. Statistics is one of the most important tools in materials science and engineering since we work with extreme values in order to investigate the time to failure of materials, looking for the rare events that yield early and perhaps unexpected failures.

Some researchers have used extreme-value statistics to evaluate the maximum pit depth [6, 7] on aluminum and wrought iron. Shibata [8] proposed that the scattering of pitting corrosion data on carbon steels and stainless steels was because of the intrinsic nature of the pitting process rather than due to uncontrolled parameters. However, the validity of this proposal remains in question, since we have control of only a few parameters such as solution condition, and not of all parameters such as the precise surface condition of all parts of each electrode (e.g., the grain orientations). Therefore, the dispersion of pitting corrosion data may result from differences in these uncontrolled experimental parameters.

Pitting corrosion of copper has been proposed to be a deterministic process and to only occur when the potential of the Cu was raised above 375 mV vs. SHE in Brussels water [9]. However, this hypothesis was rejected by Shalaby [10] who claimed that the pitting potential of Cu is not a deterministic value but rather a distributed value that depends on different factors such as scan rate, solution composition, pH, and the chemical composition of Cu.

Whether certain corrosion parameters are deterministic or distributed has been an ongoing debate between corrosion researchers for many years. For instance, the critical pitting temperature (CPT) for various types of stainless steel was determined and assumed to be a singular deterministic value [11-13]; however, Frankel and coworkers [14] determined that the CPT is a distributed value, not a deterministic value. Their research clarified that the distribution range of the CPT in 316L stainless steel is inversely proportional to the concentration of aggressive anions. Additionally, many metastable pitting events were observed at temperatures above the CPT, confirming that the CPT is neither deterministic nor an intrinsic material property. However, no researchers have yet observed a CPT in Cu materials.

Williams [15-17] introduced a stochastic pitting model that can be used to evaluate the effect of passive film breakdown on the pitting probability of stainless steel, which might also be useful for other materials such as Cu. He observed that the frequency of micropits decreased with increasing passive film thickness, specifically when the concentrations of aggressive anions were low, resulting in higher pitting potentials and a larger dispersion of values.

Provided that passive conditions can be achieved, the susceptibility to pitting is commonly evaluated by a comparison of the corrosion potential (E_{corr}), measured under open circuit conditions, to the passive film breakdown potential (E_b) measured in a potentiodynamic scan of the applied potential (E) from low to high values. Spontaneous pitting of Cu is taken to be possible if $E_{corr} \geq E_b$ [18, 19]. However, both E_{corr} and E_b are distributed parameters, due to the stochastic nature of passive film breakdown, making the boundary between non-susceptibility and susceptibility uncertain. A more conservative evaluation of susceptibility involves the evaluation of the difference between E_{corr} and the repassivation potential (E_{rp}), with the latter recorded by scanning E from above E_b, on an electrode undergoing pitting corrosion, to a value below E_b at which the measured current achieves the low value measured in the passive region. E_{rp} is commonly referred to as the critical pitting potential [19].

A number of studies have been conducted to determine the influence of various parameters relevant to DGR conditions on E_{corr}, E_b and E_{rp} of Cu [19-23]. Based on these studies, three different regions of behaviour have been claimed for Cu, based on pH [19]: uniform corrosion at pH < 7; a pitting susceptibility region between pH 7 and pH 10; and limited susceptibility at pH > 10. However, these boundaries were found to be dependent on anion type and concentration, temperature, and [O_2] (when experiments were conducted under open circuit conditions). In general terms, an increase in temperature was observed to promote active behaviour of Cu, although it has been claimed that passivity is enhanced by an increase in temperature (E_b increased) possibly due to an improvement in film properties [24]. Values of E_{rp} were found to be very dependent on the relative concentrations of various anions (Cl^-, SO_4^{2-}, HCO_3^-/CO_3^{2-}, OH^-), with Cl^- generally destabilizing passive oxide films, eventually leading to active behaviour, while HCO_3^-/CO_3^{2-} enhanced passivity, and the influence of SO_4^{2-} was ambiguous but with a tendency to promote pitting. Since Cl^- levels in a Canadian DGR are anticipated to be between 1 and 5 M [25, 26], an understanding of the corrosion process in Cl^--containing solutions and the impact of Cl^- on the properties of the oxide film on Cu are essential.

The boundary between active and passive behaviour as a function of pH and [Cl^-] was defined approximately by Qin et al. [23]. This boundary was developed based on only a small number of experiments and does not account for the statistical distributions of the parameters measured to establish it. In the current study, a Cu multielectrode array was used to produce the distributions of values in the passive region by measuring E_{corr}, E_b and E_{rp} on 30 electrodes simultaneously.

3.2 Experimental Methodology

Copper specimens were fabricated from O-free, P-doped wrought Cu supplied by the Swedish Nuclear Fuel and Waste Management Company (SKB, Solna, Sweden). Electrodes were machined in the form of bullet specimens (18 mm height $\times$ 5 mm diameter) with one rounded end (Fig. 3.1) to avoid edge effects during electrochemical experiments, with a threaded connection to a stainless steel rod to enable connection to external electrochemical equipment. Specimens used in corrosion experiments were ground with a sequence of SiC papers with grit sizes of 600, 800, 1200, 2500, and 4000.

The grinding was followed by rinsing in Type I water with a resistivity of 18.2 MΩ·cm (produced by a Thermo Scientific Barnstead Nanopure 7143 ultra-pure water system), sonication in ethanol to remove any grinding residues and organic contaminants, and finally drying in a stream of Ar gas.

Figure 3.1: O-free, P-doped copper electrodes.

3.2.1   Solution Preparation

Solutions were prepared with reagent-grade sodium chloride (NaCl, 99.0%), purchased from Fisher Scientific, and Type I water. The multielectrode array was exposed to solutions containing various concentrations of chloride in the range from 0.01 M to 1 M. The pH of the solutions was adjusted to 11 by adding small volumes of NaOH solution. It should be noted that the pH of the solutions was deliberately adjusted to a much higher value than expected in a Canadian DGR such that passivity and subsequently pitting became possible, thereby enabling an investigation of the phenomenon. As such, this work investigates an approach and methodology, but does not address the likelihood of pitting corrosion on Cu-coated containers for used nuclear fuel under anticipated DGR conditions, which is expected to be much lower than in the studies reported here.

3.2.2 Electrochemical Cell, Instrumentation, and Procedure

All potentiodynamic experiments were performed in an electrochemical cell consisting of a glass vessel containing a saturated calomel reference electrode (SCE, 0.242 V vs. SHE (standard hydrogen electrode)), a Pt plate as the counter electrode, and 30 Cu specimens, each with an exposure area of 1 cm^2, as working electrodes, with a spacing of 3 cm between each electrode. The counter electrode had a large surface area and was not a limiting factor in the current measurements.

The electrochemical cell was placed inside a Faraday cage to reduce electrical noise from external sources. E_{corr} measurements were collected and potentiodynamic polarization experiments were conducted at a scan rate of 10 mV/min using a Multichannel Microelectrode Analyzer 910 (MMA, Scribner Associates) connected to a computer equipped with MMAlive software. The instrument was equipped with 100 µA zero-resistance ammeters (ZRA) to measure the current flow to or from each electrode individually and electrometers to measure the potential of each electrode. Fig. 3.2 shows a schematic illustration of the experimental arrangement and photographs of the setup and array configuration. The E_b and E_{rp} values were measured in separate experiments to ensure that E_{rp} measurements were made on electrodes that were treated as identically as possible to eliminate some controllable sources of variations in this parameter. Typically, repassivation is measured on the return sweep of a scan used to determine the breakdown potential, but we have adopted a procedure (described below) to ensure that all 30 Cu specimens had experienced passive film breakdown for the same amount of time before repassivation. Experiments under each set of conditions were conducted two times each, such that data were collected from 60 electrodes in total under each set of test conditions.
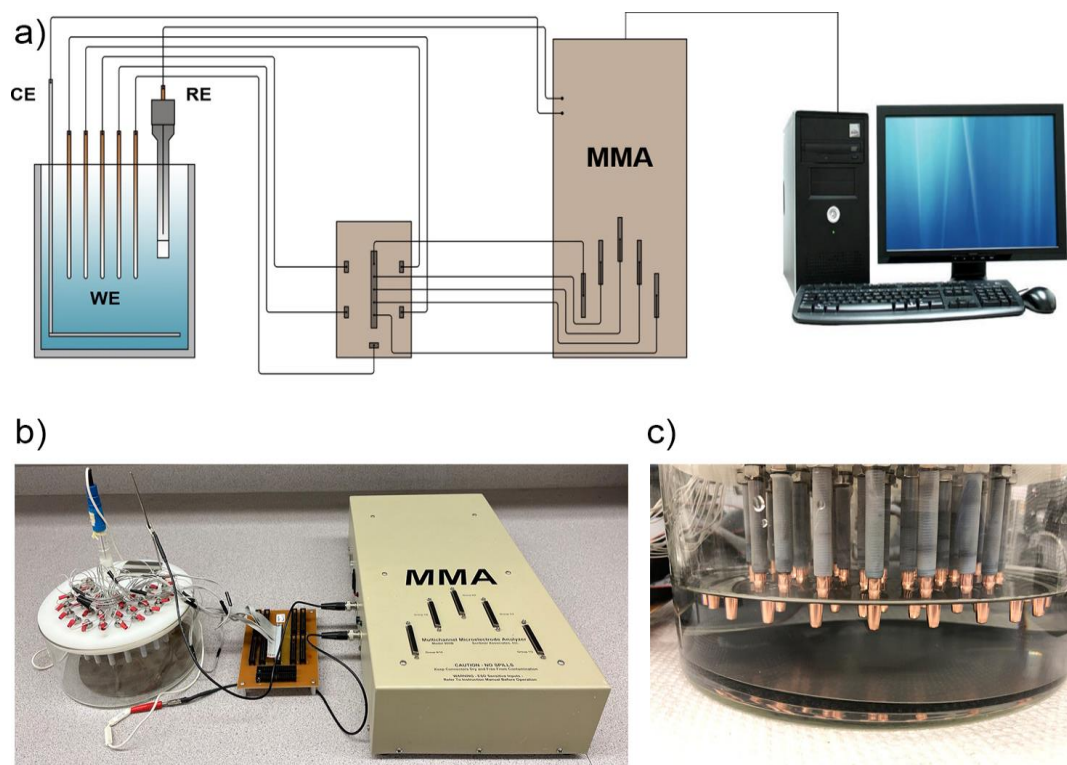
Figure 3.2: a) Schematic of multichannel microelectrode analyzer (MMA) connected to a multielectrode array b) connection between multielectrode array and MMA through the interface and c) inside view of the cell including working, and counter electrodes (Reference electrode not visible).

3.2.2.1   Breakdown Potential (E_b) Measurements

Values of E_b were measured using potentiodynamic scans in solutions containing different concentrations of [Cl$^-$]. Prior to each scan, Cu electrodes were cathodically treated at -0.85 V vs SCE for 3 minutes, a procedure known to help improve the reproducibility of many electrochemical experiments. The potential of -0.85 V vs SCE was selected because it was low enough to generate a small cathodic current (which may contribute to some oxide reduction and the desorption of organic contaminants from the electrode surface), but still above the potential (~ -0.95 V vs SCE) at which we have observed hydrogen absorption into Cu metal, which we do not want to occur. Then, E_{corr} was monitored for 30 minutes to allow a steady state to be established and to determine the range of E_{corr} values using the multielectrode array. The potential was then scanned in

the positive direction from E_{corr} at a scan rate of 10 mV/min until the current on all electrodes reached 100 µA. A schematic of this procedure is shown in Fig. 3.3a, and the measured scans are plotted in Figure 3.4a. We know from previous work (23) that, under all the conditions used in this work, this procedure results in the initiation of pitting corrosion on our Cu material. The E_b for each electrode was then determined from the intersection of the tangent to the current in the passive region with that of the rising current in the potential range after breakdown [27, 28], as demonstrated in Figure 3.4b.

Our determinations of E_b were made using a linear extrapolation from the rising current (Figure 3.4b), consistent with the Galvele IR drop theory (50), but we also investigated the consequences of extrapolating from plots of log(i) and $\sqrt{i}$ vs E (in case of activation control or increasing active surface area withing hemispherical pits, respectively); however, we found that the extrapolation method had minimal influence on the E_b values determined, shifting them by only 2-10 mV.

3.2.2.2   Repassivation Potential (E_{rp}) Measurements

The E_{rp} of Cu specimens undergoing pitting corrosion was measured under the same exposure conditions; however, to ensure that any observed variation in E_{rp} values was not a result of differences introduced during the E_b measurement (as might be the case in traditional pitting scans that sweep the potential up to find E_b then back down again to find E_{rp}, thereby repassivating surfaces with differing degrees of pit initiation and growth), an identical preparation of all specimens was attempted, in terms of both surface preparation and the state of pit development prior to repassivation scans. To do this, Cu samples were ground as described in the sample preparation section to ensure that the surface condition of each electrode was the same before the pitting process. After the cathodic treatment and a 30-minute period of oxide growth at E_{corr}, all electrodes were simultaneously polarized in one step to a potential equivalent to the highest E_b value measured previously, such that pitting should initiate on all electrodes simultaneously. To determine the E_{rp} of each Cu electrode (Fig. 3.3.b), a potentiodynamic scan in the negative direction was then conducted at a scan rate of 10 mV/min until the current of every electrode reached the mean passive current density previously measured during the scans to determine E_b (mean current in Fig. 3.5).

The E_{rp} on each electrode was taken as the potential at which the current on the negative-going scan reached the mean value of the original passive current observed in the positive-going scans.
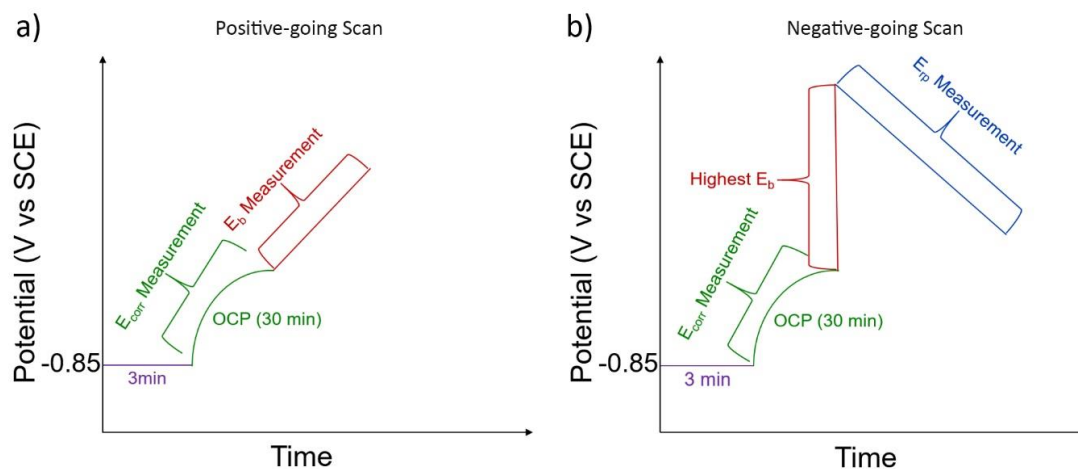
Figure 3.3: Schematic of electrochemical experiments with a) positive-going scan for measurement of E_{corr} and E_b, and b) negative-going scan for measurement of E_{rp}.
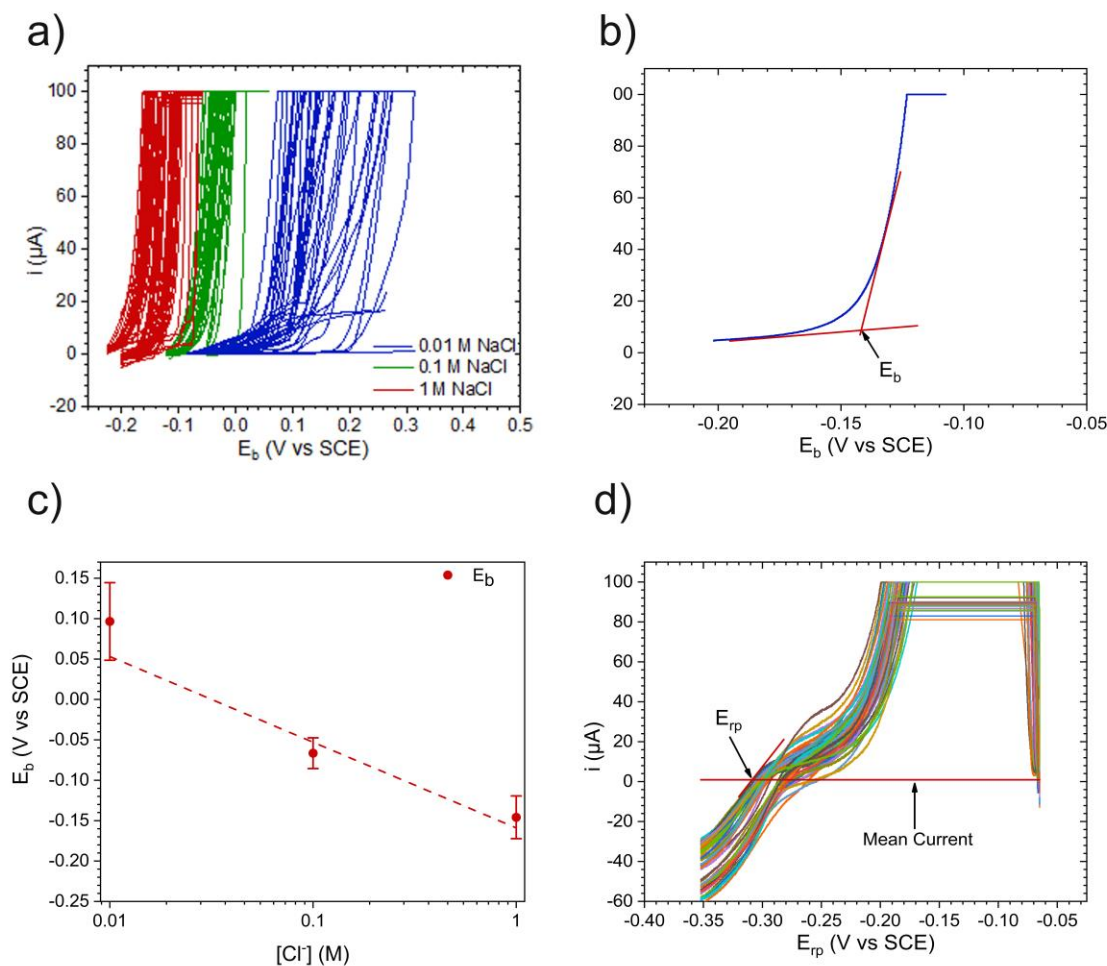
Figure 3.4: Determination of the breakdown potential of Cu from positive-going potential scans: a) the many coloured curves represent the current traces recorded simultaneously on each of the 30 electrodes in the array exposed to room temperature NaCl solution at pH 11; b) one of the scans with tangents drawn to demonstrate how the breakdown potential, E_b, was determined; c) the ranges of E_b values measured at each chloride concentration, showing the changes in both the average potential and range of the potential distribution at each chloride concentration with the slope of −113 mV/deacade; and d) a series of negative-going "repassivation" scans that all started at E = −0.06 V vs SCE with a steep initial current rise as the electrodes immediately began to suffer pitting corrosion, followed by a flat region where the pitting current reached the maximum available from the potentiostat, followed by a declining current that allowed us to determine the

repassivation potential E_{rp} at the point where the current declined to the mean value of the passive current density (red line) measured on positive-going scans under the same exposure conditions.
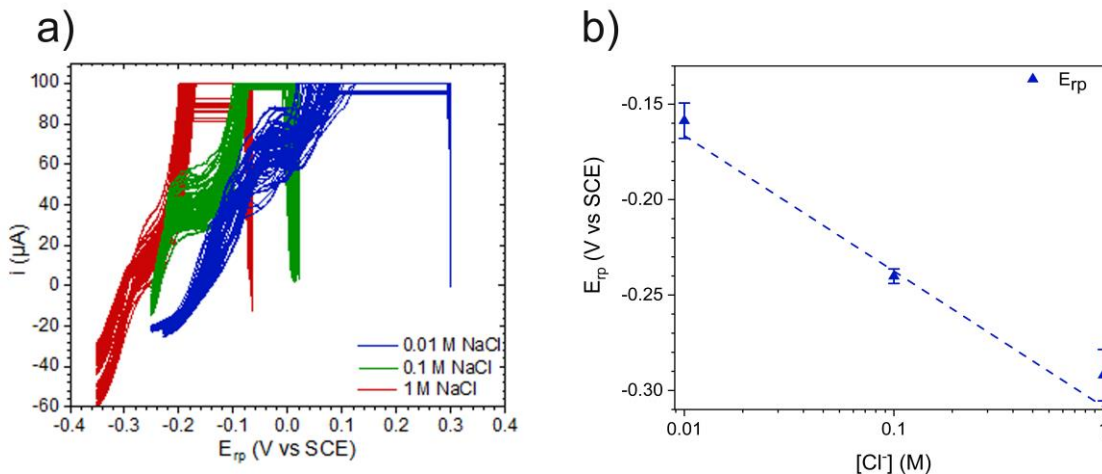
Figure 3.5: Repassivation potential of Cu electrodes in NaCl solution of pH 11 at room temperature: a) polarization scans of Cu in solutions containing 0.01, 0.1, and 1 M Cl$^-$; b) comparison of the mean and standard deviation of E_{rp} on Cu electrodes in solutions containing 0.01, 0.1, and 1 M Cl$^-$ with the slope of −103 mV/deacade.

3.2.3 Surface Analysis

After the breakdown experiment, samples were rinsed with Type I water, dried in a stream of Ar gas, and stored in an anaerobic chamber until they could undergo microscopic analysis. Scanning electron microscopy (SEM) was conducted to investigate the surface morphology and distribution of pits using a LEO 1540XB microscope (Zeiss Nano Technology System Division, Germany) located at Western Nanofabrication Facility.

3.2.4 Statistical Treatment

The multitude of E_{corr}, E_b, and E_{rp} measurements enabled by the multi-electrode array approach made it possible to perform statistical analyses of these parameters to estimate the likelihood that favourable conditions for pitting corrosion of Cu (either $E_{corr} > E_b$ or the more conservative $E_{corr} > E_{rp}$) could be achieved. The strategy employed was to

determine a distribution function for each measured electrochemical parameter and integrate the area of overlap of the normalized distribution function of E_{corr} with that of either E_b or E_{rp} to yield a pitting probability value. The biggest obstacle to using this approach was that we do not possess the fundamental mechanistic information about the determinants of E_{corr}, E_b, and E_{rp} needed to allow the objective selection of one form of distribution function over another. Therefore, the strategy employed was to fit each set of data with a wide variety of known distribution functions and then calculate the predicted pitting probability for every combination of distribution function pairs (for those distribution functions for which a reasonable fit to the data could be achieved), to get an idea of the worst-case prediction of the pitting probability in each case.

3.3 Results and Discussion

Under neutral and acidic conditions Cl^- ions stabilize $Cu(I)$ in the dissolved state as complex anions, $CuCl_x^{(x-1)-}$, with the value of x dependent on $[Cl^-]$ [24]. Under these conditions, active corrosion would be expected, with the anodic dissolution process proceeding via the reaction sequence:

$$Cu(s) + Cl^-(\text{aq}) \rightarrow CuCl_{ads} + e^- \tag{1}$$

$$CuCl_{ads} + Cl^-(\text{aq}) \rightarrow CuCl_2^-{}_{ads} \tag{2}$$

$$CuCl_2^-{}_{ads} \rightarrow CuCl_2^-(aq) \tag{3}$$

where "ads" represents a surface-adsorbed state. The mass transport of $CuCl_x^{(x-1)-}$ from the Cu surface has been claimed to be rate-determining [29, 30].

As the pH increases from neutral to more alkaline values, the likelihood of oxide formation, and hence the possibility of pitting, increases, with the initial formation of oxide involving a competition for surface sites between Cl^- and OH^-,

$$CuCl_{ads} + OH^-(\text{aq}) \rightarrow Cu(OH)_{ads} + Cl^-(aq) \tag{4}$$

$$2Cu(OH)_{ads} \rightarrow Cu_2O(s) + H_2O \tag{5}$$
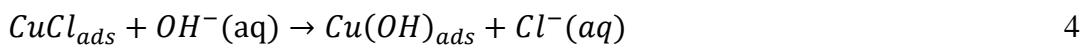
and the extent of oxide formation becoming dependent on the relative [Cl$^-$] and [OH$^-$] (i.e., pH) [24, 31-35]. Hydrolysis of dissolved $CuCl_x^{(x-1)-}$ can also result in Cu_2O growth [30]:
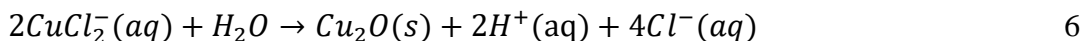
$$2CuCl_2^-(aq) + H_2O \rightarrow Cu_2O(s) + 2H^+(aq) + 4Cl^-(aq) \qquad\qquad 6$$

In the presence of a sufficient dissolved [O$_2$], the homogeneous oxidation of $CuCl_x^{(x-1)-}$ can lead to the formation of Cu^{2+} and the deposition of Cu(II) solids, with atacamite being most likely in solutions containing a sufficiently high [Cl$^-$],

$$12CuCl_2^-(aq) + 3\, O_2(aq) + 6\, H_2O \rightarrow 4Cu_2(OH)_3Cl(s) + 4Cu^{2+}(aq) + 20Cl^-(aq)\ 7$$
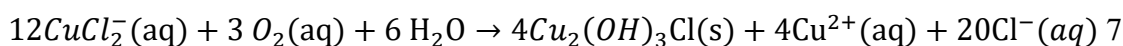
This leads to a duplex film comprising an inner layer of Cu_2O and an outer layer of deposited Cu(II) solids [19-21, 27, 30, 36]. For low [Cl$^-$] and a sufficiently high pH, the deposited outer Cu(II) film becomes a poorly characterized mixture of CuO and Cu(OH)$_2$ [20] with a thickness that increases with pH. For a sufficiently high pH ($\geq$ 12) the outer layer is dominantly Cu(OH)$_2$ [37].

What role these films play in establishing passivity remains only partially resolved, although it is clear that Cl$^-$ exerts a significant effect on the properties and stability of the films. The substitution of monovalent Cl$^-$ ions for divalent O_2^- ions in the Cu_2O lattice creates defects, resulting in films that are less protective than those formed in the absence of Cl$^-$ [27, 34, 38, 39]. It has been claimed that islands of CuCl within an otherwise protective (passive) Cu_2O film can act as initiation sites for pitting [40] which would then be supported by O$_2$ reduction on the surrounding defective semiconducting Cu_2O. This suggests that depending on the [Cl$^-$], Cu_2O films formed in Cl$^-$-containing solutions may be more susceptible to breakdown and pitting [30, 38].

3.3.1   E$_{corr}$ Measurements

Fig. 3.6a presents the E$_{corr}$ of all electrodes in solutions with different chloride concentrations. In all solutions, E$_{corr}$ increased with time, likely due to the formation of an oxide film [41, 42] and the self-repair of defects within it over time. At higher [Cl$^-$], the average E$_{corr}$ was observed at more negative values, while the range of E$_{corr}$ values

increased. The average E_{corr} and range are shown as a function of chloride concentration in Fig. 3.6b.

Both Cl⁻ and OH⁻ can adsorb on Cu surfaces at very low potentials [30, 34, 38],

$$Cu(s) + OH^-(aq) \rightarrow CuOH_{ads} + e^- \hspace{4cm} 8$$

$$Cu(s) + Cl^-(aq) \rightarrow CuCl_{ads} + e^- \hspace{4cm} 9$$

with CuOH$_{ads}$ being a precursor to oxide formation:

$$2CuOH_{ads} \rightarrow Cu_2O(s) + H_2O \hspace{4cm} 10$$

This competition offers a means for Cl⁻ to interfere with the oxide growth process, with Cl⁻ promoting dissolution, and OH⁻ mainly promoting film growth. At pH 11 the solubility of Cu$_2$O is beyond its minimum value, which occurs at ~ pH 9.2 [30]. Thus, film formation will be accompanied by dissolution,

$$CuOH_{ads} + OH^-(aq) \rightarrow Cu(OH)_2^-(aq) \hspace{4cm} 11$$

$$CuCl_{ads} + Cl^-(aq) \rightarrow CuCl_2^-(aq) \hspace{4cm} 12$$

with reaction 12 increasing in importance at higher [Cl⁻]. In addition, as noted in the introduction, it is possible that CuOH$_{ads}$ and CuCl$_{ads}$ coexist on the surface, depending on the ratio of [OH]/[Cl⁻]. Thus, the lower E_{corr} at higher [Cl⁻] can be attributed to a combination of a greater influence of Cl⁻ on passive film properties, accompanied by enhanced Cu(I) dissolution as CuCl$_2$⁻.
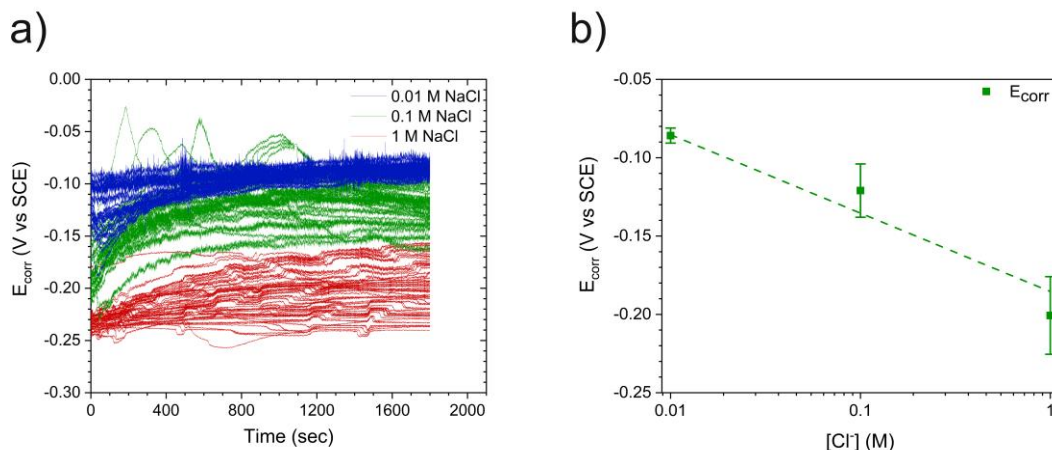
Figure 3.6: Corrosion potential of Cu electrodes in NaCl solution of pH 11 at room temperature: a) Ecorr values of Cu in solutions containing 0.01, 0.1, and 1 M Cl⁻; and b) comparison of mean and standard deviation of Ecorr values on Cu electrodes in solutions containing 0.01, 0.1, and 1 M Cl⁻ with the slope of −105 mV/decade.

3.3.2 E_b Measurements

The pitting scans are shown in Fig. 3.4a and average E_b and range are given as a function of chloride concentration in Fig. 3.4c. Scanning electron microscopy (SEM) was used to verify that pitting occurred on the Cu surfaces and to investigate the surface morphology of electrodes after pitting breakdown scans in 1 M Cl⁻ solution (Fig. 3.7). The plan views of the electrodes with the highest and lowest E_b values show surfaces extensively covered with small pits. A focused ion beam cross section through a small pit (Figure 3.7f) shows an elongated area of damage located between two grains.

The E_b values were more negative at higher chloride concentrations, in keeping with the general observations of others [18, 24, 28, 30, 39, 43-47]. Starosvetsky et al. [46] observed local copper activation (pitting) in low-chloride solutions, while activation extended rapidly over the whole electrode surface in high-chloride solutions; however, other researchers demonstrated that decreasing the chloride concentration improved the density and decreased the porosity of the passive film, which resulted in a higher E_b.

The relationship between E_b and log [Cl$^-$] has previously been proposed to be linear [48, 49], with a slope depending on the nature of the passive film, number of electrons transferred, and other features, and our results were in keeping with those expectations (Figure 3.4c). A semi-logarithmic relation between the E_b and [Cl$^-$], with the form,

$$E_b = A - B \, log[Cl^-] \qquad\qquad 13$$

where A and B are constants, has also been observed for other systems, including iron, nickel, and stainless steel [50]. However, Galvele [50] proposed that the pitting potential depends on the potential drop (IR) in the pit nucleus, so the IR drop should be subtracted from the measured E_b to get the true E_b. Fig. 3.4c shows that the E_b vs. log [Cl$^-$] plot has a slope of -113 mV/decade, suggesting a one-electron reaction, leading to a surface covered with Cu(I) oxide.
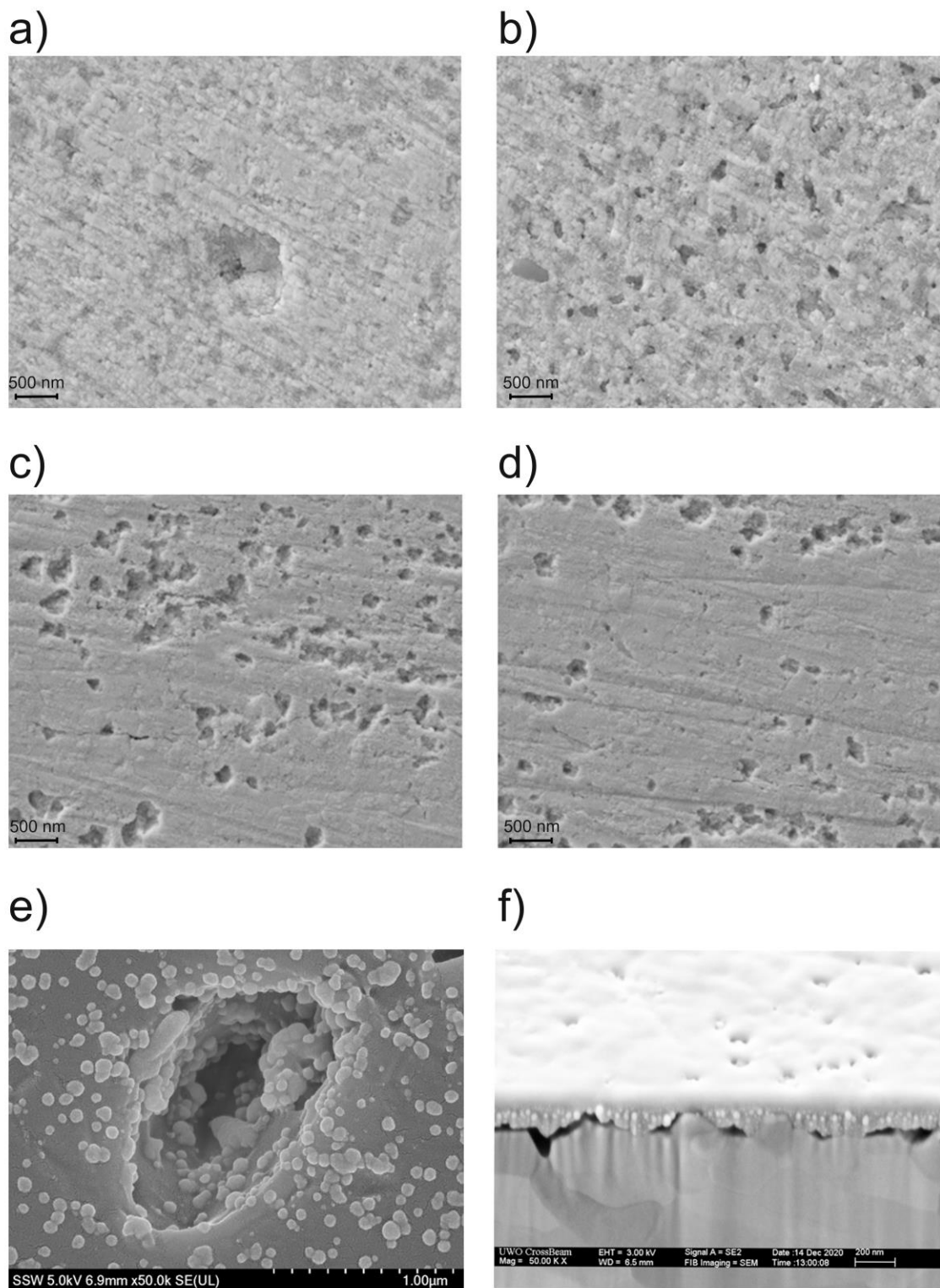
Figure 3.7: Scanning electron micrographs (SEM) of Cu surfaces after pitting experiments at room temperature in 1 M NaCl solution at pH 11: a,b) surface

morphology of Cu after exposure at the lowest E_b, c,d) surface morphology of Cu after exposure at the highest E_b e,f) surface morphology and FIB-cut of Cu at potential close to the lowest E_b.

3.3.3 E_{rp} Measurements

Fig. 3.5a shows that E_{rp} was found at more negative potentials in solutions with higher [Cl$^-$], which is in good agreement with the literature [20]. The average E_{rp} values and range are shown as a function of chloride concentration in Fig. 3.5b. These measurements suggest that pit propagation would be possible in all the chloride-containing solutions used, since the distributions of E_{rp} values were located at potentials more negative than the potential range over which E_{corr} was distributed (Fig. 3.8) [19, 21]. The distributions of E_{rp} values for Cu in solutions of different [Cl$^-$] were narrow compared to those of E_{corr} and, especially, E_b (Fig. 3.9). The magnitudes of the slopes of $dE_{corr}/d\log[\text{Cl}^-]$, $dE_b/d\log[\text{Cl}^-]$, and $dE_{rp}/d\log[\text{Cl}^-]$ were similar (Fig. 3.4c, 3.5b, 3.6b) at just over -100 mV/decade of [Cl$^-$]. Cong [20] reported a strong dependency of E_{corr} and E_b, and weak dependency of E_{rp}, on the [Cl$^-$]. By contrast, our results indicate strong dependency for E_b and similar dependencies for E_{corr} and E_{rp}, as reported for stainless steel [8, 51].
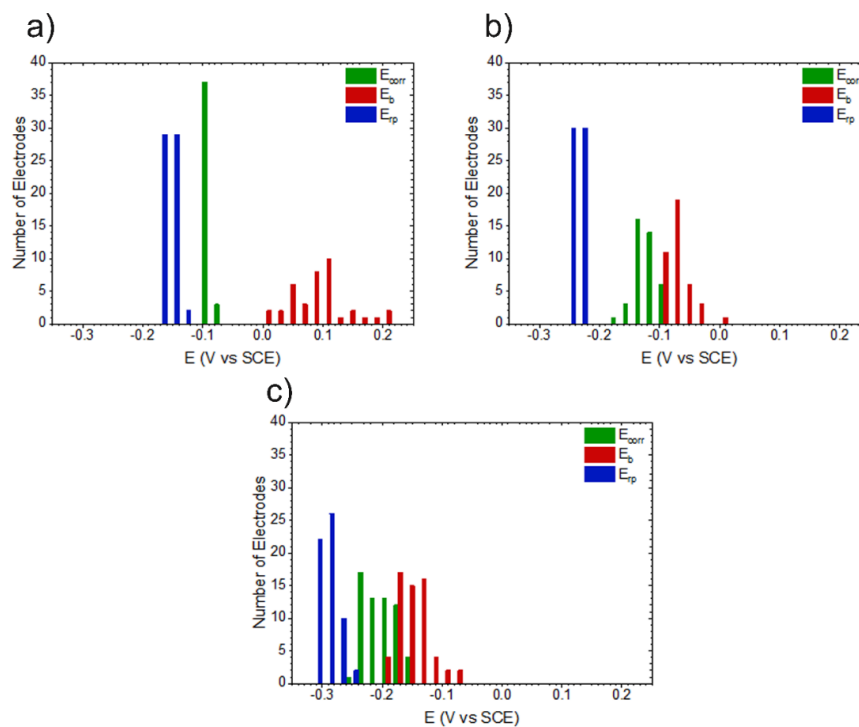
Figure 3.8: Histogram of E_{corr}, E_b, and E_{rp} values on Cu at room temperature in pH 11 solutions containing different chloride concentrations: a) 0.01 M Cl$^-$; b) 0.1 M Cl$^-$; and c) 1 M Cl$^-$.

3.3.4   Statistical Analysis

Box plots of E_{corr}, E_b, and E_{rp} are shown in Fig. 3.9. The interquartile range (IQR) of E_{corr} for different chloride concentrations indicated a wider dispersion in 1 M Cl$^-$ solution than in 0.01 and 0.1 M Cl$^-$ solutions, and no outliers were observed under any of the conditions tested, which indicated a light tail distribution under all conditions.

Increasing the chloride concentration shifted the E_{corr} in the negative direction. The dispersion of E_b decreased with increasing [Cl$^-$] up to 0.1 M; however, a further increase in [Cl$^-$] resulted in a larger IQR. Outliers were observed in the data for 0.01 and 0.1 M Cl$^-$ solutions, which indicated the possibility of a heavy tail distribution (right-skewed) under those conditions; however, no outliers were observed in the data collected from experiments conducted in 1 M Cl$^-$ solutions. The IQR of E_{rp} decreased with increasing [Cl$^-$] from 0.01 to 0.1 M, while a further increase in [Cl$^-$] to 1 M contributed to a larger

IQR, with the presence of an outlier, changing the shape of the distribution to a right-skewed distribution. This heavy tail might increase the probability of repassivation, as it is located on the right side of the E_{rp} distribution, which might result in a greater chance of $E_{corr} < E_{rp}$, which is the necessary condition for repassivation.
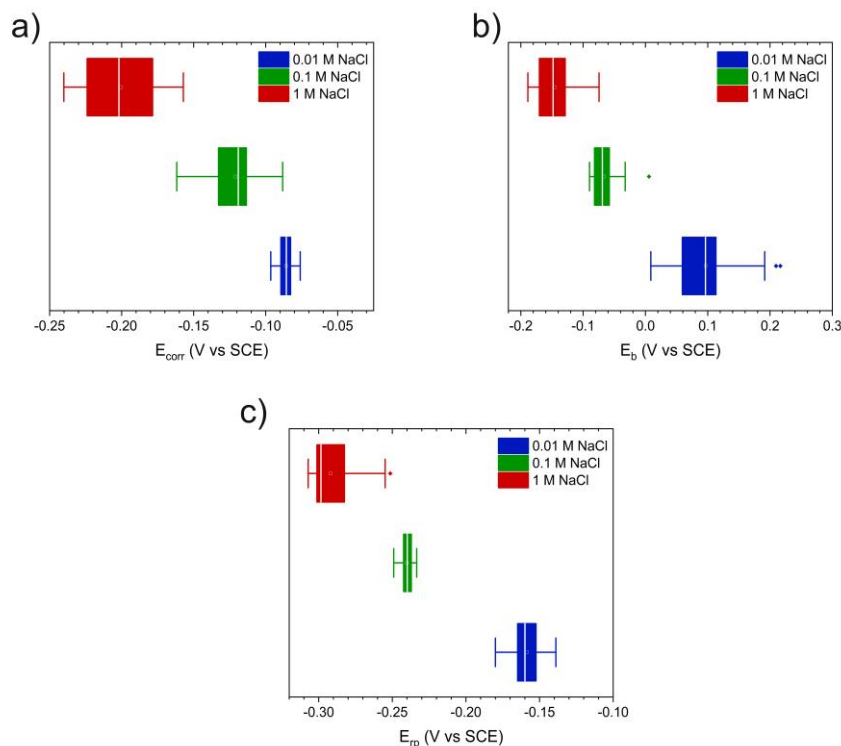
Figure 3.9: Box plot of corrosion parameters measured on Cu in NaCl solution of pH 11 at room temperature with different [Cl⁻]: a) E_{corr}, b) E_b, and c) E_{rp}.

Since we have no theoretical basis upon which to base a prediction of the distributions of the values of the measured corrosion parameters, the collections of measured E_{corr}, E_b, and E_{rp}, values were fitted with a variety of different distribution functions to determine whether any of these functions provided reasonable representations of the measured data. Some gave reasonable fits whereas others differed significantly from the measured data. In the end, five distribution functions were selected for use in the analysis, based on the quality of fit with a confidence level of 90%. One key mathematical requirement of the statistical models used is that all of the input parameters be positive-valued. To achieve this, we shifted all measured potentials by an arbitrary 1 V in the positive direction

(indicated by the artificial potential scale designated "JSE", where E (V vs JSE) = E (V vs SCE + 1 V)). Such a translation of potential values enables the statistical analysis to be applied without affecting its outcome, because it ensures that all potential values are positive in sign without changing their positions relative to each other.

The cumulative distribution functions (CDF) and probability density functions (PDF) of E_{corr}, E_b, and E_{rp} for the three chloride-containing solutions used are shown in Fig. 10 through Fig. 14. The PDF plots indicate the probability of pitting based on the overlap between the distribution curves of E_{corr} and E_b. Since we have no theoretical basis for choosing between the distribution functions that fit reasonably well, we calculated the pitting probability for every combination of distribution functions representing E_{corr} and E_b values. Table. 1 shows the pitting probabilities calculated from the overlap of each possible pair of distribution functions. To make a conservative prediction of the pitting probability, we take the highest probability value determined by this method for each data set. Under these conditions, a greater probability of Cu pitting was observed in 1 M Cl⁻ solutions than in 0.01 and 0.1 M Cl⁻ solutions. Previous publications showed the same trend of pitting probability of copper [19, 21, 43]; however, King [30] determined a lower probability of pitting in solutions with higher chloride concentrations. He determined a very low probability of pitting in an alkaline solution containing a high chloride concentration, since $E_{corr} << E_b$. It is important to note that statistical analysis should be considered based on an acceptable number of data, while King's analysis was based on only a few data points, which decreased the accuracy of the statistical analysis compared to our analysis, consisting of more than 120 data points.

The overlap between the PDFs of E_{corr} and E_{rp} in Figure 3.14 indicate the repassivation probability of Cu, since the PDF of E_{rp} is located to the left side of E_{corr} in this case. A lower probability of repassivation was observed in lower [Cl⁻] solutions than in higher [Cl⁻] solutions, possibly due to the concentration of dissolved copper species in the bottom of pits in solutions with high chloride concentration, which triggered the repassivation of Cu (Table. 2).
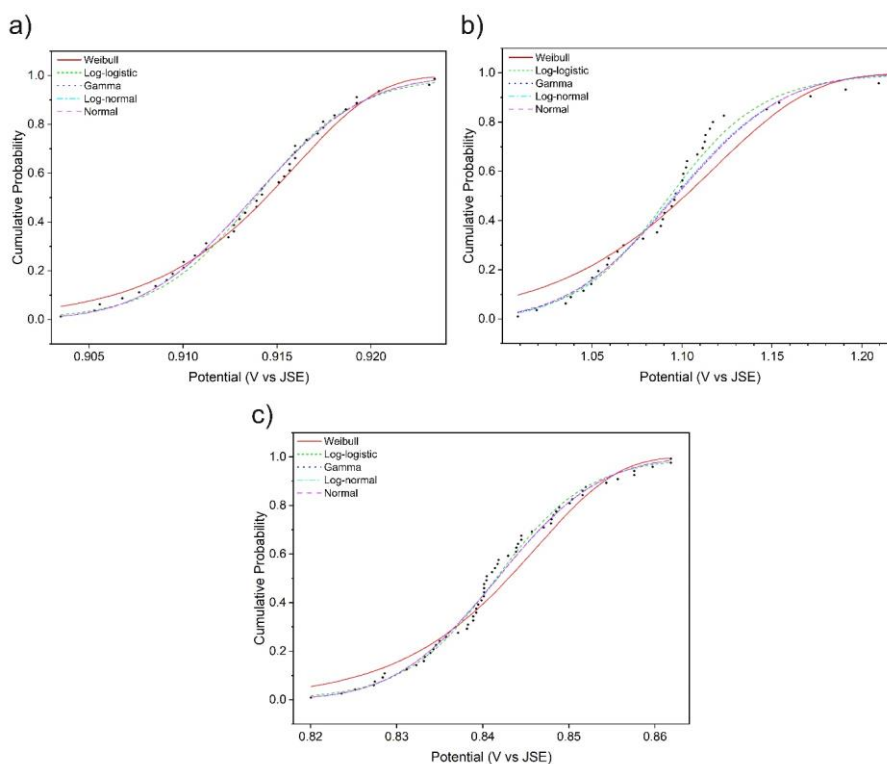
Figure 3.10: Cumulative distribution function (CDF) of experimental data and simulated models for Cu in 0.01 M NaCl solution of pH 11 at room temperature: a) E_{corr}; b) E_b; c) E_{rp}.

The cumulative distribution functions (CDF) and probability density functions (PDF) of E_{corr}, E_b, and E_{rp} for the three chloride-containing solutions used are shown in Fig. 3.12 through Fig. 3.15. The PDF plots indicate the probability of pitting based on the overlap between the distribution curves of E_{corr} and E_b. Since we have no theoretical basis for choosing between the distribution functions that fit reasonably well, we calculated the pitting probability for every combination of distribution functions representing E_{corr} and E_b values. Table. 1 shows the pitting probabilities calculated from the overlap of each possible pair of distribution functions. To make a conservative prediction of the pitting probability, we take the highest probability value determined by this method for each data set. Under these conditions, a greater probability of Cu pitting was observed in 1 M Cl⁻ solutions than in 0.01 and 0.1 M Cl⁻ solutions. Previous publications showed the same

trend of pitting probability of copper (19, 21, 43); however, King (28) determined a lower probability of pitting in solutions with higher chloride concentrations. He determined a very low probability of pitting in an alkaline solution containing a high chloride concentration, since $E_{corr} << E_b$. It is important to note that statistical analysis should be considered based on an acceptable number of data, while King's analysis was based on only a few data points, which decreased the accuracy of the statistical analysis compared to our analysis, consisting of more than 120 data points.
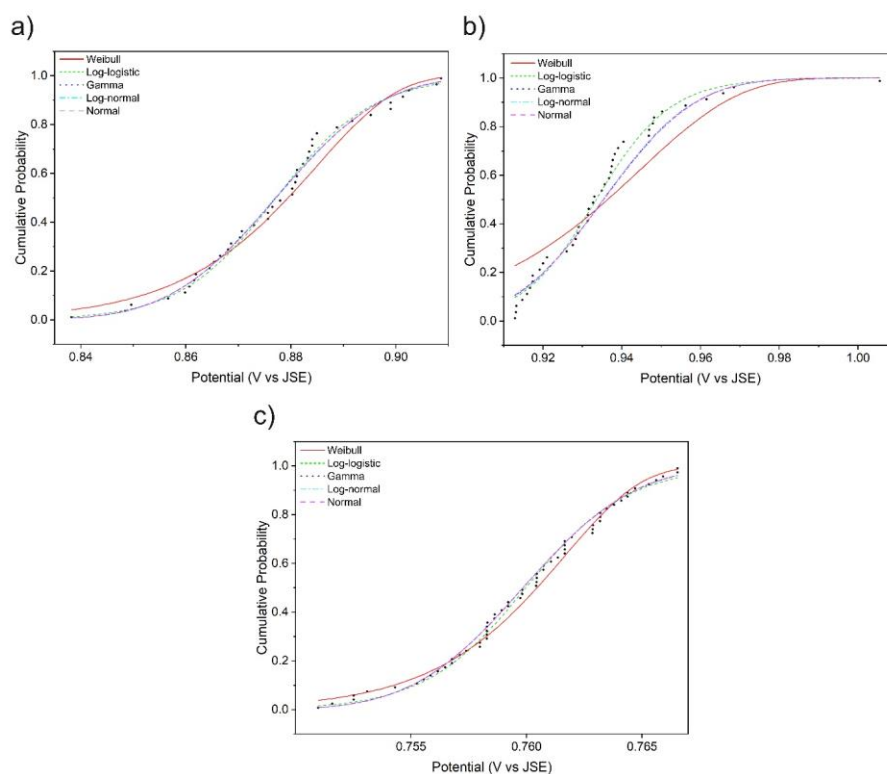
Figure 3.11: Cumulative distribution function (CDF) of experimental data and simulated models for Cu in 0.1 M NaCl solution of pH 11 at room temperature: a) E_{corr}; b) E_b; c) E_{rp}.
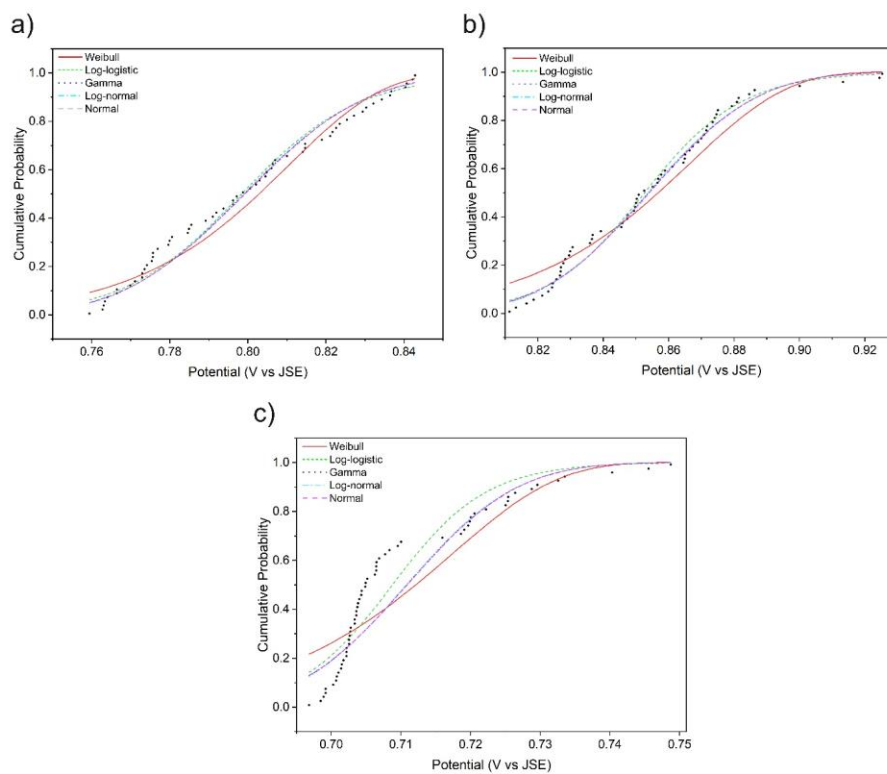
Figure 3.12: Cumulative distribution function (CDF) of experimental data and simulated models for Cu in 1 M NaCl solution of pH 11 at room temperature: a) E_{corr}; b) E_b; c) E_{rp}.
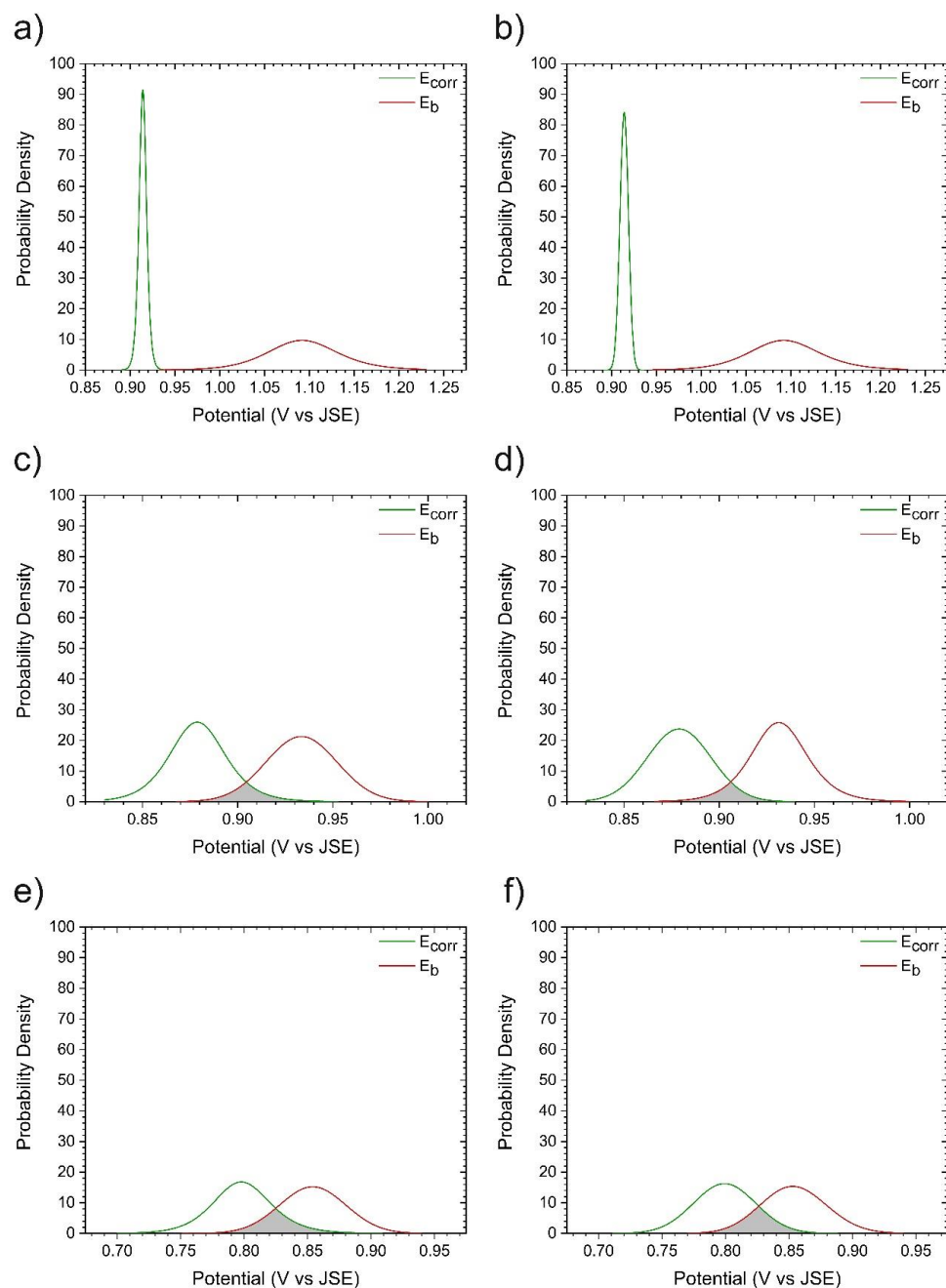
Figure 3.13: Fig 13. Probability distribution curves of E_{corr} and E_b on Cu in NaCl solution of pH 11 at room temperature: a,b) maximum and minimum overlaps between E_{corr} and E_b in 0.01 M Cl⁻ solution, respectively; c,d) maximum and minimum overlaps between E_{corr} and E_b in 0.1 M Cl⁻ solution, respectively; e,f) maximum and minimum overlaps between E_{corr} and E_b in 1 M Cl⁻ solution, respectively.
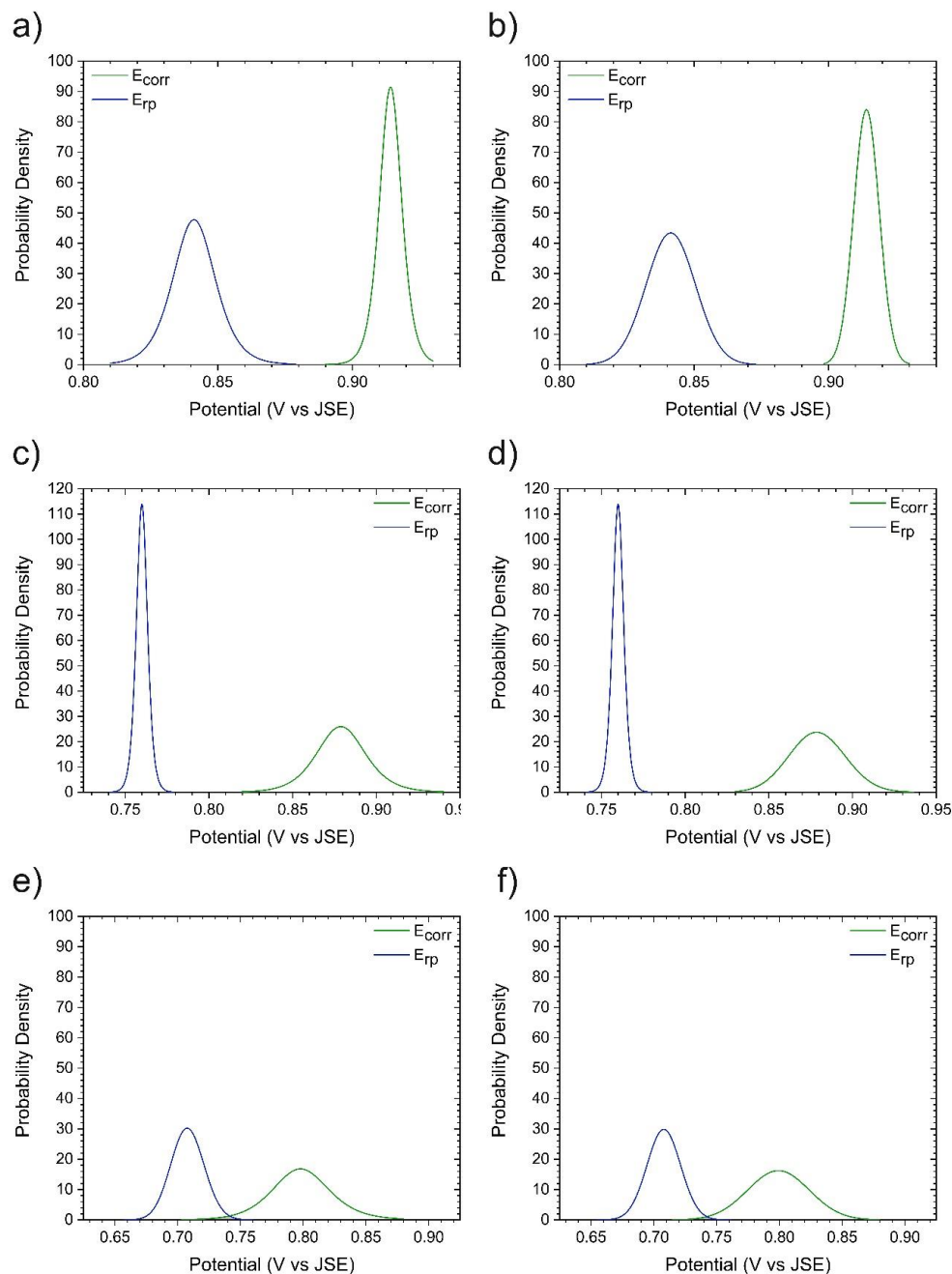
Figure 3.14: Probability distribution curves of E_{corr} and E_{rp} on Cu in NaCl solution of pH 11 at room temperature: a,b) maximum and minimum overlaps between E_{corr} and E_{rp} in 0.01 M Cl⁻, respectively; c,d) maximum and minimum overlaps between E_{corr} and E_{rp} in 0.1 M Cl⁻, respectively; e,f) maximum and minimum overlaps between E_{corr} and E_{rp} in 1 M Cl⁻, respectively.

Table 3.1: Pitting probability (%) of Cu in different chloride-containing solutions a) 0.01 M Cl⁻ b) 0.1 M Cl⁻ c) 1 M Cl⁻ based on different distribution functions.

a)

Corrosion Potential (E_{corr})

Distribution	Log-Logistic	Gamma	Log-Normal	Normal	Weibull
Log-Logistic	5.69×10^{-3}	1.52×10^{-11}	3.06×10^{-10}	1.04×10^{-10}	9.06×10^{-2}
Gamma	5.06×10^{-3}	1.52×10^{-11}	3.06×10^{-10}	1.04×10^{-10}	7.97×10^{-4}
Log-Normal	4.93×10^{-3}	1.52×10^{-11}	3.06×10^{-10}	1.04×10^{-10}	3.74×10^{-4}
Normal	5.69×10^{-3}	1.52×10^{-11}	3.06×10^{-10}	1.04×10^{-10}	3.08×10^{-3}
Weibull	1	1	1	1	1

(Row axis label: Breakdown Potential (E_b))

b)

Corrosion Potential (E_{corr})

Distribution	Log-Logistic	Gamma	Log-Normal	Normal	Weibull
Log-Logistic	12	12	12	12	10
Gamma	13	12	12	12	10
Log-Normal	12	12	12	12	1
Normal	13	13	13	13	11
Weibull	25	24	24	24	23

(Row axis label: Breakdown Potential (E_b))

c)

Corrosion Potential (E_{corr})

Distribution	Log-Logistic	Gamma	Log-Normal	Normal	Weibull
Log-Logistic	28	28	28	28	29
Gamma	28	28	28	28	29
Log-Normal	28	28	28	28	29
Normal	28	28	28	28	29
Weibull	34	34	34	34	34

(Row axis label: Breakdown Potential (E_b))

Table 3.2: Repassivation probability (%) of Cu in different chloride-containing solutions a) 0.01 M Cl⁻, b) 0.1 M Cl⁻, c) 1 M Cl⁻, based on different distribution functions.

a)

Corrosion Potential (E_{corr})

Distribution	Log-Logistic	Gamma	Log-Normal	Normal	Weibull
Log-Logistic	8.32×10^{-4}	2.12×10^{-10}	3.06×10^{-10}	1.04×10^{-10}	8.93×10^{-2}
Gamma	8.29×10^{-4}	5.20×10^{-13}	1.74×10^{-14}	8.68×10^{-14}	2.31×10^{-4}
Log-Normal	8.29×10^{-4}	5.20×10^{-13}	1.74×10^{-14}	8.68×10^{-14}	2.83×10^{-4}
Normal	8.29×10^{-4}	5.20×10^{-13}	1.74×10^{-14}	8.68×10^{-14}	1.67×10^{-3}
Weibull	9.81×10^{-10}	1.59×10^{-47}	1.59×10^{-47}	1.59×10^{-47}	2.32×10^{-5}

Repassivation Potential (E_{rp})

b)

Corrosion Potential (E_{corr})

Distribution	Log-Logistic	Gamma	Log-Normal	Normal	Weibull
Log-Logistic	1.57×10^{-4}	5.30×10^{-8}	2.16×10^{-8}	2.89×10^{-7}	8.56×10^{-2}
Gamma	1.57×10^{-4}	5.30×10^{-8}	2.16×10^{-8}	2.89×10^{-7}	3.93×10^{-3}
Log-Normal	1.57×10^{-4}	5.30×10^{-8}	2.16×10^{-8}	2.89×10^{-7}	3.63×10^{-3}
Normal	1.57×10^{-4}	5.30×10^{-8}	2.16×10^{-8}	2.89×10^{-7}	4.62×10^{-3}
Weibull	6.92×10^{-6}	1.44×10^{-21}	4.24×10^{-23}	8.62×10^{-19}	1.88×10^{-3}

Repassivation Potential (E_{rp})

c)

Corrosion Potential (E_{corr})

Distribution	Log-Logistic	Gamma	Log-Normal	Normal	Weibull
Log-Logistic	3	2	2	2	5
Gamma	2	1	1	2	5
Log-Normal	2	1	1	2	5
Normal	2	4.75×10^{-3}	4.75×10^{-3}	4.75×10^{-3}	5
Weibull	2	1	1	2	5

Repassivation Potential (E_{rp})

3.4 Conclusions

The probability of pitting corrosion of copper in pH 11 solution with different chloride concentrations has been studied using a multielectrode array to generate large numbers of data that enable the application of statistical analyses of the processes involved. The corrosion potential decreased with increasing chloride concentration and the dispersion of E_{corr} data increased with [Cl$^-$]; however, dispersion of E_b and E_{rp} decreased with increasing [Cl$^-$] up to 0.1 M and then increased with further increase of [Cl$^-$] to 1 M. Distributions in the values of E_b and E_{rp} could be due to the stochastic nature of passive film breakdown and reformation. Investigations of the pitting probability show a greater overlap between the PDFs of E_{corr} and E_b, and of E_{corr} and E_{rp}, respectively, in solutions with higher chloride concentrations, indicating a higher probability of both pit initiation and repassivation. The further development of this approach will involve investigations of scan rate, hold time, pH, dissolved anions, temperature, dissolved oxygen concentration and other likely influential parameters.

3.5 Acknowledgments

3.6   References

[1] G.R. Engelhardt, D.D. Macdonald, Monte-Carlo simulation of pitting corrosion with a deterministic model for repassivation, Journal of The Electrochemical Society, 167 (2020).

[2] Y. Zhou, A. Xu, F. Mao, J. Yu, D. Kong, C. Dong, D.D. Macdonald, Passivity breakdown on copper: Influence of borate anion, Electrochimica Acta, 320 (2019).

[3] D.D. Macdonald, M. Urquidi-Macdonald, Distribution functions for the breakdown of passive films, Electrochimica Acta, 31 (1986) 1079-1086.

[4] T. Haruna, D.D. Macdonald, Theoretical prediction of the scan rate dependencies of the pitting potential and the probability distribution in the induction time, Journal of The Electrochemical Society, 144 (1997) 1574-1581.

[5] G. Engelhardt, D.D. Macdonald, Unification of the deterministic and statistical approaches for predicting localized corrosion damage. I.Theoretical foundation, Corrosion Science, 46 (2004) 2755-2780.

[6] P.M. Aziz, Application of the statistical theory of extreme values to the analysis of maximum pit depth data for aluminum, Corrosion, 12 (1956) 35-46.

[7] G.G. Eldredge, Analysis of corrosion pitting by extreme-value statistics and its application to oil well tubing caliper surveys, Corrosion, 13 (1957) 67-76.

[8] T. Shibata, 1996 W.R. Whitney award lecture: Statistical and stochastic approaches to localized corrosion, Corrosion, 52 (1996) 813-830.

[9] V.F. Lucey, Mechanism of pitting corrosion of copper in supply waters, British Corrosion Journal, 2 (1967) 175-185.

[10] H.M. Shalaby, F.M. Al-Kharafi, V.K. Gouda, A morphological study of pitting corrosion of copper in soft tap water, Corrosion Journal, 45 (1989) 536-547.

[11] N.J. Laycock, M.H. Moayed, R.C. Newman, Metastable pitting and the critical pitting temperature, Journal of Electrochemical Society, 145 (1998) 2622-2628.

[12] R. Qvarfort, Critical pitting temperature measurements of stainless steels with an improved electrochemical method, Corrosion Science, 29 (1989) 987-993.

[13] V.M. salinas-Bravo, R.C. Newman, An alternative method to determine critical pitting temperature of stainless steels in ferric chloride solution, Corrosion Science, 36 (1994) 67-77.

[14] T. Li, J.R. Scully, G.S. Frankel, Localized corrosion: passive film breakdown vs pit growth stability: part II. A model for critical pitting temperature, Journal of The Electrochemical Society, 165 (2018) C484-C491.

[15] D.E. Williams, J. Stewart, P. Balkwill, The nucleation, growth and stability of micropits in stainless steel, Corrosion Science, 36 (1994) 1213-1235.

[16] A.M. Riley, D.B. Wells, D.E. Williams, Initiation events for pitting corrosion of stainless steel?, Corrosion Science, 32 (1991) 1307-1313.

[17] D.E. Williams, C. Westcott, M. Fleischmann, Stochastic models of pitting corrosion of stainless steels: I. modeling of the initiation and growth of pits at constant potential, Electrochemical Society, 132 (1985) 1796-1804.

[18] M.R.G.D. Chialvo, R.C. Salvarezza, D.V. Moll, A.J. Arvia, Kinetics of passivation and pitting corrosion of polycrystalline copper in borate buffer solutions containing sodium chloride., Electrochimica Acta, 30 (1985) 1501–1511.

[19] H. Cong, J.R. Scully, Use of coupled multielectrode arrays to elucidate the pH dependence of copper pitting in potable water, Journal of The Electrochemical Society, 157 (2010) 36 - 46.

[20] H. Cong, H.T. Michels, J.R. Scully, Passivity and pit stability behavior of copper as a function of selected water chemistry variables, Journal of The Electrochemical Society, 156 (2009) 16-27.

[21] H. Cong, J.R. Scully, Effect of chlorine concentration on natural pitting of copper as a function of water chemistry, Journal of The Electrochemical Society, 157 (2010) 200-211.

[22] H. Ha, C. Taxén, H. Cong, J.R. Scully, Effect of applied potential on pit propagation in copper as function of water chemistry, Journal of The Electrochemical Society, 159 (2011) C59-C73.

[23] Z. Qin, R. Daljeet, M. Ai, N. Farhangi, J.J. Noël, S. Ramamurthy, D. Shoesmith, F. King, P. Keech, The active/passive conditions for copper corrosion under nuclear waste repository environment, Corrosion Engineering, Science and Technology, 52 (2017) 45-49.

[24] A.E. Warraky, H.A.E. Shayeb, E.M. Sherif, Pitting corrosion of copper in chloride solutions, Anti-Corrosion Methods and Materials, 51 (2004) 25-61.

[25] F. King, D.S. Hall, P.G. Keech, Nature of the near-field environment in a deep geological repository and the implications for the corrosion behaviour of the container, Corrosion Engineering, Science and Technology, 52 (2017) 25-30.

[26] D.S. Hall, M. Behazin, J.W. Binns, P.G. Keech, An evaluation of corrosion processes affecting copper-coated nuclear waste containers in a deep geological repository, Progress in Materials Science, 118 (2021).

[27] G. Mankowski, J.P. Duthil, A. Giusti, The pit morphology on copper in chloride- and sulphate-containing solutions, Corrosion Science, 39 (1997) 27-42.

[28] F. Mao, C. Dong, S. Sharifi-Asl, P. Lu, D.D. Macdonald, Passivity breakdown on copper: Influence of chloride ion, Electrochimica Acta, 144 (2014) 391-399.

[29] F. King, Critical review of the literature on the corrosion of copper by water, Swedish Nuclear Fuel and Waste Management Co, 2010.

[30] F. King, Corrosion of copper in alkaline chloride environment, Swedish Nuclear Fuel and Waste Management Co, 2002.

[31] H.P. Lee, K. Nobe, Kinetics and mechanisms of Cu electrodissolution in chloride media.pdf, Journal of Electrochemical Society, 133 (1986) 2035-2043.

[32] C. C. Deslouis, B. B. Tribollet, G. Mengoli, M.M. Musiani, Electrochemical behaviour of copper in neutral aerated chloride solution. I. Steady state investigation, Journal of Apllied Electrochemistry, 18 (1988).

[33] B. Millet, C. Fiaud, C. Hinnen, E.M.M. Sutter, A correlation between electrochemical behaviour, composition and semiconducting properties of naturally grown oxide films on copper, Corrosion Science, 37 (1995) 1903-1918.

[34] F. King, L. Ahonen, C. Taxen, U. Vuorinen, L. Werme, Copper corrosion under expected conditions in a deep geologic repository, SKB, 2002.

[35] G. Kear, B.D. Barker, F.C. Walsh, Electrochemical corrosion of unalloyed copper in chloride media—a critical review, Corrosion Science, 46 (2004) 109-135.

[36] H.H. Strehblow, B. Titze, The investigation of the passive behaviour of copper in weakly acid and alkaline solutions and the examination of the passive film by ESCA and ISS, Electrochimica Acta, 25 (1980) 839-850.

[37] D.W. Shoesmith, T.E. Rummery, D. Owen, W. Lee, Anodic oxidation of copper in alkaline solutions 2—the open-circuit potential behavior of electrochemically formed cupric hydroxide films, Electrochimica Acta, 22 (1977) 1403-1409.

[38] F. King, C. Lilja, K. Pedersen, P. Pitkänen, M. Vähänen, An update of the state-of-the-art report on the corrosion of copper under expected conditions in a deep geologic repository, SKB, 2010.

[39] H. Ha, C. Taxen, K. Williams, J. Scully, Effects of selected water chemistry variables on copper pitting propagation in potable water, Electrochimica Acta, 56 (2011) 6165-6183.

[40] E. Mattson, Corrosion of Copper and Brass Practical Experience in relation to Basic Data.pdf, British Corrosion Journal, 15 (1980) 6-13.

[41] M.A. Abdulhay, A. A.Al-Suhybani, Open circuit potential for copper electrode in 1 M NaCl solutions, Materials Science and Engineering Technology, 23 (1992) 407-412.

[42] T. Standish, J. Chen, R. Jacklin, P. Jakupi, S. Ramamurthy, D. Zagidulin, P. Keech, D. Shoesmith, Corrosion of copper-coated steel high level nuclear waste containers under permanent disposal conditions, Electrochimica Acta, 211 (2016) 331-342.

[43] F. Arjmand, A. Adriaens, Influence of pH and chloride concentration on the corrosion behavior of unalloyed copper in NaCl solution: A comparative study between the micro and macro scales, Materials, 5 (2012) 2439-2464.

[44] M.R.G.D. Chialvo, R.C. Salvarezza, D.V. Moll, A.J. Arvia, Kinetics of passivation and pitting corrosion of polycrystalline copper in borate buffer solutions, Electrochimica Acta, 30 (1985) 1501-1511.

[45] M. Ochoa, M.A. Rodríguez, S.B. Farina, Corrosion of high purity copper in solutions containing NaCl, Na2SO4 and NaHCO3 at different temperatures, Procedia Materials Science, 9 (2015) 460-468.

[46] D. Starosvetsky, O. Khaselev, M. Auinat, Y. Ein-Eli, Initiation of copper dissolution in sodium chloride electrolytes, Electrochimica Acta, 51 (2006) 5660-5668.

[47] A. Nishikata, M. Itagaki, T. Tsuru, S. Haruyama, Passivation and its stability on copper in alkaline solutions containing carbonate and chloride ions, Corrosion Science, 31 (1990) 287-292.

[48] A.G.G. Allah, M.M. Abou-Romia, W.A. Badawy, H.H. Rehan, Effect of halide ions on passivation and pitting corrosion of copper in alkaline solutions, Materials and Corrosion, 42 (1991) 584-591.

[49] G. Bianchi, G. Fiori, P. Longhi, F. Mazza, Horse shoe- Corrosion of copper alloys in flowing sea water- Mechanism, and possibility of cathodic protection of condenser tubes in power generation, Corrosion, 34 (1978) 396-406.

[50] J.R. Galvele, Transport processes and the mechanism of pitting of metals, Journal of the Electrochemical Society, 123 (1976) 464-474.

[51] T. Shibata, T. Takeyama, Stochastic theory of pitting corrosion, Corrosion Journal, 33 (1977) 243-251.

Chapter 4

4 Use of Multielectrode Arrays and Statistical Analysis to Investigate the Pitting Probability of Copper: Part II. Effect of Sulfate and Bicarbonate

Abstract

High purity copper (Cu) and copper alloys have found applications in a wide range of industries. One of the main reasons Cu and its alloys are utilized widely is due to their having sufficient corrosion resistance in various environments such as seawater and anoxic solutions; however, localized corrosion processes (particularly pitting corrosion) might occur in the presence of aggressive anions, oxygen, or an increase in solution pH. In critical applications of Cu, the susceptibility of Cu to localized corrosion, specifically pitting, must be carefully considered, as it can lead to material failure. In this study, the pitting probability of Cu in unary (sulfate) and binary (sulfate + bicarbonate) solutions is investigated using electrochemical techniques in conjunction with statistical analysis. The pitting probability of Cu did not change significantly with sulfate concentration at pH 8 but was found to increase with increasing $[SO_4^{2-}]$ up to a certain concentration (0.005 M) at pH 9 and then decreased with a further increase in $[SO_4^{2-}]$. The transition from repassivation to natural pitting was found in sulfate-containing solutions, and C_{trans} was defined to be 0.005 M. The presence of bicarbonate in sulfate-containing solution resulted in a transition from natural pitting to repassivation.

4.1 Introduction

Many industries have been using Cu and its alloys as the primary materials in their products and equipment (e.g., water pipes, heat exchangers, etc.), due to their mechanical and physical properties. From both longevity and economic points of view, Cu has attracted the attention of the nuclear industry as a candidate for the corrosion barrier for used fuel containers (UFC) in a deep geological repository (DGR). Based on the current design, the UFCs will be coated (Canada) or covered (Sweden) with high-purity Cu as a corrosion barrier [1-8].

Cu oxide films are commonly present on Cu depending on the application. For example, formation of scale and Cu oxides in heat exchangers results in a decrease in heat transport efficiency. However, in corrosive environments, oxide films can protect Cu from further dissolution. In specific situations, Cu is not able to form a dense and sufficiently protective oxide film on the surface, which can lead to material failure by corrosion [9-18].

Cu is thermodynamically stable in most oxygen-free environments. However, under aerated conditions, corrosion, specifically localized corrosion in the form of pitting, becomes a possibility. The morphology and protectiveness of a passive oxide film depends on both material properties, such as the grain size and orientation, and environmental conditions, such as the concentration of aggressive anions, exposure time, etc. [19-32]. Protective films can be formed on the surface of Cu by either the dissolution-precipitation mechanism or a solid-state reaction involving nucleation and growth, with the latter leading to a passive film [31-34]. In moderately alkaline solutions, Cu forms a double-layer film comprised of an inner Cu_2O layer and an outer CuO or/and $Cu(OH)_2$ layer [27, 31, 35-37]. During the initial film growth, due to the porous structure of the Cu_2O layer, dissolution as Cu^{2+} cations can occur at the Cu surface, provided that the potential is sufficiently positive, with the Cu^{2+} cations diffusing from the Cu surface to the oxide-solution interface, leading to the deposition of CuO and/or $Cu(OH)_2$ on top of the Cu_2O inner layer [25, 31, 38-40], and in some cases, passivation.

Passive film breakdown mechanisms have been extensively investigated, and two main mechanisms proposed. The first mechanism involves the transport of aggressive anions from the solution into the oxide film, leading eventually to the generation of stress within the film which causes its mechanical breakdown [41]. The second mechanism involves the adsorption of aggressive anions on the passive film resulting in its thinning and the eventual exposure of the metal surface [42, 43].

The susceptibility of materials to pitting corrosion can be determined by a comparison of the corrosion potential (E_{corr}) to the passive film breakdown potential (E_b) measured by a potentiodynamic scan of the applied potential (E) from low to high values. All corrosion

parameters such as E_{corr}, E_b, and repassivation potential (E_{rp}, the potential at which the current on the negative-going scan achieves the value of the original passive current observed on the positive-going scan) are distributed values, due to uncontrollable variations in oxide film properties and reactivity, variations in the local environment at the oxide surface, as well as the stochastic nature of passive film rupture [35, 44]. Pitting is deemed to be possible if $E_{corr} \geq E_b$ [27, 35, 45], with the distribution of values making the boundary between non-susceptibility and susceptibility to pitting uncertain. Therefore, it is possible that pitting could occur even if $E_{corr} < E_b$, since a single value of E_{corr} is not representative of the variation in E_{corr} values and, similarly, E_b also has a range of values. A more conservative evaluation process is to investigate the susceptibility to pitting by evaluating the difference between E_{corr} and E_{rp} values. The E_{rp} can be determined by scanning E from a value above E_b to a value below E_b until the measured current reaches the low value measured in the passive region. The E_{rp} depends on a variety of factors, such as pit depth, maximum dissolution current density ($i_{diss, max}$), the potential scan rate used in potentiodynamic polarization measurements such as those described in this study, and pit initiation rate [46]. The E_{rp} is inversely proportional to the pit depth and $i_{diss, max}$, so increasing the pit depth and $i_{diss, max}$ both result in lower E_{rp}. However, E_{rp} is directly proportional to the scan rate and the pit initiation rate, since lower scan rates and/or pit initiation rates provide more time for pits to grow deeper, thus leading to a lower E_{rp}.

Many studies have been conducted to elucidate the influence of various parameters such as anion concentrations, pH, and temperature on E_{corr}, E_b, and E_{rp} [35, 44, 47-56]. The previous research found that CO_3^{2-} and OH^- enhance the passive film stability, while Cl^- and SO_4^{2-} have an aggressive effect on Cu and stainless steel [47, 49, 52, 54-58]. The dependence of passive film stability of Cu on $[Cl^-]$ has been examined extensively. The results indicate that the corrosion rate increases with increasing $[Cl^-]$ up to a certain concentration ($[Cl^-]_{crit}$), above which chloride plays an inhibiting role, due to the rapid formation of a CuCl layer [55, 56, 59, 60]. The pitting probability of Cu can also be influenced by the pH of the solution [56, 61]. Cong [35] proposed three different regions based on pH: uniform corrosion for pH < 7; a pitting susceptibility region between pH 7 and 10; and limited susceptibility for pH > 10. It is important to note that the boundary

between these regions depends on temperature, $[O_2]$, and solution composition. E_{corr}, E_b, and E_{rp} were found to depend on the concentrations of different anions (Cl^-, SO_4^{2-}, HCO_3^-/CO_3^{2-}, OH^-). Generally, Cl^- and SO_4^{2-} destabilized the passive films, leading to decreases in E_{corr} and E_b. However, the effect of SO_4^{2-} is still ambiguous and requires more research effort. The presence of HCO_3^-/CO_3^{2-} enhanced the durability of the passive film resulting in higher E_{corr} and E_b values. The properties of the passive film are particularly important when materials are in contact with solutions containing low concentrations of aggressive anions, resulting in film breakdown at relatively high potentials [62, 63]. The substitution of O^{2-} ions with aggressive anions such as Cl^- and SO_4^{2-} in an oxide film leads to the creation of defects which render the film less protective [59, 64-66].

The corrosion behaviour of Cu in different environments, such as seawater and deaerated solutions, is well established. In addition, Matin et al. [67] investigated the pitting probability of Cu in chloride-containing solutions using multielectrode arrays and statistical analysis, but there is a lack of information regarding the susceptibility of Cu to pitting corrosion in sulfate-containing solutions. The majority of the published research has been conducted based on the hypothesis that corrosion parameters are deterministic, thus ignoring the effect of distributed values. Qin et al. [48] defined the approximate active/passive boundary as a function of $[SO_4^{2-}]$ and pH. This boundary was developed based on only a small number of experiments and does not account for the statistical distributions of the parameters measured to establish it. A more thorough understanding of the pitting probability of Cu in SO_4^{2-} and HCO_3^- solutions requires the application of a method that accounts for the distributed nature of the corrosion parameters. In the studies described in this research, a Cu multielectrode array was used to determine the distributions of E_{corr}, E_b, and E_{rp} by simultaneously monitoring 30 electrodes simultaneously exposed to the same solution. Each experiment was performed twice, with 60 data points collected in total for each corrosion parameter, including E_{corr}, E_b, and E_{rp}.

4.2   Experimental Methodology

4.2.1   Sample Preparation

O-free and P-doped wrought Cu was supplied by the Swedish Nuclear Fuel and Waste Management Company (SKB, Stockholm, Sweden). Electrodes were machined in the form of bullet samples rounded at the edges (Fig. 4.1) to avoid edge effects during electrochemical experiments. A threaded connection to a stainless steel rod enabled connection to external electrochemical equipment. Specimens used in corrosion experiments were ground with a sequence of SiC papers with grit sizes of 600, 800, 1200, 2500, and 4000 followed by rinsing in type I water. The samples were then sonicated in ethanol to remove grinding residues and organic contaminants, and finally dried in a stream of Ar gas.
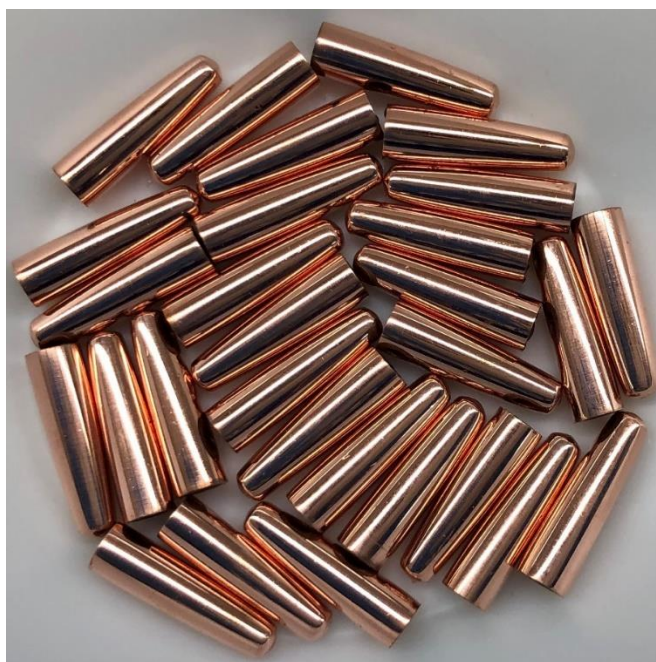
Figure 4.1: O-free and P-doped copper electrodes.

4.2.2   Solution Preparation

Solutions were prepared with reagent-grade sodium sulfate (Na_2SO_4, 99.0%) and sodium bicarbonate ($NaHCO_3$, 99.5%), provided by Fisher Scientific, and Type I water with a resistivity of 18.2 MΩ.cm, prepared using a Thermo Scientific Barnstead Nanopure 7143

system. The multielectrode array, explained in our previous paper [67], was exposed to either sulfate-containing solutions with various [SO_4^{2-}] in the range from 0.001 M to 0.1 M or binary solutions containing 0.01 M SO_4^{2-} and various [HCO_3^-]. The pH of the solutions was adjusted to 8 and 9 by adding small volumes of NaOH.

4.2.3   Electrochemical cell, Instrumentation, and Procedure

All electrochemical experiments were performed in a conventional three-electrode electrochemical cell using the multielectrode array, a Pt plate as the counter electrode, and a saturated calomel reference electrode (SCE, 0.242 V vs. SHE). The counter electrode had a large surface area (200 cm^2) and was not a limiting factor in the current measurements. The electrochemical cell was placed inside a Faraday cage to reduce electrical noise from external sources. Following E_{corr} measurements, potentiodynamic polarization experiments were conducted at 10 mV/min using a Multichannel Microelectrode Analyzer 910 (MMA, Scribner Associates) connected to a computer equipped with MMAlive software. The instrument was equipped with 100 µA zero resistance ammeters (ZRA). Fig. 4.2 shows a schematic illustration of the experimental arrangement. The E_b and E_{rp} values were measured in separate experiments to ensure that, when measuring E_{rp}, all 30 Cu specimens had experienced passive film breakdown.
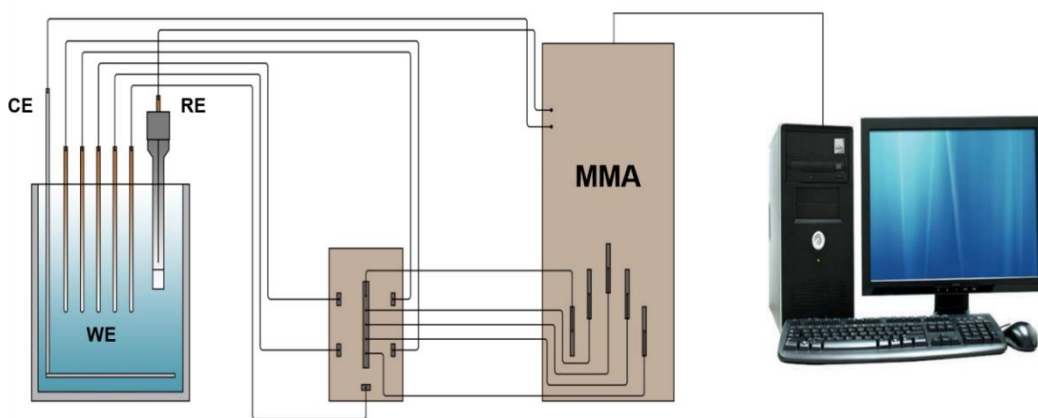
Figure 4.2: Schematic of multichannel microelectrode analyzer (MMA) connected to a multielectrode array.

4.2.3.1   Breakdown Potential (E_b) Measurements:

Values of E_b were measured in a potentiodynamic scan. Prior to the scan, Cu electrodes were cathodically cleaned at -0.85 V vs SCE for 3 minutes, a procedure known to help improve the reproducibility of many electrochemical experiments [67]. Then, the corrosion potential (E_{corr}) was monitored for 30 minutes to allow a steady state to be established and to determine the range of values for the 30 electrodes on the multielectrode array. The potential was then scanned from E_{corr} in the positive direction at a scan rate of 10 mV/min until the current on all electrodes reached 100 µA. The E_b was determined from the intersection of the tangent to the current in the passive range and the tangent to the rising current in the potential range after breakdown [59, 68]. A schematic of this procedure is shown in Fig. 4.3.a, as well as in our previous paper [67]. Two runs using 30 electrodes each were conducted for each set of experimental conditions.

4.2.3.2   Repassivation Potential (E_{rp}) Measurements:

To achieve a starting condition that was as nearly identical as possible for all electrodes in each experiment, the Cu surfaces were prepared as described in section 2.1, then cathodic cleaning and E_{corr} measurement were performed. Next, a potential equal to the highest breakdown potential previously determined in E_b scans under the same conditions was applied to stimulate passive film breakdown on every electrode in the array. . The potential was then scanned in the negative direction at a rate of 10 mV/min (Fig. 4.3.b) until the current on each electrode reached the mean passive current previously determined in E_b scans under the same conditions (Fig. 4.4).

The potential at which this current was achieved on each electrode was taken as the E_{rp} value for that electrode. Two runs using 30 electrodes each were conducted for each set of experimental conditions. We note that we conducted these experiments in naturally aerated solutions.
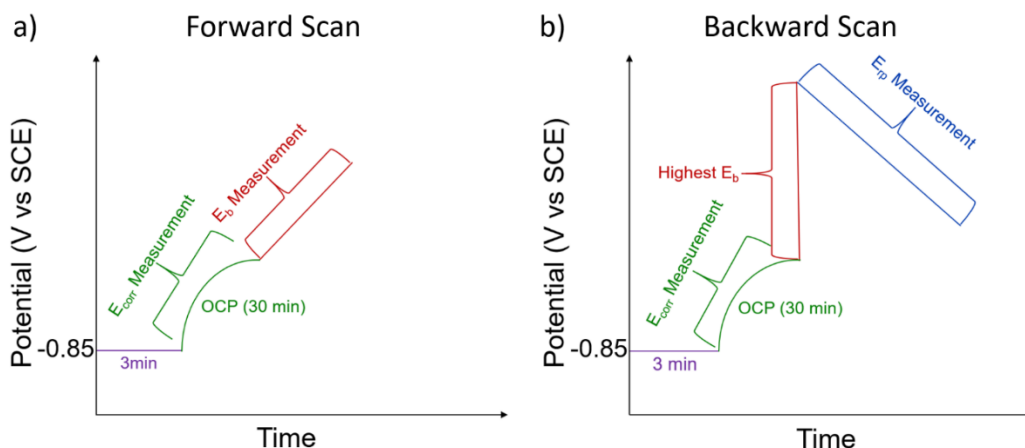
Figure 4.3: Schematic of potentiodynamic experiment a) positive-ongoing scan for measurement of E$_{corr}$ and E$_b$ b) negative-ongoing scan for measurement of E$_{rp}$.
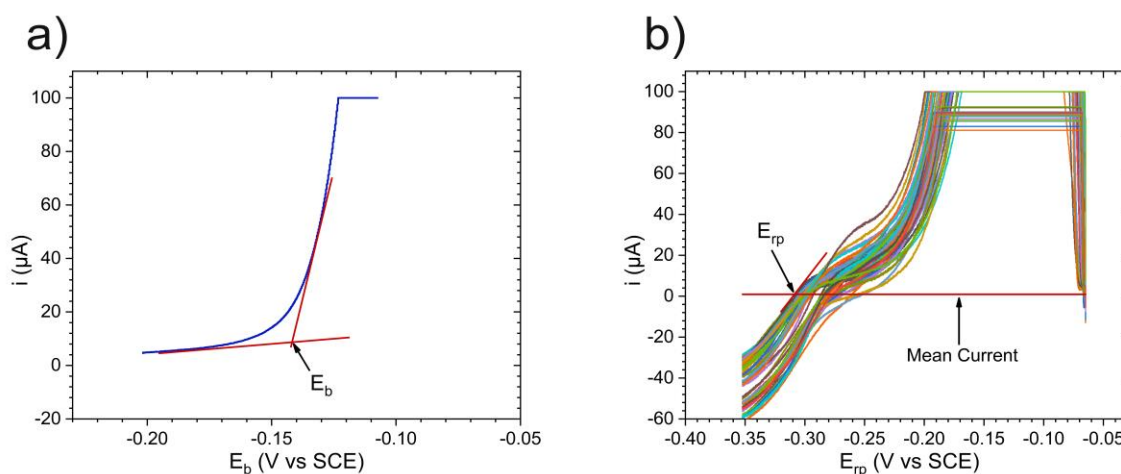
Figure 4.4: Determination of the breakdown potential of Cu from positive-going potential scans: a) one of the scans with tangents drawn to demonstrate how the breakdown potential, Eb, was determined; b) a series of negative-going "repassivation" scans that all started at E = −0.06 V vs SCE with a steep initial current rise as the electrodes immediately began to suffer pitting corrosion, followed by a flat region where the pitting current reached the maximum available from the potentiostat, followed by a declining current that allowed us to determine the repassivation potential Erp at the point where the current declined to the mean value of the passive current density (red line) measured on positive-going scans under the same exposure conditions.

4.2.4   Statistical Analysis

The group measurements of E_{corr}, E_b, and E_{rp} enabled by the multi-electrode array approach made it possible to perform statistical analyses of these parameters to estimate the pitting probability (likelihood of either $E_{corr} > E_b$ or $E_{corr} > E_{rp}$) and repassivation probability (likelihood that $E_{corr} < E_{rp}$) of Cu. A comprehensive statistical treatment process can be found in our previous paper [67].

4.3   Results and Discussion

4.3.1   Effect of Sulfate Concentration and pH on E_{corr}

Fig. 4.5 shows the E_{corr} of all electrodes measured in solutions with different $[SO_4^{2-}]$ and pH. At all concentrations of SO_4^{2-}, E_{corr} increased with time due to the formation of an oxide film on the Cu surface [4, 69]. At pH 8 (Fig. 4.5a), the average E_{corr} shifted to slightly more negative values as $[SO_4^{2-}]$ was increased up to 0.01 M, and then dropped significantly with a further increase to 0.1 M. The distribution range of E_{corr} values as expressed by the standard deviation did not change for all concentrations at pH 8 (Fig. 4.5b). There is a competition between the adsorption of OH^- and SO_4^{2-} on the oxide surface [65, 66, 70]; as a result, SO_4^{2-} interferes with oxide film formation, whilst OH^- promotes film growth. Al-Khariafi [29] discussed the competition between the adsorption of halide ions and OH^- on the copper surface and reported that halieds with a larger ionic radius yields a lower Cu dissolution rate; although, Kong [47] proposed that the ability of halied ions to polarize copper is directly proportional to the size of the ions and a larger peak current density was observed for halides with a larger radius. In our case, E_{corr} decreased with increasing $[SO_4^{2-}]$, which is in good aggrement with our observation in chloride-containing solution [67], but it is not in good agreement with the results of Ochoa et al. [71], whos howed that E_{corr} increased slightly with increasing $[SO_4^{2-}]$. The reason for this discrepancy could be that Ochoa et al. [71] did not acquire enough data to properly define the trend; however, in this study, 60 data acquired in two runs of 30 simultaneous measurements were averaged.

When the pH was increased to 9, the distribution in values of E_{corr} decreased in width with increasing $[SO_4^{2-}]$ (Fig. 4.5d) compared to the range recorded at pH 8. As a result,

there is a critical [OH$^-$] above which the distribution range of E$_{corr}$ will decrease with increasing [SO$_4^{2-}$]. The distribution of E$_{corr}$ values may affect the pitting and repassivation probabilities by changing the overlap between values of E$_{corr}$, E$_b$ and E$_{corr}$, E$_{rp}$ respectively.
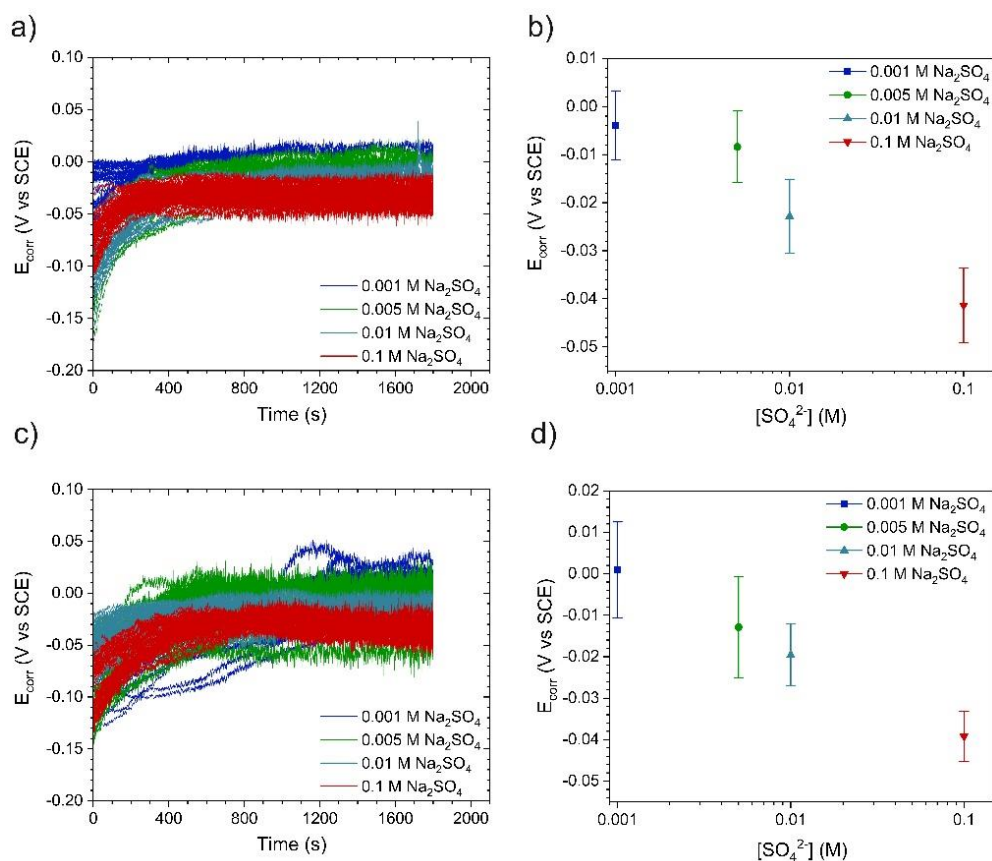
Figure 4.5: Corrosion potential of Cu electrodes; a) E$_{corr}$ of Cu in a solution containing 0.001, 0.005, 0.01, and 1 M SO$_4^{2-}$ at pH 8, b) comparison of mean and standard deviation of Cu electrodes in a solution containing 0.001, 0.005, 0.01, and 1 M SO$_4^{2-}$ at pH 8, c) E$_{corr}$ of Cu in a solution containing 0.001, 0.005, 0.01, and 1 M SO$_4^{2-}$ at pH 9, and d) comparison of mean and standard deviation of Cu electrodes in a solution containing 0.001, 0.005, 0.01, and 1 M SO$_4^{2-}$ at pH 9.

4.3.2   Effect of Sulfate Concentration and pH on E$_b$

The pitting potentials (E$_b$) measured in solutions containing different [SO$_4^{2-}$] and [OH$^-$] are plotted in Fig. 6. At both pH 8 and pH 9, E$_b$ shifted toward negative potentials with

increasing [SO$_4{}^{2-}$], indicating a decrease in the protectiveness of the film at higher [SO$_4{}^{2-}$] [72]. However, increasing the pH shifted E$_b$ to more positive values (Fig. 4.6-b, d) [18, 53, 54]. The relationship between E$_b$ and log [SO$_4{}^{2-}$] appears to be linear and can be represented by Equation 1[71, 73, 74]:

$$E_b = A - B \log[SO_4^{2-}] \qquad\qquad 1$$

With an increase in the concentration of aggressive anions up to a certain level, the adsorption of aggressive anions such as SO$_4{}^{2-}$ became more favourable than OH$^-$ adsorption, leading to a shift in E$_b$ to a more negative value. As a result, the distribution of E$_b$ would be more likely to be below the distribution of E$_{corr}$, resulting in a higher probability of passive film breakdown. Another factor that will influence the pitting probability is the distribution range of E$_b$. The distribution range of E$_b$ in sulfate-containing solutions at pH 8 did not change significantly with [SO$_4{}^{2-}$], while for pH 9 the distribution range was wide at small concentrations (0.001 M and 0.005 M) but became very narrow at higher concentrations (0.01 M and 0.1 M). These results showed that the pitting probability, as expressed by the distribution range of E$_b$, was dependent on both [SO$_4{}^{2-}$] and pH.

Based on the distribution curve of corrosion parameters, when the [SO$_4{}^{2-}$]/[OH$^-$] ratio is equal to or smaller than 500, then OH$^-$ is the dominant anion enforcing the formation of a dense passive film on the surface. As a result, it would be difficult for [SO$_4{}^{2-}$] to adsorb on the surface and promote passive film breakdown, resulting in a greater distribution range of E$_b$ (Fig. 4.6-d). On the other hand, when [SO$_4{}^{2-}$]/[OH$^-$] > 500, the distribution range of E$_b$ decreases significantly due to the increased frequency of passive film breakdown. This claim has been made by other researchers [46, 62, 75], but not justified on a statistically relevant scale.
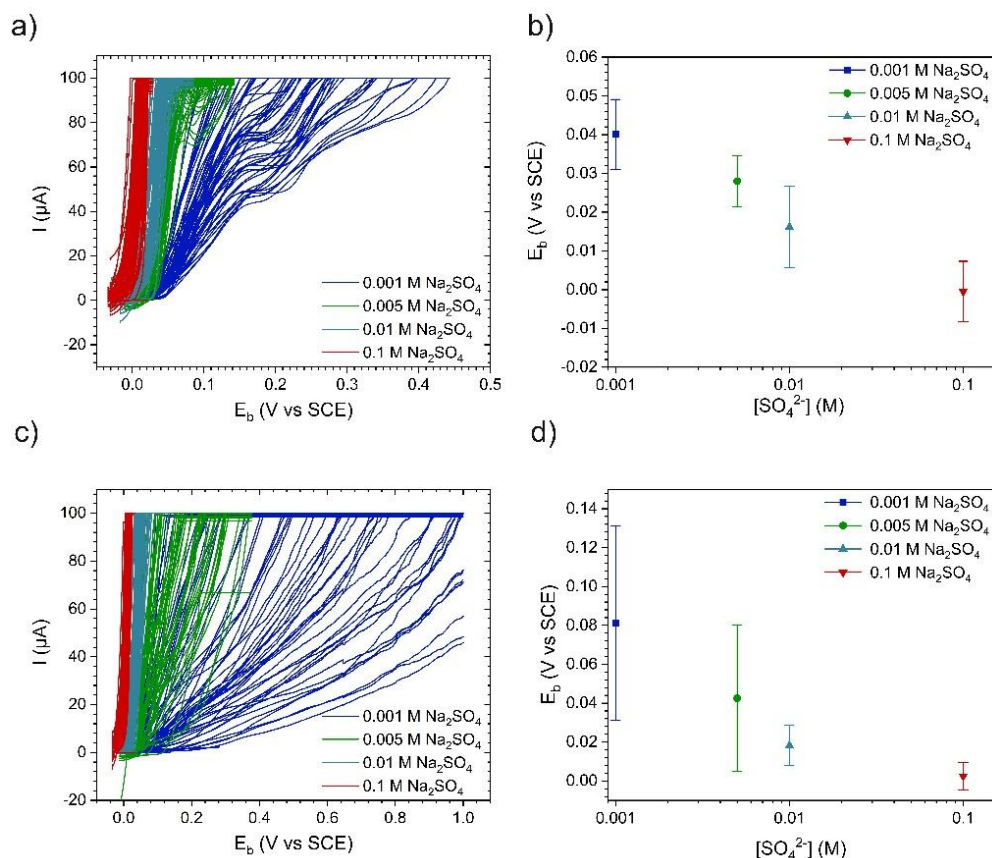
Figure 4.6: Breakdown potential of Cu electrodes; a) E_b of Cu in a solution containing 0.001, 0.005, 0.01, and 1 M SO_4^{2-} at pH 8 b) comparison of mean and standard deviation of Cu electrodes in a solution containing 0.001, 0.005, 0.01, and 1 M SO_4^{2-} at pH 8 c) E_b of Cu in a solution containing 0.001, 0.005, 0.01, and 1 M SO_4^{2-} at pH 9 d) comparison of mean and standard deviation of Cu electrodes in a solution containing 0.001, 0.005, 0.01, and 1 M SO_4^{2-} at pH 9.

4.3.3   Effect of Sulfate Concentration and pH on E_{rp}

The E_{rp} of Cu in sulfate-containing solutions at various pH values is shown in Fig. 4.7. Increasing $[SO_4^{2-}]$ shifted E_{rp} to more positive values, the opposite of our observations in chloride-containing solutions [67]. This increase with increasing $[SO_4^{2-}]$ may increase the probability to repassivate, depending on and the relative influence on the range of E_{corr}. When the distribution of E_{rp} values is located at lower potentials than that of E_{corr}, then the area of their overlap indicates the probability that repassivation might be possible (Fig.4.8). On the other hand, if the distribution of E_{rp} values is located at higher

potentials than that of E_{corr} the area of overlap indicates the probability of spontaneous pitting (Fig.4.8). It is important to note that the definition of the natural pitting probability is different than the pitting probability (distributions of E_{corr} and E_b). Pitting probability is the overlap between the distributions of E_{corr} and E_b; however, natural pitting probability is the overlap between the distributions of E_{corr} and E_{rp}, when distribution curve of E_{corr} is located on the left side of distribution curve of E_{rp} as shown in Fig. 4.8.b [51].

Many researchers [33, 53, 54] have proposed that E_{rp} is not dependent on the concentration of aggressive anions which is in good agreement with our results. Moreover, our results indicate a dependency of distribution range of E_{rp} on the $[SO_4^{2-}]$. Increasing the pH shifted the average values of E_{rp} to a more negative value in 0.001 M SO_4^{2-} but exhibited no significant effect at higher $[SO_4^{2-}]$, as shown in Fig. 4.7. Our results indicate that $[OH^-]$ strongly affects the distribution range of E_b values, whereas the distribution ranges of E_{corr} and E_{rp} were not largely affected by $[OH^-]$.
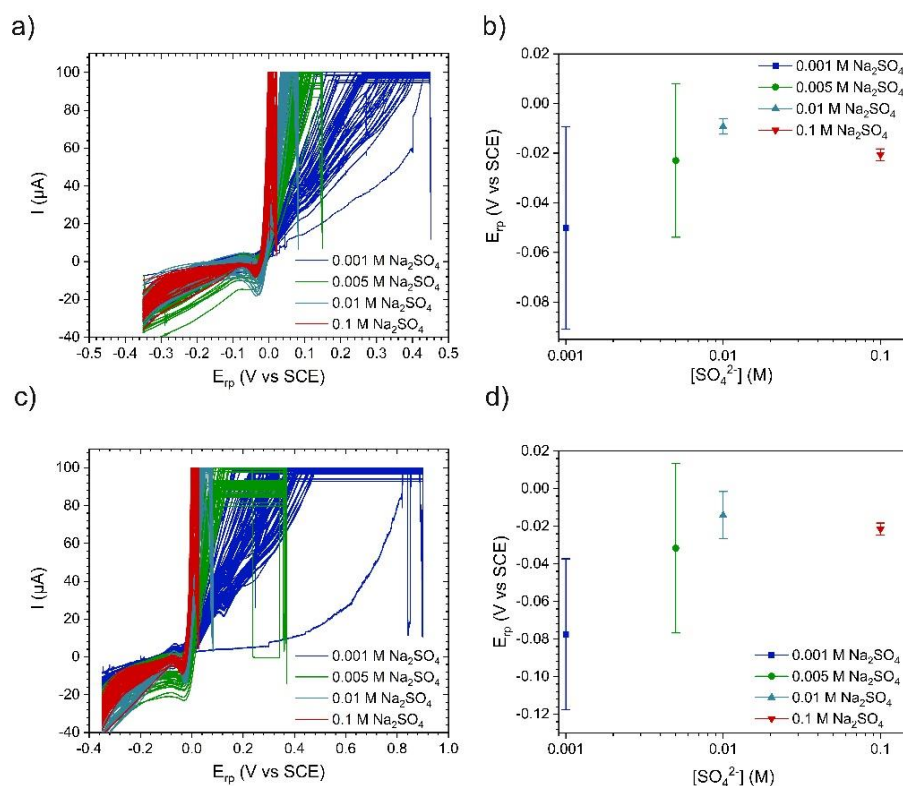
Figure 4.7: Repassivation potential of Cu electrodes; a) E_{rp} of Cu in a solution containing 0.001, 0.005, 0.01, and 1 M SO_4^{2-} at pH 8 b) comparison of mean and

standard deviation of Cu electrodes in a solution containing 0.001, 0.005, 0.01, and 1 M SO_4^{2-} at pH 8 c) E_{rp} of Cu in a solution containing 0.001, 0.005, 0.01, and 1 M SO_4^{2-} at pH 9 d) comparison of mean and standard deviation of Cu electrodes in a solution containing 0.001, 0.005, 0.01, and 1 M SO_4^{2-} at pH 9.
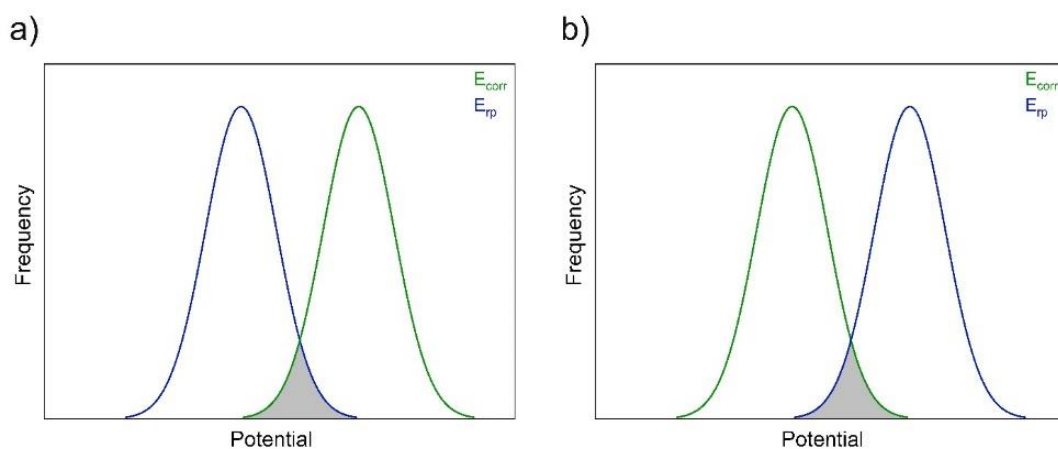
Figure 4.8: Overlap between distributions of corrosion potential and repassivation potential. probability can be measured from the overlap of distribution functions when the distribution of corrosion potentials is located to the right of the distribution of repassivation potentials. b) natural pitting probability is the overlap between the distributions of E_{corr} and E_{rp}, when distribution curve of E_{corr} is located on the left side of distribution curve of E_{rp}.

4.3.4   Effect of Bicarbonate on E_{corr}, E_b, and E_{rp}

The E_{corr} values recorded in sulfate-containing solutions with and without HCO_3^- are shown in Fig. 4.9. At both pH 8 and 9, the addition of HCO_3^- shifted E_{corr} to more positive values and increased the distribution range. The average E_b shifted to more positive values in the presence of HCO_3^- as illustrated in Fig. 4.10, indicating an increase in the stability of the passive film. The addition of HCO_3^- also increased the distribution range of values, in good agreement with the observation of Frankel et al. [46, 57, 62, 75-77] regarding the effect of passive film quality on the distribution of E_b. The pitting probability of Cu in the presence of HCO_3^- depends on the influence of HCO_3^- on E_b values and their distribution ranges.

Increasing [HCO_3^-] led to a shift in E_{rp} to more negative values and widened the distribution of values (Fig. 4.11). Both of these features could increase the probability of repassivation if the distribution curve for E_{rp} was located at potentials lower than the distribution of E_{corr} values. The mean and standard deviations in E_{corr}, E_b, and E_{rp} are plotted in Fig. 4.12 to demonstrate their relative positions on the potential scale as a function of [SO_4^{2-}] and [HCO_3^-]. The probability of film breakdown, as defined by the relative positions of the three key potentials, did not change significantly in the presence of HCO_3^-.
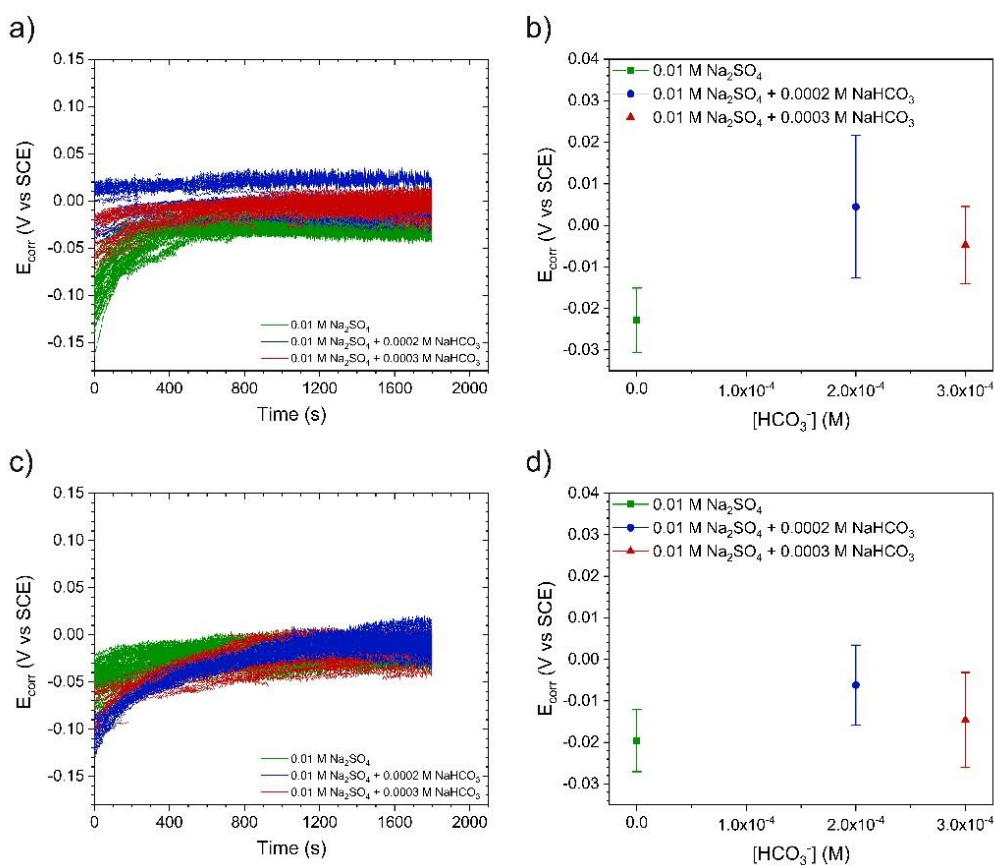
Figure 4.9: Corrosion potential of Cu electrodes in 0.01 M SO_4^{2-} solution with different [HCO_3^-]; a,c) E_{corr} values of Cu in solutions containing 0, 0.2 and 0.3 mM HCO_3^- at pH 8 and pH 9, respectively, b,d) comparison of mean and standard deviation of E_{corr} values on Cu electrodes in solutions containing 0, 0.2 and 0.3 mM HCO_3^- at pH 8 and pH 9, respectively.
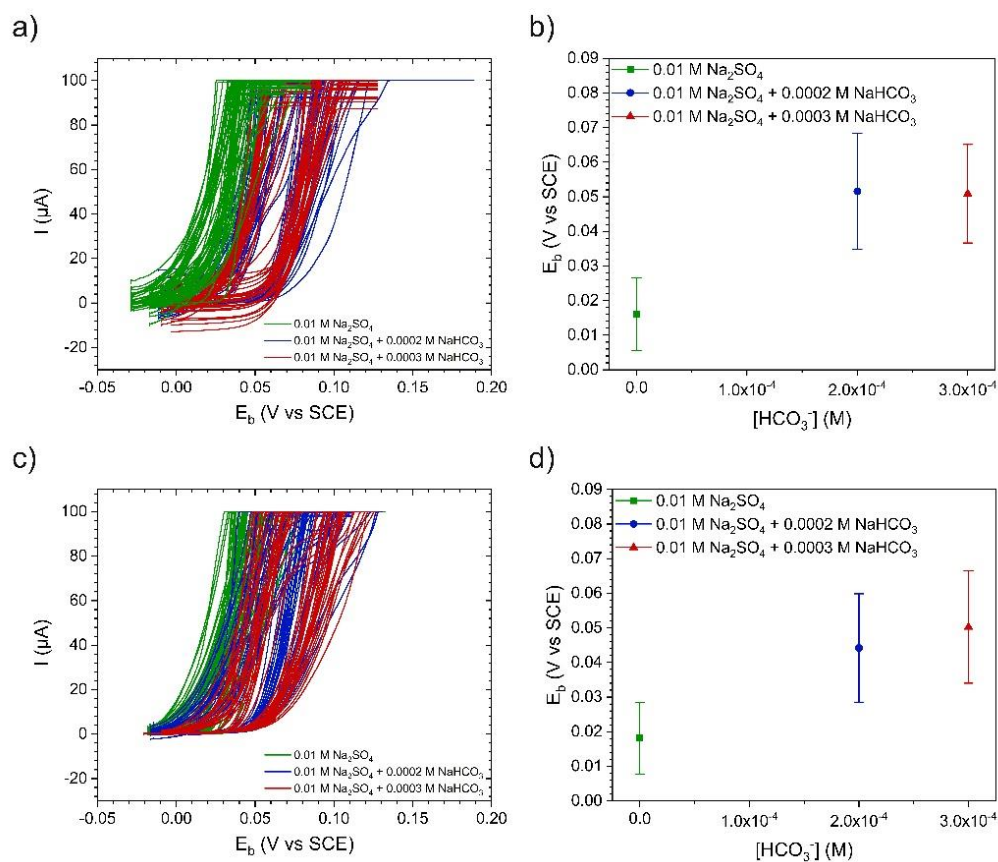
Figure 4.10: Breakdown potential of Cu electrodes in 0.01 M SO$_4^{2-}$ solution with different [HCO$_3^-$]; a,c) E$_b$ values of Cu in solutions containing 0.2 and 0.3 mM HCO$_3^-$ at pH 8 and pH 9, respectively, b,d) comparison of mean and standard deviation of E$_b$ values on Cu electrodes in solutions containing 0.2 and 0.3 mM HCO$_3^-$ at pH 8 and pH 9, respectively.
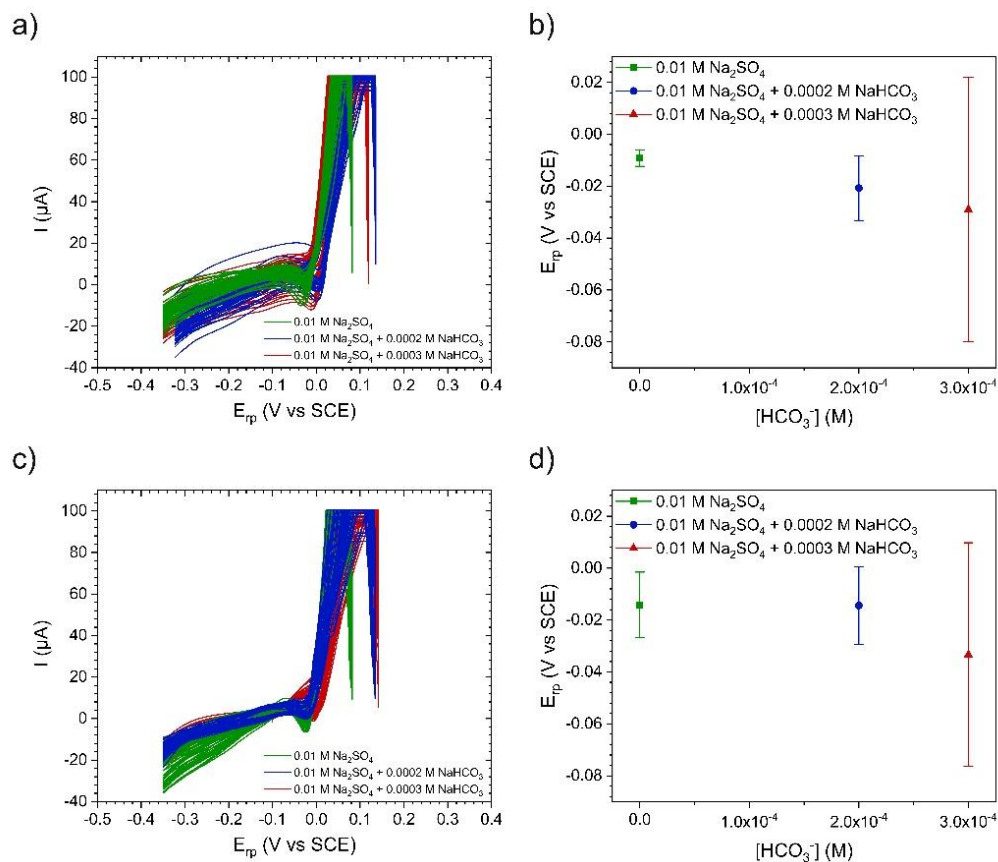
Figure 4.11: Repassivation potential of Cu electrodes in 0.01 M SO$_4^{2-}$ solution with different [HCO$_3^-$]; a,c) E$_{rp}$ values of Cu in solutions containing 0.2 and 0.3 mM HCO$_3^-$ at pH 8 and pH 9, respectively, b,d) comparison of mean and standard deviation of E$_{rp}$ values on Cu electrodes in solutions containing 0.2 and 0.3 mM HCO$_3^-$ at pH 8 and pH 9, respectively.
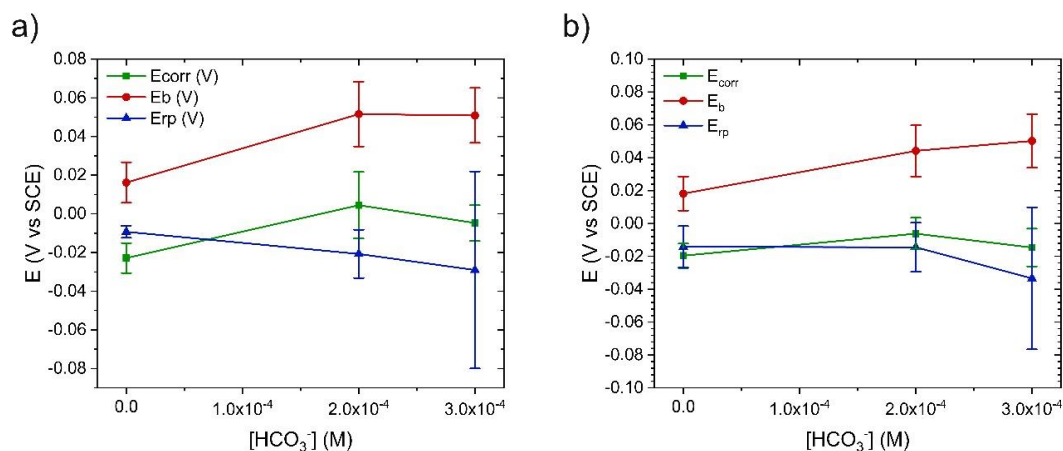
Figure 4.12: Mean and standard deviation of E_{corr}, E_b, and Erp values of Cu electrodes in 0.01 M SO_4^{2-} solution with different $[HCO_3^-]$; a) pH 8 b) pH 9. The points are the mean and the range represented by the bars is the standard deviation.

4.3.5 Statistical Analysis

4.3.5.1 Effect of Sulfate on Pitting and Repassivation Probabilities

Histograms and box plot charts of E_{corr}, E_b, and E_{rp} values measured in solutions with different $[SO_4^{2-}]$ and pH are shown in Fig. 4.13 through Fig. 4.16. The histogram and interquartile range (IQR) of E_{corr} for different $[SO_4^{2-}]$ at pH 8 indicated the same distribution for all concentrations as illustrated in Fig. 4.14 and 4.16. However, outliers were observed on the higher potential side of the IQR for 0.005 M and 0.1 M SO_4^{2-} solutions (Fig. 4.14a), which could suggest an increase in the pitting probability due to the formation of right-skewed distribution curves. In sulfate-containing solutions at pH 9, the IQR became narrower with increasing $[SO_4^{2-}]$, resulting in a narrower distribution range as shown in Fig. 4.16. Outliers were observed on the high-potential side of the distribution curve of E_{corr} in 0.001 M and 0.1 M SO_4^{2-}, which could suggest an increase in the pitting probability (i.e., increased overlap between E_{corr} and E_b) (Fig 4.16a). On the other hand, outliers were located on the low-potential side of the distribution curve of E_{corr} in 0.005 M SO_4^{2-}, which suggests a possible increase in the probability of repassivation (i.e., the overlap between E_{corr} and E_{rp}, with Erp below Ecorr) (Fig 4.16a). The distribution of E_b values did not change significantly with $[SO_4^{2-}]$ at pH 8 (Fig 4.14b). However, at pH 9, the distribution of E_b values decreased significantly in

solutions with $[SO_4^{2-}]$ higher than 0.005 M. Outliers were observed in 0.001 M and 0.005 M SO_4^{2-} at pH 9, which indicates the presence of a significant tail to the distribution curve (left-skewed) that might result in a greater overlap between E_{corr} and E_b values (Fig 4.16b). The IQR of E_{rp} decreased with increasing $[SO_4^{2-}]$ at both pH 8 and 9, indicating a narrower distribution of values at higher $[SO_4^{2-}]$ (Fig 4.14c and 4.16c). Outliers were observed at all $[SO_4^{2-}]$ except 0.001 M. These outliers suggest an increase in the probability of either repassivation or pitting, depending on the position of E_{rp} relative to E_{corr}.

The frequency plots of measured E_{corr}, E_b, and E_{rp} values were fitted with a variety of different distribution functions to determine whether any of these functions provided reasonable representations of the measured data. Some gave reasonable fits whereas others differed significantly from the measured data. In the end, five distribution functions (Normal, Log-normal, Log-logistic, Gamma, and Weibull) were selected for use in the analysis, based on the quality of f it achievable. The probability density functions (PDF) showing the overlap between E_{corr} and E_b in solutions with different $[SO_4^{2-}]$ and pH values are shown in Fig. 4.17 and Fig. 4.18. Note that the application of these statistical analyses required that all of the potential values be positive numbers, to avoid the complications of a sign change in the independent variable within the distribution range; to that end we conceived and used an artificial potential scale, designated "JSE", representing an arbitrarily chosen potential reference point selected solely to yield positive potential values for all measurements (i.e., a simple translation of all values along the potential axis to make them all have a positive sign).

The maximum pitting probability of Cu estimated in this fashion did not change significantly with increasing $[SO_4^{2-}]$ from 1 mM to 0.1 M at pH 8 and was in the range of 3.81% – 6.58% (Table. 1). The highest pitting probability was observed in 0.01 M SO_4^{2-}. An increase in $[SO_4^{2-}]$ up to 0.01 M led to an increase in pitting probability (Table. 1), a further increase in $[SO_4^{2-}]$ to 0.1 M caused the probability of pitting to decrease.

Increasing the pH from 8 to 9 shifted the critical $[SO_4^{2-}]$ to 0.005 M with the highest pitting probability of 53.26% (Table. 2), an approximately one order of magnitude

respective decrease in the critical [SO_4^{2-}] and increase in the pitting probability, demonstrating the strong effects pH has on the pitting process on Cu. A higher pH resulted in a much wider distribution of E_b values, due to the formation of a more protective passive film, which makes it more difficult for aggressive anions to diffuse into the passive film and induce film breakdown [44, 64]. There is a critical concentration (C_{crit}) above which the range of E_b values (Fig. 4.16b) decreases significantly, contributing to a lower pitting probability of Cu as shown in Table 2. Our results indicate that the reliability of predictions on the corrosion outcome for Cu under these conditions (e.g., whether pitting corrosion will occur) is dependent on acquisition of a statistically significant* number of experimental data, due to the stochastic nature of the various corrosion parameters.

_____

*In this case, statistically significant implies sufficient to clearly define a distribution function for the parameters in question.

The overlap between the PDFs of E_{corr} and E_{rp} indicates either the repassivation or pitting probability depending on the position of the E_{rp} distribution relative to that of E_{corr} (Fig. 4.19 **and** Fig. 4.20). The repassivation probability increased with increasing [SO_4^{2-}] up to 0.005 M; however, the distribution of E_{rp} shifted to higher potentials relative to E_{corr} with a further increase in [SO_4^{2-}] for both pH 8 and 9. As a result, the overlap between E_{rp} and E_{corr} will provide information about the natural pitting. It is important to note that this transition from repassivation to natural pitting is only dependent on [SO_4^{2-}] rather than pH. The greatest repassivation probabilities in sulfate-containing solutions at pH 8 and pH 9 (0.005 M) were 66.48% and 57.63%, respectively, and the highest conservative pitting probabilities (in 0.01 M sulfate solutions at pH 8 and 9) were 22.50% and 73.00%, respectively (Tables 3 and 4). Our results indicate that increasing the SO_4^{2-} up to a certain concentration increases the repassivation probability, but moves the E_{rp} distribution to the right side of the E_{corr} distribution, increasing the likelihood of pitting corrosion and decreasing the probability that the system will repassivate. Our statistical analyses proposed that deciding the best and worst corrosion environments for Cu should

be based on a number of experiments sufficient to clearly define the properties of the distribution curve, such as the type of tail, variance, etc., for each distributed parameter in the system.
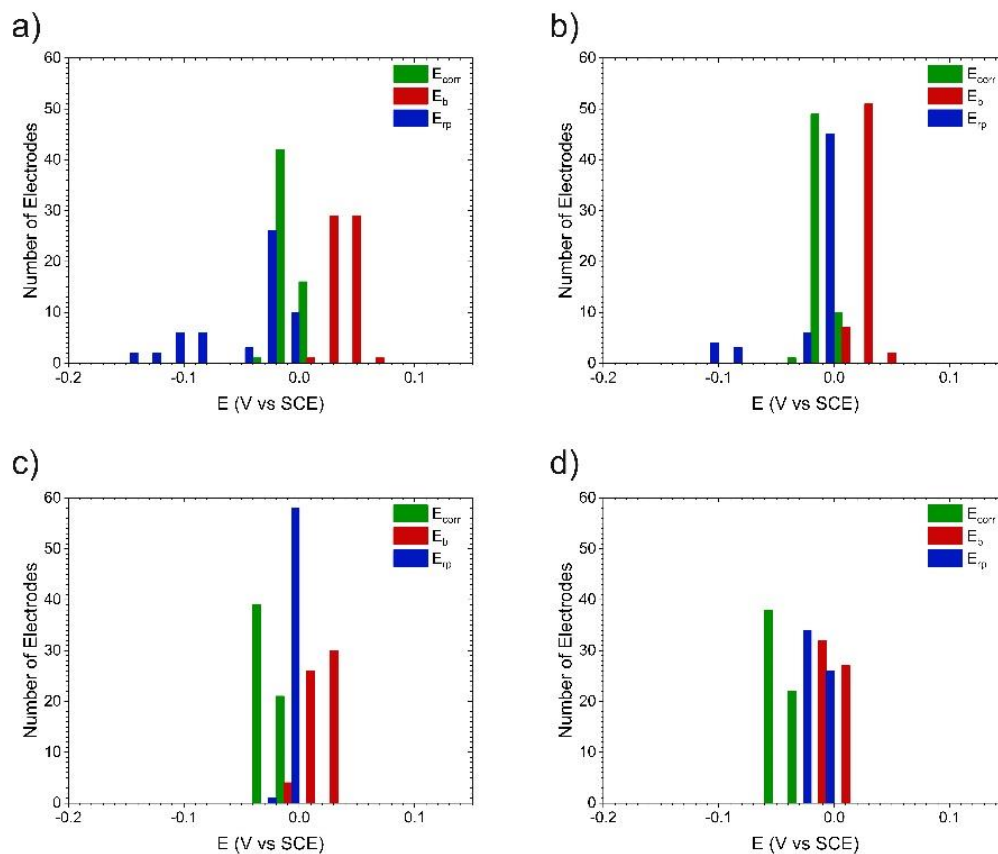
Figure 4.13: Histograms of E$_{corr}$, E$_b$, and E$_{rp}$ values with various sulfate concentrations at pH 8; a) 0.001 M b) 0.005 M c) 0.01 M d) 0.1 M.
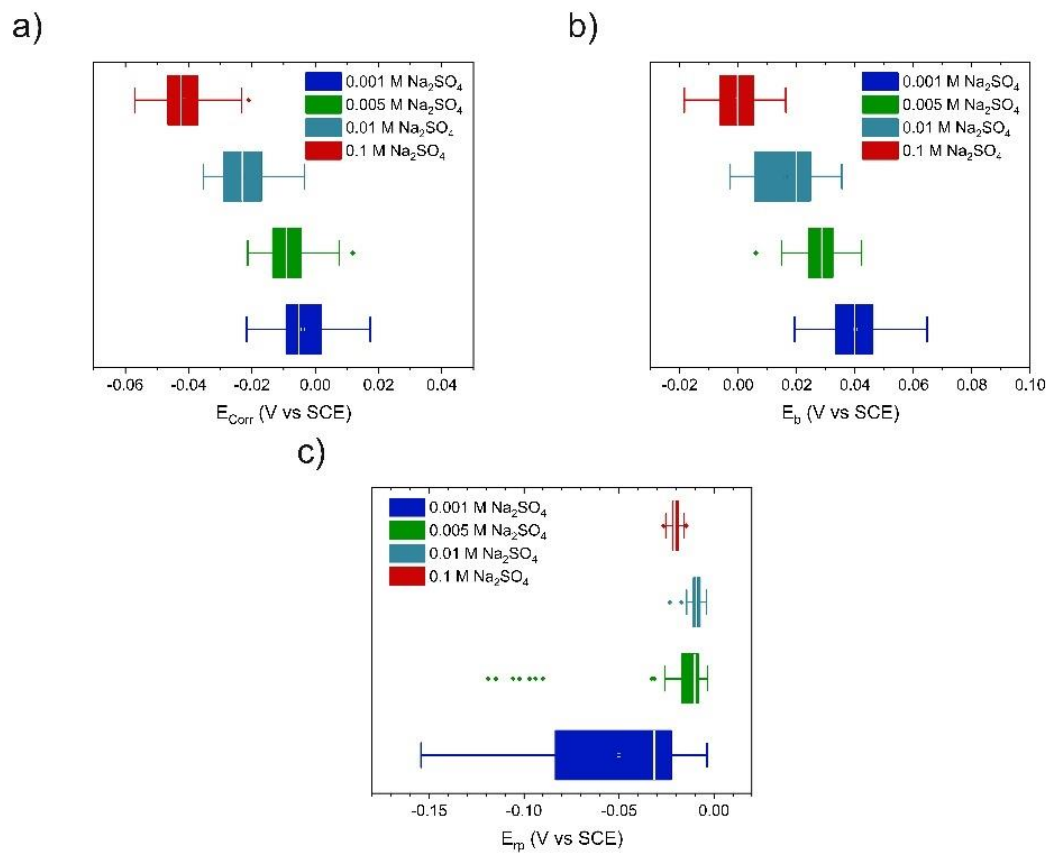
Figure 4.14: Box plot of corrosion parameters in solutions of different [SO$_4^{2-}$] at pH 8; a) E$_{corr}$, b) E$_b$, and c) E$_{rp}$.
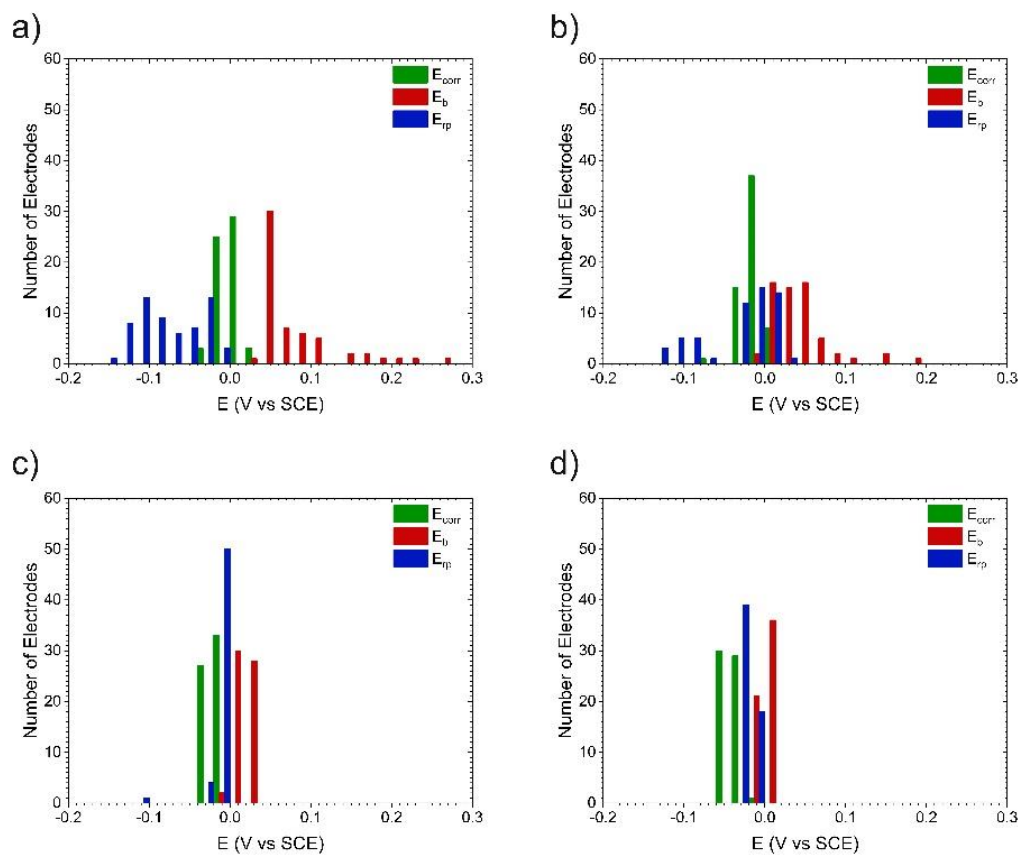
Figure 4.15: Histogram of E$_{corr}$, E$_b$, and E$_{rp}$ in solutions containing different sulfate concentrations at pH 9; a) 0.001 M b) 0.005 M c) 0.01 Md) 0.1 M.
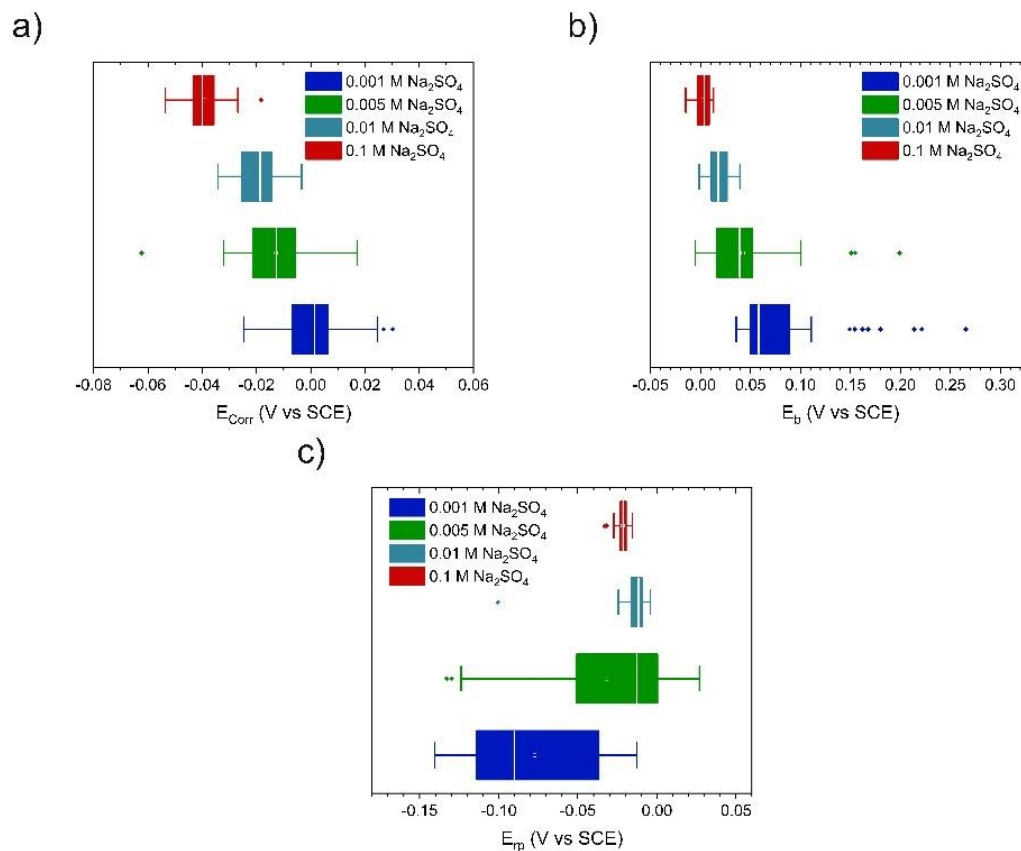
Figure 4.16: Box plot of corrosion parameters measured on Cu in solutions with different [SO$_4^{2-}$] at pH 9; a) E$_{corr}$, b) E$_b$, and c) E$_{rp}$.
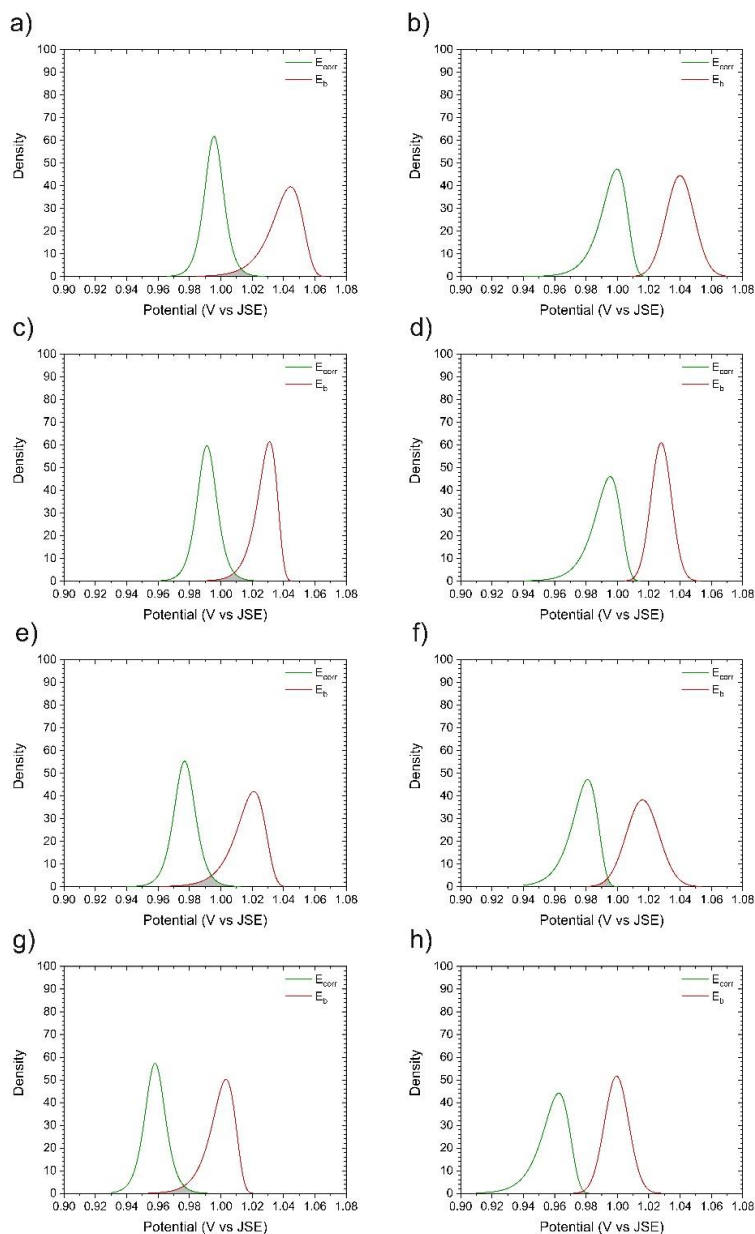
Figure 4.17: Probability distribution curves of E_corr and E_b on Cu in Na_2SO_4 solution of pH 8 at room temperature; a,b) maximum and minimum overlaps between E_corr and E_b, respectively, in 0.001 M SO_4^{2−} solution; c,d) maximum and minimum overlaps between the distribution curves for E_corr and E_b, respectively, in 0.005 M SO_4^{2−} solution; e,f) maximum and minimum overlaps between the distribution curves for E_corr and E_b, respectively, in 0.01 M SO_4^{2−} solution; g,h) maximum and minimum overlaps between the distribution curves for E_corr and E_b, respectively, in 0.1 M SO_4^{2−} solution.

Figure 4.18: Probability distribution curves of E$_{corr}$ and E$_b$ on Cu in Na$_2$SO$_4$ solution of pH 9 at room temperature; a,b) maximum and minimum overlaps between the distribution curves for E$_{corr}$ and E$_b$, respectively, in 0.001 M SO$_4^{2-}$ solution; c,d) Maximum and minimum overlaps between the distribution curves for E$_{corr}$ and E$_b$, respectively, in 0.005 M SO$_4^{2-}$ solution; e,f) maximum and minimum overlaps between the distribution curves for E$_{corr}$ and E$_b$, respectively, in 0.01 M SO$_4^{2-}$ solution; g,h) maximum and minimum overlaps between the distribution curves for E$_{corr}$ and E$_b$, respectively, in 0.1 M SO$_4^{2-}$ solution.

Table 4.1: Pitting probability (%) of Cu in sulfate-containing solutions of different concentrations at pH 8; a) 0.001 M SO$_4^{2-}$; b) 0.005 M SO$_4^{2-}$; c) 0.01 M SO$_4^{2-}$; and d) 0.1 M SO$_4^{2-}$, based on the overlap of different E$_b$ and E$_{corr}$ distribution functions, as indicated.

a)   Corrosion Potential (E$_{corr}$)

	Distribution	Log-Logistic	Gamma	Log-Normal	Normal	Weibull
	Log-Logistic	1.57	1.13	1.14	1.12	0.79
	Gamma	1.03	0.62	0.63	0.61	0.33
Breakdown Potential (E$_b$)	Log-Normal	1.01	0.61	0.62	0.60	0.32
	Normal	1.05	0.64	0.65	0.63	0.35
	Weibull	4.55	4.03	4.04	4.01	3.55

b)   Corrosion Potential (E$_{corr}$)

	Distribution	Log-Logistic	Gamma	Log-Normal	Normal	Weibull
	Log-Logistic	1.67	1.19	1.19	1.17	0.80
	Gamma	1.36	0.88	0.89	0.87	0.51
Breakdown Potential (E$_b$)	Log-Normal	1.36	0.88	0.89	0.86	0.50
	Normal	1.38	0.90	0.90	0.88	0.52
	Weibull	3.81	3.29	3.30	3.27	2.81

c) Corrosion Potential (E_{corr})

Distribution	Log-Logistic	Gamma	Log-Normal	Normal	Weibull
Log-Logistic	4.87	4.00	4.01	3.97	3.11
Gamma	3.93	3.05	3.07	3.03	2.17
Log-Normal	3.91	3.03	3.05	3.01	2.15
Normal	3.97	3.1	3.11	3.07	2.21
Weibull	6.58	5.68	5.70	5.65	4.77

Breakdown Potential (E_b)

d) Corrosion Potential (E_{corr})

Distribution	Log-Logistic	Gamma	Log-Normal	Normal	Weibull
Log-Logistic	1.82	1.37	1.38	1.36	0.96
Gamma	1.23	0.80	0.81	0.79	0.01
Log-Normal	1.22	0.80	0.80	0.78	0.01
Normal	1.25	0.82	0.83	0.81	0.46
Weibull	3.92	3.46	3.47	3.44	2.96

Breakdown Potential (E_b)

Table 4.2: Pitting probability (%) of Cu in sulfate-containing solutions of different concentrations at pH 9; a) 0.001 M SO$_4^{2-}$; b) 0.005 M SO$_4^{2-}$; c) 0.01 M SO$_4^{2-}$; and d) 0.1 M SO$_4^{2-}$, based on the overlap of different E$_b$ and E$_{corr}$ distribution functions, as indicated.

a)

Corrosion Potential (E$_{corr}$)

Distribution	Log-Logistic	Gamma	Log-Normal	Normal	Weibull
Log-Logistic	13.18	12.53	12.55	12.49	12.37
Gamma	13.95	13.26	13.28	13.22	13.01
Log-Normal	13.68	13.02	13.04	12.98	12.64
Normal	14.45	13.69	13.71	13.66	13.77
Weibull	16.56	15.53	15.54	15.53	17.80

(Breakdown Potential (E$_b$))

b)

Corrosion Potential (E$_{corr}$)

Distribution	Log-Logistic	Gamma	Log-Normal	Normal	Weibull
Log-Logistic	19.26	19.45	19.51	19.33	17.73
Gamma	48.88	50.71	50.76	50.59	53.26
Log-Normal	20.97	21.11	21.17	20.99	19.23
Normal	21.49	21.55	21.61	21.44	19.99
Weibull	22.44	22.25	22.29	22.17	23.20

(Breakdown Potential (E$_b$))

c)   Corrosion Potential (E_{corr})

	Distribution	Log-Logistic	Gamma	Log-Normal	Normal	Weibull
	Log-Logistic	5.21	4.18	4.19	4.14	2.94
	Gamma	4.23	3.20	3.22	3.17	1.99
Breakdown Potential (E_b)	Log-Normal	4.20	3.18	3.19	3.14	1.96
	Normal	4.28	3.25	3.26	3.22	2.03
	Weibull	8.19	7.08	7.10	7.05	5.74

d)   Corrosion Potential (E_{corr})

	Distribution	Log-Logistic	Gamma	Log-Normal	Normal	Weibull
	Log-Logistic	0.66	4.23×10^{-3}	4.27×10^{-3}	4.16×10^{-3}	0.33
	Gamma	0.30	3.79×10^{-4}	4.19×10^{-4}	3.07×10^{-4}	8.30×10^{-5}
Breakdown Potential (E_b)	Log-Normal	0.30	3.79×10^{-4}	4.19×10^{-4}	3.07×10^{-4}	7.14×10^{-5}
	Normal	0.31	3.79×10^{-4}	4.19×10^{-4}	3.07×10^{-4}	1.12×10^{-4}
	Weibull	1.30	1.02	1.03	1.01	0.88
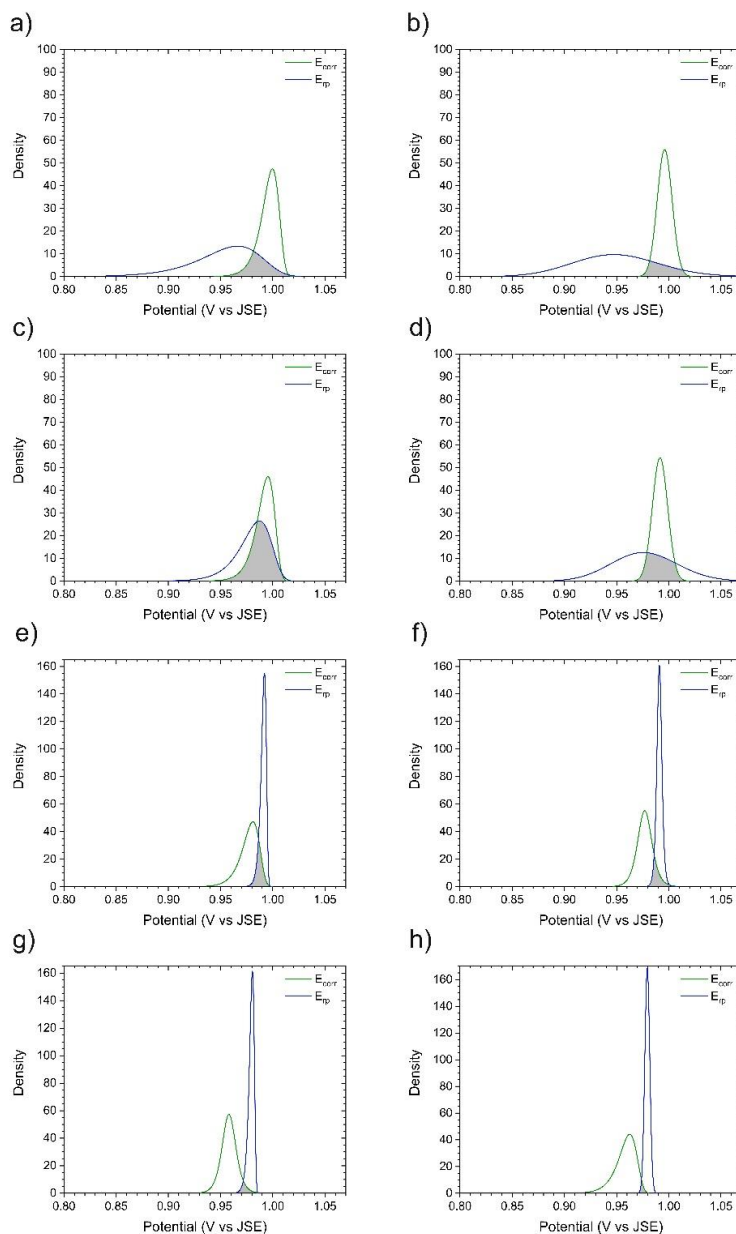
Figure 4.19: Probability distribution curves for E_{corr} and E_{rp} on Cu in Na$_2$SO$_4$ solution of pH 8 at room temperature; a,b) maximum and minimum overlaps between the distribution curves for E_{corr} and Erp respectively in 0.001 M SO$_4$$^{2-}$ solution; c,d) maximum and minimum overlaps between the distribution curves for E_{corr} and E_{rp} respectively in 0.005 M SO$_4$$^{2-}$ solution; e,f) maximum and minimum overlaps between the distribution curves for E_{corr} and E_{rp}, respectively, in 0.01 M SO$_4$$^{2-}$ solution; g,h) maximum and minimum overlaps between the distribution curves for E_{corr} and E_{rp}, respectively, in 0.1 M SO$_4$$^{2-}$ solution.

Figure 4.20: Probability distribution curves for E_{corr} and E_{rp} on Cu in Na_2SO_4 solution of pH 9 at room temperature; a,b) maximum and minimum overlaps between the distribution curves for E_{corr} and E_{rp}, respectively, in 0.001 M SO_4^{2-} solution; c,d) maximum and minimum overlaps between the distribution curves for E_{corr} and E_{rp}, respectively, in 0.005 M SO_4^{2-} solution; e,f) maximum and minimum overlaps between the distribution curves for E_{corr} and E_{rp}, respectively, in 0.01 M SO_4^{2-} solution; g,h) maximum and minimum overlaps between the distribution curves for E_{corr} and E_{rp}, respectively, in 0.1 M SO_4^{2-} solution.

Table 4.3: Repassivation and pitting probabilities (%) for Cu in sulfate-containing solutions of different concentrations at pH 8; a) 0.001 M SO$_4^{2-}$; b) 0.005 M SO$_4^{2-}$; c) 0.01 M SO$_4^{2-}$; and d) 0.1 M SO$_4^{2-}$, based on the overlap of different E$_{rp}$ and E$_{corr}$ distribution functions, as indicated.

a)   Corrosion Potential (E$_{corr}$)

Distribution	Log-Logistic	Gamma	Log-Normal	Normal	Weibull
Log-Logistic	21.01	19.67	19.65	19.70	25.71
Gamma	19.70	18.35	18.34	18.38	24.12
Log-Normal	19.53	18.18	18.17	18.21	23.91
Normal	20.03	18.69	18.67	18.72	24.54
Weibull	21.01	20.11	20.09	20.16	27.15

Repassivation Potential (E$_{rp}$)

b)   Corrosion Potential (E$_{corr}$)

Distribution	Log-Logistic	Gamma	Log-Normal	Normal	Weibull
Log-Logistic	50.76	50.18	50.16	50.23	57.67
Gamma	37.24	36.14	36.13	36.19	43.36
Log-Normal	36.81	35.70	35.68	35.74	42.89
Normal	38.09	37.03	37.01	37.07	44.29
Weibull	60.97	60.49	60.48	60.54	66.48

Repassivation Potential (E$_{rp}$)

c)

Corrosion Potential (E_{corr})

Distribution	Log-Logistic	Gamma	Log-Normal	Normal	Weibull
Log-Logistic	15.58	16.39	16.39	16.39	18.80
Gamma	17.02	18.22	18.22	18.24	21.51
Log-Normal	17.03	18.22	18.22	18.25	21.51
Normal	17.01	18.21	18.21	18.23	21.49
Weibull	18.03	19.36	19.36	19.39	22.50

Repassivation Potential (E_{rp})

d)

Corrosion Potential (E_{corr})

Distribution	Log-Logistic	Gamma	Log-Normal	Normal	Weibull
Log-Logistic	3.91	3.79	3.81	3.76	3.60
Gamma	8.74×10^{-4}	8.74×10^{-4}	8.74×10^{-4}	8.74×10^{-4}	6.60×10^{-5}
Log-Normal	9.17×10^{-4}	9.17×10^{-4}	9.17×10^{-4}	9.17×10^{-4}	6.57×10^{-5}
Normal	7.90×10^{-4}	7.90×10^{-4}	7.90×10^{-4}	7.90×10^{-4}	6.68×10^{-5}
Weibull	6.15	6.47	6.48	6.44	6.74

Repassivation Potential (E_{rp})

Table 4.4: Repassivation and pitting probabilities (%) for Cu in sulfate-containing solutions of different concentrations at pH 9; a) 0.001 M SO_4^{2-}; b) 0.005 M SO_4^{2-}; c) 0.01 M SO_4^{2-}; and d) 0.1 M SO_4^{2-}, based on the overlap of different E_{rp} and E_{corr} distribution functions, as indicated.

a) Corrosion Potential (E_{corr})

Distribution	Log-Logistic	Gamma	Log-Normal	Normal	Weibull
Log-Logistic	11.39	10.53	10.50	10.57	15.25
Gamma	11.03	10.33	10.30	10.38	15.43
Log-Normal	11.09	10.37	10.34	10.42	15.43
Normal	10.89	10.22	10.19	10.28	15.40
Weibull	9.79	9.27	9.23	9.34	15.06

Repassivation Potential (E_{rp})

b) Corrosion Potential (E_{corr})

Distribution	Log-Logistic	Gamma	Log-Normal	Normal	Weibull
Log-Logistic	43.62	45.14	45.20	45.03	47.40
Gamma	39.35	40.53	40.58	40.43	42.93
Log-Normal	38.90	40.05	40.10	39.94	42.46
Normal	40.25	41.51	41.56	41.40	43.88
Weibull	53.21	55.52	55.58	55.38	57.63

Repassivation Potential (E_{rp})

c) Corrosion Potential (E_{corr})

Distribution	Log-Logistic	Gamma	Log-Normal	Normal	Weibull
Log-Logistic	58.46	58.87	58.83	58.95	65.00
Gamma	69.37	68.53	68.51	68.57	72.78
Log-Normal	69.13	68.27	68.25	68.31	72.67
Normal	69.82	69.00	68.97	69.04	73.00
Weibull	58.22	59.66	59.61	59.77	66.53

(Left axis label: Repassivation Potential (E_{rp}))

d)   Corrosion Potential (E_{corr})

Distribution	Log-Logistic	Gamma	Log-Normal	Normal	Weibull
Log-Logistic	4.62	4.98×10^{-4}	5.38×10^{-4}	4.26×10^{-4}	6.00
Gamma	4.74	3.79×10^{-4}	4.19×10^{-4}	3.07×10^{-4}	6.62
Log-Normal	4.74	3.79×10^{-4}	4.19×10^{-4}	3.07×10^{-4}	6.61
Normal	4.74	3.79×10^{-4}	4.19×10^{-4}	3.07×10^{-4}	6.62
Weibull	6.99	7.54	7.54	7.52	9.18

(Left axis label: Repassivation Potential (E_{rp}))

4.3.5.2   Effect of Bicarbonate on the Pitting and Repassivation Probabilities

The probability density functions (PDF) for E_{corr} and E_b in 0.01 M [SO_4^{2-}] solutions with different [HCO_3^-] and pH, and the overlap between them, are shown in Fig. 25 and Fig. 26. The highest pitting probability increased from 6.58% to 21.20% with the addition of 0.0002 M HCO_3^- at pH 8 and dropped dramatically to around 4.48% when the concentration of HCO_3^- was increased to 0.0003 M (Table 5). This analysis revealed that

adding 0.0002 M [HCO_3^-] resulted in a wider distribution range of E_{corr} and E_b values (Fig. 4.23 a and b), which in turn led to a higher pitting probability. This makes the C_{crit} of anions the key parameter in determining the pitting behaviour. The distribution range of E_{corr} values in a 0.01 M SO_4^{2-} solution at pH 9 did not change significantly with the addition of 0.0002 M HCO_3^-. However, the distribution range of E_{corr} values increased with a further increase of HCO_3^- to 0.0003 M. On the other hand, the distribution range of E_b values had a small dependency on HCO_3^-. The effect of HCO_3^- on the pitting probability was found to be minimal, with the highest pitting probabilities in a 0.01 M SO_4^{2-} solution containing 0.0002 M and 0.0003 M HCO_3^- being 7.75% and 4.08%, respectively (Table 6).

Fig. 4.27 and Fig. 4.28 show the overlap between the probability density functions (PDF) of E_{corr} and E_{rp} for Cu electrodes in 0.01 M SO_4^{2-} solutions with various [HCO_3^-] and pH. The presence of HCO_3^- decreased the E_{rp} distribution range below that of E_{corr}. The addition of 0.0002 M HCO_3^- to a 0.01 M SO_4^{2-} solution at pH 8 increased the pitting probability from 22.5% to nearly 100% and decreased the probability of repassivation to 73.99% (Table 7). A further increase in [HCO_3^-] decreased the probability of repassivation to around 42.27%, indicating that the highest repassivation probability was obtained when the [HCO_3^-] = 0.0002 M. The same behaviour was observed at pH 9 (Table 8), indicating that pH (in this range) plays an insignificant role in the shift of pitting and repassivation probabilities.
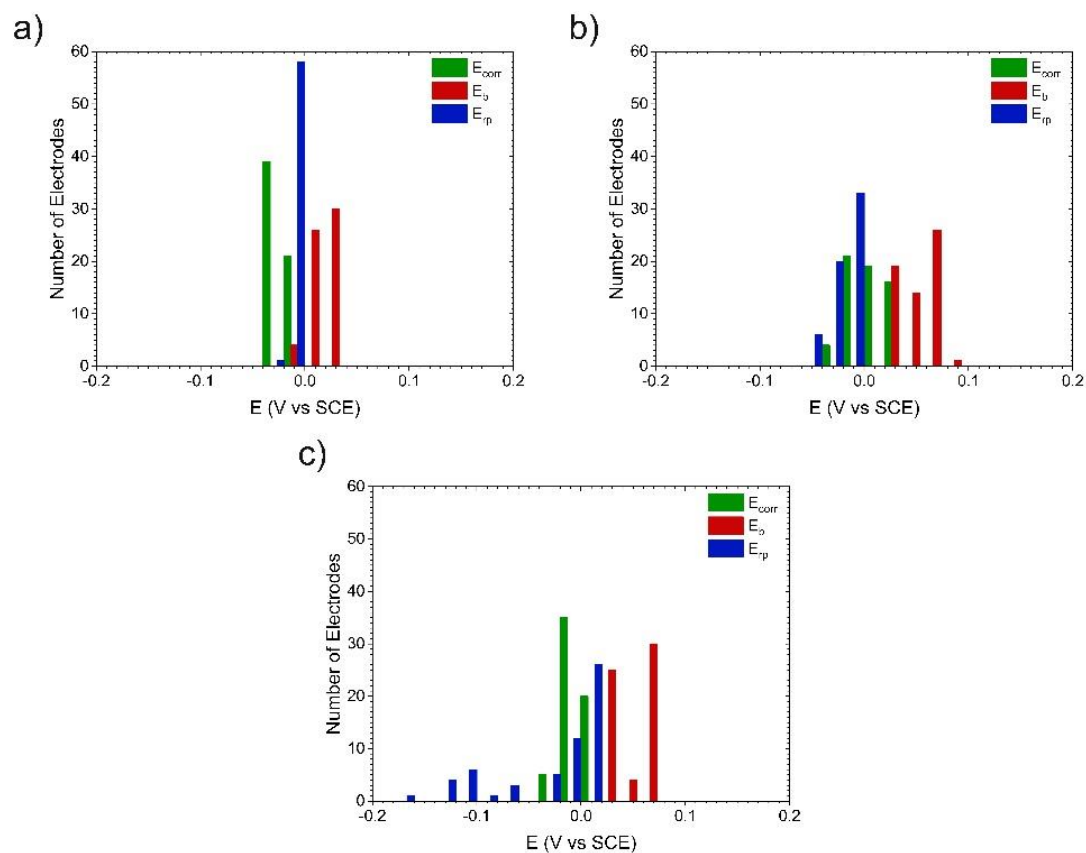
Figure 4.21: Histogram of E$_{corr}$, E$_b$, and E$_{rp}$ in sulfate-containing solutions with various bicarbonate concentrations at pH 8; a) 0.01 M SO$_4^{2-}$ b) 0.01 M SO$_4^{2-}$ + 0.0002 M HCO$_3^-$ c) 0.01 M SO$_4^{2-}$ + 0.0003 M HCO$_3^-$.
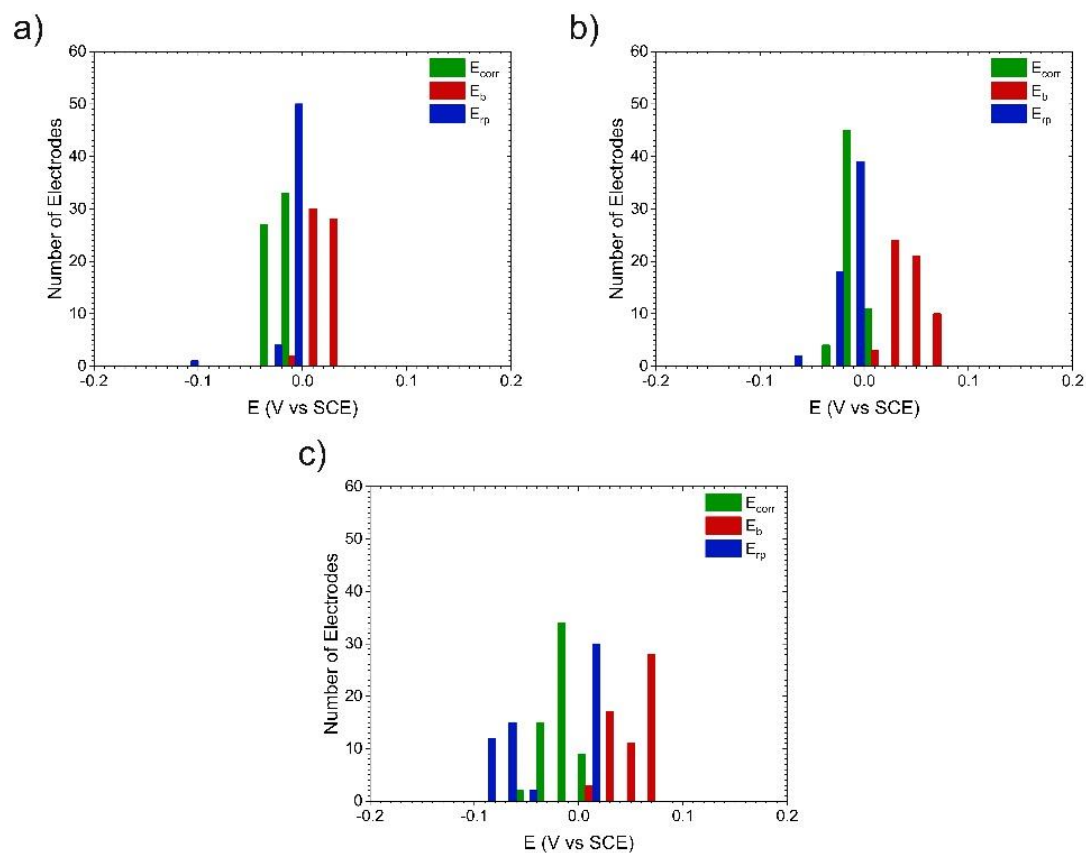
Figure 4.22: Histogram of E$_{corr}$, E$_b$, and E$_{rp}$ in sulfate-containing solutions with various bicarbonate concentrations at pH 9; a) 0.01 M SO$_4^{2-}$ b) 0.01 M SO$_4^{2-}$ + 0.0002 M HCO$_3^-$ c) 0.01 M SO$_4^{2-}$ + 0.0003 M HCO$_3^-$.
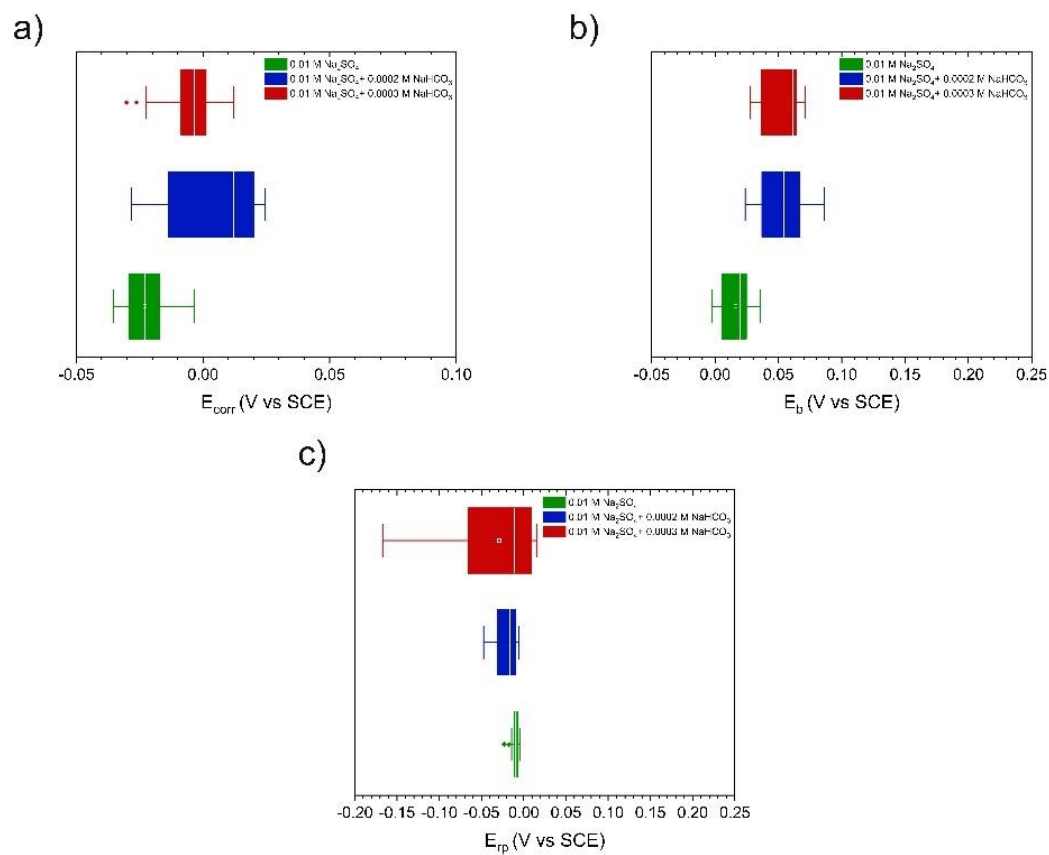
Figure 4.23: Box plot of corrosion parameters measured on Cu in sulfate-containing solutions with various [HCO$_3^-$] at pH 8; a) E$_{corr}$; b) E$_b$; and c) E$_{rp}$.
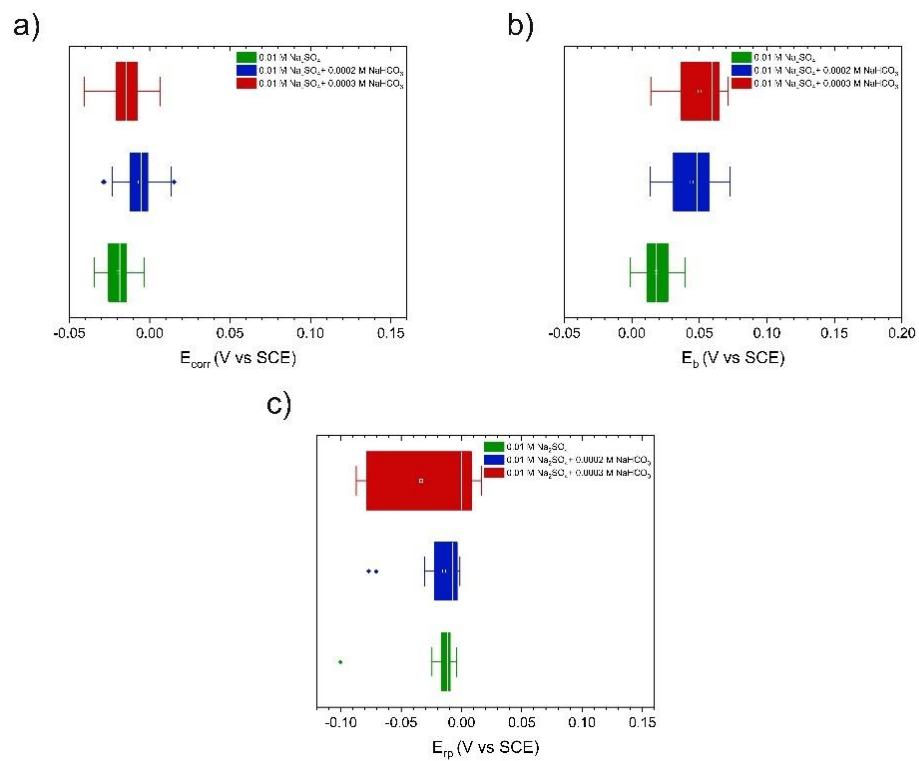
Figure 4.24: Box plot of corrosion parameters measured on Cu in sulfate-containing solutions with various [HCO$_3^-$] at pH 9; a) E$_{corr}$; b) E$_b$; and c) E$_{rp}$.
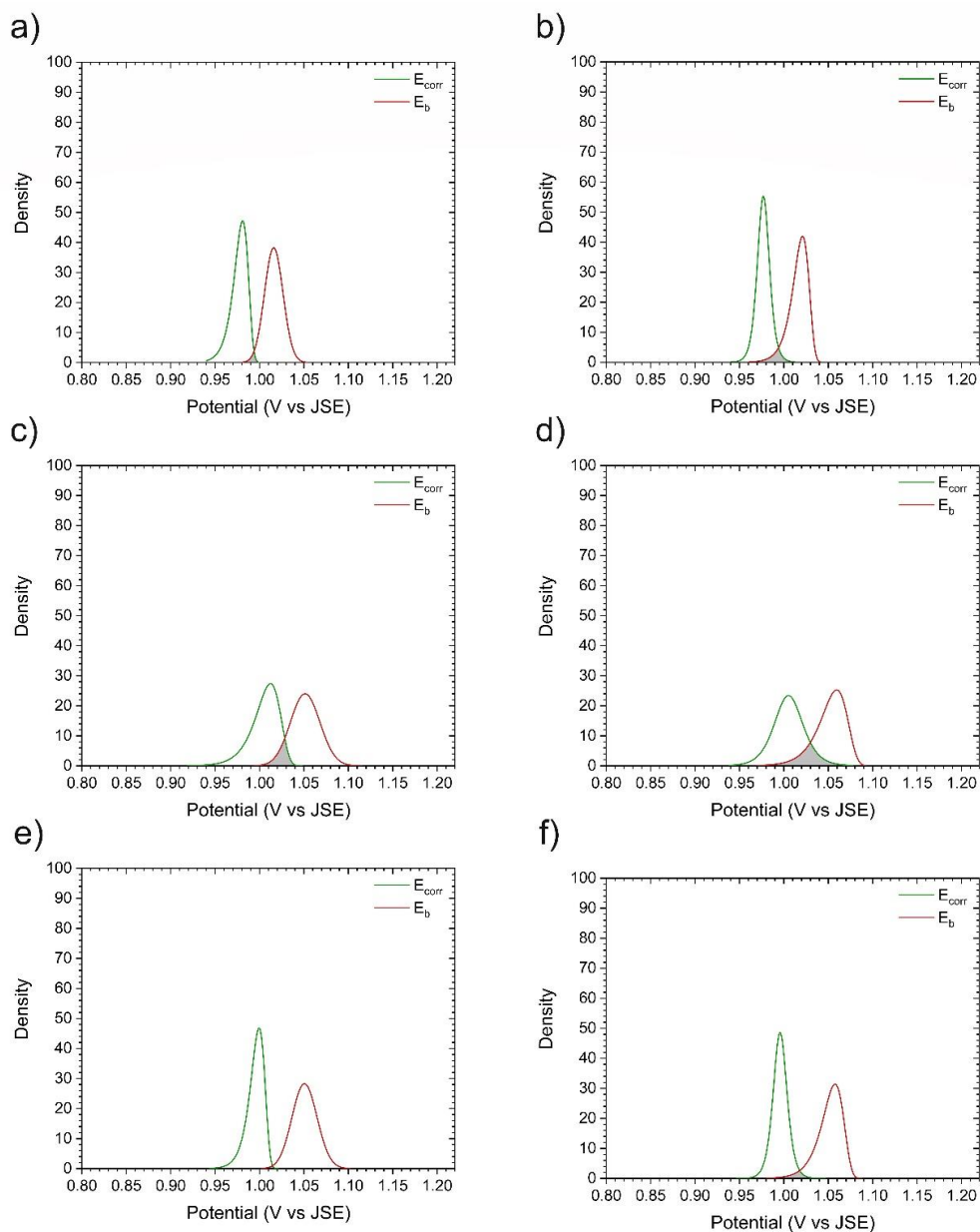
Figure 4.25: Probability distribution curves for E_{corr} and E_b on Cu in Na_2SO_4 solutions with various $[HCO_3^-]$ at pH 8 and room temperature; a,b) maximum and minimum overlaps between the distribution curves for E_{corr} and E_b, respectively, in 0.01 M SO_4^{2-} solution; c,d) maximum and minimum overlaps between the distribution curves for E_{corr} and E_b, respectively, in 0.01 M SO_4^{2-}+0.0002 M HCO_3^- solution; e,f) maximum and minimum overlaps between the distribution curves for E_{corr} and E_b, respectively, in 0.01 M SO_4^{2-}+0.0003 M HCO_3^- solution.

Figure 4.26: Probability distribution curves for E_{corr} and E_b on Cu in Na₂SO₄ solutions with various [HCO₃⁻] at pH 9 and room temperature; a,b) maximum and minimum overlaps between the distribution curves for E_{corr} and E_b, respectively, in 0.01 M SO₄²⁻ solution; c,d) maximum and minimum overlaps between the distribution curves for E_{corr} and E_b, respectively, in 0.01 M SO₄²⁻+0.0002 M HCO₃⁻ solution; e,f) maximum and minimum overlaps between the distribution curves for E_{corr} and E_b, respectively, in 0.01 M SO₄²⁻+0.0003 M HCO₃⁻ solution.

Table 4.5: Pitting probability (%) for Cu in 0.01 M SO$_4^{2-}$ solution with various [HCO$_3^-$] at pH 8; a) 0.0002 M HCO$_3^-$; and b) 0.0003 M HCO$_3^-$, based on the overlap of different E$_b$ and E$_{corr}$ distribution functions, as indicated.

a) Corrosion Potential (E$_{corr}$)

Distribution	Log-Logistic	Gamma	Log-Normal	Normal	Weibull
Log-Logistic	19.6	17.12	17.18	16.99	12.89
Gamma	18.72	16.24	16.30	16.12	12.04
Log-Normal	18.68	16.21	16.27	16.09	21.20
Normal	18.69	16.30	16.36	16.18	12.10
Weibull	21.20	18.76	18.82	18.63	14.54

Breakdown Potential (E$_b$)

b) Corrosion Potential (E$_{corr}$)

Distribution	Log-Logistic	Gamma	Log-Normal	Normal	Weibull
Log-Logistic	3.73	3.05	3.07	3.00	1.71
Gamma	2.28	1.64	1.66	1.61	0.60
Log-Normal	2.25	1.62	1.63	1.58	0.58
Normal	2.33	1.70	1.71	1.66	0.63
Weibull	4.48	3.78	3.80	3.73	2.39

Breakdown Potential (E$_b$)

Table 4.6: Pitting probability (%) for Cu in 0.01 M SO$_4^{2-}$ solution with various [HCO$_3^-$] at pH 9; a) 0.0002 M HCO$_3^-$; and b) 0.0003 M HCO$_3^-$, based on the overlap of different E$_b$ and E$_{corr}$ distribution functions, as indicated.

a)

Corrosion Potential (E$_{corr}$)

Distribution	Log-Logistic	Gamma	Log-Normal	Normal	Weibull
Log-Logistic	5.98	5.53	5.55	5.49	4.56
Gamma	4.68	4.24	4.26	4.19	3.27
Log-Normal	4.64	4.20	4.22	4.16	3.23
Normal	4.76	4.31	4.34	4.27	3.35
Weibull	7.75	7.27	7.29	7.23	6.35

Breakdown Potential (E$_b$)

b)

Corrosion Potential (E$_{corr}$)

Distribution	Log-Logistic	Gamma	Log-Normal	Normal	Weibull
Log-Logistic	3.21	2.74	2.77	2.69	1.59
Gamma	2.25	1.78	1.81	1.74	0.76
Log-Normal	2.22	1.76	1.79	1.71	0.30
Normal	2.30	1.83	1.86	1.79	0.80
Weibull	4.08	3.60	3.63	3.55	2.36

Breakdown Potential (E$_b$)
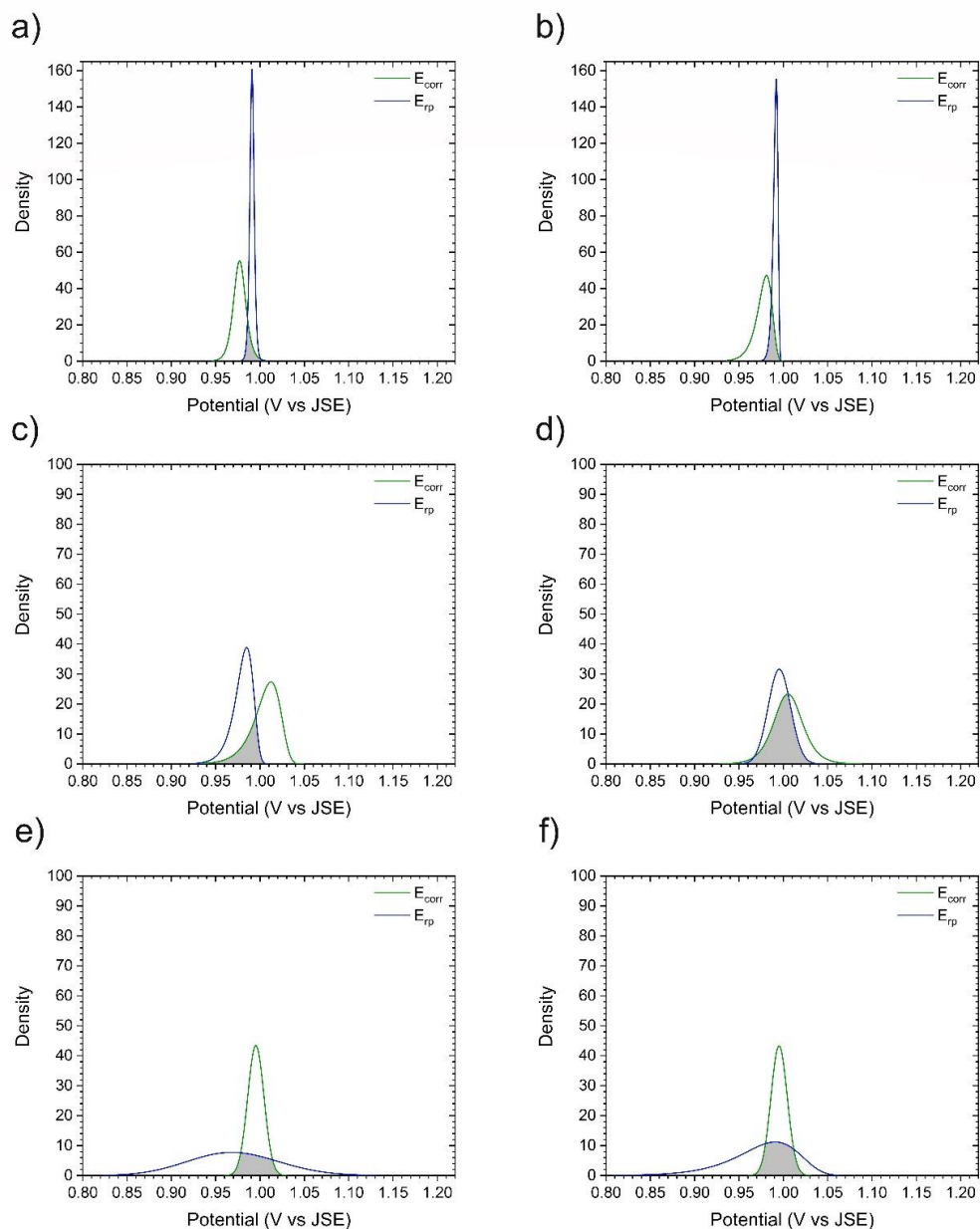
Figure 4.27: Probability distribution curves for E_{corr} and E_{rp} on Cu in Na_2SO_4 solution with various $[HCO_3^-]$ at pH 8 and room temperature; a,b) maximum and minimum overlaps between the distribution curves for E_{corr} and E_{rp}, respectively, in 0.01 M SO_4^{2-} solution; c,d) maximum and minimum overlaps between the distribution curves for E_{corr} and E_{rp}, respectively, in 0.01 M SO_4^{2-}+0.0002 M HCO_3^- solution; and e,f) maximum and minimum overlaps between the distribution curves for E_{corr} and E_{rp}, respectively, in 0.01 M SO_4^{2-}+0.0003 M HCO_3^- solution.

Figure 4.28: Probability distribution curves for E_{corr} and E_{rp} on Cu in Na$_2$SO$_4$ solution with various [HCO$_3^-$] at pH 9 and room temperature; a,b) maximum and minimum overlaps between the distribution curves for E_{corr} and E_{rp}, respectively, in 0.01 M SO$_4^{2-}$ solution; c,d) maximum and minimum overlaps between the distribution curves for E_{corr} and E_{rp}, respectively, in 0.01 M SO$_4^{2-}$+0.0002 M HCO$_3^-$ solution; and e,f) maximum and minimum overlaps between the distribution curves for E_{corr} and E_{rp}, respectively, in 0.01 M SO$_4^{2-}$+0.0003 M HCO$_3^-$ solution.

Table 4.7: Repassivation probability (%) of Cu in sulfate-containing solutions of different concentrations at pH 8; a) 0.0002 M HCO$_3^-$; and b) 0.0003 M HCO$_3^-$, based on the overlap of different E$_{rp}$ and E$_{corr}$ distribution functions, as indicated.

a) Corrosion Potential (E$_{corr}$)

Distribution	Log-Logistic	Gamma	Log-Normal	Normal	Weibull
Log-Logistic	39.34	40.74	40.81	40.61	35.85
Gamma	70.37	73.85	73.99	73.58	64.17
Log-Normal	37.13	38.63	38.70	38.50	33.54
Normal	37.02	38.52	38.59	29.96	33.41
Weibull	33.00	34.66	34.74	34.50	29.20

Repassivation Potential (E$_{rp}$)

b) Corrosion Potential (E$_{corr}$)

Distribution	Log-Logistic	Gamma	Log-Normal	Normal	Weibull
Log-Logistic	33.34	32.93	32.95	32.88	33.39
Gamma	29.56	28.96	28.98	28.92	29.61
Log-Normal	35.84	35.97	35.98	35.92	36.49
Normal	30.44	29.88	29.89	29.83	30.48
Weibull	42.24	42.25	42.27	42.18	42.17

Repassivation Potential (E$_{rp}$)

Table 4.8: Repassivation probability (%) of Cu in sulfate-containing solutions of different concentrations at pH 9; a) 0.0002 M HCO$_3^-$; and b) 0.0003 M HCO$_3^-$, based on the overlap of different E$_{rp}$ and E$_{corr}$ distribution functions, as indicated.

a)

Corrosion Potential (E$_{corr}$)

	Distribution	Log-Logistic	Gamma	Log-Normal	Normal	Weibull
Repassivation Potential (E$_{rp}$)	Log-Logistic	76.42	74.16	74.20	74.07	65.49
	Gamma	66.69	67.83	67.85	67.78	69.24
	Log-Normal	66.46	67.60	67.62	67.55	69.07
	Normal	67.15	68.27	68.29	68.22	69.57
	Weibull	75.76	76.90	76.96	76.96	72.37

b)

Corrosion Potential (E$_{corr}$)

	Distribution	Log-Logistic	Gamma	Log-Normal	Normal	Weibull
Repassivation Potential (E$_{rp}$)	Log-Logistic	38.00	38.50	38.53	38.45	40.03
	Gamma	39.41	40.01	40.04	39.96	41.73
	Log-Normal	39.13	39.72	39.75	39.67	41.45
	Normal	39.95	40.58	40.62	40.53	42.28
	Weibull	45.78	46.77	46.81	46.71	48.35

4.4 Conclusions

Potentiodynamic experiments to determine E_{corr}, E_b and E_{rp} were performed, and statistical analyses of the values were obtained, to investigate the pitting and repassivation probabilities of Cu in unary (SO_4^{2-}) and binary ($SO_4^{2-} + HCO_3^-$) solutions. We determined that E_{corr} values decreased with increasing $[SO_4^{2-}]$, due to the higher solubility of Cu oxides. The distribution range of E_{corr} decreased with increasing pH and $[SO_4^{2-}]$, indicating a lower pitting probability. Also, E_b shifted to more positive values with increasing pH. These observations indicate a relationship between the distribution range of E_b, $[SO_4^{2-}]$, the pH, and passive film breakdown. Our statistical analyses showed a dependency of E_{rp} on $[SO_4^{2-}]$. The critical $[SO_4^{2-}]$ decreased and the pitting probability increased with an increase in pH. The addition of HCO_3^- led to an improvement in the resistance to pitting corrosion, as indicated by a shift in E_b to more positive potentials compared to E_b in the same solution without HCO_3^-. The addition of HCO_3^- to a sulfate-containing solution contributed to a negative shift in E_{rp} values.

4.5 Acknowledgment

4.6   References

[1] D.S. Hall, M. Behazin, J.W. Binns, P.G. Keech, An evaluation of corrosion processes affecting copper-coated nuclear waste containers in a deep geological repository, Progress in Materials Science, 118 (2021).

[2] Electric power, annual generation by class of producer, Statistics Canada, Statistics Canada, 2020.

[3] D.S. Hall, P.G. Keech, An overview of the Canadian corrosion program for the long-term management of nuclear waste, Corrosion Engineering, Science and Technology, 52 (2017) 2-5.

[4] T. Standish, J. Chen, R. Jacklin, P. Jakupi, S. Ramamurthy, D. Zagidulin, P. Keech, D. Shoesmith, Corrosion of copper-coated steel high level nuclear waste containers under permanent disposal conditions, Electrochimica Acta, 211 (2016) 331-342.

[5] C.H. Boyle, S.A. Meguid, Mechanical performance of integrally bonded copper coatings for the long term disposal of used nuclear fuel, Nuclear Engineering and Design, 293 (2015) 403-412.

[6] P.G. Keech, P. Vo, S. Ramamurthy, J. Chen, R. Jacklin, D.W. Shoesmith, Design and development of copper coatings for long term storage of used nuclear fuel, Corrosion Engineering, Science and Technology, 49 (2014) 425-430.

[7] J.R. Scully, M. Edwards, Review of the NWMO copper corrosion allowance, Nuclear Waste Management Organization, 2013.

[8] G.M. Kwong, Status of corrosion studies for copper used fuel containers under low salinity conditions, NWMO, Nuclear Waste Mangemenrt Organization, 2011.

[9] G.S. Frankel, N. Sridhar, Understanding localized corrosion, Materials Today, 11 (2008) 38-44.

[10] R.C. Newman, 2001 W.R. Whitney award lecture- understanding the corrosion of stainless steel, Corrosion, 57 (2001) 1030-1041.

[11] N.J. Laycock, M.H. Moayed, R.C. Newman, Metastable pitting and the critical pitting temperature, Journal of the Electrochemical Society, 145 (1998) 2622-2628.

[12] G.S. Frankel, Pitting corrosion of metals: A review of the critical factors, Journal of Electrochemical Society, 145 (1998) 2186-2198.

[13] V.M. Salinas-Bravo, R.C. Newman, An alternative method to determine critical pitting temperature of stainless steels in ferric chloride solution, Corrosion Science, 36 (1994) 66-77.

[14] S.T. Pride, J.R. Scully, J.L. Hudson, Metastable pitting of aluminum and criteria for the transition to stable pit growth, Journal of the Electrochemical Society, 141 (1994) 3028-3040.

[15] P.C. Pistorius, G.T. Burstein, Metastable pitting corrosion of stainless steel and the transition to stability, Royal Society London, 341 (1992) 531-559.

[16] G.S. Frankel, L. Stockert, F. Hunkeler, H. Boehni, Metastable pitting of stainless steel, Corrosion, 43 (1987) 429-436.

[17] G.T. Gaudet, W.T. Mo, T.A. Hatton, J.W. Tester, J. Tilly, H.S. Isaacs, R.C. Newman, Mass transfer and electrochemical kinetic interactions in localized pitting corrosion, AlChE Journal, 32 (1986) 949-958.

[18] J.R. Galvele, Transport processes and the mechanism of pitting of metals, Journal of the Electrochemical Society, 123 (1976) 464-474.

[19] E. Martinez-Lombardia, Y. Gonzalez-Garcia, L. Lapeire, I. De Graeve, K. Verbeken, L. Kestens, J.M.C. Mol, H. Terryn, Scanning electrochemical microscopy to study the effect of crystallographic orientation on the electrochemical activity of pure copper, Electrochimica Acta, 116 (2014) 89-96.

[20] A. Naseer, A.Y. Khan, A study of growth and breakdown of passive film on copper surface by electrochemical impedance spectroscopy, Turkish Journal of Chemistry, 33 (2009) 739 - 750.

[21] K.A. Lill, A.W. Hassel, G. Frommeyer, M. Stratmann, Scanning droplet cell investigations on single grains of a FeAlCr light weight ferritic steel, Electrochimica Acta, 51 (2005) 978-983.

[22] J. Kunze, V. Maurice, L.H. Klein, H.-H. Strehblow, P. Marcus, In situ STM study of the duplex passive films formed on Cu(111) and Cu(001) in 0.1 M NaOH, Corrosion Science, 46 (2004) 245-264.

[23] C.J. Park, M.M. Lohrengel, T. Hamelmann, M. Pilaski, H.S. Kwon, Grain-dependent passivation of surfaces of polycrystalline zinc, Electrochimica Acta, 47 (2002) 3395-3399.

[24] M. Drogowska, L. Brossard, H. Menard, Comparative study of copper behaviour in bicarbonate and phosphate aqueous solutions and effect of chloride ions, Journal of Apllied Electrochemistry, 24 (1994).

[25] M.R.G.d. Chialvo, J.O. Zerbino, S.L. Marchiano, Correlation of electrochemical and ellipsometric data in relation to the kinetics and mechanism of Cu2O electroformation in alkaline solutions, Journal of Apllied Electrochemistry, 16 (1986) 517-526.

[26] S.B. Adeloju, H.C. Hughes, The corrosion of copper pipes in high chloride-low carbonate mains water, Corrosion Science, 26 (1986) 851-870.

[27] M.R.G.D. Chialvo, R.C. Salvarezza, D.V. Moll, A.J. Arvia, Kinetics of passivation and pitting corrosion of polycrystalline copper in borate buffer solutions containing sodium chloride., Electrochimica Acta, 30 (1985) 1501–1511.

[28] M.R.G.d. Chialvo, A.J. Arvia, The electrochemical behaviour of copper in alkaline solutions containing sodium sulphide, Journal of Apllied Electrochemistry, 15 (1985) 685-696.

[29] F.M. Al-Kharafi, Y.A. El-Tantawy, Passivation of copper: Role of some anions in the mechanism of film formation and breakdown, Corrosion Science, 22 (1982) 1-12.

[30] V. Ashworth, D. Fairhurst, The anodic formation of Cu2O in alkaline solutions, Journal of the Electrochemical Society, 124 (1977) 506-517.

[31] D.W. Shoesmith, T.E. Rummery, D. Owen, W. Lee, Anodic oxidation of copper in alkaline solutions- nucleation and growth of cupric hydroxide films, Journal of the Electrochemical Society, 123 (1976) 790-799.

[32] J. Ambrose, R.G. Barradas, D.W. Shoesmith, Investigation of copper in aqueous alkaline solutions by cycling voltammetry, Electroanalytical Chemistry and Interfacial Electrochemistry, 47 (1973) 47-64.

[33] I. Milosev, M. Metikos-Hukovic, M. Drogowska, H. Menard, Breakdown of passive film on copper in bicarbonate solutions containing sulfate ions, Journal of the Electrochemical Society, 139 (1992) 2409-2418.

[34] B. Miller, Split-Ring disk study of the anodic processes at a copper electrode in alkaline solution, Journal of Electrochemical Society, 116 (1969).

[35] H. Cong, J.R. Scully, Use of coupled multielectrode arrays to elucidate the pH dependence of copper pitting in potable water, Journal of The Electrochemical Society, 157 (2010) 36 - 46.

[36] H.D. Speckmann, M.M. Lohrengel, J.W. Schultze, H.H. Strehblow, The growth and reduction of duplex oxide films on copper, Ber. Bunsenges. Phys. Chem, 89 (1985) 392-402.

[37] J. Ambrose, R.G. Barradas, D.W. Shoesmith, Rotating copper disk electrode studies of the mechanism of the dissolution-passivation step on copper in alkaline solutions, Electrochemical Chemistry and Interfacial Electrochemistry, 47 (1973) 65-80.

[38] A. Kolics, J.C. Polkinghorne, A. Wieckowski, Adsorption of sulfate and chloride ions on aluminum.pdf, Electrochimica Acta, 43 (1998) 2605-2618.

[39] A.G.G. Allah, M.M. Abou-Romia, W.A. Badawy, H.H. Rehan, Effect of halide ions on passivation and pitting corrosion of copper in alkaline solutions, Materials and Corrosion, 42 (1991) 584-591.

[40] N.S. McIntyre, S. Sunder, D.W. Shoesmith, F.W. Stanchell, Chemical information from XPS—applications to the analysis of electrode surfaces, Journal of Vacuum Science and Technology, 18 (1981) 714-721.

[41] N. Sato, A theory for breakdown of anodic oxide films on metals, Electrochimica Acta, 16 (1971) 1683-1692.

[42] X. Wei, C. Dong, P. Yi, A. Xu, Z. Chen, X. Li, Electrochemical measurements and atomistic simulations of Cl$^-$-induced passivity breakdown on a Cu2O film, Corrosion Science, 136 (2018) 119-128.

[43] S.Y. Yu, W.E. O'Grady, D.E. Ramaker, P.M. Natishan, Chloride ingress into aluminum prior to pitting corrosion-an investigation by XANES and XPS, Journal of Electrochemical Society, 147 (2000).

[44] H. Cong, H.T. Michels, J.R. Scully, Passivity and pit stability behavior of copper as a function of selected water chemistry variables, Journal of Electrochemical Society, 156 (2009) 16-27.

[45] F. King, C. Lilja, Localised corrosion of copper canisters, Corrosion Engineering, Science and Technology, 49 (2014) 420-424.

[46] T. Li, J. Wu, G.S. Frankel, Localized corrosion: Passive film breakdown vs. Pit growth stability, Part VI: Pit dissolution kinetics of different alloys and a model for pitting and repassivation potentials, Corrosion Science, 182 (2021).

[47] D. Kong, C. Dong, X. Wei, C. Man, X. Lei, F. Mao, X. Li, Size matching effect between anion vacancies and halide ions in passive film breakdown on copper, Electrochimica Acta, 292 (2018) 817-827.

[48] Z. Qin, R. Daljeet, M. Ai, N. Farhangi, J.J. Noël, S. Ramamurthy, D. Shoesmith, F. King, P. Keech, The active/passive conditions for copper corrosion under nuclear waste repository environment, Corrosion Engineering, Science and Technology, 52 (2017) 45-49.

[49] D. Kong, C. Dong, M. Zhao, X. Ni, C. Man, X. Li, Effect of chloride concentration on passive film properties on copper, Corrosion Engineering, Science and Technology, 53 (2017) 122-130.

[50] H. Ha, C. Taxén, H. Cong, J.R. Scully, Effect of applied potential on pit propagation in copper as function of water chemistry, Journal of The Electrochemical Society, 159 (2011) C59-C73.

[51] H. Cong, J.R. Scully, Effect of chlorine concentration on natural pitting of copper as a function of water chemistry, Journal of The Electrochemical Society, 157 (2010) 200-211.

[52] F. King, M.J. Quinn, C.D. Litke, Oxygen reduction on copper in neutral NaCl solution, Journal of Electrochemical Society, 385 (1995) 45-55.

[53] R.M. Souto, S. Gonzalez, R.C. Salvarezza, A.J. Arvia, Kinetics of copper passivation and pitting corrosion in Na_2SO_4 containing dilute NaOH aqueous solution, Electrochimica Acta, 39 (1994) 2619-2628.

[54] G. Ruijini, S.C. Srivastava, M.B. Ives, Pitting corrosion behavior of UNS N08904 stainless steel in a chloride-sulfate solution, Corrosion, 45 (1989).

[55] S.M. Mayanna, T.H.V. Setty, Role of chloride ions in relation to copper corrosion and inhibition, Proceeding of Indian Academy of Science - Section A, 80 (1974) 184-193.

[56] H.P. Leckie, H.H. Uhlig, Environmental factors affecting the critical potential for pitting in 18–8 stainless steel, Journal of the Electrochemical Society, 113 (1966) 1262-1267.

[57] T. Li, J.R. Scully, G.S. Frankel, Localized corrosion: passive film breakdown vs pit growth stability: part V. Validation of a new framework for pit growth stability using one-dimensional artificial pit electrodes, Journal of The Electrochemical Society, 166 (2019) C3341-C3354.

[58] S.B. Adeloju, Y.Y. Duan, Influence of bicarbonate ions on stability of copper oxides and copper pitting corrosion, British Corrosion Journal, 29 (1994) 315-320.

[59] G. Mankowski, J.P. Duthil, A. Giusti, The pit morphology on copper in chloride- and sulphate-containing solutions, Corrosion Science, 39 (1997) 27-42.

[60] N.G. Smart, J.O.M. Bockris, Effect of Water Activity on Corrosion, Corrosion, 48 (1992) 277-280.

[61] K. Venu, K. Balakrishnan, K.S. Rajagopalan, A potentiokinetic polarization study of the behaviour of steel in NaOH-NaCl system, Corrosion Science, 5 (1965) 59-69.

[62] G.S. Frankel, T. Li, J.R. Scully, Localized corrosion: Passive film breakdown vs pit growth stability, Journal of The Electrochemical Society, 164 (2017) C180-C181.

[63] R. Huang, D.J. Horton, F. Bocher, J.R. Scully, Localized corrosion resistance of Fe-Cr-Mo-W-B-C bulk metallic glasses containing Mn+Si or Y in neutral and acidified chloride solution, Corrosion, 66 (2010).

[64] H. Ha, C. Taxen, K. Williams, J. Scully, Effects of selected water chemistry variables on copper pitting propagation in potable water, Electrochimica Acta, 56 (2011) 6165-6183.

[65] F. King, C. Lilja, K. Pedersen, P. Pitkänen, M. Vähänen, An update of the state-of-the-art report on the corrosion of copper under expected conditions in a deep geologic repository, SKB, 2010.

[66] F. King, L. Ahonen, C. Taxen, U. Vuorinen, L. Werme, Copper corrosion under expected conditions in a deep geologic repository, SKB, 2002.

[67] S. Matin, A. Tahmasebi, M. Momeni, M. Behazin, M. Davison, D.W. Shoesmith, J.J. Noël, Use of multielectrode arrays and statistical analysis to investigate the pitting probability of Copper. Part I: The effect of chloride, Journal of The Electrochemical Society, 169 (2022).

[68] F. Mao, C. Dong, S. Sharifi-Asl, P. Lu, D.D. Macdonald, Passivity breakdown on copper: Influence of chloride ion, Electrochimica Acta, 144 (2014) 391-399.

[69] M.A. Abdulhay, A. A.Al-Suhybani, Open circuit potential for copper electrode in 1 M NaCl solutions, Materials Science and Engineering Technology, 23 (1992) 407-412.

[70] F. King, Corrosion of copper in alkaline chloride environment, 2002.

[71] M. Ochoa, M.A. Rodríguez, S.B. Farina, Corrosion of high purity copper in solutions containing NaCl, Na2SO4 and NaHCO3 at different temperatures, Procedia Materials Science, 9 (2015) 460-468.

[72] A.E. Warraky, H.A.E. Shayeb, E.M. Sherif, Pitting corrosion of copper in chloride solutions, Anti-Corrosion Methods and Materials, 51 (2004) 25-61.

[73] A. Nishikata, M. Itagaki, T. Tsuru, S. Haruyama, Passivation and its stability on copper in alkaline solutions containing carbonate and chloride ions, Corrosion Science, 31 (1990) 287-292.

[74] G. Bianchi, G. Fiori, P. Longhi, F. Mazza, Horse shoe- Corrosion of copper alloys in flowing sea water- Mechanism, and possibility of cathodic protection of condenser tubes in power generation, Corrosion, 34 (1978) 396-406.

[75] T. Li, J.R. Scully, G.S. Frankel, Localized corrosion: passive film breakdown vs pit growth stability: part II. A model for critical pitting temperature, Journal of The Electrochemical Society, 165 (2018) C484-C491.

[76] T. Li, J.R. Scully, G.S. Frankel, Localized corrosion: passive film breakdown vs. pit growth stability: part IV. The role of salt film in pit growth: A mathematical framework, Journal of The Electrochemical Society, 166 (2019) C115-C124.

[77] T. Li, J.R. Scully, G.S. Frankel, Localized corrosion: Passive film breakdown vs. pit growth stability: Part III. A unifying set of principal parameters and criteria for pit stabilization and salt film formation, Journal of The Electrochemical Society, 165 (2018) C762-C770.

Chapter 5

5   Susceptibility of Copper to Pitting Corrosion in Bicarbonate Buffer Solutions: Effect of Chloride

Abstract

The pitting corrosion, passive film morphology, and surface composition of copper were studied in chloride-containing bicarbonate buffer solutions using multielectrode arrays and single electrodes. Cu was shown to be susceptible to pitting in 0.01 and 0.1 M Cl$^-$, but to experience active dissolution in 1 M Cl$^-$. The passive film morphology and composition were investigated using the single-electrode setup. Surface analyses showed the presence of pits in both 0.01 and 0.1 M Cl$^-$ buffer solutions. The results indicated the dependency of passive film morphology and composition on both charge density and applied potential.

5.1   Introduction

Copper and copper alloys are used in various industries including oil and gas, marine, construction, and nuclear. Different types of oxide films can be formed on a Cu surface depending on the environment to which it is exposed. As a result, Cu oxides may have either a positive or negative influence on corrosion performance in specific applications. For instance, the formation of corrosion products can decrease the efficiency of a cooling system by inducing a lower heat transfer rate. Additionally, an oxide layer may protect the base metal from further degradation in corrosive environments or, if unstable in harsh environments, result in unpredictable material failures [1-10].

Some metals form a thin, dense, and uniform oxide film on the surface, commonly referred to as a passive film, which protects them from further dissolution. Two different mechanisms have been proposed for protective film formation: (1) metal dissolution as cations followed by their precipitation as oxides or/and hydroxides on the metal surface (dissolution-precipitation mechanism) [11-13]; and (2) nucleation and growth of a passive film via a solid-state reaction [12, 14]. The morphology and properties of oxide

films depend on parameters such as applied potential, solution composition, grain orientation, and exposure time [12, 14-26]. For instance, the formation of passive films on Cu in moderately alkaline solutions leads to a dual layer film structure with inner Cu_2O and outer CuO or/and $Cu(OH)_2$ layers [12, 22, 27-29]. The Cu_2O is commonly porous, allowing Cu^{2+} ions to diffuse into solution and precipitate to form an outer layer of CuO or/and $Cu(OH)_2$. The properties of this double-layer film on the Cu surface depend on the pH of the solution [12, 17, 30-32].

While the formation of a passive film will decrease the general corrosion rate, any localized damage to the film can result in accelerated corrosion rates at discrete locations. Pitting is a common form of localized corrosion, and a major concern due to its unpredictability, ability to penetrate the bulk material, and self-sustaining nature. Many studies have been conducted on the properties of passive films, such as their structure, composition, and thickness and their role in pitting [4, 8, 33-46].

Two main mechanisms have been proposed to explain pitting: (1) mechanical breakdown of the passive film due to the transport of aggressive anions from the solution through the oxide film to produce a large interfacial stress at the metal surface [47]; and (2) local thinning of the passive film due to surface adsorption of aggressive anions from solution [34, 48]. Defining the rate-determining step is of key importance in understanding the mechanism of pitting, and two rate-determining steps have been proposed: (1) passive film breakdown; and (2) the transition from metastable to stable pit growth. The role of passive film breakdown is negligible if the repassivation potential (E_{rp}) is just below the breakdown potential (E_b) when pit propagation will be slow, but breakdown becomes rate-determining when pitting occurs at relatively high potentials when the subsequent process of pit propagation will be rapid due to the resistivity of the passive film [49]. Pitting comprises a number of steps, including metastable initiation, a metastable-to-stable pitting transition, and stable pit growth. While a specific system might experience a large number of metastable pits, few of them are generally able to transition to stable pits.

Different parameters have been introduced to characterize stable pit growth, such as ix, ir, $i\sqrt{t}$, and $i_{diss, max}$ where i is the pit current density, x is the pit depth in a 1D pit, r is the depth of a hemispherical pit, t is time, and $i_{diss,max}$ is the maximum dissolution current density [1, 8, 10, 38, 45]. While Silverman [50] reported that the presence of a salt film at the base of a passive film breakdown site could prevent the transition from metastable to stable pit growth, Frankel [39-42, 51, 52] demonstrated that this transition could occur even in the presence of the salt film and that pit growth could be either a charge transfer- or diffusion-controlled process [5, 7, 53].

A common method to determine the susceptibility of materials to pitting is to compare the corrosion potential (E_{corr}) to E_b and E_{rp} [29, 54]. However, these potentials are distributed parameters due to variations in surface properties, variations in the local environment at the metal surface, and the stochastic nature of passive film breakdown. Pitting becomes possible when E_{corr} is equal to or more positive than E_b [29, 54, 55], and subsequently proceeds via four main steps: (1) initiation, (2) metastable growth, (3) stable growth, and (4) repassivation [3, 9, 13]. Pitting starts with the nucleation of pits on the surface of materials due to the breakdown of the passive film, with some of the metastable pits initially formed subsequently transitioning into stable pits. It is commonly accepted that the stability of a pit depends on the aggressiveness of the solution inside the pit [2-8, 36, 37, 39-42, 56-61], with the concentration of this solution necessarily higher than a critical concentration (C_{crit}) required to sustain active dissolution.

Anions can have a positive (e.g., CO_3^{2-} and OH^-) or a negative effect (e.g., Cl^- and SO_4^{2-}) on the stability of passive films, which will affect the key pitting parameters, E_{corr}, E_b, E_{rp}, and the critical pitting temperature (CPT). The CPT is defined as the lowest temperature required for the formation of stable pits in a given environment. When multiple anions are present, there is competition between the adsorption of aggressive and inhibiting anions on the oxide surface [62, 63]. The aggressive anions, Cl^- and SO_4^{2-}, play a significant role in passive film breakdown and pit initiation [53, 55, 64-66], while CO_3^{2-} exerts an inhibiting effect by increasing the stability of the passive film [67]. Some studies have proposed that the behaviour of aggressive anions varies [62, 64, 68, 69]. For example, Cl^- ions can accelerate corrosion at relatively low concentrations but behave

like inhibitors at higher concentrations, due to the rapid rate of CuCl formation on the surface once the solubility of CuCl has been reached [64]. Another factor that could affect the pitting probability of materials is the solution pH, with the dependency of the E_b on pH having been debated for decades [62, 70, 71].

In general, three mechanisms have been proposed to explain the pitting of metals: the Salina-Bravo and Newman (SBN); the Point Defect (PDM); and the Li, Scully, and Frankel (LSF) models [2, 40-42, 51, 52, 72]. In the SBN model, it is proposed that a salt film exists on the metal surface inside the pit [2]. This film can be formed on the metal surface if the critical current density (i_{crit}) increases to a value equal to or greater than the anodic limiting current density (i_L) and then the pit will grow under diffusion control. The SBN model was not able to explain why the measured current density was lower than i_L while metastable-to-stable pit growth was observed. The PDM proposed the mechanical breakdown of the passive film through the accumulation of cation vacancies at the metal/oxide interface by transport from the oxide/solution interface; however, other types of pitting mechanisms are not covered in this model. To overcome the limitations inherent to the SBN and PDM models, Frankel and coworkers [39-42, 51, 52] developed the LSF model. Based on the LSF model, passive film breakdown is the critical factor when metal is exposed to a less aggressive environment or the microstructure of the material is less susceptible to pitting. In this case, the rate of passive film breakdown is low, but when it occurs, the pit grows rapidly. On the other hand, when a material is exposed to an aggressive solution, pit growth becomes the critical factor, due to the high frequency of passive film breakdown events and the formation of a large number of metastable pits.

Cu and its alloys have been shown to be corrosion resistant in environments such as seawater and anoxic solutions. However, localized corrosion processes can occur under aerated conditions in the presence of aggressive anions, or when the pH of the solution is increased. Many studies have been performed to investigate the pitting of Cu in a range of environments, with corrosion parameters considered to be deterministic, not distributed [18, 22, 26, 27, 29, 31, 54, 65-67]. However, we showed the stochastic nature of corrosion parameters in our previous papers [73]. Here, we investigate the pitting

probability, passive film morphology, and composition of oxide films in solutions with different chloride concentrations, using electrochemical, surface analysis, and statistical techniques to determine the pitting mechanism of Cu.

5.2   Experimental Methodology

5.2.1   Sample Preparation

O-free and P-doped wrought Cu were supplied by the Swedish Nuclear Fuel and Waste Management Company (SKB, Solna, Sweden). Electrodes were machined as either "bullets" (used in multielectrode arrays, Fig. 5.1) or as cylindrical samples (with a 10 mm diameter and 4 mm thickness, used in single-electrode experiments). Bullet samples were used to avoid edge effects during electrochemical experiments. For multielectrode experiments, Cu specimens were prepared by rotating at 2700 RPM while grinding with a sequence of SiC papers (P600, P800, P1200, P2500, and P4000). The specimens were then rinsed with Type I water (18.2 MΩ.cm) prepared using a Millipore Milli-Q plus system, sonicated in ethanol, and dried in a stream of Ar gas prior to each experiment.

For single-electrode experiments, cylindrical Cu samples were mounted in epoxy and subjected to a vacuum for 5 minutes to remove bubbles from the epoxy, and to avoid the formation of crevices between the sample and the epoxy. Cu specimens were ground with a sequence of SiC papers (P600, P800, P1200, P2500, and P4000), followed by a final polish using a 1 µm diamond suspension, to achieve a mirror surface finish. Then, the samples were rinsed in Type I water, sonicated in ethanol and dried in a stream of Ar gas prior to each experiment.

Figure 5.1: O-free and P-doped copper electrodes.

5.2.2   Solution Preparation

Solutions were prepared with reagent-grade sodium chloride (NaCl, 99.0%), sodium carbonate (Na_2CO_3, 99.5%), and sodium bicarbonate ($NaHCO_3$, 99.7%) provided by Fisher Scientific, using Type I water. The solutions were composed of a 0.005 M Na_2CO_3/ $NaHCO_3$ buffer solution containing various concentrations of NaCl within the range from 0.01 M to 0.1 M. The pH of the solutions was adjusted to 9 using the 0.005 M Na_2CO_3/ $NaHCO_3$ buffer solution.

5.2.3   Electrochemical Cell, Instrumentation, and Procedure

All potentiodynamic and potentiostatic experiments were performed in a conventional three-electrode electrochemical cell using either 30 Cu bullets as working electrodes (multielectrode arrays) or a single Cu working electrode, a Ti plate or Pt wire as the counter electrode, and a saturated calomel reference electrode (SCE, 0.242 V vs. SHE) as reference. In the multielectrode array experiments, the counter electrode had a surface area of 200 cm^2, and was just smaller than the cell bottom. The electrochemical cell was placed inside a Faraday cage to reduce electrical noise from external sources.

5.2.3.1   Multielectrode Arrays

Corrosion potential (E_{corr}) and potentiodynamic polarization experiments were conducted using a Multichannel Microelectrode Analyzer 910 (MMA, Scribner Associates) connected to a computer equipped with MMAlive software. The instrument was equipped with five 100 µA zero resistance ammeters (ZRA). Fig. 5.2 shows a schematic of the instrument and multielectrode array used. In potentiodynamic experiments only the positive-going scan was conducted to measure E_b. Prior to the scan, electrodes were cathodically cleaned at -0.85 V vs SCE for 3 minutes to reduce any air-formed oxides. Then, E_{corr} was monitored for 30 minutes to allow a steady-state condition to be established and to determine the range of E_{corr} values on the multielectrode array. The potential was then scanned from E_{corr} in the positive direction at a scan rate of 10 mV/min until the current on all electrodes reached 100 µA, followed by a negative-going scan at the same scan rate as the positive-going scan until all currents reached the passive current density. A schematic of the positive-going scan is shown in Fig. 5.3. Histograms of E_{corr} and E_b determined under passive conditions were plotted to facilitate the selection of applied potentials to be used in potentiostatic experiments. The applied potentials for potentiostatic experiments were chosen to be a) the maximum observed E_{corr} value + 20 mV and b) the minimum observed E_b value – 20 m V.. These values were chosen to cover the tails of the E_{corr} and E_b distribution curves where there are concerns about the pitting probability [73].
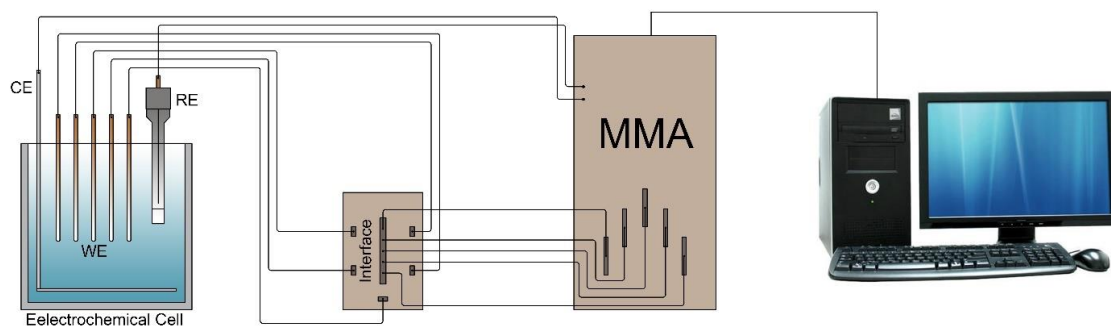
Figure 5.2: Schematic of multichannel microelectrode analyzer (MMA) connected to a multielectrode array.
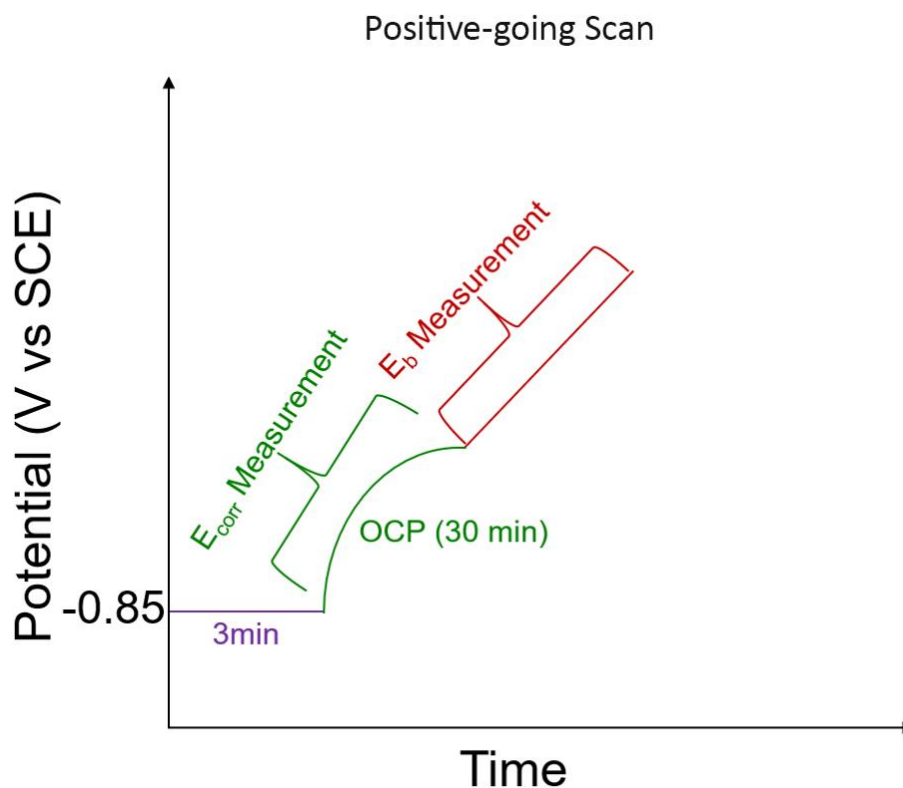
Figure 5.3: Schematic of potentiodynamic experiment for the measurement of E_{corr} and E_b.

E_b was identified as the potential at which the current abruptly increased, and was determined from the intersection of the tangent to the current in the passive range and the rising current in the potential range after breakdown [69, 74]. We confirmed in every case that E_b was truly a breakdown potential, and not a value related to transpassive or uniform corrosion, by reversing the scan direction to negative-going to confirm observation of the expected positive hysteresis.

5.2.3.2   Single Electrode

5.2.3.2.1   Potentiodynamic Experiment

The active-passive behaviour of Cu was investigated using the potentiodynamic technique. A ModuLab XM ECS Solartron potentiostat and XM-studio software were used to perform the potentiodynamic experiments. Before each scan, electrodes were

prepared as described in section 2.3.1. After 30 min on open circuit to establish a steady E_{corr} value, scans were performed as described in section 2.3.1 for multielectrode arrays but with an additional negative-going scan at the same scan rate at the end. The negative-going scan was terminated when the current density became equal to that recorded as the passive current on the positive-going scan.

5.2.3.2.2   Potentiostatic Experiment

Potentiostatic experiments were conducted using a ModuLab XM ECS Solartron potentiostat and XM-studio software. Applied potentials ranging from E_{corr} + 20 mV to E_{corr} + 105 mV were selected, based on measured histograms (Section 1.3.1). A second set of potentials, ranging from -27 mV vs SCE to 58 mV vs SCE, was selected to investigate the dependence of passive film morphology and composition on applied potential and charge density. Samples were immersed in the solution immediately after the surface preparation process and a potentiostatic experiment was then performed for 6 hours.
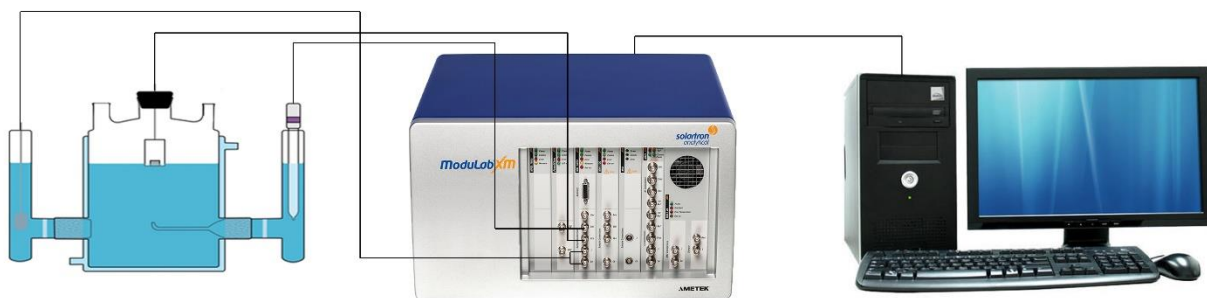
Figure 5.4: Schematic of single electrode cell setup.

5.2.4   Surface Analysis

On completion of electrochemical experiments, specimens were rinsed with Type I water, dried in a low stream of Ar gas to avoid damage to oxide films, and stored in an anaerobic chamber until surface analysis could be performed. In some cases, corrosion products were removed by exposing the specimen to an Ar-sparged 9.1 wt% $HClO_4$ solution containing 3.5 g/L of $C_6H_{12}N_4$ as an inhibitor to prevent further Cu corrosion.

Scanning electron microscopy (SEM) and energy dispersive X-ray spectroscopy (EDS) were used to investigate the surface morphology and composition of the film using a Hitachi SU8230 (Regulus Ultra High-Resolution Field Emission SEM) equipped with a FlatQuad EDS (Bruker X-Flash FQ5060 Annular Quad) at Surface Science Western (SSW). A LEO 1540XB SEM equipped with a focused ion beam (FIB) (Zeiss Nano Technology System Division, Germany) at Western Nanofabrication Facility was used to examine the cross-sectional morphology and thickness of oxide films.

A Kratos AXIS Supra equipped with a monochromatic Al-Kα X-ray source (1486.6 eV) was used for X-ray photoelectron spectroscopic analyses. The instrument work function was calibrated to give a binding energy (BE) of 83.96 eV for the Au $4f_{7/2}$ line for metallic Au and the spectrometer dispersion was adjusted to give a BE of 932.62 eV for the Cu $2p_{3/2}$ line of metallic Cu. Survey spectra were recorded over a BE range of 0 to 1200 eV using a pass energy of 160 eV at a step size of 1 eV. High-resolution spectra were collected for the Cu $2p_{3/2}$ and C 1s lines and the $CuL_3M_{4,5}M_{4.5}$ Auger peak using a pass energy of 20 eV and a step size of 0.1 eV. In all cases, the Cu $2p_{3/2}$ and Auger LMM lines were collected first to mitigate the effect of X-ray degradation of the Cu(II) state. All spectra were corrected for charging using the adventitious carbon peak (C 1s, 284.8 eV). Data processing was carried out using CasaXPS (v. 2.3.14) software with a Shirley background subtraction. The deconvolution procedures were performed using previously determined fitting parameters [75].

5.3 Results and Discussion

5.3.1 Potentiodynamic Polarization

Fig. 5.5 shows that E_{corr} values, measured in aerated solutions containing different $[Cl^-]$, increased with time towards a steady-state value which decreased with increasing $[Cl^-]$. This decrease with increasing $[Cl^-]$ can be attributed to acceleration of the anodic dissolution of Cu in Cl^--containing solutions, which proceeds via a sequence of electrochemical and chemical steps, as shown in reactions 1 to 3 [76],

$$Cu + Cl^- \rightarrow CuCl_{ads} + e^- \qquad\qquad 1$$

$$CuCl_{ads} + Cl^- \rightarrow CuCl_2^- \text{ (surface)} \qquad\qquad 2$$

$$CuCl_2^- \text{ (surface)} \rightarrow ClCl_2^- \text{ (bulk) Rate determining step} \qquad\qquad 3$$
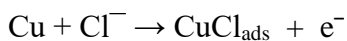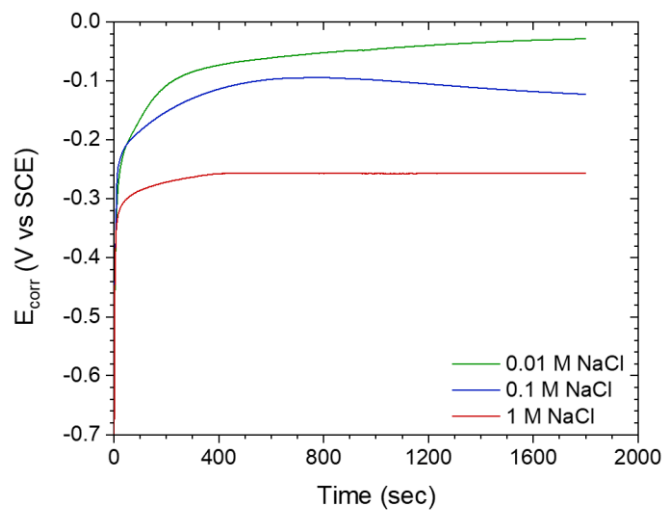
Figure 5.5: Corrosion potential (E$_{corr}$) of Cu in chloride-containing solutions.
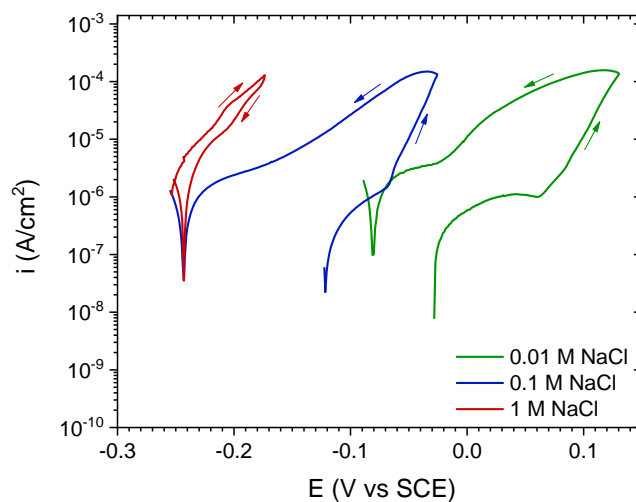
Figure 5.6: Potentiodynamic polarization (PDP) scans recorded on Cu in Cl$^-$-containing solutions.

Fig. 5.6 shows cyclic polarization scans recorded on Cu in solutions with different [Cl⁻]. In 0.01 M Cl⁻, a passive region is clearly visible on the positive-going scan, followed by film breakdown, indicated by the current increase at more positive potentials. The positive hysteresis observed on the negative-going scan confirmed that the surface was more active on the negative-going scan, most likely due to the initiation of pitting corrosion sites on the negative-going scan. In 0.1 M Cl⁻, the passive region was considerably narrower (Fig. 5.6), indicating that oxide breakdown was more readily achieved. The large hysteresis shows that repassivation was not readily achieved at this concentration. For 1 M NaCl, the rapid increase in current on the positive-going scan, the absence of a clear passive region, and the maintenance of the current on the negative-going scan indicate active corrosion behaviour. There is a possibility that the rapid dissolution of the CuCl layer (reaction 1-b), followed by hydrolysis (reaction 4), caused deposition of a marginally protective Cu_2O film on the surface, resulting in the slight negative hysteresis in the negative-going scan

$$2CuCl_x^{(1-x)-} + 2OH^- \rightarrow Cu_2O + H_2O + 2xCl^- \qquad\qquad 4$$
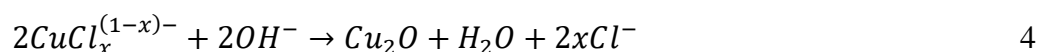
Fig. 5.7 shows SEM micrographs recorded on Cu surfaces exposed to solutions of different [Cl⁻] (after potentiodynamic polarization experiments). Clear evidence for passive film breakdown was only observed in 0.01 M Cl⁻ solution (Fig. 5.7-a,b). The passive film present after polarization in 0.01 M NaCl solution appears to have been formed by a combination of localized breakdown and transpassive dissolution, since the oxide was electrochemically unstable and could be dissolved simultaneously as the pit tried to propagate, resulting in the formation of shallow pits [27]. A uniform film was observed on Cu in 0.1 M Cl⁻, with the presence of a number of porous sites on the surface (Fig. 5.7-c,d). In 1 M Cl⁻ solution, a generally porous oxide film was observed, with no visible sign of localized attack (Fig. 5.7-e,f). The porosity of the oxide film could be due to the higher dissolution rate of Cu (via reactions 1 to 3) followed by the formation of Cu_2O on the Cu surface via reaction 4. The presence of this film could obscure the presence of localized corrosion sites.
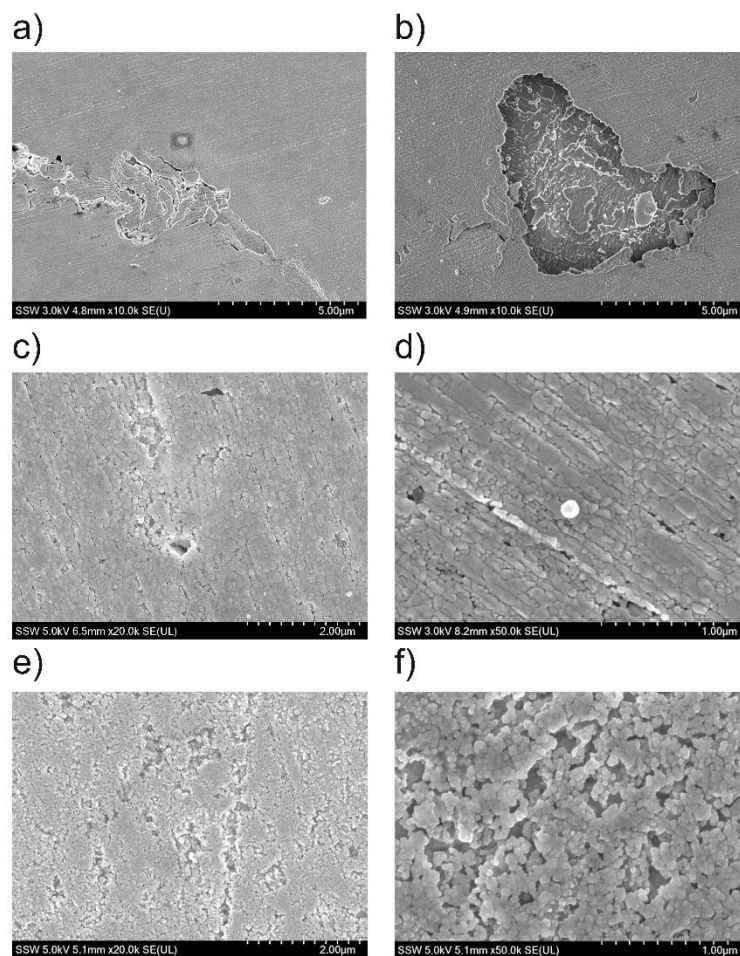
Figure 5.7: Passive film morphology of Cu surfaces after potentiodynamic polarization scans recorded in buffer solutions with different [Cl⁻]: a,b) 0.01 M Cl⁻; c,d) 0. 1 M Cl⁻; e,f) 1 M Cl⁻.

5.3.2 Statistical Analysis

Fig. 5.8 shows sets of E_{corr} profiles (a and c) and polarization scans (b and d) recorded at two [Cl⁻] on a multielectrode array, with the latter showing E_b. Fig. 5.9 shows the corresponding histograms and box plots for measured E_{corr} and E_b values. Both E_{corr} and E_b distributions shifted to more negative values with increasing [Cl⁻], as expected based on the results in Figures 5.5 and 5.6. Also, the difference between E_{corr} and E_b ($|E_b$-$E_{corr}|$) decreased with the increase in [Cl⁻] (Fig. 5.9a and b). This is consistent with the formation of a more protective film in 0.01 M Cl⁻ under open-circuit conditions, leading to a wider range of E_{corr} values compared to those recorded in 0.1 M Cl⁻. A possible

explanation is that more Cl^- adsorbed on the oxide films in 0.1 M Cl^- promoting breakdown, leading to a shift in E_b to more negative values, and allowing the enhancement of Cu dissolution (Fig 5.9b and d).

Less dispersion of E_{corr} and E_b values was observed in solutions containing a higher $[Cl^-]$, Fig. 5.9a and b. The frequency of breakdown was higher at the higher $[Cl^-]$ which created a narrower distribution of E_b values. At the lower $[Cl^-]$, the passive film was more stable and breakdown required a higher potential, with a decreased frequency of breakdown leading to a wider distribution in E_b values. The distribution range of E_b was greater than that for E_{corr} in 0.01 M Cl^- (Fig. 5.9a); however, the same distribution range and shape were observed in 0.1 M Cl^- for both E_{corr} and E_b (Fig. 5.9b).

The pitting probability is determined by the statistical distributions of measured values, as defined by the shape parameter and scale factor of the distribution, and the difference between the highest E_{corr} and lowest E_b values. The shape of the distribution of E_b in 0.01 M Cl^- was left-skewed, which might increase the pitting probability of Cu by generating a greater overlap between E_{corr} and E_b. The difference between E_b and E_{corr} (E_b^{min}-E_{corr}^{max}) was 74 mV and 51 mV in 0.01 M and 0.1 M Cl^- solutions, respectively (Fig. 5.9a and b); as a result, a greater pitting probability would be expected at the higher $[Cl^-]$. It is important to note that passive behaviour was observed in solutions with $[Cl^-]$ up to 0.1 M, followed by active corrosion at higher $[Cl^-]$.

Box plots show the presence of extreme values for both parameters except E_{corr} at 0.01 M Cl^-, Fig. 5.9c and d. The pitting probability depends on the overlap between E_{corr} and E_b, so extreme values increase the pitting probability of Cu significantly, specifically when they are located on the left side of the E_b distribution or the right side of the E_{corr} distribution.
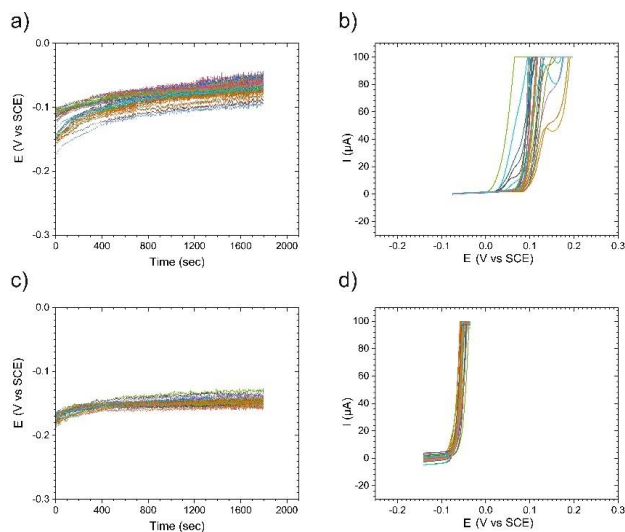
Figure 5.8: Corrosion potentials (E_corr) and polarization curve of Cu multielecrode arrays a,b) 0.01 M Cl⁻ c,d) 0.1 M Cl⁻ .
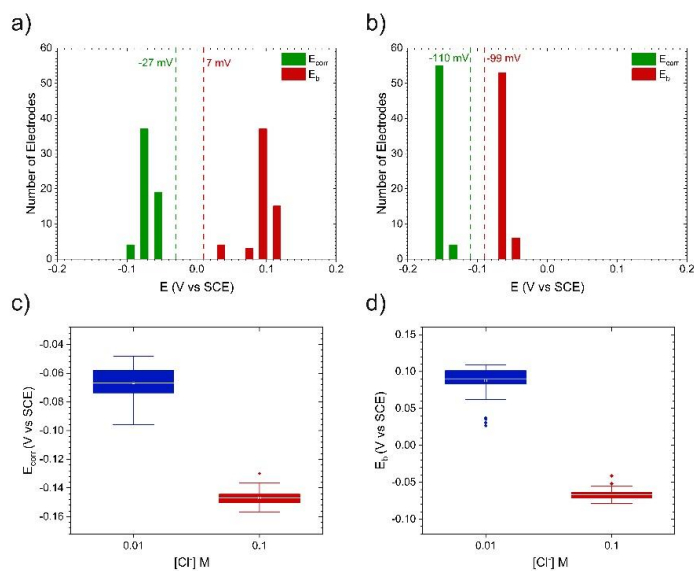
Figure 5.9: Histograms and box plots for Cu multielectrode arrays; a) histogram of E_corr and E_b values in 0.01 M NaCl, b) histogram of E_corr and E_b values in 0.1 M NaCl. c) Box plot of E_corr values in carbonate buffer solutions containing 0.01 and 0.1 M NaCl. d). Box plot of E_b in carbonate buffer solutions containing 0.01 and 0.1 M NaCl. Green and red dashed lines in Fig. 9a and b define the E_corr+20 mV and E_b-20 mV potentials, respectively. Points in box plots are extreme values.

5.3.3   Potentiostatisc Polarization

The current-time transients shown in Fig. 5.10 can be interpreted from two points of view: (I) nucleation and growth of oxide films; (II) initiation and growth of pits.

(I) Nucleation and growth of oxide films:

Generally, nucleation and growth processes exhibit a current peak attributable to the acceleration of growth of nuclei followed by suppression of growth as the nuclei grow and coalesce to block the surface. In 0.01 M Cl⁻ at an applied potential of -27 mV vs SCE (i.e., 20 mV greater than the maximum E_{corr} measured in the multielectrode array experiments), the current-time transient exhibited a sharp decrease (not shown) followed by the establishment of a very low current plateau over the first 21,600 seconds (Fig. 5.10-b). The current did not exhibit any metastable pitting transients over the full duration of the experiment, indicating the formation of a protective oxide film. At an applied potential of 7 mV vs. SCE (i.e, 20 mV less than the minimum E_b measured in the multielectrode array experiments), the initial current decreased to a similarly low value but that was followed by an abrupt increase, indicating the breakdown of the initially formed oxide, followed by metal dissolution and the nucleation and growth of oxide and/or hydroxide films. Once the current reached the apex, it decreased at longer times to a lower value approaching a steady-state plateau, indicating the formation of a deposit. The current density did not achieve the extremely low values associated with passivity; this showed that the film was not completely protective, and allowed local dissolution of Cu to continue at a low rate. The initial exponential decay in current over short times (around 70 seconds) suggested film growth via the solid-state mechanism defined by the point defect model (Fig. 5.10b and d) [12, 13, 72, 77]. The current-time transients were similar to each other in the solution containing 0.1 M Cl⁻ for both applied potentials (defined in Fig. 5.9), since E_b was only slightly different to E_{corr} (Fig 5.10-d).

(II) Pit growth mechanism:

For an applied potential of -27 mV vs. SCE, the current decreased sharply within a short period of time (around 40 seconds) to a value of 0.6 $\mu A/cm^2$, eventually reaching a

constant value of 0.03 µA/cm^2). This extremely low value is consistent with the presence of a passive film. The absence of sharp peaks indicated that there was no metastable pit initiation (Fig. 5.10-b). The SEM micrograph of the surface, Fig. 5.11.b, confirms the presence of a thin film with some apparent porosity that suggests there would be a small current observable at longer times.

The current transient recorded at an applied potential close to the lowest E_b (7 mV vs SCE) exhibited an early sharp decrease, similar to that observed at the lower applied potential of -27 mV vs SCE before breakdown occurred, suggesting the formation of a passive Cu$_2$O film prior to breakdown. Subsequently, the current density increased steadily to a maximum after 30 minutes, indicating that film breakdown is a relatively slow, evolving process. The observed current density behaviour suggests that pit growth was under charge transfer control during the early stage as the surface concentration (C_{surf}) of dissolved Cu increased, before switching to diffusion control as the current density decreased with time. This could be attributed to an increase in pit depth to a value greater than the critical pit depth (r_{sat}), accompanied by corrosion product deposition [52]. The pit growth continued at a very low rate, since the pit was very deep and the deposit was thick (Fig. 5.11e); therefore, the actual potential at the pit surface was lower than the applied potential, close to E_{corr}. It is noteworthy that the current did not reach a value indicating passivity. The current density is given by equation (1), in which i is the current density at the pit surface, F the faraday constant, D_e the effective diffusion coefficient, and r the pit depth.

$$i = 3nFD_eC/2\pi r \qquad\qquad\qquad 1$$

In a 0.1 M Cl$^-$ solution, the current density increased to a maximum value after 5,400 and 6,360 seconds at applied potentials of -110 mV and -99 mV vs SCE, respectively. Then the current density decayed to a plateau close to 0.5 µA/cm^2, a value lower than that recorded in the 0.01 M NaCl solution. This indicates that pit growth became very slow or even negligible, since this value is close to the expected passive current densities for both -99 mV and -110 mV potentials (Fig. 5.10.d).
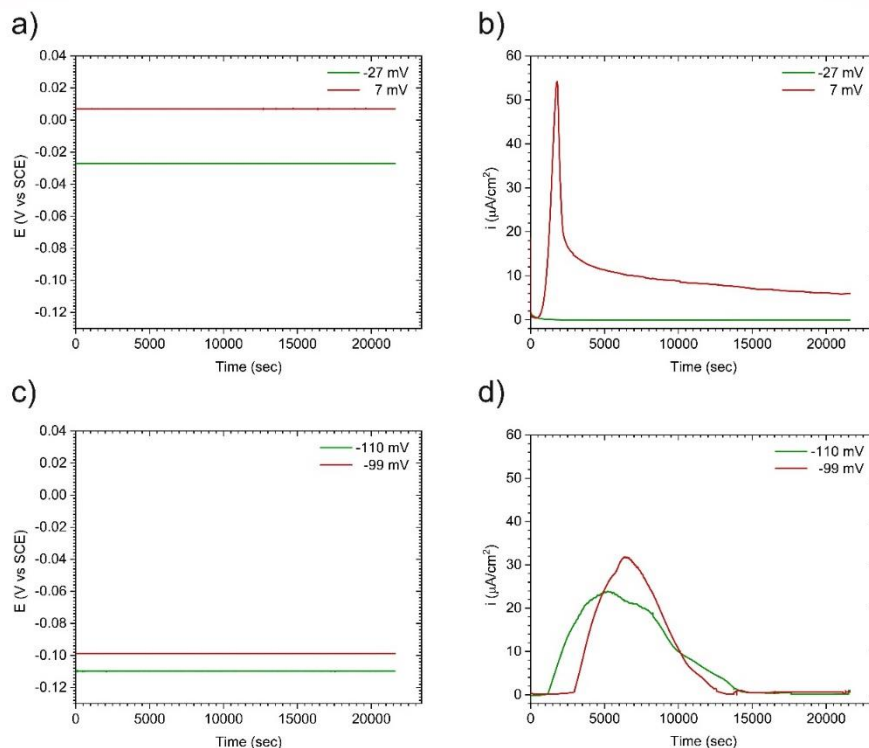
Figure 5.10: Potential-time and current-time transients recorded on Cu in Na₂CO₃/ NaHCO₃ solutions containing different [Cl⁻]: a) transients at two different applied potentials in Na₂CO₃/ NaHCO₃ buffer solution containing 0.01 M NaCl; b) current-time transient in Na₂CO₃/ NaHCO₃ buffer solution containing 0.01 M NaCl; c) transients recorded at two different applied potentials in Na₂CO₃/ NaHCO₃ buffer solution containing 0. 1 M NaCl; d) current-time transient in Na₂CO₃/ NaHCO₃ buffer solution containing 0.1 M NaCl.

5.3.4   Surface Morphology

The morphologies of Cu after exposure to 0.01 M Cl⁻ solution at different applied potentials are shown in Fig. 5.11. After oxidation at -27 mV vs SCE, a thin uniform oxide film covered the surface, with no evidence of any localized attack; no pitting was observed at this applied potential (Fig. 5.11a and b). At 7 mV vs. SCE, passive film breakdown was observed, as shown in Fig. 5.11c and d, with the surface deposit formed spalling from the Cu surface most likely after the electrode was removed and dried, as observed in Figure 11-c. Fig. 5.11-d indicated that such a process could propagate in a

longitude direction. A very deep pit with a film at the pit surface was observed, in agreement with a pit growth mechanism achieving diffusion control (Fig. 5.11-e). Pit initiation and propagation at the intersection of grain boundaries was detected in FIB-cut cross sections (Fig. 5.11-f). This could be due to the affinity of grain boundaries for adsorbing Cl^-, thereby making them preferential locations for localized corrosion [78].

After removing the passive film from the surface by immersing the Cu sample in an Ar-sparged 9.1 wt% $HClO_4$ + 3.5 g/L $C_6H_{12}N_4$ solution, another porous oxide film was observed as an inner layer (Fig. 5.11-h). The inner oxide film was adhesive and was not removed by immersion of the sample in Ar-sparged 9.1 wt% $HClO_4$ + 3.5 g/L $C_6H_{12}N_4$ solution for 5 minutes. Fig. 5.11-g shows the localized dissolution of Cu leading to the formation of two adjacent pits. Over an extended time period it is possible that the two pits could coalesce into one elongated pit.
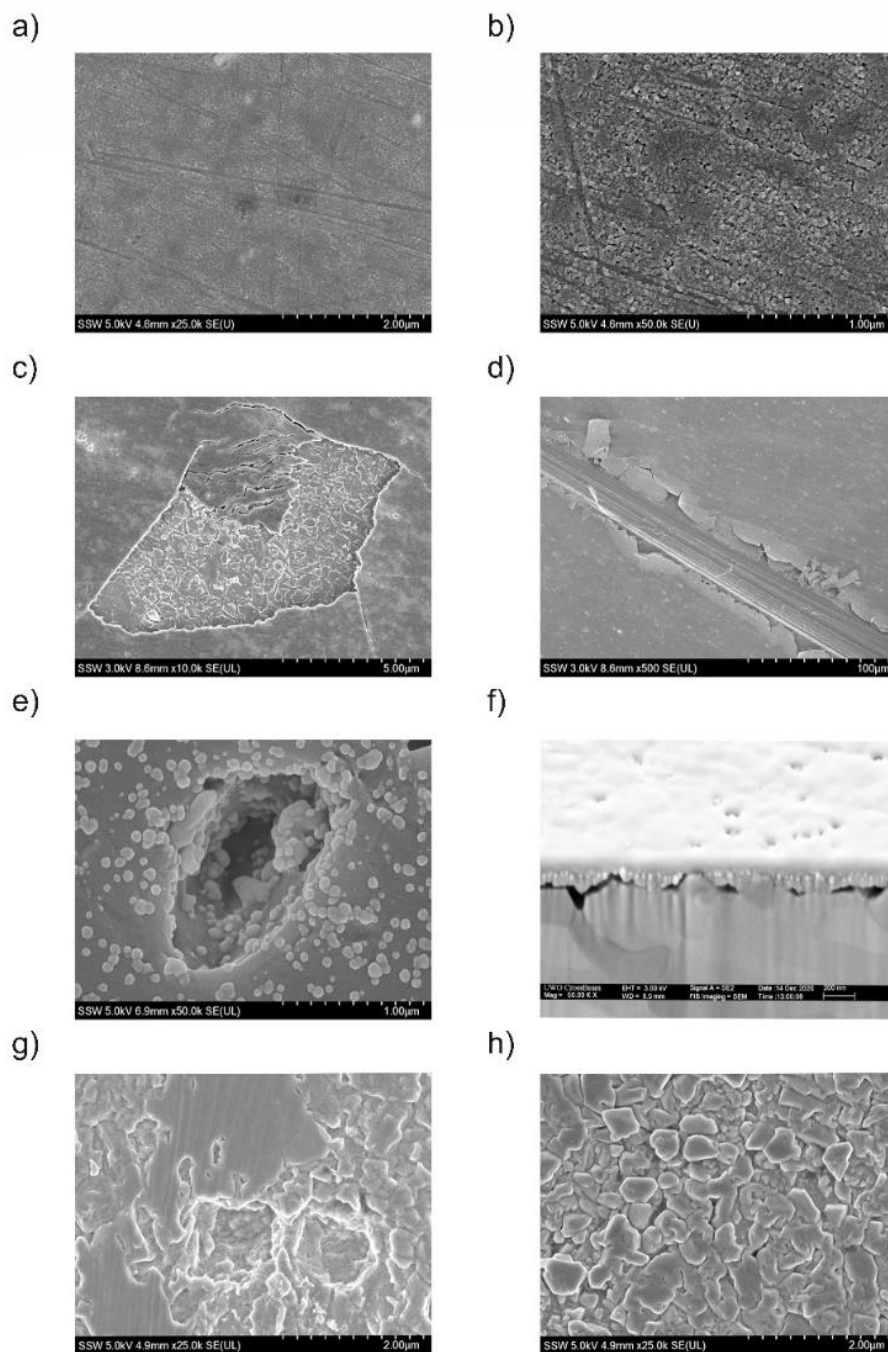
Figure 5.11: Surface morphology of Cu in Na$_2$CO$_3$/ NaHCO$_3$ buffer solution containing 0.01 M Cl$^-$; a,b) oxide film on Cu at the applied potential of -27 mV vs SCE, c-e) oxide film on Cu at the applied potential of 7 mV vs SCE, f) cross-section of the oxide film on Cu at the applied potential of 7 mV vs SCE, g,h) Cu surface at the applied potential of 7 mV vs SCE after the top oxide layer was removed from the surface.

Energy dispersive X-ray analyses (EDX) confirm the exposure of Cu in areas where film rupture has occurred, Figure 5.12, allowing localized dissolution of Cu in those areas, as seen in Fig. 5.12b and f.
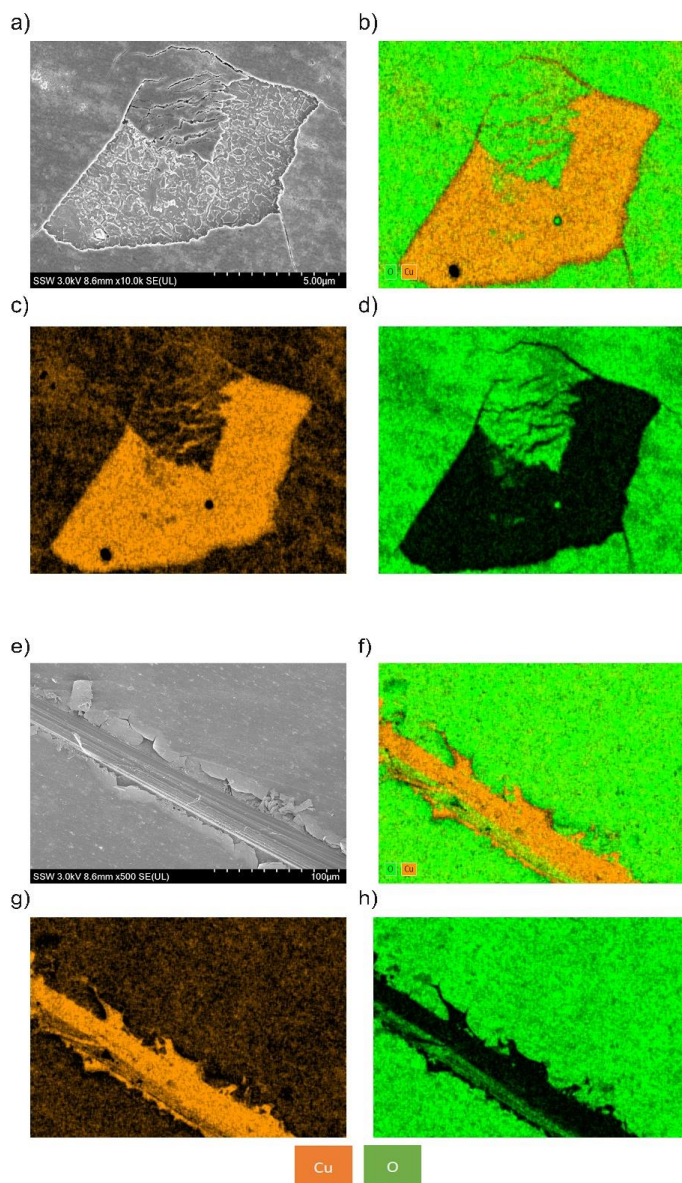
Figure 5.12: EDX map of the passive film on Cu in Na$_2$CO$_3$/ NaHCO$_3$ buffer solution containing 0.01 M Cl⁻ at an applied potential of 7 mV vs SCE: a,e) SEM images of passive film breakdown sites; b,f) high-resolution EDX maps of copper and oxygen distributions; c,g) high-resolution EDX maps of copper distribution; d,h) high-resolution EDX maps of oxygen distribution.

Fig. 5.13 shows the composition of the passive film formed in Na_2CO_3/ $NaHCO_3$ buffer solution containing 0.01 M NaCl at the applied potentials of -27 mV and 7 mV vs SCE. At a potential of -27 mV vs SCE (representative of E_{corr}) (Fig 5.13-a,c), the top surface was dominantly Cu_2O, with small detectable signals for CuO and $Cu(OH)_2$. The detection of Cu(0) demonstrates that the Cu_2O was present as a thin passive layer, as indicated by the current-time transient in Figure 5.10b. At the higher applied potential (7 mV vs SCE) the surface was mostly covered with $Cu(OH)_2$, with minimal amounts of CuO and Cu_2O detected (Fig. 5.13-b,c). The hydroxide/oxide film was thick enough that no underlying Cu metal was detectable. The dominance of $Cu(OH)_2$ at the higher applied potential (representative of breakdown conditions) can be attributed to a combination of a higher dissolution rate of bare Cu, via the reaction sequence 1a to 1c, and the transpassive oxidation of Cu_2O to Cu^{2+}. As dissolved Cu diffused out of the pores in the passive Cu_2O layer, soluble Cu^+ (as $CuCl_2^-$) would have been oxidized by soluble O_2 and the Cu^{2+} deposited as $Cu(OH)_2$ [25,29]:

$$2CuCl_2^- \ + \ O_2 \ + \ 2H_2O \ + 2e^- \rightarrow \ 2Cu(OH)_2 \ + \ 4Cl^- \hspace{2cm} 5$$

Despite the presence of HCO_3^-/CO_3^{2-}, $CuCO_3.Cu(OH)_2$ was not deposited, which is in agreement with the observations of Adeloju and coworkers [67]. They claimed that HCO_3^-/CO_3^{2-} stabilized the copper oxide film and did not form another film, (e.g., $CuCO_3.Cu(OH)_2$) on the surface. As the carbonate concentration increased, its adsorption stabilized the oxide film by preventing Cl^- adsorption. It was claimed that the minimum required concentration of HCO_3^-/CO_3^{2-} required for this effect to dominate was equal to or greater than 0.005 M. Nishakata [79] claimed that the presence of carbonate hindered the formation of $Cu(OH)_2$; however, our results demonstrated the presence of $Cu(OH)_2$ under both conditions. In addition, the absence of a peak at ~289.3 eV (+/- 0.6 eV) in the C1s spectrum confirmed the absence of surface carbonate species. As a result, we can propose that the formation and amount of $Cu(OH)_2$ was not dependent on HCO_3^-/CO_3^{2-} but on the potential.
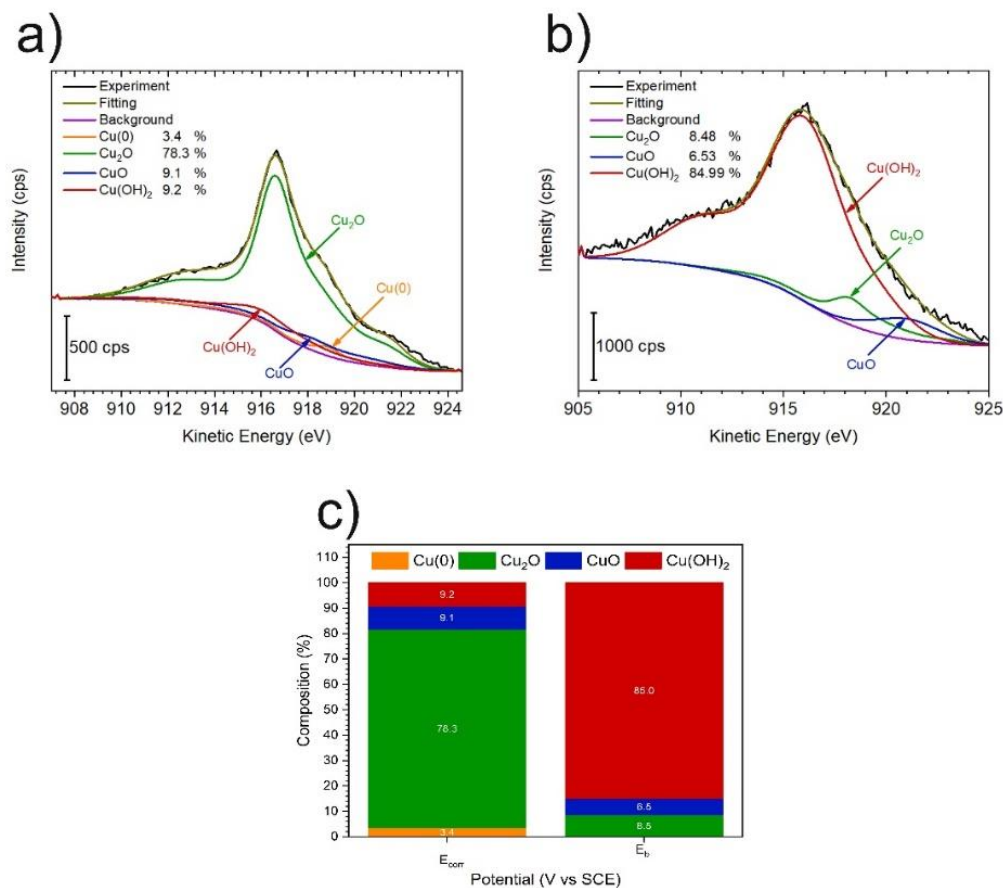
Figure 5.13: CuL$_3$M$_{4,5}$M$_{4,5}$ Auger spectra recorded after oxidation in a HCO$_3^-$/CO$_3^{2-}$ solution containing 0.01 M Cl$^-$; a) at -27mV (representative of E$_{corr}$), the surface is mostly covered with Cu(0) and Cu$_2$O, b) at -7mV (after film breakdown (E$_b$)), surface is mostly covered with Cu(II) oxide and hydroxide with the absence of Cu(0), c) normalized relative film compositions (At%).

The form of the current-time transient at the applied potential of 7 mV vs SCE was consistent with the formation of a Cu(OH)$_2$ outer layer, Fig. 5.10b. The current density increase can be attributed to increased exposure of the dissolving Cu surface as breakdown progressed, with the current density peak occurring once deposition of Cu(OH)$_2$ overwhelmed the dissolution, leading to a decrease in current density. At pH 9, the solubility of Cu^{2+} is very low [80] and local saturation readily achieved. The leveling off of the current density at a moderate value shows the deposited Cu(OH)$_2$ to be porous. The partial detachment of the initially formed Cu$_2$O is consistent with the combination of

metal dissolution and transpassive dissolution ($Cu_2O \rightarrow Cu^{2+}$) occurring simultaneously. While pitting was expected, due to the breakdown of the initially formed Cu_2O layer, it was likely to have been obscured by the dissolution-deposition process.

Fig. 5.14 shows the morphology of Cu surfaces after applying potentials of –110 mV and –99 mV vs SCE in a solution containing 0.1 M Cl⁻. At the lower potential, the surface was covered by a deposited film with a particle size of ~0.3 to ~0.5 µm, with some areas exhibiting minor prosity. This porosity runs linearly and diagonally across the surface shown in Figure 5.14a. At higher magnification, Figure 5.14b reveals small areas where the deposited oxide film appears to have been detached, most likely after removal of the specimen from solution. Other areas experienced shallow pitting and were covered by a thickened deposit with a porous centre, Figure 5.14d.

At the higher potentials, similar detachment of the surface deposit was observed, exposing visible preferential attack of the metal surface at triple points, Figure 5.14g. Also, as shown in Figure 5.14h, corrosion tended to spread across the surface in some areas. Removal of the surface films while avoiding further Cu corrosion revealed both deep pitted locations, Figure 5.14j, and elongated channels, Figure 5.14i. It can be noted that the elongated corrosion morphology may reflect the expectation that corrosion could be enhanced in areas covered by porous deposits, as shown in Figure 5.14a.
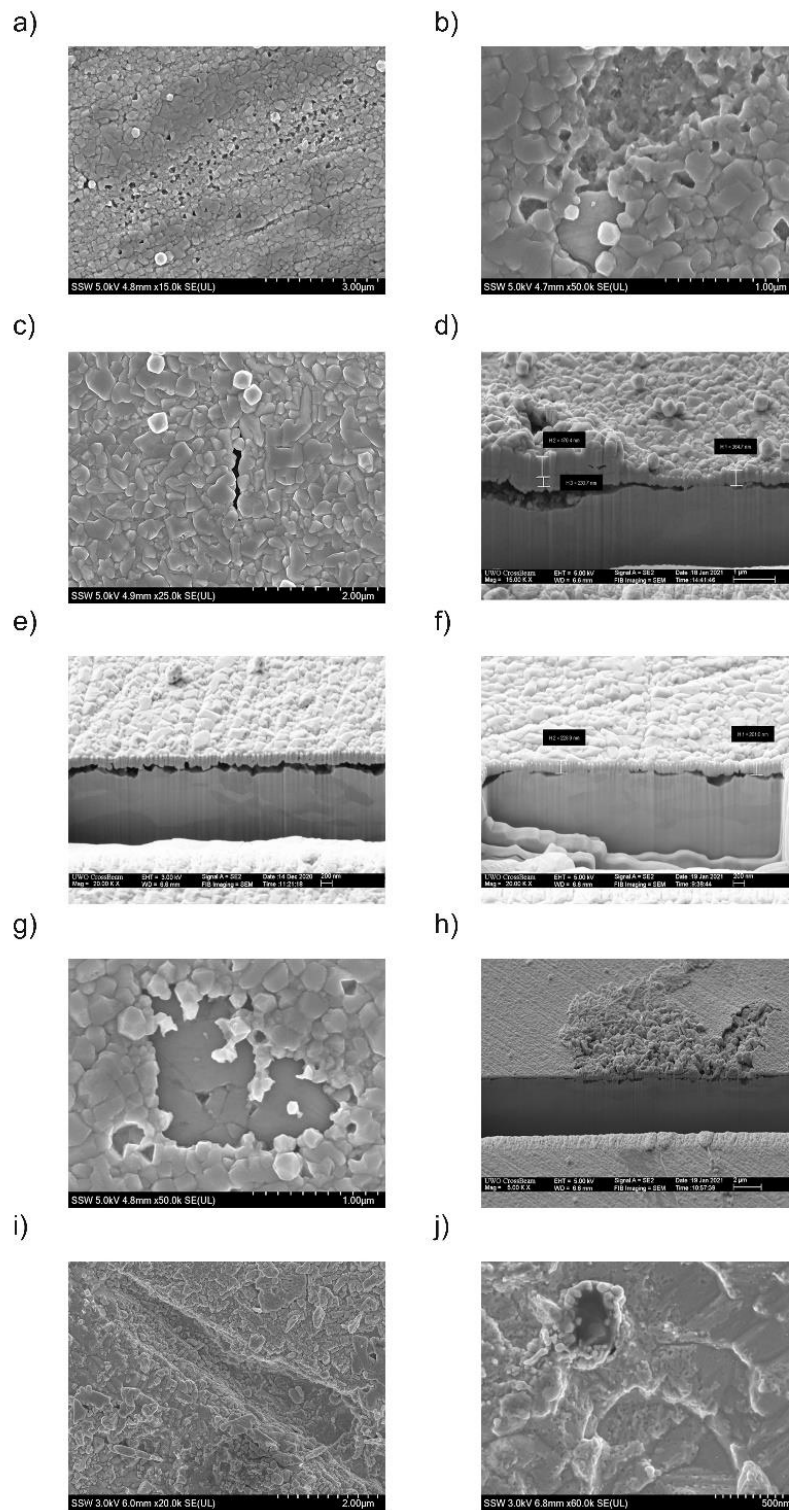
Figure 5.14: Surface morphology of Cu exposed to buffer solutions with 0.1 M Cl⁻ at certain potentials: a-d) E$_{corr}$; e-h) E$_b$, before film removal; i,j) E$_b$, after film removal.

Figure 5.15 shows the composition of oxide films formed in 0.1 M NaCl solution at the two different applied potentials as determined by Auger electron spectroscopy. The oxide film was composed of Cu_2O and $Cu(OH)_2$, without any detectable amount of CuO.

The O 1s spectrum (not shown here) was analyzed to confirm the presence of hydroxide on the Cu sample after exposure at an applied potential of E_b. XPS results showed that the uniformly distributed film (Fig. 5.14 e and f) was a very compact deposit of Cu_2O. Since Cu is more likely to dissolve as $CuCl_x^{(1-x)-}$ and the film was dominantly Cu_2O, this would suggest that the deposit was formed predominantly via reaction 2. This observation is in good agreement with the current-time transient (Fig. 5.10d) which shows an initial period of passivity followed by breakdown. Following the breakdown, there was a large, slow current transient, followed by the re-establishment of a very low current, consistent with a coherent protective film, as shown in Fig. 5.14 e and f. Several sites experienced obvious shallow pitting, as presented in Fig. 5.14d, followed by the accumulation of a thicker deposit, which appears to be porous at the center. The pits were not backfilled with corrosion product deposits. A probability would be the formation of $CuCl_x^{(1-x)-}$ in the presence of a substantial $[Cl^-]$. Since this reaction consumes OH^-, it would decrease the pH locally, which could disturb buffering by HCO_3/CO_3^{2-} and inhibit Cu^{2+} formation within the pore by increasing its solubility. Beyond the pore, this pH suppression would be neutralized and Cu_2O formation promoted, which could account for the thicker deposit at this location.
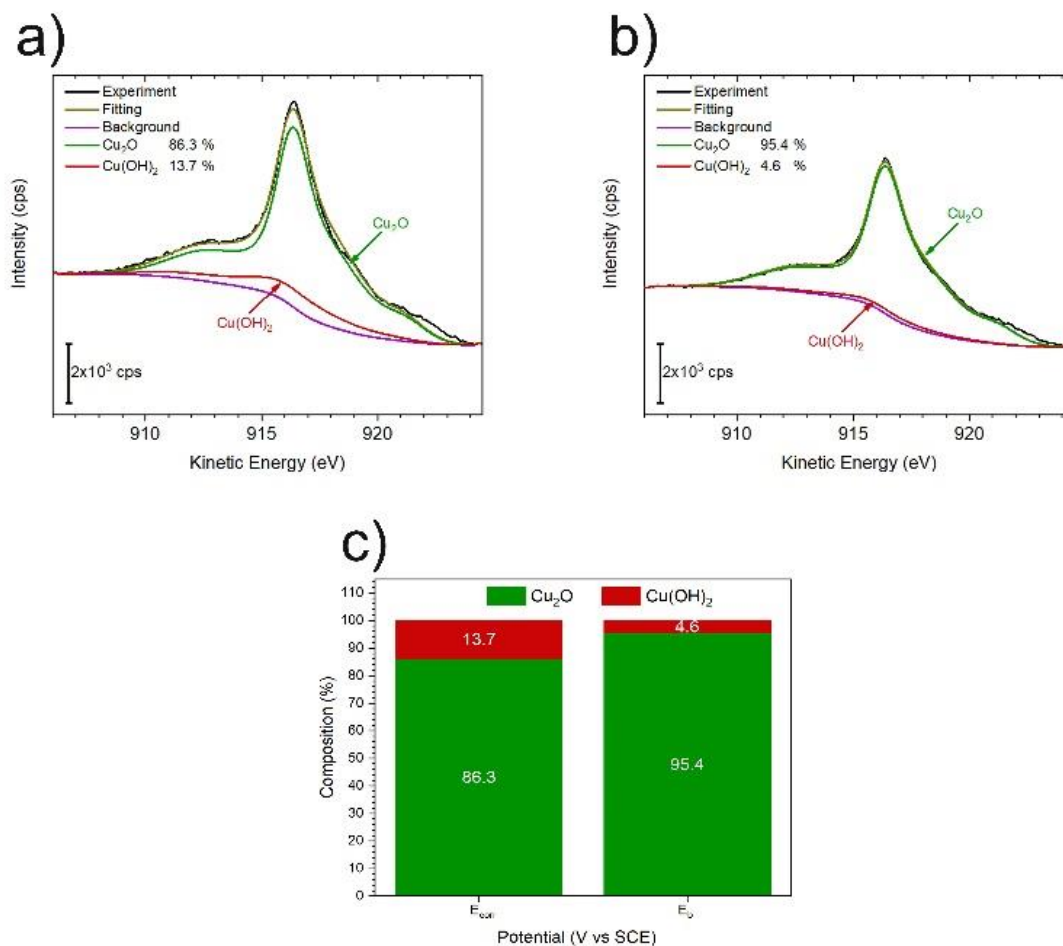
Figure 5.15: CuL₃M₄,₅M₄,₅ Auger spectra recorded after oxidation in a HCO₃⁻/CO₃²⁻ solution containing 0.1 M Cl⁻ at various potentials: a) -110 mV (representative of E_corr); b) -99mV (representative of film breakdown, E_b); c) normalized relative film compositions (at%) at E_corr and E_b.

Fig. 5.16 shows the compositions determined from Auger spectra for two different [Cl⁻] and four different applied potentials. Increasing chloride concentration to 0.1 M hindered the formation of CuO. Another important point was the dependency of Cu_2O and $Cu(OH)_2$ on applied potential, since the surface was mostly covered with Cu_2O at potentials lower than -27 mV vs SCE; however, Cu_2O was converted to $Cu(OH)_2$ with further increases of potential to 7 mV vs SCE.
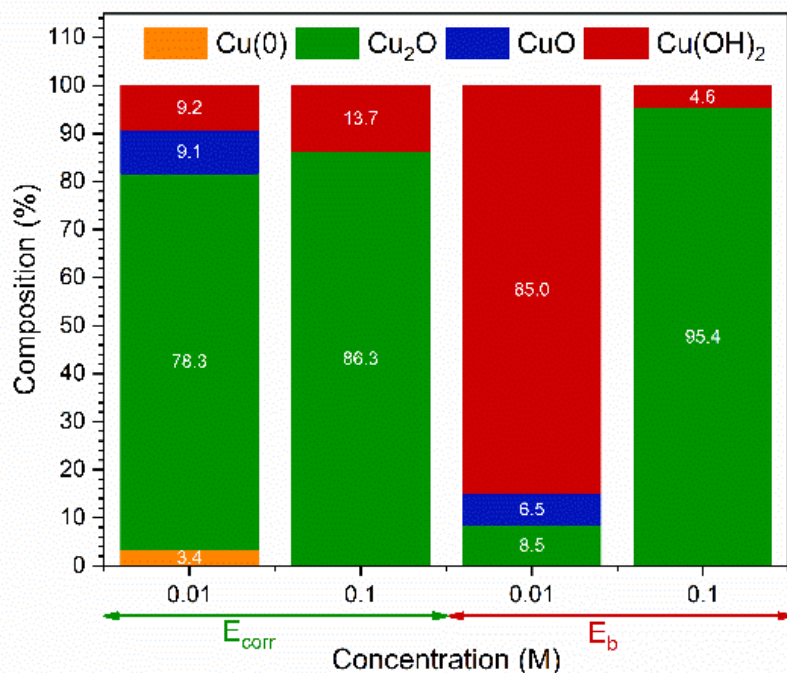
Figure 5.16: Composition of the passive film on Cu in buffer solutions with different [Cl⁻] as determined by Auger electron spectroscopy.

Generally speaking the surface compositions were dominated by either Cu_2O or $Cu(OH)_2$, as shown in Fig. 516. The amounts of CuO were minimal, making this phase of marginal importance. When the Cu was anodically oxidized at -27mV (in 0.01 M Cl⁻), when only a low current was observed, Cu_2O was dominantly formed as a passive layer. When the [Cl⁻] was maintained at 0.01M and the potential increased from -27 mV to +7 mV, $Cu(OH)_2$ dominated on the surface; although it was most likely that a sublayer of Cu_2O persisted but was difficult to detect by XPS. The current density behaviour (Fig 5.10) confirmed that a short period of passivation, attributable to the formation of Cu_2O, existed prior to breakdown and an increase in current density, followed by a subsequent decrease in current density, was attributable to the deposition of $Cu(OH)_2$. There are three possible mechanisms of formation of the Cu^{2+} (to form $Cu(OH)_2$):

   I.   Reaction of $CuCl^{2-}$ with dissolved O_2;

  II.   Direct metal dissolution as Cu^{2+};

 III.   Conversion of Cu_2O to Cu^{2+}.

Reactions II and III are likely for the reasons noted below and because the applied potential in this case (7mV vs SCE) is the most positive of the four potentials investigated.

When the [Cl⁻] was increased to 0.1 M, the potentials applied were considerably lower (-110mV and -99mV vs SCE). In both cases Cu_2O was dominant, with only minimal amounts of $Cu(OH)_2$ formed. This could be attributable to the inhibiting effect of Cl⁻ on the reaction of $CuCl^{2-}$ with O_2 (to yield Cu^{2+}) as shown by Sharma and Millero[81]. This study showed that the rate decreased by many orders of magnitude as [Cl⁻] was increased). At the lower [Cl⁻], Cu^{2+} formation occured (leading to $Cu(OH)_2$ deposition), suggesting that it could be formed by the reaction of $CuCl^{2-}$ with dissolved O_2. These observations indicate that the dominant influence on the behaviour was potential. If breakdown did not occur until the specimen was polarized to a positive potential at which the direct ($Cu \rightarrow Cu^{2+}$: $Cu_2O \rightarrow Cu^{2+}$) and indirect ($Cu^+ + O_2 \rightarrow Cu^{2+}$) reactions were dominant, $Cu(OH)_2$ deposition dominated, yielding only partial passivation.

A combination of Cl⁻ and high potential is supported by the differences in the initial current density behaviour on first applying the potential. The initial passive period is short at high potentials (7 mV) but extended at lower potentials (-110 mV and -99 mV). Other features to be explained are the longer current density transients at low potential and high [Cl⁻] and the observation that the film eventually formed at the lower potentials (-110 mV and -99 mV) and higher [Cl⁻] is considerably more protective, despite a protracted period of high current density. This indicates that, despite film breakdown, extensive dissolution, and the possibility of pitting, redeposition of Cu_2O eventually blocks the surface. Three mechanisms are possible [76]:

I. The combination of

$$CuCl_{ads} \;+\; OH^- \;\leftrightarrow\; Cu(OH)_{ads} \;+\; Cl^- \qquad\qquad 6$$

and

$$2Cu(OH)_{ads} \;\rightarrow\; Cu_2O \;+\; H_2O \qquad\qquad 7$$

II. Hydrolysis of $CuCl_2^-$

$$2CuCl_2^- \ + \ H_2O \ \rightarrow Cu_2O \ + \ 2H^+ \ + \ 4Cl^- \qquad\qquad 8$$

$$2CuCl_{ads} \ + \ H_2O \ \rightarrow Cu_2O \ + \ 2H^+ \ + \ 2Cl^- \qquad\qquad 9$$

III. Conversion to Cu^{2+} does occur to some extent (by reaction with O_2), followed by the reaction:

$$Cu \ + \ Cu^{2+} \ + \ H_2O \ \rightarrow \ Cu_2O \ + \ 2H^+ \qquad\qquad 10$$

Since the Cu_2O is formed compactly on the surface (i.e., the current density is strongly suppressed), all reactions except reaction 8 seem possible, although we were not able to separate them with current results.

5.3.5 Effect of Applied Potential on Pitting Probability of Cu

Different applied potentials were selected within the highest range of E_{corr} and extreme values of E_b to investigate the pitting susceptibility of Cu in bicarbonate buffer solutions containing 0.01 M Cl^- at pH 9 (Fig. 5.17).
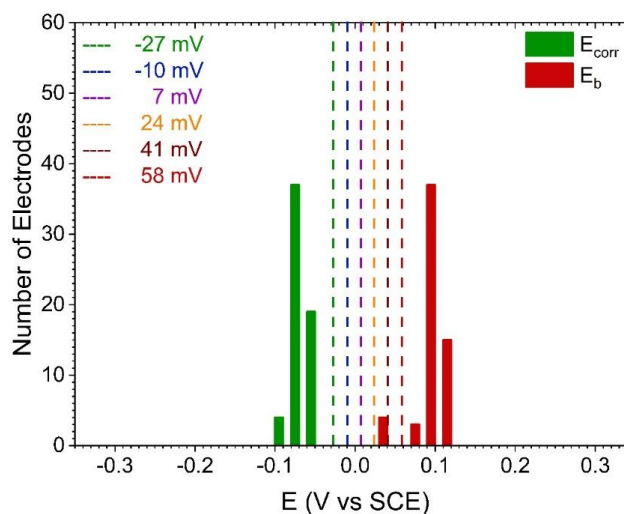
Figure 5.17: Range of applied potentials in bicarbonate buffer solutions containing 0.01 M Cl^- based on the histograms of E_{corr} and E_b values.

Fig. 5.18-a shows the current-time transients at different applied potentials. The peak current density changed slightly from -10 mV to 24 mV; however, the peak current density increased significantly with further increase of the applied potential to 41 mV (greater charge density) (Fig. 5.18-d,e). The time of pit initiation is the time at which the current begins to increase. Since only passive film formation occured at the lowest potential (-27 mV vs SCE), this can be considered as establishing a baseline for the other current-time transients. Although a considerably larger charge was consumed at the two highest applied potentials, the current recorded at longer times only increased slightly as the potential was increased. This suggested that the overall reactivity of the surface was not particularly dependent on potential; i.e., the $Cu(OH)_2$ film became protective except for the residual breakdown sites.

Pitting was observed for potentials greater than -10 mV vs SCE (Fig. 5.18-a). Increasing the potential to 41 mV caused a longitudinal breakdown of the passive films, leading to the pitting corrosion of Cu along the breakdown sites. Also, a covered pit was observed (Fig 5.19-i). Based on the LSF framework [40-42, 51, 52], the pit interior could be either smooth or crystallographic, depending on the perforation size (a) of the covered pit. The pit is under diffusion control if $a < a_{sat}$ and under charge transfer control when $a_{sat} < a < a_{crit}$. However, we did not remove the oxide film to investigate the morphology of the underlying pit and the size of the perforation. As shown in Fig. 5.19-k through n, at an applied potential of 58 mV, a large portion of the passive film was dissolved, and this exposed the bare Cu to the aggressive solution. Shoesmith et al. [12] proposed the same anodic charge and oxide film morphology for different applied potentials when the potential was equal to or greater than -220 mV, suggesting that passive film morphology was independent of potential and a charge dependent phenomena; however, our result indicated an increase of charge density with potential (Fig. 5.18-d). Also, the oxide film morphology was determined to be a potential-dependent parameter.
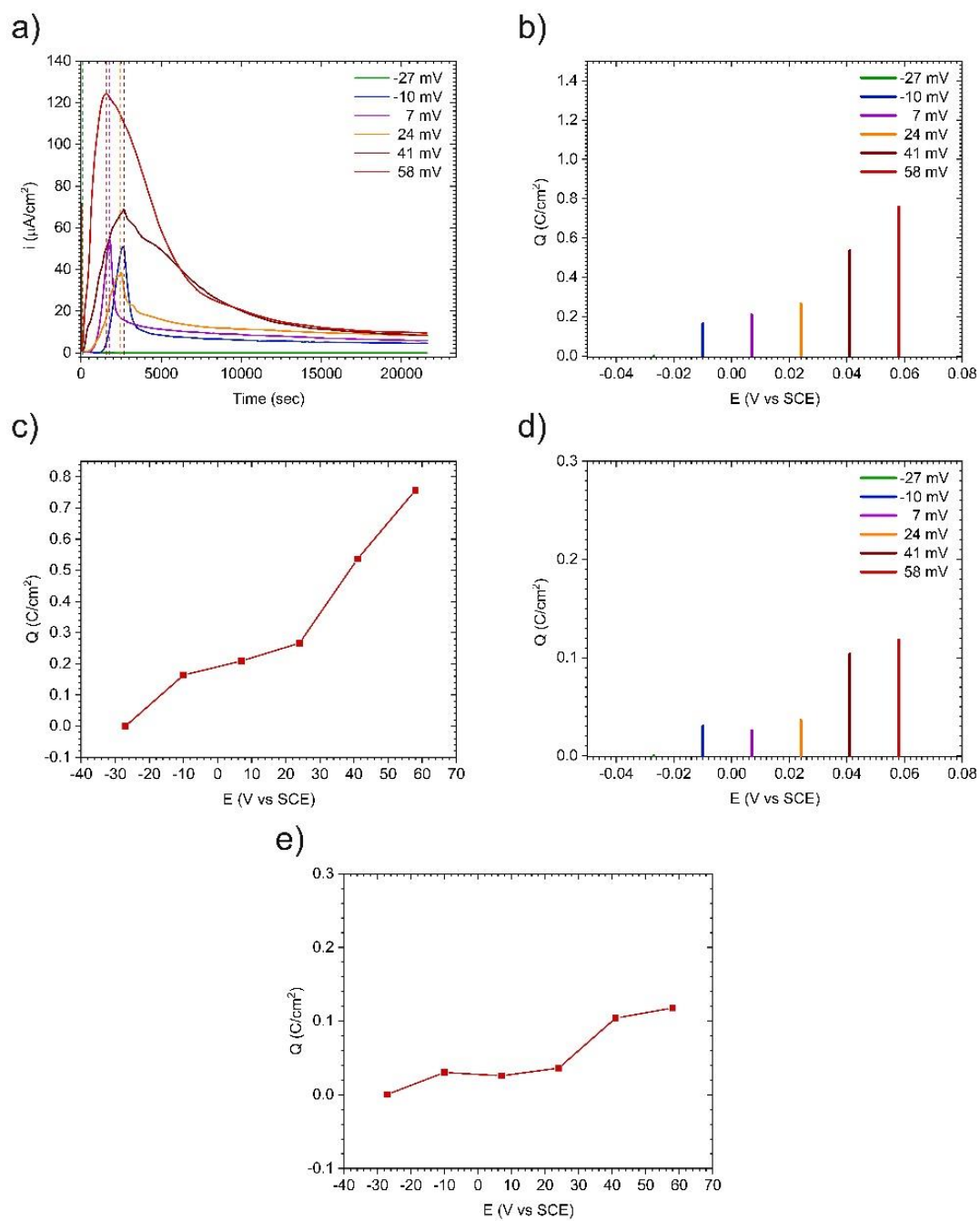
Figure 5.18: a) Current-time transients at different applied potentials b,c) cumulative charge density at different applied potentials d,e) cumulative charge density (peak current) at different applied potentials.

Different pitting morphologies have been observed, depending on the applied potential (Fig. 5.19-a through j). At lower applied potentials, the passive film was almost intact and only a few small pits were observed on the surface (Fig. 5.19-a to d). Increasing the applied potential to 7 mV resulted in breakdown of the passive film. Also, hemispherical pits were observed, with the presence of chloride at the pit surface (Fig. 5.19-e). The pitting morphology was different at 41 and 58 mV since the pits propagated longitudinally. This could be the result of pit propagation along the grain boundaries. Also, a large amount of the passive film was completely dissolved at these applied potentials and a large frequency of covered pits was observed at higher applied potentials (Fig. 5.19-i through n). It is noteworthy to mention that corrosion product deposits grew perpendicular to the passive film, which might result in the mechanical breakdown of the passive film (Fig. 5.19-h,k). Increasing the applied potential contributed to the dissolution of a large area of the passive film, as observed in Fig. 5.19-k. EDX results (Fig. 5.20) indicated the presence of copper chloride species ($CuCl$ or $CuCl_2$) on the Cu surface where the passive film was ruptured. These could eventually oxidize to Cu^{2+}, yielding $Cu(OH)_2$, as shown in the XPS results (Fig. 5.21). Also, formation of Cu_2O via reaction 2 appears not to have been the dominant reaction, based on the XPS results (Fig. 5.21). Our results indicate extensive and severe damage (pitting corrosion) at higher potentials; more dissolution of the oxide film and higher susceptibility to breakdown have been observed in samples with higher charge densities.
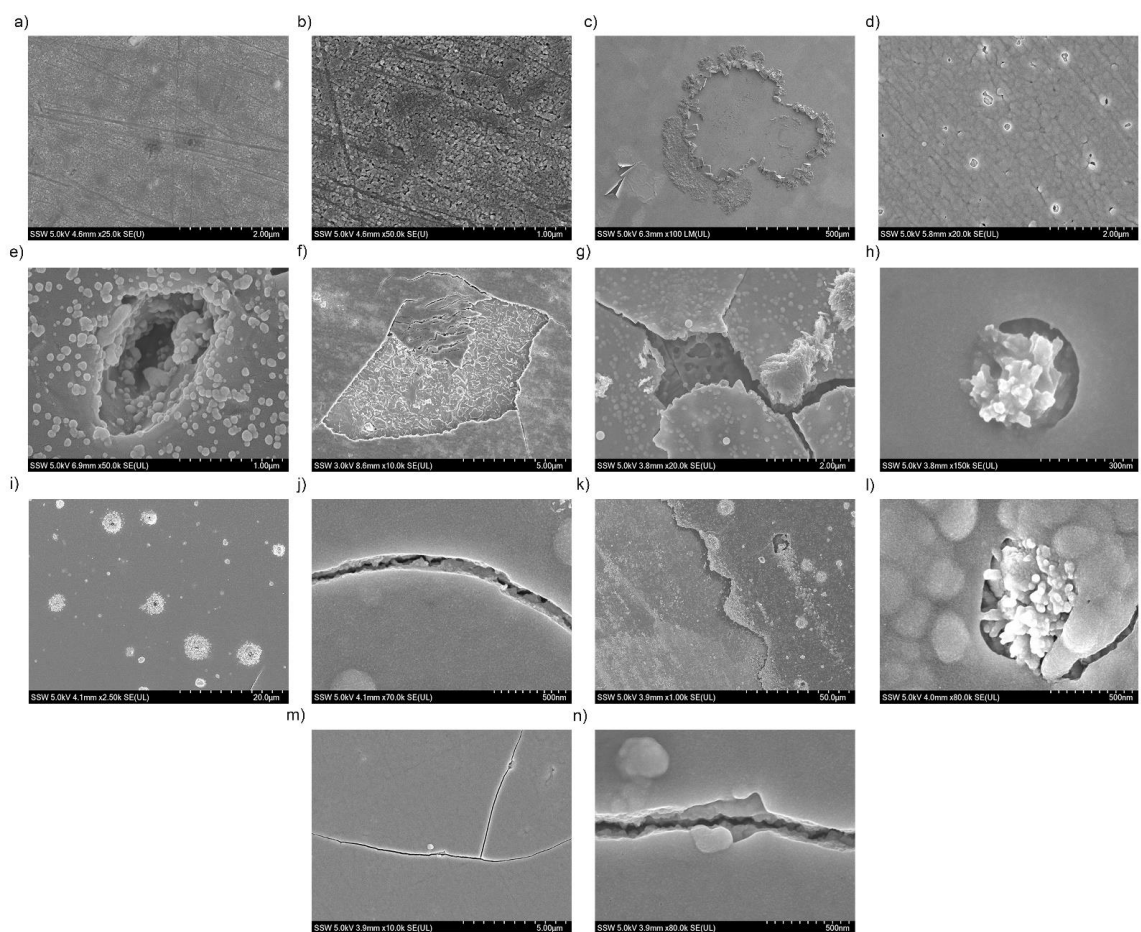
Figure 5.19: Surface morphology of Cu in buffer solutions with 0.01 M Cl⁻ and different applied potentials: a,b) -27 mV; c,d) -10 mV; e,f) 7 mV; g,h) 24 mV; i,j) 41 mV; k,l,m,n) 58 mV.
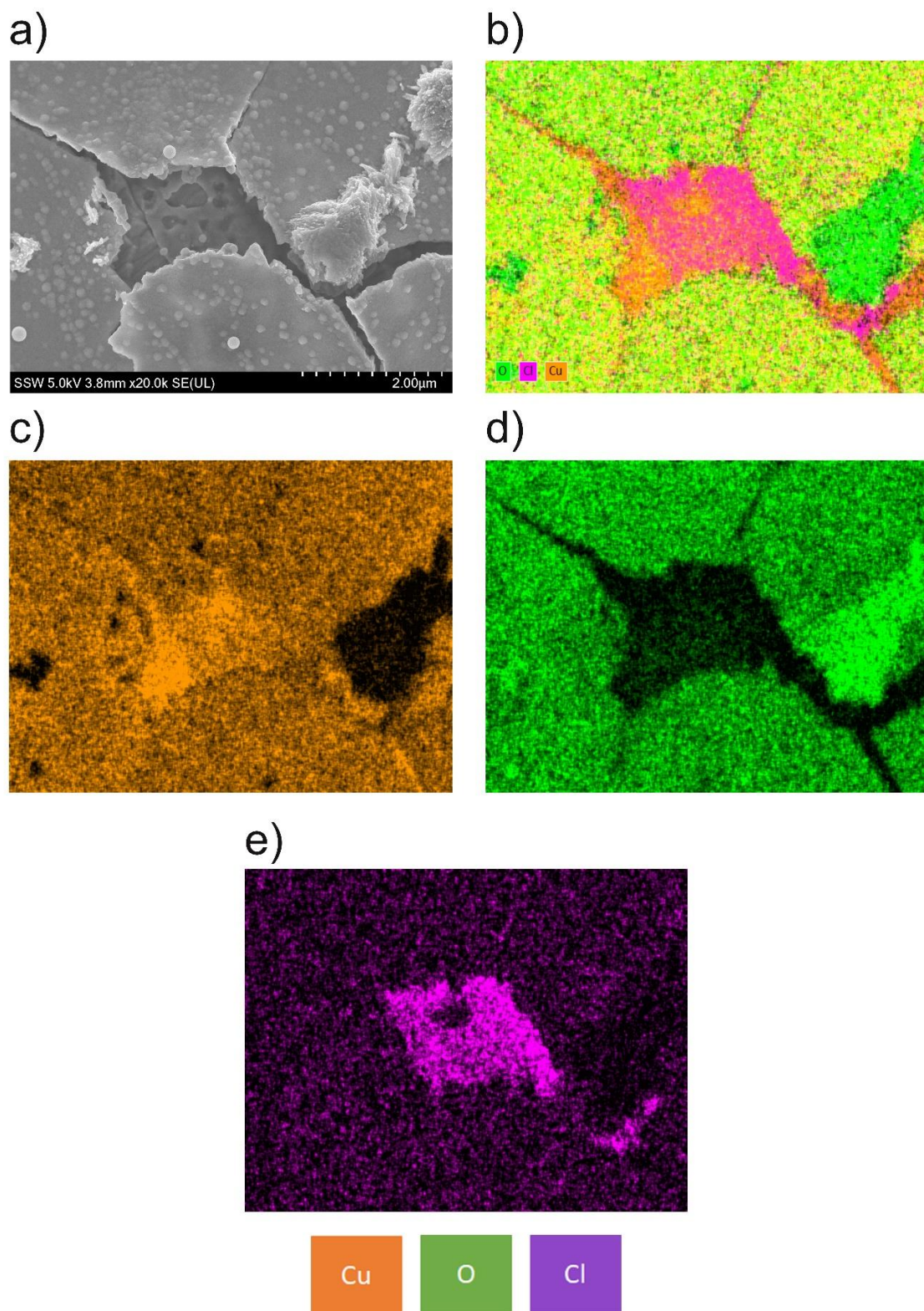
Figure 5.20: EDX map of passive film after exposure to buffer solution with 0.01 M Cl⁻ at an applied potential of 24 mV vs. SCE.

The compositions of oxide films are shown in Fig. 5.21. A small amount of Cu(0) is observed only at a potential of -27 mV (close to E_{corr}), while the surface is mostly covered with a passive film of Cu_2O. The minimal amounts of $CuO/Cu(OH)_2$ may reflect a minor reactivity. Even though the film had not broken down, it clearly shows what looks like some chemical attack that could have led to $Cu(OH)_2$ formation. The surface was covered, mostly with $Cu(OH)_2$, by a further increase of applied potential, which occurred either directly from base Cu or/and from the conversion of Cu_2O and CuO through the reactions 11 to 14. In this case, Cu(0) was undetectable [82].

$$Cu = Cu^{2+} + 2e^- \qquad\qquad 11$$

$$Cu^{2+} + 2OH^- = Cu(OH)_2 \qquad\qquad 12$$

$$Cu_2O + H_2O + 2OH^- = 2Cu(OH)_2 + 2e^- \qquad\qquad 13$$

$$CuO + H_2O = Cu(OH)_2 \qquad\qquad 14$$
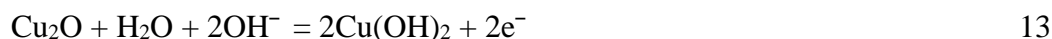
The greatest amount of $Cu(OH)_2$ was observed at 7 mV (close to the lowest E_b) and then the percentage of $Cu(OH)_2$ decreased and the amount of CuO increased with further increase of applied potential, probably due to the conversion of $Cu(OH)_2$ to CuO via reaction 15:

$$Cu(OH)_2 = CuO + H_2O \qquad\qquad 15$$

Moreover, the amount of Cu_2O increased with further increases in applied potential, due to the reduction of $Cu(OH)_2$ to Cu_2O via reaction 16:

$$2Cu(OH)_2 + 2e^- = Cu_2O + H_2O + 2OH^- \qquad\qquad 16$$

As shown in Fig. 5.21, XPS results indicate that increasing the potential from -27 mV to 7 mV resulted in the conversion of Cu(0) and Cu_2O to $Cu(OH)_2$, while the amount of CuO changed slightly. For potentials greater than 7 mV, two possible conversions could happen depending on the range of applied potential. The $Cu(OH)_2$ was converted to CuO and Cu_2O with increasing the potential from 7 mV to 24 mV, and then a further increase of the applied potential to 41 mV resulted in the conversion of Cu_2O to CuO and

$Cu(OH)_2$. Finally, the amount of $Cu(OH)_2$ decreased while CuO and Cu_2O increased with increasing of the potential to 58 mV. It is important to note that the amount of CuO increased with applied potential, but $Cu(OH)_2$ and Cu_2O either increased or decreased with increases in the applied potential. As a result, no clear relationship was observed between the composition of the film and the applied potential. One reason could be that XPS only shows the composition of the top 5-8 nm of the surface, so it does not convey the fractional composition of the total film.

Shoesmith et al. [12] claimed that passive film morphology was independent of applied potential but a charge-dependent phenomenon; however, our XPS and electrochemical results indicated the dependency of passive film morphology on both the potential and the charge density. At lower applied potentials, the rate of metal dissolution and supersaturation is low at the metal surface, so the surface will be mostly covered by Cu_2O. On the other hand, the dissolution rate increases with further increases in the applied potential, leading to the minimum required supersaturation condition on the metal surface. In this case, the surface will be covered mostly with CuO or/and $Cu(OH)_2$.
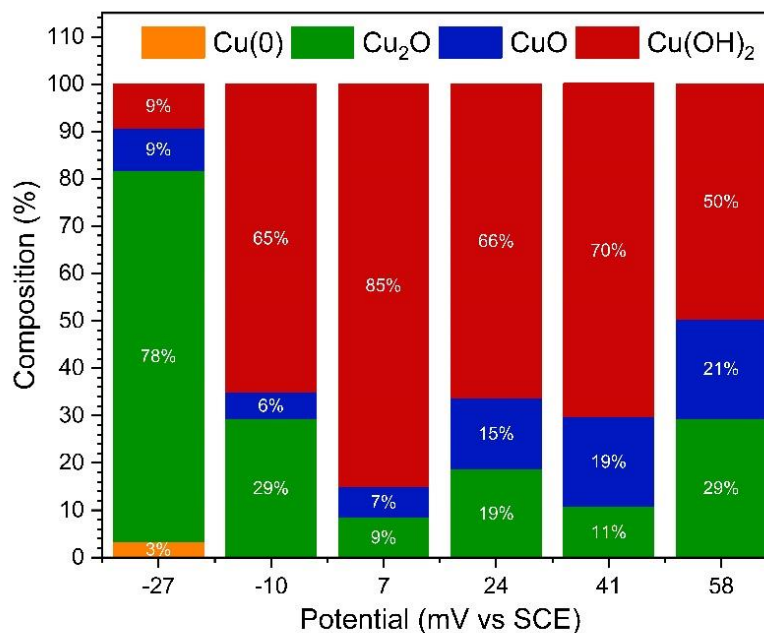
Figure 5.21: Compositions of passive films grown at different applied potentials in buffer solution with 0.01 M Cl⁻.

5.4   Conclusions

A series of potentiodynamic and potentiostatic experiments were conducted in bicarbonate buffer solutions with different chloride concentrations to study the pitting susceptibility and passive film morphology of Cu. The surface compositions of samples were examined using the XPS technique to create a solid understanding of the effect of applied potential and charge density on the morphology and composition of the passive film. E_{corr} shifted to more negative values at higher [Cl⁻] due to the greater rate of dissolution. SEM images of specimens after potentiodynamic experiments showed a large passive film breakdown at lower [Cl⁻] while uniform corrosion was observed at higher [Cl⁻]. The frequency of breakdown increased with [Cl⁻] resulting in a narrower distribution of E_b. The pitting probability of Cu increased with increasing [Cl⁻] due to the lower difference between E_{corr} and E_b ($E_{corr} - E_b$) in 0.1 M Cl⁻ solution. In 0.01 M Cl⁻ solution, no pitting was observed when the applied potential was close to E_{corr}; however,

deep pits were observed when the applied potential was chosen to be close to E_b (7 mV vs SCE). Increasing the [Cl^-] resulted in initiation and propagation of pits even at potentials close to E_{corr}, which was in good agreement with our statistical analysis. XPS analysis indicated a mixed oxide layer composed of Cu_2O, CuO, and $Cu(OH)_2$. Cu(0) was only observed on specimens that were exposed to 0.01 M Cl^- solution at potentials close to E_{corr}, due to the formation of a porous and non-protective film on the Cu surface. The composition of the passive film was dependent on both the [Cl^-] and the applied potential. Both the passive film morphology and the charge density were dependent on the applied potential, so different breakdown mechanisms and passive film compositions were determined at the different applied potentials.

5.5   Acknowledgment

5.6 References

[1] R.C. Newman, 2001 W.R. Whitney award lecture-Understanding the corrosion of stainless steel, Corrosion, 57 (2001) 1030-1041.

[2] V.M. Salinas-Bravo, R.C. Newman, An alternative method to determine critical pitting temperature of stainless steels in ferric chloride solution, Corrosion Science, 36 (1994) 66-77.

[3] G.T. Gaudet, W.T. Mo, T.A. Hatton, J.W. Tester, J. Tilly, H.S. Isaacs, R.C. Newman, Mass transfer and electrochemical kinetic interactions in localized pitting corrosion, AlChE Journal, 32 (1986) 949-958.

[4] N.J. Laycock, M.H. Moayed, R.C. Newman, Metastable pitting and the critical pitting temperature, Journal of The Electrochemical Society, 145 (1998) 2622-2628.

[5] P.C. Pistorius, G.T. Burstein, Metastable pitting corrosion of stainless steel and the transition to stability, Royal Society London, 341 (1992) 531-559.

[6] S.T. Pride, J.R. Scully, J.L. Hudson, Metastable pitting of aluminum and criteria for the transition to stable pit growth, Journal of The Electrochemical Society, 141 (1994) 3028-3040.

[7] G.S. Frankel, L. Stockert, F. Hunkeler, H. Boehni, Metastable pitting of stainless steel, Corrosion, 43 (1987) 429-436.

[8] G.S. Frankel, Pitting corrosion of metals: A review of the critical factors, Journal of The Electrochemical Society, 145 (1998) 2186-2198.

[9] J.R. Galvele, Transport processes and the mechanism of pitting of metals, Journal of The Electrochemical Society, 123 (1976) 464-474.

[10] G.S. Frankel, N. Sridhar, Understanding localized corrosion, Materials Today, 11 (2008) 38-44.

[11] B. Miller, Split-Ring disk study of the anodic processes at a copper electrode in alkaline solution, Journal of Electrochemical Society, 116 (1969).

[12] D.W. Shoesmith, T.E. Rummery, D. Owen, W. Lee, Anodic oxidation of copper in alkaline solutions I. Nucleation and growth of cupric hydroxide films, Journal of The Electrochemical Society, 123 (1976) 790-799.

[13] I. Milosev, M. Metikos-Hukovic, M. Drogowska, H. Menard, Breakdown of passive film on copper in bicarbonate solutions containing sulfate ions, Journal of The Electrochemical Society, 139 (1992) 2409-2418.

[14] J. Ambrose, R.G. Barradas, D.W. Shoesmith, Investigation of copper in aqueous alkaline solutions by cycling voltammetry, Journal of Electroanalytical Chemistry and Interfacial Electrochemistry, 47 (1973) 47-64.

[15] V. Ashworth, D. Fairhurst, The anodic formation of Cu_2O in alkaline solutions, Journal of The Electrochemical Society, 124 (1977) 506-517.

[16] M. Drogowska, L. Brossard, H. Menard, Comparative study of copper behaviour in bicarbonate and phosphate aqueous solutions and effect of chloride ions, Journal of Applied Electrochemistry, 24 (1994).

[17] M.R.G.d. Chialvo, J.O. Zerbino, S.L. Marchiano, Correlation of electrochemical and ellipsometric data in relation to the kinetics and mechanism of Cu_2O electroformation in alkaline solutions, Journal of Applied Electrochemistry, 16 (1986) 517-526.

[18] S.B. Adeloju, H.C. Hughes, The corrosion of copper pipes in high chloride-low carbonate mains water, Corrosion Science, 26 (1986) 851-870.

[19] M.R.G.d. Chialvo, A.J. Arvia, The electrochemical behaviour of copper in alkaline solutions containing sodium sulphide, Journal of Applied Electrochemistry, 15 (1985) 685-696.

[20] C.J. Park, M.M. Lohrengel, T. Hamelmann, M. Pilaski, H.S. Kwon, Grain-dependent passivation of surfaces of polycrystalline zinc, Electrochimica Acta, 47 (2002) 3395-3399.

[21] J. Kunze, V. Maurice, L.H. Klein, H.-H. Strehblow, P. Marcus, In situ STM study of the duplex passive films formed on Cu(111) and Cu(001) in 0.1 M NaOH, Corrosion Science, 46 (2004) 245-264.

[22] M.R.G.D. Chialvo, R.C. Salvarezza, D.V. Moll, A.J. Arvia, Kinetics of passivation and pitting corrosion of polycrystalline copper in borate buffer solutions containing sodium chloride., Electrochimica Acta, 30 (1985) 1501–1511.

[23] K.A. Lill, A.W. Hassel, G. Frommeyer, M. Stratmann, Scanning droplet cell investigations on single grains of a FeAlCr light weight ferritic steel, Electrochimica Acta, 51 (2005) 978-983.

[24] E. Martinez-Lombardia, Y. Gonzalez-Garcia, L. Lapeire, I. De Graeve, K. Verbeken, L. Kestens, J.M.C. Mol, H. Terryn, Scanning electrochemical microscopy to study the effect of crystallographic orientation on the electrochemical activity of pure copper, Electrochimica Acta, 116 (2014) 89-96.

[25] A. Naseer, A.Y. Khan, A study of growth and breakdown of passive film on copper surface by electrochemical impedance spectroscopy, Turkish Journal of Chemistry, 33 (2009) 739 - 750.

[26] F.M. Al-Kharafi, Y.A. El-Tantawy, Passivation of copper: Role of some anions in the mechanism of film formation and breakdown, Corrosion Science, 22 (1982) 1-12.

[27] J. Ambrose, R.G. Barradas, D.W. Shoesmith, Rotating copper disk electrode studies of the mechanism of the dissolution-passivation step on copper in alkaline solutions, Journal of Electroanalytical Chemistry and Interfacial Electrochemistry, 47 (1973) 65-80.

[28] H.D. Speckmann, M.M. Lohrengel, J.W. Schultze, H.H. Strehblow, The growth and reduction of duplex oxide films on copper, Ber. Bunsenges. Phys. Chem, 89 (1985) 392-402.

[29] H. Cong, J.R. Scully, Use of coupled multielectrode arrays to elucidate the pH dependence of copper pitting in potable water, Journal of The Electrochemical Society, 157 (2010) 36 - 46.

[30] N.S. McIntyre, S. Sunder, D.W. Shoesmith, F.W. Stanchell, Chemical information from XPS—applications to the analysis of electrode surfaces, Journal of Vacuum Science and Technology, 18 (1981) 714-721.

[31] A.G.G. Allah, M.M. Abou-Romia, W.A. Badawy, H.H. Rehan, Effect of halide ions on passivation and pitting corrosion of copper in alkaline solutions, Materials and Corrosion, 42 (1991) 584-591.

[32] H.H. Strehblow, B. Titze, The investigation of the passive behaviour of copper in weakly acid and alkaline solutions and the examination of the passive film by ESCA and ISS, Electrochimica Acta, 25 (1980) 839-850.

[33] A. Kolics, J.C. Polkinghorne, A. Wieckowski, Adsorption of sulfate and chloride ions on aluminum.pdf, Electrochimica Acta, 43 (1998) 2605-2618.

[34] S.Y. Yu, W.E. O'Grady, D.E. Ramaker, P.M. Natishan, Chloride ingress into aluminum prior to pitting corrosion-an investigation by XANES and XPS, Journal of Electrochemical Society, 147 (2000).

[35] P.M. Natishan, W.E. O'Grady, Chloride ion interactions with oxide-covered aluminum leading to pitting corrosion: A Review, Journal of The Electrochemical Society, 161 (2014) C421-C432.

[36] T. Li, L. Liu, B. Zhang, Y. Li, F. Wang, Growth of single corrosion pit in sputtered nanocrystalline stainless steel film, Corrosion Science, 111 (2016) 186-198.

[37] N.J. Laycock, R.C. Newman, Localised dissolution kinetics, salt films and pitting potentials, Corrosion Science, 39 (1997) 1771-1790.

[38] P. Marcus, V. Maurice, H.H. Strehblow, Localized corrosion (pitting): A model of passivity breakdown including the role of the oxide layer nanostructure, Corrosion Science, 50 (2008) 2698-2704.

[39] G.S. Frankel, T. Li, J.R. Scully, Localized corrosion: Passive film breakdown vs pit growth stability, Journal of The Electrochemical Society, 164 (2017) C180-C181.

[40] T. Li, J.R. Scully, G.S. Frankel, Localized corrosion: passive film breakdown vs pit growth stability: part II. A model for critical pitting temperature, Journal of The Electrochemical Society, 165 (2018) C484-C491.

[41] T. Li, J.R. Scully, G.S. Frankel, Localized Corrosion: Passive film breakdown vs. pit growth stability: Part III. A unifying Set of principal parameters and criteria for pit stabilization and salt film formation, Journal of The Electrochemical Society, 165 (2018) C762-C770.

[42] T. Li, J.R. Scully, G.S. Frankel, Localized corrosion: passive film breakdown vs. pit growth stability: part IV. The role of salt film in pit growth: A mathematical framework, Journal of The Electrochemical Society, 166 (2019) C115-C124.

[43] D.C. Kong, C.F. Dong, X.Q. Ni, A.N. Xu, C. He, K. Xiao, X.G. Li, Long-term polarisation and immersion for copper corrosion in high-level nuclear waste environment, Materials and Corrosion, 68 (2017) 1070-1079.

[44] J. Srinivasan, R.G. Kelly, One-dimensional pit experiments and modeling to determine critical factors for pit stability and repassivation, Journal of The Electrochemical Society, 163 (2016) C759-C767.

[45] V. Maurice, W.P. Yang, P. Marcus, X-ray photoelectron spectroscopy and scanning tunneling microscopy study of passive films formed on (100) Fe-18Cr-13Ni single-crystal surfaces, Journal of The Electrochemical Society, 145 (1998) 909-920.

[46] V. Maurice, W.P. Yang, P. Marcus, XPS and STM investigation of the passive film formed on Cr(110) single-crystal surfaces, Journal of The Electrochemical Society, 141 (1994) 3016-3027.

[47] N. Sato, A theory for breakdown of anodic oxide films on metals, Electrochimica Acta, 16 (1971) 1683-1692.

[48] X. Wei, C. Dong, P. Yi, A. Xu, Z. Chen, X. Li, Electrochemical measurements and atomistic simulations of Cl^--induced passivity breakdown on a Cu_2O film, Corrosion Science, 136 (2018) 119-128.

[49] R. Huang, D.J. Horton, F. Bocher, J.R. Scully, Localized corrosion resistance of Fe-Cr-Mo-W-B-C bulk metallic glasses containing Mn+Si or Y in neutral and acidified chloride solution, Corrosion, 66 (2010).

[50] D.C. Silverman, Practical corrosion prediction using electrochemical techniques, John Wiley & Sons, Inc.2011.

[51] T. Li, J. Wu, G.S. Frankel, Localized corrosion: Passive film breakdown vs. Pit growth stability, Part VI: Pit dissolution kinetics of different alloys and a model for pitting and repassivation potentials, Corrosion Science, 182 (2021).

[52] T. Li, J.R. Scully, G.S. Frankel, Localized corrosion: passive film breakdown vs pit growth stability: part V. Validation of a new framework for pit growth stability using one-dimensional artificial pit electrodes, Journal of The Electrochemical Society, 166 (2019) C3341-C3354.

[53] R.M. Souto, S. Gonzalez, R.C. Salvarezza, A.J. Arvia, Kinetics of copper passivation and pitting corrosion in Na_2SO_4 containing dilute NaOH aqueous solution, Electrochimica Acta, 39 (1994) 2619-2628.

[54] H. Cong, H.T. Michels, J.R. Scully, Passivity and pit stability behavior of copper as a function of selected water chemistry variables, Journal of The Electrochemical Society, 156 (2009) 16-27.

[55] G. Ruijini, S.C. Srivastava, M.B. Ives, Pitting corrosion behavior of UNS N08904 stainless steel in a chloride-sulfate solution, Corrosion, 45 (1989).

[56] N. Sridhar, G.A. Cragnolino, Applicability of repassivation potential for long-term prediction of localized corrosion of alloy 825 and type 316L stainless steel, Corrosion, 49 (1993) 885-894.

[57] M.T. Woldemedhin, J. Srinivasan, R.G. Kelly, Effects of environmental factors on key kinetic parameters relevant to pitting corrosion, Journal of Solid State Electrochemistry, 19 (2015) 3449-3461.

[58] J. Srinivasan, C. Liu, R.G. Kelly, Geometric evolution of flux from a corroding one-dimensional pit and its implications on the evaluation of kinetic parameters for pit stability, Journal of The Electrochemical Society, 163 (2016) C694-C703.

[59] D.S. Dunn, N. Sridhar, G.A. Cragnolino, Long-term prediction of localized corrosion of alloy 825 in high-level nuclear waste repository environments, Corrosion, 52 (1996) 115-124.

[60] J. Srinivasan, R.G. Kelly, On a recent quantitative framework examining the critical factors for localized corrosion and its impact on the Galvele pit stability criterion, Corrosion, 73 (2017) 613-633.

[61] N.J. Laycock, R.C. Newman, Temperature dependence of pitting potentials for austenitic stainless steels above their critical pitting temperature, Corrosion Science, 40 (1998) 887-902.

[62] H.P. Leckie, H.H. Uhlig, Environmental factors affecting the critical potential for pitting in 18–8 stainless steel, Journal of The Electrochemical Society, 113 (1966) 1262-1267.

[63] F. King, M.J. Quinn, C.D. Litke, Oxygen reduction on copper in neutral NaCl solution, Journal of The Electrochemical Society, 385 (1995) 45-55.

[64] S.M. Mayanna, T.H.V. Setty, Role of chloride ions in relation to copper corrosion and inhibition, Proceedings of the Indian Academy of Sciences - Section A, 80 (1974) 184-193.

[65] D. Kong, C. Dong, M. Zhao, X. Ni, C. Man, X. Li, Effect of chloride concentration on passive film properties on copper, Corrosion Engineering, Science and Technology, 53 (2017) 122-130.

[66] D. Kong, C. Dong, X. Wei, C. Man, X. Lei, F. Mao, X. Li, Size matching effect between anion vacancies and halide ions in passive film breakdown on copper, Electrochimica Acta, 292 (2018) 817-827.

[67] S.B. Adeloju, Y.Y. Duan, Influence of bicarbonate ions on stability of copper oxides and copper pitting corrosion, British Corrosion Journal, 29 (1994) 315-320.

[68] N.G. Smart, J.O.M. Bockris, Effect of Water Activity on Corrosion, Corrosion, 48 (1992) 277-280.

[69] G. Mankowski, J.P. Duthil, A. Giusti, The pit morphology on copper in chloride- and sulphate-containing solutions, Corrosion Science, 39 (1997) 27-42.

[70] K. Venu, K. Balakrishnan, K.S. Rajagopalan, A potentiokinetic polarization study of the behaviour of steel in NaOH-NaCl system, Corrosion Science, 5 (1965) 59-69.

[71] M.G. Alvarez, J.R. Galvele, Pitting of high purity Zinc and pitting potential significance, Corrosion, 32 (1976) 284-294.

[72] D. Macdonald, The point defect model for the passive state, Journal of The Electrochemical Society, 139 (1992) 3434-3449.

[73] S. Matin, A. Tahmasebi, M. Momeni, M. Behazin, M. Davison, D.W. Shoesmith, J.J. Noël, Use of multielectrode arrays and statistical analysis to investigate the pitting probability of Copper. Part I: The effect of chloride, Journal of The Electrochemical Society, 169 (2022).

[74] F. Mao, C. Dong, S. Sharifi-Asl, P. Lu, D.D. Macdonald, Passivity breakdown on copper: Influence of chloride ion, Electrochimica Acta, 144 (2014) 391-399.

[75] Biesinger, M. C., Advanced analysis of copper X-ray photoelectron spectra, Surface and Interface Analysis, 49 (2017) 1325-1334.

[76] F. King, C. Lilja, K. Pedersen, P. Pitkänen, M. Vähänen, An update of the state-of-the-art report on the corrosion of copper under expected conditions in a deep geologic repository, SKB, 2010.

[77] D.D. Macdonald, The history of the Point defect model for the passive state: A brief review of film growth aspects, Electrochimica Acta, 56 (2011) 1761-1772.

[78] J. Kunze, V. Maurice, L.H. Klein, H.-H. Strehblow, P. Marcus, In situ STM study of the effect of chlorides on the initial stages of anodic oxidation of Cu(111) in alkaline solutions, Electrochimica Acta, 48 (2003) 1157-1167.

[79] A. Nishikata, M. Itagaki, T. Tsuru, S. Haruyama, Passivation and its stability on copper in alkaline solutions containing carbonate and chloride ions, Corrosion Science, 31 (1990) 287-292.

[80] C.F. Baes, R.E. Mesmer, The hydrolysis of cations, John Wiley & Sons, New York, 1976.

[81] V.K. Sharma, F.J. Millero, The oxidation of Cu (I) in electrolyte solutions, Journal of Solution Chemistry, 17 (1988) 581-599.

[82] F. King, Corrosion of copper in alkaline chloride environment, Swedish Nuclear Fuel and Waste Management Co, 2002.

Chapter 6

6 Conclusions and Future Work

6.1 Conclusions

The main goal of this research was to investigate the pitting probability of Cu in various unary and binary environments containing chloride, sulfate, and bicarbonate. A wide range of electrochemical, statistical, and surface analysis techniques were performed to evaluate the pitting properties, oxide composition, and surface morphology of Cu in the above mentioned environments.

The first part of this research (Chapter 4) was focused on the evaluation of pitting susceptibility of Cu in chloride-containing solution using electrochemical and statistical analysis. The surface morphology of corroded specimens was investigated using SEM. On all specimens, E_{corr} increased with time due to the formation of an oxide layer, followed by a self-repairing process within it over time. Increasing [Cl$^-$] resulted in a lower average E_{corr}, while the range of E_{corr} values increased. The lower average value of E_{corr} can be due to the aggressive effect of Cl$^-$ on the passive film, particularly dissolution of Cu(I) as $CuCl_2^-$. The E_b and E_{rp} were also shifted to more negative values with increasing [Cl$^-$]. A higher pitting probability of Cu was observed at higher [Cl$^-$]. Also, these measurements suggest that pit propagation would be possible in all the chloride-containing solutions used, since the distributions of E_{rp} values were located at potentials lowert than the potential range over which E_{corr} was distributed. A strong dependency of E_b, and similar dependencies of E_{corr} and E_{rp}, on the [Cl$^-$] were observed in this research. From statistical point of view, the IQR of E_{corr} for different chloride concentrations indicated a wider dispersion at higher [Cl$^-$], with no outliers under any of the conditions tested. The dispersion of E_b decreased with increasing [Cl$^-$] up to 0.1 M; however, a further increase in [Cl$^-$] resulted in a larger IQR with the presence of outliers in 0.01 and 0.1 M Cl$^-$ solutions. The IQR of E_{rp} decreased with increasing [Cl$^-$] from 0.01 to 0.1 M, while a further increase in [Cl$^-$] to 1 M contributed to a larger IQR, with the presence of an outlier, changing the shape of the distribution to a right-skewed distribution. This

heavy tail might increase the probability of repassivation, as it is located on the right side of the Erp distribution, which might result in a greater chance of Ecorr < Erp. The measured values were fitted with a variety of different distribution functions to determine whether any of these functions provided reasonable representations of the measured data. Finally, five distribution functions were selected for use in the analysis, based on the quality of fit with a confidence level of 90%. The pitting probability of Cu under different conditions was calculated for every combination of distribution functions representing E_{corr} and E_b values. As a result, a greater probability of Cu pitting was observed in 1 M Cl^- solutions than in 0.01 and 0.1 M Cl^- solutions. Since the the PDF of E_{rp} was located to the left side of that for E_{corr}, overlap between the PDFs of E_{corr} and E_{rp} could be understood asindicating the repassivation probability of Cu. Our investigation showed a lower probability of repassivation in lower $[Cl^-]$ solutions that might be due to the higher concentration of dissolved copper species in the bottom of pits in solutions with high chloride concentration, which enhanced the repassivation process.

In the second part of this research (Chapter 4), the pitting probability of Cu in unary (sulfate) and binary (sulfate + bicarbonate) solutions was investigated using electrochemical techniques in combination with statistical analysis. E_{corr} increased with time at all concentrations of SO_4^{2-} due to the formation of an oxide film on the Cu surface. The distribution range of E_{corr} was almost contatnt for all concentrations at pH 8; however, the distribution range of E_{corr} decreased with increasing $[SO_4^{2-}]$ at pH 9. At both pH 8 and pH 9, E_b shifted to more negative values with increasing $[SO_4^{2-}]$, signifying a lower protectiveness of the film at higher $[SO_4^{2-}]$. The experimental results showed that the pitting probability was dependent on both $[SO_4^{2-}]$ and pH. Increasing $[SO_4^{2-}]$ shifted E_{rp} to more positive values, the opposite of what we observed in chloride-containing solutions. The addition of HCO_3^- shifted E_{corr} to more positive values and increased its distribution range at both pH 8 and pH 9. The average E_b shifted to more positive values in the presence of HCO_3^-, as illustrated, indicating an increase in the stability of the passive film. Increasing $[HCO_3^-]$ resulted in a shift in E_{rp} to more negative values and widened the distribution range. Based on the IQR and histogram of E_{corr} values for different $[SO_4^{2-}]$ at pH 8, the same distribution was observed for all concentrations; however, outliers were observed on the higher potential side of the IQR

for 0.005 M and 0.1 M SO_4^{2-} solutions. The presence of outliers might increase the pitting probability, due to the formation of right-skewed distribution curves. At pH 9, the IQR became narrower with increasing $[SO_4^{2-}]$, leading to a narrower distribution range. Also, outliers were observed on the high-potential side of the distribution curve of E_{corr} in 0.001 M and 0.1 M SO_4^{2-}, which could suggest an increase in the pitting probability. At pH 8, increasing $[SO_4^{2-}]$ did not change the distribution of E_b values significantly, while, at pH 9, the distribution of E_b values decreased significantly in solutions with $[SO_4^{2-}]$ higher than 0.005 M. Outliers were observed in 0.001 M and 0.005 M SO_4^{2-} at pH 9, indicating the presence of a heavy tail distribution curve that might result in a greater pitting probability. The IQR of E_{rp} decreased with increasing $[SO_4^{2-}]$ at both pH 8 and pH 9, indicating a narrower distribution of values at higher $[SO_4^{2-}]$. Outliers were observed at all $[SO_4^{2-}]$ except 0.001 M, which might increase the probability of either pitting or repassivation, depending on the position of E_{rp} relative to E_{corr}. The maximum pitting probability was observed at 0.01 M SO_4^{2-} at pH 8 and while it happened at 0.005 M SO_4^{2-} at pH to 9. The repassivation probability increased with increasing $[SO_4^{2-}]$ up to 0.005 M; however, the distribution of E_{rp} shifted to higher potentials relative to that of E_{corr} with a further increase in $[SO_4^{2-}]$ for both pH 8 and pH 9 (natural pitting).. In 0.01 M $[SO_4^{2-}]$ solutions with different $[HCO_3^-]$ and pH, the highest pitting probability was observed in solution with 0.0002 M HCO_3^- at pH 8. On the other hand, HCO_3^- had minimal effect on the pitting probability of Cu in 0.01 M $[SO_4^{2-}]$ at pH 9. The presence of bicarbonate in sulfate-containing solution resulted in a transition from natural pitting to repassivation.

In chapter 5, the pitting behaviour, surface composition, and passive film morphology of Cu in chloride-containing buffer solutions were studied. Increasing the $[Cl^-]$ shifted the corrosion behaviour from passive to active dissolution. E_{corr} decreased with increasing chloride concentration, due to a higher dissolution rate. Passive film analysis was performed using SEM. In 0.01 M $[Cl^-]$, breakdown of the passive film was observed; however, a uniform film with small numbers of breakdown events was observed at 0.1 M $[Cl^-]$. In 1 M $[Cl^-]$ solution, a porous oxide film was observed, without any sign of localized attack. Multielectrode arrays were used to find the range of potentials in which pitting might occur. Then a potentiostatic technique was used to investigate the pitting

susceptibility of Cu under simulated conditions. In 0.01 M [Cl⁻], with applied potential close to E_{corr}, the the current-time transient showed a sharp decrease in current followed by a plateau. At applied potential close to E_b, a sharp drop in current was observed, followed by an abrupt increase due to the nucleation and growth of oxide and hydroxide films. After the current reached the apex, it decreased over time until it became a plateau. In the solution containing 0.1 M [Cl⁻], the current-time transient showed the same behaviour for both applied potentials, due to the slight difference between E_b and E_{corr}. The only difference was that the current drop was not observed in the early stage of the experiment for either applied potential, which indicated that the formation of the passive film was not a progressive nucleation process, unlike in 0.01 M [Cl⁻]. The surface morphology of Cu in 0.01 M [Cl⁻] was studied at different applied potentials. No pitting was detected at an applied potential of -27 mV vs SCE. At applied potential of 7 mV vs SCE, a very deep pit with salt at the pit surface was observed, which is in good agreement with the pit growth mechanism under diffusion control. XPS results showed the presence of both Cu (I) and Cu (II) oxides at different applied potentials, while the percentages of each oxide were different depending on the applied potential. It is important to note that $CuCO_3.Cu(OH)_2$ was not observed on any samples. Carbonate played a role as a stabilizer of the copper oxide film and did not form another film on the surface to protect the oxide film. Increasing the carbonate concentration resulted in higher buffer capacity of solution which in turn led to the adsorption of greater amount of carbonate on the oxide film. As a result, oxide film was stabilized and protected by avoding the adsorption of chloride on the surface.. The surface morphology of Cu in 0.1 M [Cl⁻] was studied. Various dissolution processes were observed, such as a large frequency of small pits followed by pit propagation, formation of the second layer of oxide or/and hydroxide film on top of the first oxide film where the local breakdown happened, local dissolution of Cu at triple points, active dissolution of Cu after passive film breakdown, and elongated pitting corrosion. The presence of pits with different morphologies in the same solution confirmed the stochastic nature of the pitting process. XPS results showed the presence of Cu_2O and $Cu(OH)_2$, without any traceable amount of CuO. Increasing the [Cl⁻] to 0.1 M hindered the formation of CuO. Moreover, the surface was mostly covered with Cu_2O at potentials lower than -27 mV vs SCE; although,

conversion of Cu_2O to $Cu(OH)_2$ occurred with increasing of the potential to 7 mv VS SCE.

6.2 Future Work

Through this research, electrochemical experiments combined with statistical analysis were performed to investigate the pitting probability of Cu in different unary and binary solutions including those containing aggressive anions such as chloride and sulfate. This study has shown that chloride increases the pitting probability and sulfate has either positive or negative effect on the pitting probability of Cu, depending on the concentration. However, a significant number of issues remain to be solved.

i.   Studies on electrodeposited and cold spray Cu specimens are required since they are more representative of the used fuel container coatings. These studies will provide more insight about the pitting probability of Cu in Canadian DGR and how the surface condition and microstructure of the used fuel containers could affect the pitting probability of Cu.

ii. In this research, unary and binary solutions were investigated; however, under real conditions, more anions will be in the environment in contact with Cu so, it is important to investigate the pitting behaviour of Cu in different environments such as ternary solutions containing chloride, sulfate, and bicarbonate as well as simulated groundwaters with their full natural complexities to see how aggressive anions behave when both are present in the solution.

iii. The container will be covered with bentonite clay in the DGR; as a result, investigation of pitting susceptibility of Cu in the presence of bentonite and aggressive anions is necessary.

iv. This research has mostly focused on electrochemical results and statistical analysis, while surface analysis and evaluation of oxide film morphology in different corrosive environments will give more information about the stochastic nature of passive film breakdown.

v.   All experiments were performed using either potentiodynamic polarization or potentiostatic polarization tests within a short time; longer-term exposure of Cu to

different environments could provide useful information about the corrosion processes as well as the type of oxide films on the surface.

Curriculum Vitae

Sina Matin

EDUCATION

Doctor of Philosophy, Physical and Analytical Chemistry	2017-2023
Western University, London, ON	

Master of Science, Materials Engineering, Corrosion	2011-2013
Shiraz University, Shiraz, Iran	

Bachelor of Science, Materials Engineering	2005-2009
Malek Ashtar University of Technology, Isfahan, Iran	

PROFESSIONAL EXPERIENCE

Account Manager / Business Development Specialist	August 2022 – Present
ThermoFisher Scientific, Southwestern Ontario	

Research and Teaching Assistant	September 2017 – August 2022
Western University, London, ON	

Corrosion Engineer Consultant (Part-Time)	June 2021 – June 2022
Corrsolution LTD & MEG Energy, Calgary, AB	

HONOURS, SCHOLARSHIPS, AND AWARDS

NACE Dennis B Dutton Award for Student Leadership Excellence Scholarship	2022
Dr. N. Stewart McIntyre Award in Surface Science	2021
NACE Graduate Student Excellence Award	2021
PRiME Travel Grant Award (ECS)	2020
NACE Travel Assistance Award	2020
NACE Graduate Student Book Award	2020

Best Poster Award — NACE Northern Area Eastern Conference	2019
Best Poster Award — NACE SOSS	2019
Christian Sivertz Scholarship	2017
Nanofabrication Support Award	2017
Western Graduate Research Scholarship	2017
Top Downloaded Paper — Journal of Advanced Materials and Processes	2017
Ranked first in the Nationwide Ph.D. entrance examination in Materials Science and Engineering	2016
Top Student Award	2013
Best Oral Presentation Award — National Corrosion Congress	2013
Encouragement Support for Nanotechnology Activity Scholarship	2012

SELECTED PEER-REVIEWED PUBLICATIONS

1. Matin S., Henderson J. D., Kobe B., Biesinger M., Shoesmith D., Noël J.J., "Investigating the pitting susceptibility, passive film morphology, and surface composition of copper exposed to bicarbonate solutions containing chloride or sulfate". (Journal of NPJ Materials Degradation, Nature Partner Journal, under review).

2. Matin S., Morgan A., Tahmasebi A., Zagidulin D., Behazin, M., Shoesmith D., Davidson M., Noël J.J., "Use of multielectrode arrays and statistical analysis to investigate the pitting probability of copper Part II: The effect of sulfate and bicarbonate", (Journal of The Electrochemical Society, under review).

3. Vander Zee A., Laundry-Mottiar L., Nikpour S., Matin S., Henderson Jeffrey, Biesinger M., Noël J.J., Hedberg Y. S., "Effect of amino acids on the corrosion and Metal release from copper and stainless steel", Journal of the Electrochemical Society, Vol.170, No.2, 2023.

4. Matin S., Tahmasebi A., Momeni M., Behazin, M., Shoesmith D., Davidson M., Noël J.J., "Use of multielectrode arrays and statistical analysis to investigate the pitting probability of copper Part I: The effect of chloride", Journal of The Electrochemical Society, Vol. 169, No. 6, 2022.

5. Matin S., Pakshir M., "Evaluation of the pitting corrosion behaviour of Al-nano ZrO_2 composite produced by accumulative roll bonding (ARB) process", Journal of Advanced Processes in Materials, Vol.10, No.2, 2016.

6. Morshed Behbahani K., Pakshir M, Matin S., "Comparison of solution-treatment effect on intergranular corrosion of 304 and 321 stainless steel by electrochemical impedance technique", Journal of Advanced Processes in Materials, Vol.8, No.1, 2014.

CERTIFICATES

Foundation of Project Management   2020
MITACS Organization, London, ON

Master the Entrepreneurship Skill   2020
Ivey Business School, Western University, London, ON

Laboratory Safety Hazardous Waste Management   2017
Western University, London, ON

Supervisor and Worker Health and Safety   2017
Western University, London, ON

ASNT VT, PT, MT, and UT Level II   2010
Gamma Rad, Shiraz, Iran

MEMBERSHIPS

Ontario Society of Professional Engineers (OSPE)   2018 – Present

Association for Materials Protection and Performance (AMPP)   2017 – Present

Electrochemical Society (ECS)   2017 – Present

Canadian Nuclear Society (CNS)   2017 – Present

American Society of Mechanical Engineers (ASME)   2010 – Present